EXPERIMENTAL AND NUMERICAL STUDIES OF GEOSYNTHETIC-REINFORCED CLAYS AND SILTS UNDER ENVIRONMENTAL-INDUCED SWELLING

by

Yadav Prasad Pathak

A Thesis
Submitted to the Faculty of Graduate Studies
in Partial Fulfillment of the Requirements
for the Degree of

DOCTOR OF PHILOSOPHY

Department of Civil Engineering
University of Manitoba
Winnipeg, Manitoba

ABSTRACT

Current design guidelines for reinforced soil walls and slopes recommend the use of granular soils such as gravels and sands as select fills. Cost savings could potentially be realized by using on-site clays and silts. Some clays are swelling and silts are frost susceptible. When considering the use of swelling clays and frost susceptible silts as fills, environmental loading due to swelling-shrinkage and freeze-thaw effects from environmental changes could become a design issue.

To examine the hypothesis that consideration of environmental loading during design will produce improvements in the performance of geosynthetic-reinforced soil structures that use clays or silts as fill materials, experimental and numerical studies were undertaken. Geosynthetic-reinforced clay specimens were subjected to wetting and drying in a model test apparatus developed and commissioned for this study. In separate test set-up, reinforced silt specimens were subjected to freezing and thawing. Tests on unreinforced specimens were also performed in otherwise identical conditions for comparison purposes. Movements of the specimens, soil strains, reinforcement strains, soil suctions and soil temperatures were monitored during the application of environmental loading in addition to mechanical loading from external stresses.

The results of the laboratory model tests showed that reinforcements reduced horizontal displacements of the clay specimens during wetting and drying. The

same is true for the case of silt during freezing and thawing. The environmental loading induced strains, and therefore stresses in the reinforcements. The measured geogrid strain during the wetting-drying of reinforced clay specimen was up to 0.75%. Similarly, the measured geogrid strain in the reinforced silt specimen during freezing-thawing cycles was up to 0.57%. The strains were greater than the strains generated by mechanical loading for the range of applied stresses used in this study.

Numerical models were developed to simulate wetting only induced swelling of reinforced clays and freezing only induced expansion of reinforced silts specimens. They were used to simulate the results of laboratory model tests. The performance of geosynthetic-reinforced soil slopes with swelling clay fills and frost susceptible silt fills was evaluated. Parametric studies were performed to determine important parameters affecting the performance of reinforced clay and silt slopes.

ACKNOWLEDEMENT

It is a pleasure to thank the many people who made this thesis possible.

I would like to express my profound and sincere gratitude to my advisor Dr. Marolo C. Alfaro, for his endless patience, continuous guidance, encouragement and friendship from the very early stage of this research. He always provided his valuable time, knowledge and great effort to explain every aspect of this research clearly and simply. I would have been lost without him.

I gratefully acknowledge to Dr. Jim Graham and Dr. James Blatz for their many helpful discussions throughout the research work and for invaluable advice, encouragement and friendship. Thanks to Dr. Raghavan Jayaraman, Department of Mechanical and Manufacturing Engineering, University of Manitoba for serving in my research committee and providing very important comments and suggestion.

Thanks to Kerry Lynch and Norang Piamsalee (Tai) for their technical support and advice in the laboratory. Their hard work made the experimental program a successful one.

The author gratefully acknowledges the financial support of the Natural Sciences and Engineering Research Council of Canada (NSERC) and Manitoba Infrastructure and Transportation. Financial support to the author was provided

by Neil Burgess Memorial Scholarship. I am thankful to Andy Anderson of Tensar Earth Technology Inc., Atlanta, Georgia, USA for donating geogrid reinforcements used for this research.

During this work, I have collaborated with many colleagues within the Department of Civil Engineering, for whom I have great regards, and I appreciate their help with my work and their friendship.

Lastly, and most importantly, I wish to thank to my family: my wife Kabita Pathak and my daughter Sneha Pathak, my parents Jagannath and Krishnamaya Pathak, my brothers, sisters-in-law, nephews, nieces, parents-in-law and brothers-in-law for their love, support and encouragement during this study.

TABLE OF CONTENTS

LIST OF SYMBOLS AND ABBREVIATIONS

Symbols

A	- Cross-sectional area (m^2)
a_1, c_1, a_3, c_3	- Dimensionless soil properties in logarithmic functions
B	- Skempton's pore pressure parameter (%)
c	- Soil cohesion (kN/m^2)
C	- Specific heat capacity of soil (J/kg °C)
C_c	- Coefficient of curvature of soil particle size distribution curve
C_i	- Specific heat capacity of ice (J/kg °C)
C_s	- Specific heat capacity of soil particle (J/kg °C)
C_u	- Coefficient of uniformity of soil particle size distribution
C_w	- Specific heat capacity of water (J/kg °C)
D_{10}	- Soil particle diameter at which 10% of the soil is finer (m)
D_{30}	- Soil particle diameter at which 30% of the soil is finer (m)
D_{60}	- Soil particle diameter at which 60% of the soil is finer (m)
$d\varepsilon^e_s$	- Elastic shear strain increment (%)
$d\varepsilon^e_v$	- Elastic volumetric strain increment (%)
$d\varepsilon^p_q$	- Plastic deviatoric strain increment (%)
$d\varepsilon^p_{vp}$	- Plastic volumetric strain increment (%)
$d\varepsilon^p_{vs}$	- Plastic volumetric strain increment in SI yield surface (%)
E	- Young's modulus of elasticity (kN/m^2)
e	- Void ratio

G - Elastic shear modulus of soil (kN/m^2)

G_S - Specific gravity

H - Height (m)

I_p - Plasticity index

K - Elastic bulk modulus of soil (kN/m^2)

k - Thermal conductivity of soil ($W/m°C$)

K_0 - at-rest lateral or horizontal earth pressure coefficient

K_b - Soil-reinforcement interface shear stiffness (kN/m/m)

L - Reinforcement length (m)

M - Slope of the critical state line

$N(s)$ - Specific volume at reference pressure on NCL at s = const

p - Net mean stress (kN/m^2) = $(\sigma_1+2\sigma_3)/3$

p' - Mean principal effective stress (kN/m^2)

p_0 - Preconsolidation stress at the current value of suction (kN/m^2)

p_0^* - Preconsolidation stress at full saturation (kN/m^2)

p_{atm} - Atmospheric pressure (kN/m^2)

p^c - Reference stress (kN/m^2)

peri - Reinforcement exposed perimeter (m)

q - Deviator stress (kN/m^2) = $\sigma_1-\sigma_3$

q^T - Heat-flux vector (W/m^2)

q^T_v - Volumetric heat source intensity (W/m^3)

r - Soil parameter describing $\lambda(s)$

s - Matric suction (kN/m^2)

S_b - Soil-geosynthetic interface cohesive strength (kN/m)

T - Temperature (°C)

t - Time (sec)

u_a - Pore air pressure (kN/m^2)

u_w - Pore water pressure (kN/m^2)

V - Specific volume = 1+e

V_0 - Initial specific volume

w - Soil moisture content (%)

W - Width (m)

w_f - Frozen water content (%)

w_L - Liquid limit (%)

w_{opt} - Optimum moisture content (%)

w_p - Plastic limit (%)

w_u - Unfrozen water content (%)

x,y,z - Co-ordinate axes (m)

ycomp - Reinforcement compressive yield limit (kN)

yield - Reinforcement Tensile yield limit (kN)

Δu - Change in pore pressure (kN/m^2)

$\Delta\sigma_{xw}$ - Wetting-induced stress in x - direction (kN/m^2)

$\Delta\sigma_{yw}$ - Wetting-induced stress in y - direction (kN/m^2)

$\Delta\sigma_{zw}$ - Wetting-induced stress in z - direction (kN/m^2)

α - Coefficient of linear thermal expansion (1/°C)

β - Soil parameter describing $\lambda(s)$

δ - Soil-geosynthetic interface interface frictional angle (^{o})

δ_{ij} - Kronecker delta

δ_{x1}, δ_{x2} - Horizontal soil displacement at the middle of soil specimen (m)

δ_{xb} - Horizontal displacement at bottom of soil specimen (m)

δ_{xt} - Horizontal displacement at top of soil specimen (m)

δ_y - Vertical displacement of soil specimen (m)

ε, ε_{x1}, ε_{x2}, ε_{x3} - Soil strain (%)

ε_1 - Axial strain (%)

ε^T_{ij} - Thermal strain (%)

ε_{xw} - Wetting-induced strain in x-direction (%)

ε_{yw} - Wetting-induced strain in y-direction (%)

ε_{zw} - Wetting-induced strain in z-direction (%)

ϕ'_{cs} - Internal angle of friction at critical state (^{o})

γ_{dmax} - Maximum dry unit weight (kN/m^3)

γ_{dry} - Dry unit weight (kN/m^3)

κ - Elastic compressibility parameter for change in net mean stress

$\lambda(0)$ - Compressibility parameter for changes in net mean stress for virgin states of the soil at $s = 0$

$\lambda(s)$ - Compressibility parameter for changes in net mean stress for virgin states of the soil at the current values of s

λ_s - Stiffness parameter for changes in suction for virgin states of soil

κ_s - Elastic stiffness parameter for changes in suction

μ_1, μ_2 - Scalar multipliers

ν - Poisson's ratio

ρ - Density of soil (kg/m^3)

σ" - Net normal stress (kN/m^2)

σ_1, σ_y - Vertical total principal stress (pressure) (kN/m^2)

σ_3, σ_x - Horizontal total principal stress (pressure) (kN/m^2)

σ_c' - Effective consolidation pressures (kN/m^2)

σ^T_{ij} - Thermal stress (kN/m^2)

ζ_T - Stored heat per unit volume (J/m^3)

Abbreviations

AASHTO - American Association of State Highway and Transportation Officials

ASTM - American Society for Testing and Materials

BBM - Barcelona Basic Model

CH - High plastic clay

CL - Lean clay

CID - Isotropically consolidated drained test

CIŪ - Isotropic consolidated undrained test

CSL - Critical State Line

DA - Data acquisition

EWR - Electrical wire resistance

FHWA - Federal Highway Administration

FLAC - Fast Lagrangian Analysis of Continua

GRI - Geosynthetics Research Institute

GRS - Geosynthetic-reinforced soil

LC - Loading collapse

LPS - Linear position sensor

LVDT - Linear variable displacement transducer

MD - Machine direction

NAGS - North American Geosynthetics Society

NCHRP - National Cooperative Highway Research Project

NCL - Normally consolidated line

RP - Reinforced specimen for clay

RT - Reinforced specimen for silt

SGIP - Soil-geosynthetic interactive performance

SI - Suction increase

UCD - Unit cell device

UP - Unreinforced specimen for clay

USCS - Unified Soil Classification System

UT - Unreinforced specimen for silt

UU - Unconsolidated undrained

XMD - Cross-machine direction

LIST OF TABLES

LIST OF FIGURES

CHAPTER 1

INTRODUCTION

1.1 RESEARCH BACKGROUND

Geosynthetics have been in use as tensile reinforcement in stabilizing soil slopes and embankments since the early 1970's. Soil masses containing horizontally placed layers of geosynthetic reinforcement are commonly referred to as geosynthetic-reinforced soil (GRS) structures. When subject to a vertical load, a GRS structure typically exhibits higher load carrying capacity than the same soil retaining structure without the reinforcement. The increase in strength is a result of an internal restraining effect imposed by the geosynthetic reinforcement on the GRS structure. Geosynthetic reinforcement restrains deformation of the GRS structure along the axial direction of the reinforcement because of soil and geosynthetic interaction through interface friction (Vidal 1969). The GRS system has been proven to be a valuable alternative for retaining soil in geotechnical and transportation related projects where there is restricted right-of-way. Otherwise conventional reinforced concrete retaining walls would be needed, which could be very costly. For example, the reinforced soil retaining wall system has been very popular worldwide because of its relatively low cost, good aesthetics, simple construction, and ability for use in a wide variety of site conditions. An estimated

900,000 m^2 of reinforced soil wall facing are constructed annually in the United States alone (Walters 2004).

Current design guidelines of the American Association of State Highway and Transportation Officials (AASHTO 2000) and Federal Highway Administration (FHWA 2001) for reinforced soil walls and slopes recommend granular soils (also called coarse-grained soil or select fills). Select fills are generally gravel and sand with fine contents less than 15% (Zornberg and Kang 2005, Stulgis 2005a). Consequently, the economic benefits of reinforced soil walls and slopes are largely limited by the availability of granular fill that is usually imported to the construction site. The use of granular soils as select fills has been reported to be the most expensive component of reinforced soil retaining systems, typically corresponding to 40% of the total construction costs (Zornberg and Kang 2005). Cost savings could potentially be realized by using on-site native soils or lower cost quarried materials, mostly fine-grained soils (marginal soils or non-select fills). The potential savings from replacing AASHTO reinforced fill materials with marginal fill could be in the range of 20 to 30% of the current cost of reinforced soil walls and slopes (Stulgis 2005a). Concerns about using marginal soils as backfill in the reinforced zones of the GRS structures include the low permeability of such soils and their high susceptibility to environmental changes. Consideration must be given to stresses induced by frost heave and shrinkage and swelling of fine-grained soils when they are used as reinforced fill (Christopher and Stulgis 2000). A fully-instrumented full-scale field test is

currently being performed in the US under the National Cooperative Highway Research Project (NCHRP) to develop selection guidelines, soil parameters, testing methods, and construction specifications that will allow the use of a wider range of reinforced fill materials (Stulgis, 2005b).

1.2 JUSTIFICATION OF RESEARCH

In Manitoba, Canada there are ample possibilities for using geosynthetics to stabilize highway slopes and embankments, flood protection dykes, as well as for creating steeper slopes at highway interchanges and bridge sites to minimize the need for Right-of-Way acquisition that would otherwise require wider embankments with larger footprints. Cost savings can be realized further when locally available silts and clays are used instead of select granular fills that need to be imported. However, clays in Manitoba are generally swelling-clays due to their high content of montmorillonite, while silts are frost susceptible. Furthermore, the prairie region of Canada where Manitoba is located is known for its severe climatic conditions. When considering the use of swelling clays and frost susceptible silts, environmental effects (swelling-shrinkage potential and freeze-thaw) may become an important consideration. Presently, there is no design and construction guideline using locally-available clays and silts where environmental changes are extreme such as in places like Northern and Western Canada.

Few research studies are found in literature on GRS structures that use clay and silts as fills in the cold regions. Additional research is required to understand the effects of environmental changes on the performance of the GRS structures using non-select backfills and to evaluate possible additional stress in the geosynthetic reinforcement.

1.3 HYPOTHESIS

This thesis document examines the following hypothesis: Consideration of environmental loading during design will produce improvements in the performance of GRS structures that use swelling clays and frost-susceptible silts as backfill materials.

1.4 RESEARCH OBJECTIVES AND SCOPES

This study mainly focuses on the effects of environmental loading on GRS structures with swelling clays and frost susceptible silts. The swelling-shrinkage upon wetting-drying of reinforced swelling clay and heave-consolidation upon freezing-thawing of reinforced silt is investigated. The main objectives of this research are:

(a) To evaluate the additional strains/stresses induced in geosynthetic reinforcement due to frost heave of silty soils during freezing and swelling of clays during wetting.

(b) To investigate the deformation behaviour in geosynthetic-reinforced soil during environmental-induced swelling.

Additional internal strains and stresses induced by environmental changes (wetting-drying cycles of swelling clay and freezing-thawing cycles of frost susceptible silt) may have considerable effects on the performance of reinforced soil structures. Laboratory tests have been carried out on geosynthetic-reinforced clay/silt blocks in plane-strain under working load condition. The tests have been performed under wetting-drying and freezing-thawing cycles. Numerical analyses have been carried out to closely simulate wetting and freezing conditions in the reinforced clay and silt respectively, and provide more information on the performance of reinforced soil with non-select fills.

The scope of this research includes the following:

- Develop a large-scale plane-strain testing apparatus at the University of Manitoba.
- Carry out wetting-drying tests on geogrid-reinforced clay specimens and freezing-thawing tests on geogrid-reinforced silt specimens.
- Develop FISH code for the Barcelona Basic Model in Fast Lagrangian Analysis of Continua (FLAC) computer program to simulate response of reinforced soil under mechanical loading.

- Develop simple constitutive model in FLAC to simulate the swelling response of reinforced swelling clay during wetting.
- Use a built-in simple thermal-mechanical model in FLAC to simulate the expansion of frost susceptible silt during freezing.
- Validate the numerical models with the laboratory test results.
- Use of models developed to examine hypothetical clay and silt reinforced slopes and carry out parametric studies in GRS structures to determine important parameters affecting the performance of such structures subjected to environmental loading.

1.5 THESIS ORGANIZATION

The thesis is organized as follows: Chapter 2 provides the summary of a literature review of existing researches in geosynthetic-reinforced soil using marginal soil backfill. Emphasis has been given to the researches which take into account the environmental effects (wetting-drying and freezing-thawing). The literature review is organized into aspects of laboratory tests, numerical modelling and full-scale tests on geosynthetic-reinforced soil structures with marginal soil backfill.

Chapter 3 discusses the laboratory testing program. Development of plane-strain test apparatus and test set-up for wetting-drying and freezing-thawing tests are described. Properties of soils and geogrid are presented. Details of wetting-

drying test and freezing-thawing test procedures, instrumentation and monitoring are also described in this chapter.

Chapter 4 presents details of the instrumentation of laboratory test data in terms of geogrid strain, soil deformation, soil suction and soil temperature. The performance of the reinforced specimens is discussed in terms of soil specimen deformation, reinforcement strains and soil-geogrid interaction.

Chapter 5 deals with development of numerical models to simulate wetting-induced expansion in swelling clay and freezing-induced expansion in frost susceptible silt in the geosynthetic-reinforced soil specimens. Details of the stress-deformation analysis in the FLAC program are described. Validation of the numerical models is presented with laboratory test results in this chapter.

Chapter 6 presents the numerical analysis of the geosynthetic-reinforced slopes with marginal soil backfill under wetting and freezing condition using numerical models developed in the Chapter 5. Soil deformation and reinforcement load and strain are analyzed. Reinforced and unreinforced soil slopes are analyzed for comparison purposes. A parametric study of the geosynthetic-reinforced soil slopes is presented to evaluate the most important parameters for the performance of reinforced slopes with marginal soil backfill.

Finally, Chapter 7 summarizes the conclusions of this research program based on the laboratory test and numerical analysis. Recommendations for future research are also discussed at the end of this chapter.

CHAPTER 2

LITERATURE REVIEW

2.1 INTRODUCTION

There are no general design guidelines for reinforced soil structures using marginal soil backfills. More research is required to formulate a consistent design methodology for such structures with marginal soil backfills. However, there have been a number of studies published in the literature that investigated separate issues associated with using marginal fills for reinforced soil structures. This chapter presents the summary of previous laboratory, numerical and large scale field studies related to the use of fine-grained soils in geosynthetic-reinforced soil structures. The emphasis of this literature review is to look at previous studies that take the effects of environmental loading (wetting-drying and freezing-thawing) into design considerations for geosynthetic-reinforced soil structures with marginal fills.

2.2 LABORATORY TESTS IN FINE-GRAINED SOIL

2.2.1 Geosynthetic-Reinforced Fine-grained Soils under Mechanical Loading Only

To understand the overall behaviour of GRS structures using marginal soils, one has first to look into the behaviour of such structures under mechanical loading. This loading condition has been studied using common laboratory tests such as triaxial compression (Broms 1977, Holtz *et al.* 1982) and plane-strain compression (McGown *et al.* 1978, Tatsuoka and Yamauchi 1986, Whittle *et al.* 1992) in the case of reinforced sand. Laboratory tests on reinforced clay were also conducted using triaxial compression tests (Ingold 1983, Ingold and Miller 1983, Tatsuoka and Yamauchi 1986) and plane-strain compression tests (Ling and Tatsuoka 1994). Triaxial compression tests have been commonly used because of their simplicity and flexibility in controlling the stress and boundary conditions, although plane-strain conditions generally prevails in typical GRS structures. The above-indicated plane-strain compression tests on reinforced soil specimens were performed on relatively small specimens (dimensions less than 100 mm). Small specimen dimensions prohibit testing of a representative reinforced-soil specimen of a typical GRS structure. Nevertheless, they offered insight into the mechanisms of interaction between soil and reinforcement.

Boyle (1995) carried out laboratory tests on reinforced sand specimens in the plane-strain loading condition using a unit cell device (UCD) as shown in Figure

2.1 to study the composite behaviour of GRS structures. The unit cell specimen was representative of an element within a multilayered GRS structure. Construction-induced vertical stress in an element in the GRS structure was simulated by increasing the pressure on the top and bottom of the specimen. The specimen was laterally confined. The tests were performed under working stress conditions for short durations of loading. Vertical and horizontal displacements, vertical stress and the tensile load in the reinforcement of the GRS specimens were measured directly. Boyle (1995) observed that the geosynthetic reinforcement improved the load supporting capabilities of dense cohesionless soils by increasing the effective lateral confining pressure acting on the soil during lateral straining. Higher modulus reinforcement provided greater strength improvement, and reduced the deformation for a given applied load.

Wu and Helwany (1996) developed a large-scale laboratory test as shown in Figure 2.2, known as the soil-geosynthetic interactive performance (SGIP) test, to investigate the long term behaviour of reinforced soil specimens under plane-strain loading conditions. They conducted the tests both in clay and sand. They found soil deformed more than the geosynthetic reinforcement in clay backfill. As a result of soil geosynthetic interaction, the creep strains obtained from in-isolation tests were underestimated by a factor of 4. On the other hand, in sand backfill tests, the soil deformed less than the geosynthetic reinforcement, and the creep strains from in-isolation tests were overestimated by a factor of 2.5. This is also true for the short-term loading of reinforced soil specimens that were loaded

to failure. The in-soil stress-strain characteristics of geosynthetics are different from that of in-isolation (McGown *et al.* 1995**).** Ketchart and Wu (2002) modified Wu and Helwany's previous SGIP test set-up to simplify the sample preparation and testing procedure but they maintained the main features of the previous tests. The longitudinal direction of the test specimen was unconfined in the modified SGIP test (Figure 2.3) wherein the specimen was enclosed with rubber membrane. In the original SGIP test set-up (Figure 2.2), the lateral sides of the specimen were supported by flexible steel plates and the geosynthetic reinforcement was clamped on these flexible steel plates. Ketchart and Wu (2002) used a modified SGIP test apparatus for evaluating short- and long-term deformation behaviour of soil-geosynthetic composites. In the test, a specimen of soil-geosynthetic composite, with dimensions of 305 mm wide, 605 mm long, and 305 mm high, was subjected to a vertical sustained loads under plane-strain conditions. The applied load was transferred from the soil to the geosynthetic, and it allowed the soil and geosynthetic to deform in an interactive manner. Lateral and vertical displacements of the test specimen and strains in the reinforcement were measured. They conducted the tests in clay and road base soils (coarse-grained soil) to provide insights on their behaviour. Lesser vertical and horizontal displacements in reinforced specimens were observed than in unreinforced specimens. The reinforced specimens had higher failure loads than the unreinforced ones.

These results demonstrate the reinforcing effects resulting from reinforcement layers in the GRS mass. It was also observed that at small displacements, unreinforced and reinforced soil specimens showed almost identical deformation responses. The reinforcement inhibited specimen deformations after some vertical and horizontal displacements had occurred. This behaviour can be explained by the load transfer mechanism of the GRS mass. Under a vertical load, the GRS mass deforms in both vertical and horizontal directions. The horizontal deformation induces load on the reinforcement through interface friction. When deformations are small, the magnitude of the horizontal deformation may not be sufficient to mobilize tensile load in the reinforcement. That results in the same deformation response of unreinforced and reinforced soil masses at small strains.

The studies described earlier were carried out only under mechanical loading (self-weight of soil and surcharge load). The effects of environmental loading were not considered. Stresses induced by environmental loading (heave-consolidation of silty soils under freeze-thaw cycles; and swelling-shrinkage of swelling clay under wetting-drying cycles) under environmental changes need to be investigated when using fine-grained soils as fill materials in reinforced soil structures (Christopher and Stulgis 2000).

2.2.2 Geosynthetic-Reinforced Fine-grained Soils with Wetting-Drying Effect

Wetting-induced swelling strains and stresses in unreinforced compacted swelling clays have been investigated by Lawton *et al.* (1992) and Noorany *et al.* (1992) using one dimensional and triaxial swell tests. A significant amount of additional swelling strains due to wetting of clay was observed. Laboratory studies on the effects of wetting-drying cycles on swelling-shrinkage behaviour of unreinforced swelling clays are also investigated using one-dimensional and triaxial tests (Allam and Sridharan 1981, Dif and Bluemel 1991, Day 1994, Rao *et al.* 2001). Soil specimens used in those studies have sizes that are commonly used in one-dimensional and triaxial tests, that is, of the order of tens of millimetres only.

Laboratory studies have also been performed by several investigators (Al-Omari and Hamodi 1991, Al-Omari and Oraibi 2000, Vessely and Wu 2002) to explore the possibility of using geosynthetic reinforcement for reducing expansion of swelling clays. Al-Omari and Hamodi (1991) and Al-Omari and Oraibi (2000) used a large oedometer test set-up (soil sample dimensions of diameter = 150 mm and height = 90 mm) and placed the reinforcement vertically in circular fashion (diameter = 70 mm) in the soil samples. Al-Omari and Hamodi (1991) have shown that the reinforcement significantly reduced the swelling during water flooding. The reduction increased with increasing reinforcement stiffness, indicating that there was a reasonable bonding between soil and reinforcement.

A subsequent study by Al-Omari and Oraibi (2000) on the behaviour of reinforced swelling clays during wetting-drying cycles reported reduction of swelling deformations. The improvement factor, defined as the percentage of reduction in soil deformation due to reinforcement inclusion, ranged from 55% to 81% depending on the stiffness of the reinforcement. There was also a slight reduction in the number of cycles required to attain an equilibrium state of soil deformation during swelling and shrinkage. However, the vertical placement of reinforcement in soil specimens does not represent well the field conditions of reinforced slopes. Nevertheless, their study provided ideas for developing the design of laboratory tests in the present study.

Vessely and Wu (2002) studied laboratory tests on geosynthetic-reinforced and unreinforced clay blocks that were compacted to field moisture-density (Figure 2.4). The clay used by Vessely and Wu (2002) was lean clay (CL) which had liquid limit (w_L) = 46 - 49% and plasticity index (I_p) = 23 - 28%. The geosynthetic-reinforced and unreinforced clay blocks were introduced with water through moist sponges all around and allowed to swell freely. There was no vertical and lateral confining pressures applied to the clay blocks. Only external deformations of soil samples were measured and there was no measurement made on the reinforcement strain and internal deformations of the soil samples. Vessely and Wu observed that the geosynthetic reinforcement reduced the average horizontal swelling in soil specimen by 30% to 40% compared with the specimen without geosynthetic inclusion. However, no reduction in vertical swelling was observed.

In fact, vertical strain in the reinforced clay block was more than the case without reinforcement.

2.2.3 Fine-grained Soils with Freezing-Thawing Effect

Freezing and thawing of soils is a common phenomenon in cold climate regions. In Western Canada in particular, soils in these areas are subjected to at least one freezing-thawing cycle every year. At shallow depths, the number of freezing-thawing cycles can be more than one due to fluctuation of air temperatures. In the field, as the air temperature drops, heat is lost from the soil surface. When sufficient heat is lost, the water in the soil begins to freeze. During freezing, water moves upward towards the freezing front to fill soil voids and freeze or to form ice layers or lenses within a soil mass. The effect of freezing-thawing in soils mainly depends on soil type, availability of water in soil, intensity of freezing, overburden stress and soil density (Gatto and Ferrick 2003, Konrad 1993). Only fine-grained soils when exposed to freezing-thawing cycles generally experience volume changes (Eigenbrod 1996, Viklander 1998, Viklander and Eigenbrod 2000), loss in shear strength and increased compressibility (Graham and Au 1985).

Silty soils show the highest potential of frost-susceptibility (Gatto and Ferric 2003, Hansson and Lundin 2006, Konrad 1993). Silty soils absorb water rapidly because they have particles small enough to provide comparatively high capillary rise and large enough pore spaces to allow quick flow of water. These

characteristics lead to rapid increase in water content within the soil upon freezing. Coarser grained soils do not absorb water as rapidly. Konrad (1993) stated that significant amounts of unfrozen water exist in clays at temperatures lower than -10°C, whereas in silty soils most of the pore water freezes within a few tenths of a degree below 0°C. Thus, silty soils with available soil water are most susceptible to substantial seasonal changes due to freezing-thawing cycles. However, Janson (1963) reports that even sand may become frost-susceptible if it is well compacted and well graded.

A group of researchers (Eigenbrod 1996, Viklander 1998, Viklander and Eigenbrod 2000) conducted one-dimensional freezing-thawing cycles in cylindrical specimens of size less than 250 mm (high) and 100 mm (diameter). Tests were done with an open-drainage system (in which one end of soil sample is connected to an external water supply in order to facilitate unrestricted ice lens formation during freezing and drainage during thawing) as well as with a closed-drainage system (in which soil sample has no access to external water). In those studies, soil was frozen at -10°C and thawed at +20°C. Those tests were performed in unreinforced soil samples. Vertical deformation and temperature measurements were monitored in those studies. To the author's knowledge, there is no laboratory test found in the literature that deals with the use of geosynthetic as reinforcement in soils under freezing-thawing conditions.

2.3 FULL-SCALE TESTS ON GEOSYNTHETIC-REINFORCED SOIL STRUCTURES WITH FINE-GRAINED SOIL BACKFILL

Laboratory tests have certain limitations such as the small volume of samples, sample disturbance and boundary effects. Numerical analyses have also limitations since they are based on assumptions dealing with constitutive relationships of material, strain compatibility, deformation patterns, interaction between soil and reinforcement, etc. It is essential that these limitations and assumptions be justified in practice, especially by well-instrumented full-scale field tests. Well-instrumented full-scale field tests are the main source to verify laboratory and numerical models so that they both can be useful in practice. Several geosynthetic-reinforced soil structures using fine-grained soil backfill have already been tested and their performances reported in the literature.

Liu *et al.* (1994) carried out a well-instrumented full-scale test on a geogrid-reinforced embankment near Devon, Alberta, Canada. Their research was intended to determine how individual geogrid layers reinforce a mass of cohesive soil. They indirectly measured the stress transfer from the soil to the geogrids within the embankment using strain gauges. Their studies provided information to the understanding of the performance of a geogrid-reinforced slope using locally available silty clay (low to medium plasticity; clay fraction largely contained montmorillonite) as backfill under varying weather conditions (freezing-thawing). The test embankment was 12 m high with 1:1 side slopes. There were three sections corresponding to two sections with different geogrid materials (Figure

2.5) and one unreinforced test section. The test embankments were designed with a low factor of safety to develop lateral strains in the soil that would mobilize the tensile loads in the geogrids. Three primary reinforcing layers at a 2 m vertical spacing were installed in the bottom half of the test fill. Secondary reinforcement layers were installed at 1 m vertical spacing all throughout the height of the embankment. Extensive instrumentation was installed to measure the performance of the foundation, the fill soil and the geogrids. The strains in the geogrids were monitored using inductance coil sensors (as strain gauges) and electrical wire resistance (EWR) strain gauges. The positions of the strain gauge were at 0.5 m and 1.0 m and then at 1 m intervals from the slope surface and strain gauges were installed in the primary reinforcement only (refer to Zarnani *et al.* 2005 for the position of the strain gauges). Movements of the soil in the fill and the foundation were monitored using extensometers and inclinometers, installed both horizontally and vertically in the fill, and vertically in the foundation soils. Pneumatic piezometers were installed within the fill and the foundation soils to measure the pore pressure response.

Tensile strains in the geogrids and horizontal soil strains within the reinforced slopes were developed during the placement of the fill. Strain gauges attached to the geogrids showed that the strains increased (up to 2% - 2.8%) when fill height reached to 12 m. Within four years after completion of the fill, no significant time-dependent strains were observed. Geogrid strains and horizontal soil strains

within the reinforced slopes were similar, indicating nearly perfect bonding between soil and reinforcement.

Geogrid reinforcements did not significantly reduce horizontal movements of the slope in the study by Liu *et al* because the reinforced slopes were designed at low factor of safety by having few reinforcements. Nevertheless, strains induced in the geogrids were clear indication of good soil-geogrid reinforcement interaction and therefore good load transfer from soil to reinforcement. The rate of settlements and generation of pore pressure in the slope and foundation increased during the fill placement and decreased between and after the construction periods. This test embankment was subjected to wetting due to rainfall as well as freezing-thawing cycles over the years. Shallow slope surface movements were evident after completion of the embankment construction, both in reinforced and unreinforced slopes. A series of tension cracks parallel to the crest (maximum width of cracks about 100 mm and deepest crack was 2 to 3 m behind the crest of the slope) were observed in the unreinforced section following heavy rainfall. No similar instability was observed in the reinforced sections. It was implied that reinforcement helped to reduce the strain localization within the reinforced soil mass.

Hayden *et al.* (1991) presented a case history of a geogrid-reinforced swelling clay embankment constructed in Arkansas State Highway 16, US in 1988. The embankment was 244 m long with a maximum fill height of 23.2 - 24.4 m (Figure

2.6). The embankment was constructed using locally available borrow soil and different types of geogrid reinforcements. Figure 2.7 shows one of the critical design cross-sections of the geogrid-reinforced clay embankment. The side slopes for the embankment were 2H:1V along the full length. The heights of the embankment fill side slope ranged from 6.1 to 12.2 m along much of the embankment to a maximum of 23.2 - 24.4 m. The borrow soils were highly plastic swelling clays with plasticity indexes of 20% to 40%. Undrained shear strength of compacted samples of clay was 43 kN/m^2 with effective shear strength parameters $\phi' = 20°$ and $c' = 2.4\ kN/m^2$. Limit equilibrium methods were used for the stability analyses of the reinforced embankment. The embankment was designed for both end-of-construction and long-term conditions taking the minimum factor of safety equal to 1.3 for all slope stability analyses of the critical section.

The typical layout of the reinforcement is shown in Figure 2.7. Primary reinforcements have 1.8 m vertical spacing. Three types of uniaxial geogrid reinforcements: type 1, type 2 and type 3 with allowable 120-years design strengths of 14.6, 29.2 and 43.8 kN/m respectively in machine direction were used. Secondary reinforcements consisted of biaxial geogrid (Tensar BX1100) of 1.4 m length used at 0.3 m vertical spacing between the primary reinforcements. The secondary reinforcements were used for reduction of surface displacement of slope faces due to the swelling nature of the soil. Hayden *et al.* (1991) reported that constructing a geogrid-reinforced clay embankment resulted to a

cost saving of US$ 1.1 million over conventional alternatives such as the use of imported granular fills.

The geogrid-reinforced clay embankment was monitored for its performance with respect to horizontal and vertical movements of the soil, horizontal strain in the geogrid, and soil pore pressure and moisture content. Extensive instrumentation included extensometers, inclinometers, settlement stakes, strain gauges and piezometers. Hayden *et al.* (1991) presented instrumentation results that were limited to measurements of horizontal movements and strains from the extensometers, inclinometers, and strain gauges. Instrumentation results were presented for the first 24 months after completion of embankment construction. The horizontal soil extension strains were higher in the outer 3 m of the embankment than at deep locations in the embankment. Average horizontal soil strain measured in the outer 3 m of the embankment was approximately 0.5%, while the average strain in the zone 3 – 15 m from the face was only 0.1%. The large soil strain near the slope surface was believed to be related to the swelling nature of clay soils which had access to the moisture at the slope face.

The strong indication of significant near-surface soil movements even in the presence of secondary reinforcement shows the need for closer vertical spacing of reinforcements. It also implies that the length of secondary reinforcement in swelling clay slopes should be longer than the 1.4 m length used by Hayden *et al.* (1991) in their project. The geogrid strains of -0.04% to +0.30% (average of

about 0.1%) were measured in sets of strain gauges from 5 – 21 m behind the slope face, which was in good agreement with the soil strain measured in that zone. From the field measurement and analyses, it was concluded that the small deformations in the soil and the geogrids indicated satisfactory overall performance of the embankment and the relatively low levels of load in the geogrid reinforcement.

Full-scale field tests of reinforced walls are being currently conducted in the United States in order to establish properties for high fines reinforced soils and determine associated design controls that will result in acceptable performance of mechanically stabilized earth walls with marginal fill materials (Stulgis 2005b). The test walls consist of four sections. One section used a granular soil as reinforced fill to provide a baseline of performance for current AASHTO standards. A second section used non-plastic silty sand with up to 35% fines as reinforced fill to demonstrate that this soil can provide suitable reinforced fill for the reinforced walls. The third and fourth sections used silty soil with 50% fines (low to moderate plasticity) as reinforced fill (but two different reinforcement materials), in this case to demonstrate that marginal soils can provide suitable reinforced fill for reinforced walls. Each wall is 6 m high, 4 m wide and 18 m long (Figure 2.8).

The tests have been fully instrumented and monitored to measure the effects of pore water pressure and surcharge loading on the overall performance of the

reinforced soil structures. The test walls were constructed in summer of 2005 and monitoring is still going on.

The test walls are also experiencing freezing-thawing cycles. The test results have not been published yet. My research would complement their studies but would focus mostly on Manitoba local soils and environmental conditions.

2.4 CONSTITUTIVE MODEL FOR UNSATURATED CLAY SOIL

2.4.1 Barcelona Basic Model (BBM)

The mechanical behaviour of unsaturated soil can be described by two independent stress variables: the net normal stress defined as the excess of total stress over air pressure and the matric suction via constitutive relationships (Fredlund and Rahardjo 1993, Alonso *et al.* 1990). Alonso *et al.* (1990) proposed a constitutive model formulated in the framework of hardening elasto-plasticity to describe the stress-strain behaviour of unsaturated swelling soils. This model is now often referred to as the Barcelona Basic Model (BBM) and is the one most widely used to date. This model extends the modified Cam clay model (see Wood 1990 for a detailed discussion on the modified Cam clay model) by involving four state variables: net mean stress, $p = (\sigma_1 + 2\sigma_3)/3 - u_a$; deviator stress, $q = (\sigma_1 - \sigma_3)$; matric suction, $s = (u_a - u_w)$; and specific volume, $v = (1 + e)$, where e = void ratio, σ_1 = vertical total principal stress, σ_3 = horizontal total

principal stress, u_a = air pressure and u_w = water pressure. A key element of the model is the dependency of the yield locus on suction, which can be represented in the *p*-*q*-*s* diagram by the LC surface (Figure 2.9). The model features elastic strains when the soil state lies inside a state boundary hyper-surface, and plastic strains starting when the state boundary hyper-surface is reached. Plastic behaviour, as the soil state traverses the state boundary hyper-surface, corresponds to an expansion of a yield surface in (*p*-*q*-*s*) space. This model is intended for moderate- to low-plastic soils and a low range of suction values.

A detailed description of the constitutive model for BBM is given by Alonso *et al.* (1990). Only brief details will be provided here for sake of completeness. The main features of the model can be summarized as follows.

Basic stress variables:

Net normal stress,

$$\sigma'' = \sigma - u_a \tag{2.1}$$

Matric suction,

$$s = u_a - u_w \tag{2.2}$$

Yield surfaces

There are two yield surfaces in the BBM. The first, known as the loading collapse (LC) yield surface, is related to the irreversible compression that can occur on increase of *p* or *q* (loading):

$$F_1 = q^2 - M^2(p + p_s)(p_0 - p) \tag{2.3}$$

where, M is the slope of the critical state line, p_s is related to the effect of suction on the cohesion of the soil and p_0 is the preconsolidation stress at the current value of suction (s). In the yield surface equation F_1, the parameters p_s and p_0 depend on the suction. They are defined as follows:

$$p_s = k\, s \tag{2.4}$$

$$\frac{p_0}{p^c} = \left(\frac{p_0^*}{p^c} \right)^{[\lambda(0) - \kappa]/[\lambda(s) - \kappa]} \tag{2.5}$$

where k is a parameter describing the increase in cohesion, p_0^* is the preconsolidation stress at zero suction (saturated conditions), p^c is a reference stress, κ is the elastic compressibility parameter for change in net mean stress, and $\lambda(s)$ and $\lambda(0)$ are the values of the compressibility parameter for changes in net mean stress for virgin states of the soil at the current values of s and $s = 0$, respectively. $\lambda(s)$ varies with suction according to

$$\lambda(s) = \lambda(0)\left[(1 - r)\exp(-\beta\, s) + r\right] \tag{2.6}$$

where, β and r are additional soil parameters.

With p_0 and p_s varying with suction, Equation (2.3) describes a family of elliptical yield curves associated with different suction values. The major axis of the ellipse describing the LC yield curve at constant suction will span the segment $-p_s$ to p_0. The second yield surface, known as the suction increase (SI) yield surface, is related to the irreversible compression that can occur on increase of suction:

$$F_2 = s - s_0 \tag{2.7}$$

where, s_0 is the maximum previously attained value of the suction.

Flow rules

This model assumes a non-associated plastic flow rule in conjunction with yield locus F_1 (LC) and an associated plastic flow rule with yield locus F_2 (SI).

$$Q_1 = \alpha\, q^2 - M^2 (p + p_s)(p_0 - p) \tag{2.8}$$

$$Q_2 = s - s_0 \tag{2.9}$$

where, α is a constant which is derived by requiring that for saturated soil the direction of the plastic strain increment for zero lateral deformation

$$\frac{d\varepsilon_q^p}{d\varepsilon_{vp}^p} = \frac{2}{3}\frac{1}{\left[1 - \kappa/\lambda(0)\right]} \tag{2.10}$$

is found for stress states satisfying K_0 conditions. This yields

$$\alpha = \frac{M(M-9)(M-3)}{9(6-M)}\left(\frac{1}{1-\kappa/\lambda(0)}\right) \tag{2.11}$$

In the above, $d\varepsilon^p_{vp}$ is the plastic volumetric strain increment caused by yielding on F_1, and $d\varepsilon^p_q$ is the corresponding plastic deviatoric strain increment.

The plastic strains are often expressed in terms of volumetric and deviatoric components, which for this case are

$$d\varepsilon^p_{vp} = \mu_1 \partial Q_1 / \partial p = \mu_1 M^2 (2p + p_s - p_0) \tag{2.12}$$

$$d\varepsilon^p_q = \mu_1 \partial Q_1 / \partial q = \mu_1 2\alpha q \tag{2.13}$$

$$d\varepsilon^p_{vs} = \mu_2 \partial Q_2 / \partial s = \mu_2 \tag{2.14}$$

where, $d\varepsilon^p_{vs}$ is the plastic volumetric strain increment caused by yielding on the SI yield surface. For the SI yield surface, the plastic deviatoric strain increment is zero. Both μ_1 and μ_2 are scalar multipliers. Thus, for the LC yield surface,

$$\frac{d\varepsilon^p_q}{d\varepsilon^p_{vp}} = \frac{2\alpha q}{M^2[2p + p_s - p_0(s)]} \tag{2.15}$$

Hardening laws

The expansion of the yield surfaces is controlled by hardening parameters p_0* and s_0 as plastic volumetric strains develop. They depend on the total plastic volumetric strain increment $d\varepsilon_v^p$ as follows:

$$\frac{dp_0^*}{p_0^*} = \frac{v}{\lambda(0) - \kappa} d\varepsilon_v^p \tag{2.16}$$

$$\frac{ds_0}{(s_0 + p_{atm})} = \frac{v}{\lambda_s - \kappa_s} d\varepsilon_v^p \tag{2.17}$$

where, p_{atm} is the atmospheric pressure, λ_s is the stiffness parameter for changes in suction for virgin states of soil and κ_s is an elastic stiffness parameter for changes in suction.

Elastic strains

The elastic volumetric and shear components of strain are given by:

$$d\varepsilon_v^e = \frac{\kappa}{v}\frac{dp}{p} + \frac{\kappa_s}{v}\frac{ds}{(s + p_{atm})} \tag{2.18}$$

$$d\varepsilon_s^e = (1/3G)dq \tag{2.19}$$

where, K and G are the bulk and shear modulus respectively of the soil.

BBM has been used in this research to determine the stress state in swelling soils during the mechanical loading conditions prior to wetting of soil.

2.4.2 Swell Model

The BBM has incorporated swelling of unsaturated clays during wetting. However, several parameters are needed and they require sophisticated laboratory tests to determine their values. Instead, a much simpler swelling model is used in this study that needs only few parameters and only requires simple tests.

Wetting-induced deformations in swelling clay have been investigated by Noorany *et al.* (1999) using a elastic wetting model, which is referred to here as the *Swell Model*. They used triaxial wetting test results to establish the wetting constitutive relationship. The wetting-induced strains in swelling soils under various confining stress levels were modelled in laboratory triaxial tests. The samples were prepared so that they simulated field moisture contents and dry densities. These were loaded anisotropically to the desired stress levels, after which water was introduced to the soil samples. Vertical and lateral wetting deformations were measured during wetting until the soil was almost fully saturated.

As mentioned earlier, the swell model was selected for use in this study because of its simplicity, with few numbers of required parameters. These parameters can easily be determined from the laboratory test set-up in my study.

Figure 2.10 shows a typical wetting stress-strain relationship from the wetting tests. A positive strain means swelling (expansion). It can be seen from Figure 2.10 that the clay produces swelling at low overburden pressures. It is interesting to note that compression can occur during wetting at high confining stress levels.

From the relationships shown in Figure 2.10, wetting-induced strains can be expressed by the following logarithmic functions in terms of vertical stress (σ_y), normalized by the atmospheric pressure (p_a):

$$\varepsilon_{yw} = c_1 \log\{a_1(\sigma_y / p_a)\} \tag{2.20}$$

$$\varepsilon_{xw} = \varepsilon_{zw} = c_3 \log\{a_3(\sigma_y / p_a)\} \tag{2.21}$$

where, ε_{yw} = vertical wetting-induced strain, and ε_{xw} = ε_{zw} = wetting-induced strains in horizontal directions. Upper bound values of ε_{yw}, ε_{xw}, and ε_{zw} are defined by the measured swelling under zero confining stress. It should be noted that σ_y is the vertical stress component prior to wetting and is not modified in the above equations during the calculations since this is conveniently assumed constant throughout (such that, change of σ_y due to change in the unit weight of soil from unsaturated to saturated state is assumed negligible). The parameter

set a_1, c_1, a_3, c_3 in logarithmic functions are dimensionless soil properties. They were determined from the triaxial wetting test results in Noorany *et al.* (1999).

For implementation in numerical analysis, relevant wetting strains were evaluated using Equations 2.20 and 2.21 based on the equilibrium stress state prior to wetting. Then, the corresponding wetting-induced stresses are derived by the incremental form of Hooke's law as follows:

$$\Delta\sigma_{xw} = -\left\{\alpha_1 \varepsilon_{xw} + \alpha_2 \left(\varepsilon_{yw} + \varepsilon_{zw}\right)\right\}$$

$$\Delta\sigma_{yw} = -\left\{\alpha_1 \varepsilon_{yw} + \alpha_2 \left(\varepsilon_{xw} + \varepsilon_{zw}\right)\right\} \qquad (2.22)$$

$$\Delta\sigma_{zw} = -\left\{\alpha_1 \varepsilon_{zw} + \alpha_2 \left(\varepsilon_{xw} + \varepsilon_{yw}\right)\right\}$$

where,

$$\alpha_1 = K + \frac{4}{3}G$$
$$\alpha_2 = K - \frac{2}{3}G \qquad (2.23)$$

K and G are the bulk and shear modulus respectively of the soil.

2.5 THERMAL-MECHANICAL MODEL IN FLAC FOR FROZEN SILT

FLAC has the capability to model transient heat transfer in materials, such as soil and rock, including the development of thermally induced displacements and stresses. The modelling of heat transfer is performed using a FLAC built-in "thermal model" independent of the mechanical calculation. The thermal model can also be coupled with the mechanical model to capture the effects of heat transfer/solid interaction. A brief mathematical formulation of thermal-mechanical coupling in the FLAC is described here.

The variables involved in heat conduction in the thermal model are the temperature and two components of the heat-flux. These variables are related through the energy-balance equation and transport laws derived from Fourier's law of heat conduction.

Energy-Balance Equation:

The differential expression of the energy balance has the form

$$-\nabla . q^T + q_v^T = \frac{\partial \zeta_T}{\partial t} \qquad (2.24)$$

where, q^T = heat-flux vector (W/m^2)

q_v^T = volumetric heat source intensity (W/m^3)

ζ_T = stored heat per unit volume (J/m^3)

t = time (second)

A thermal constitutive law relates temperature changes to the heat storage (ζ_T), so the energy balance equation can be written as

$$-\nabla . q^T + q_v^T = \rho C \frac{\partial T}{\partial t} \tag{2.25}$$

where, ρ = mass density of medium (kg/m^3)

C = specific heat at constant volume (J/kg °C)

T = temperature (°C)

Heat Transport Law:

The basic law that defines the relation between the heat-flux vector and the temperature gradient is Fourier's law. For a stationary, homogeneous, isotropic solid, this constitutive law is given in the form

$$q^T = -k \nabla T \tag{2.26}$$

where, k = thermal conductivity tensor (W/m°C)

Substitution of Fourier's law (Equation 2.26) in energy balance equation (Equation 2.25) yields the differential equation of heat conduction. This model is used in this study to simulate the temperature distribution in soil during freezing and thawing.

Changes in the soil temperature induce thermal strains,

$$\frac{\partial \varepsilon_{ij}^{T}}{\partial t} = \alpha \frac{\partial T}{\partial t} \delta_{ij} \tag{2.27}$$

where, ε_{ij}^{T} = thermal strain

α = coefficient of linear thermal expansion (1/°C)

δ_{ij} = Kronecker delta

Thermal strains in soils are introduced by thermal mechanical coupling at any time during a transient simulation. The coupling occurs in one direction only – that is, the temperature may result in stress changes, but mechanical changes in the soil resulting from force application do not result in temperature change. The thermal strain resulting from stress change in the soil is given by,

$$\frac{\partial \sigma_{ij}^{T}}{\partial t} = -\alpha \; 3K \frac{\partial T}{\partial t} \delta_{ij} \tag{2.28}$$

where, K = bulk modulus of soil (kN/m^2)

σ_{ij}^{T} = thermal stress

This stress is added to the zone stress state prior to application of the constitutive law. Details of the thermal-mechanical models and their coupling procedures are found in FLAC 4.0 Thermal Option Manual (Itasca Consulting Group 2001). The thermal-mechanical coupling is used in this study to analyze the freezing-induced deformation in the silt soil.

2.6 SUMMARY

Laboratory tests, numerical modelling and full-scale field studies related to geosynthetic-reinforced fine-grained soils found in the literature have been discussed. The following summarizes this chapter:

1) Laboratory studies on the behaviour of geosynthetic-reinforced fine-grained soils are found in the literature under mechanical loading only (gravity load and externally applied load if any). Triaxial compression and small scale (less than 100 mm specimen dimensions) plane-strain tests have been reported. However, plane-strain conditions generally prevail in typical GRS structures. Laboratory test set-ups should follow this condition.
2) A large-scale laboratory test, known as soil-geosynthetic interactive performance (SGIP) test, was developed by a group of researchers to investigate the long term behaviour of GRS structures under plane-strain loading conditions. A geosynthetic reinforcement layer was placed at the middle-height of the soil specimen. They conducted tests on geosynthetic reinforced clay and sand. They found the soil deformed more than the

geosynthetic reinforcement in the clay backfill; whereas in the sand backfill, they observed less soil deformation than in the geosynthetic reinforcement.

3) Early works on laboratory tests on geosynthetic-reinforced and unreinforced clay blocks subjected to wetting were conducted. The clay blocks were introduced with water through moist sponges all around and allowed to swell freely. There was no vertical and lateral confining pressures applied to the clay blocks. The presence of geosynthetic reinforcement reduced the average horizontal swelling in soil specimens by 30% to 40% compared with the specimen without geosynthetic inclusion. No measurements were made of strains in the reinforcement or of the internal deformations of the soil samples.
4) The effects of freezing-thawing in fine-grained soils have been investigated by researchers using one-dimensional freezing-thawing cycles in cylindrical specimens. The tests have been conducted only on unreinforced soil specimens.
5) A number of well-instrumented full-scale field tests have been reported in the literature using fine-grained soil backfill in geosynthetic-reinforced soil structures. The full-scale structures were subjected to wetting and freezing conditions. The tests were done in an attempt to establish design and construction guidelines when using locally-available fine-grained soils as fill materials.

6) The Basic Barcelona Model (BBM) and the Swell model provide constitutive relations for the behaviour of unsaturated swelling clay under wetting. BBM describes the stress-strain behaviour of swelling clays in the framework of hardening elasto-plasticity. BBM extends the modified Cam clay model including effect of suction change. A key element of the model is the dependency of the yield locus on suction. The model features elastic strains when soil states lie inside a state boundary hyper-surface, and plastic strains when the soil state boundary hyper-surface is reached. BBM needs several parameters which require sophisticated laboratory tests to determine their values. Instead, the Swell model describes the constitutive relation of swelling clay under wetting using a simpler elastic stress-strain relationship that needs only a few parameters that can be determined easily from simple laboratory tests.
7) The built-in thermal-mechanical model in the FLAC computer program can simulate transient heat transfer in soils including thermally induced displacements and stresses. Changes in the soil temperatures introduce thermal strains via mechanical coupling and the thermal strains result to stress changes in the soil. These stresses are added to the zone stress state prior to application of the constitutive law in FLAC.
8) The current research extends early studies and focuses on Manitoba local soils and environmental conditions.

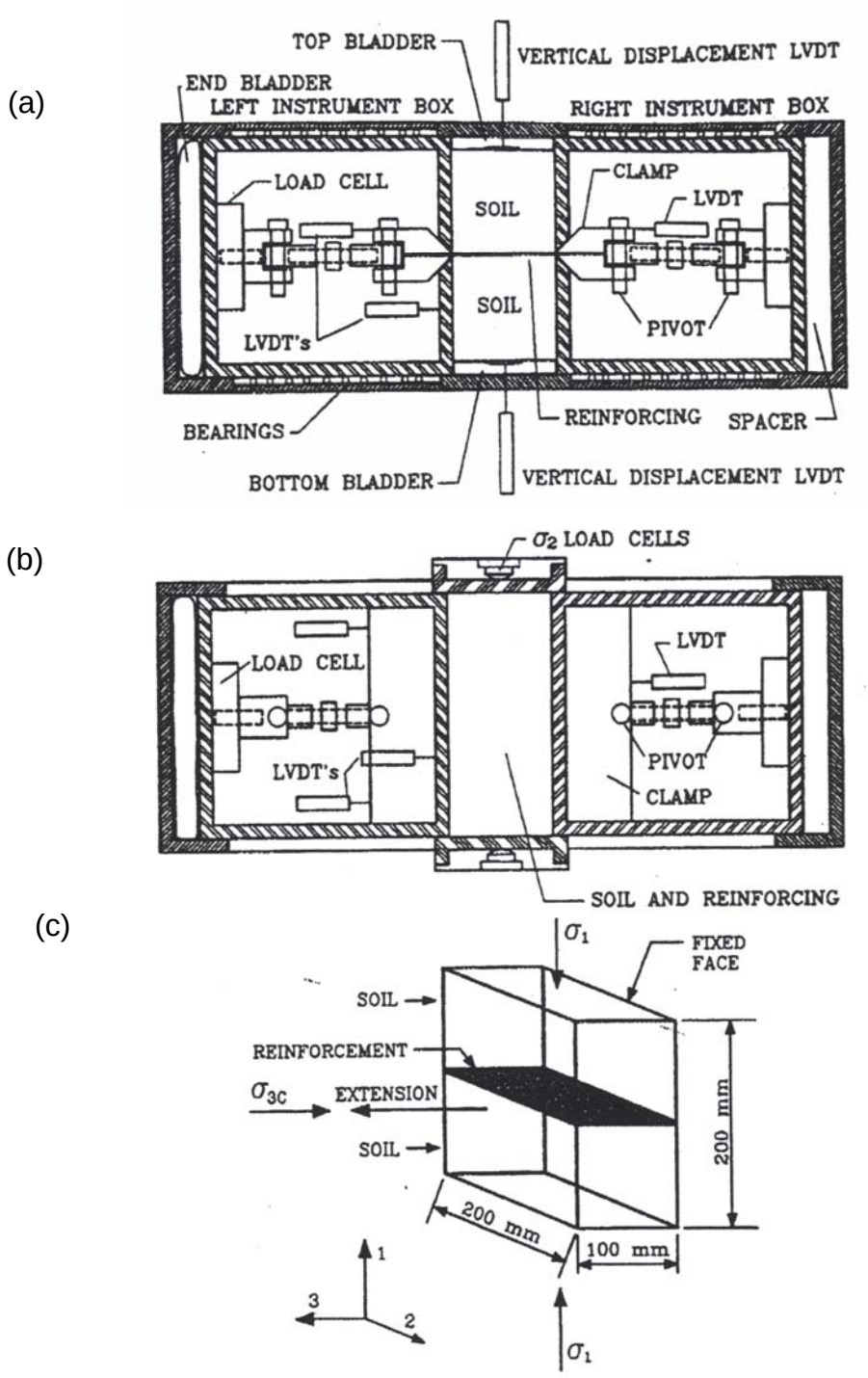

Figure 2.1 Schematic of Unit Cell Device: (a) Profile, (b) Plan and (c) UCD principle of operation and specimen dimensions (Boyle 1995 – reproduced with permission of North American Geosynthetics Society, March 2, 2009)

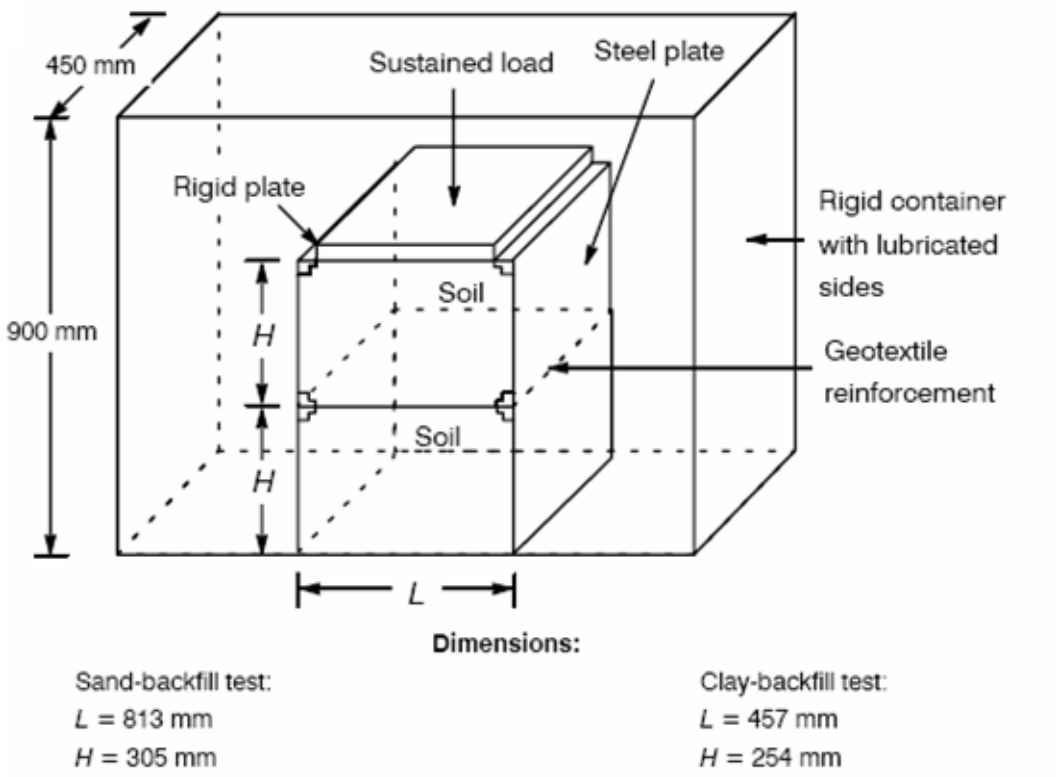

Figure 2.2 Schematic diagram of soil-geosynthetic interactive performance (SGIP) test apparatus (Wu and Helwany 1996 – reproduced with permission of Geosynthetics International, March 2, 2009)

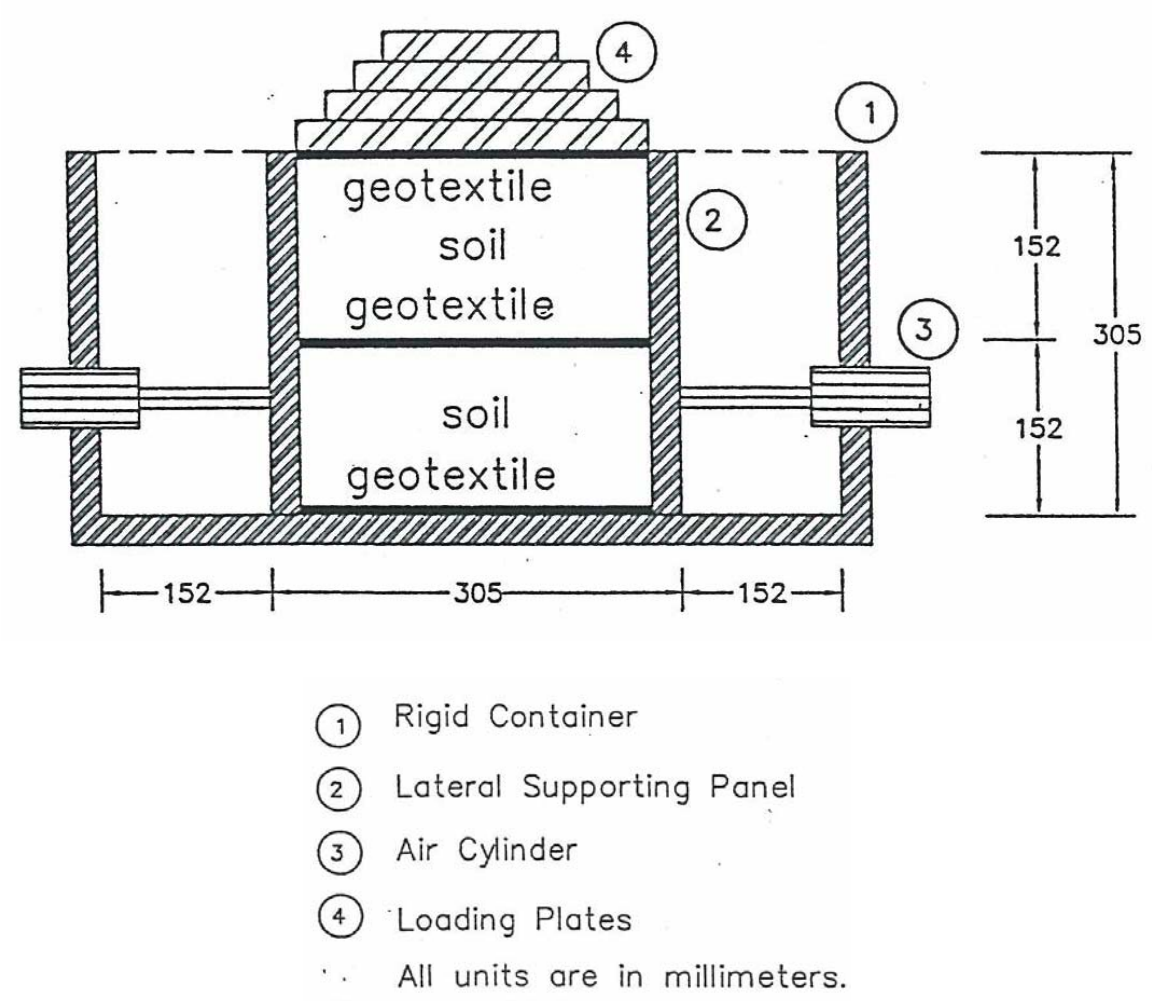

Figure 2.3 Schematic profile of modified soil-geosynthetic interactive performance (SGIP) test apparatus (Ketchart and Wu 2002 – reproduced with permission of ASTM International, March 6, 2009)

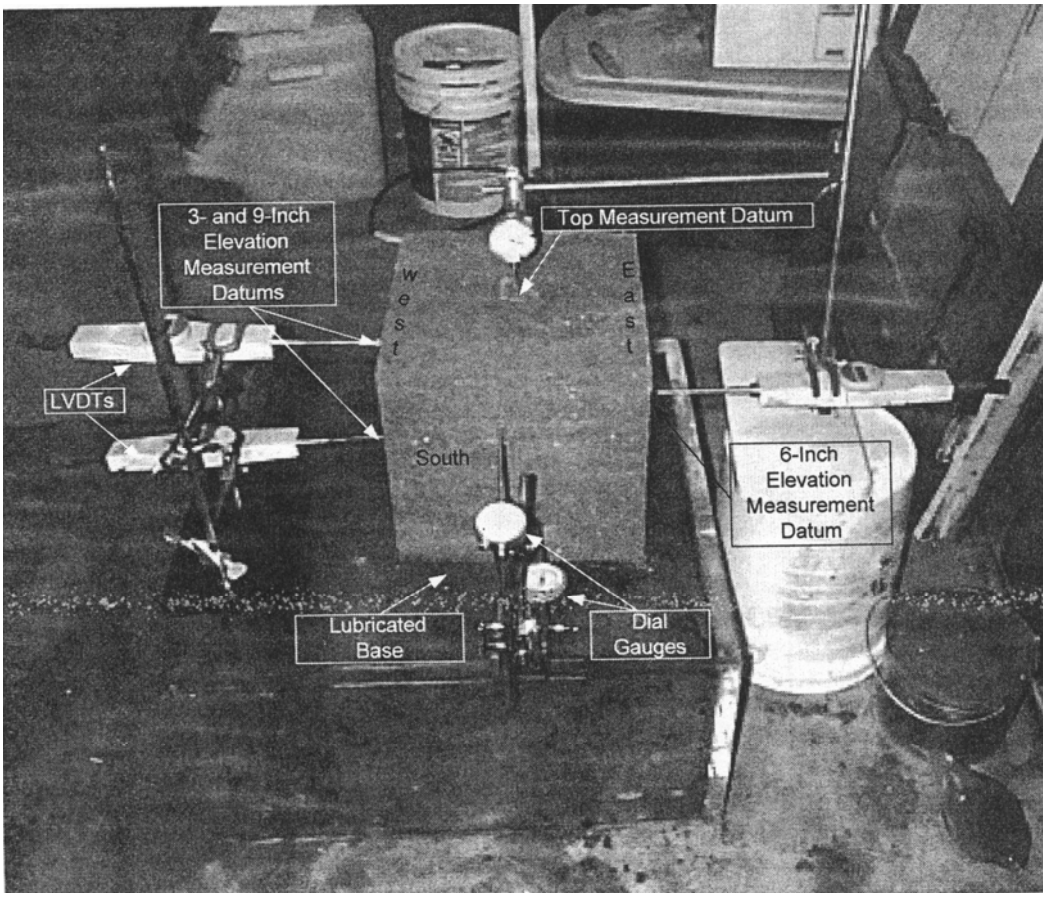

Figure 2.4 Typical specimen set-up for wetting in GRS block (Vessely and Wu 2002 – reproduced with permission of Transportation Research Board, February 25, 2009; and J. T. H. Wu, March 2, 2009)

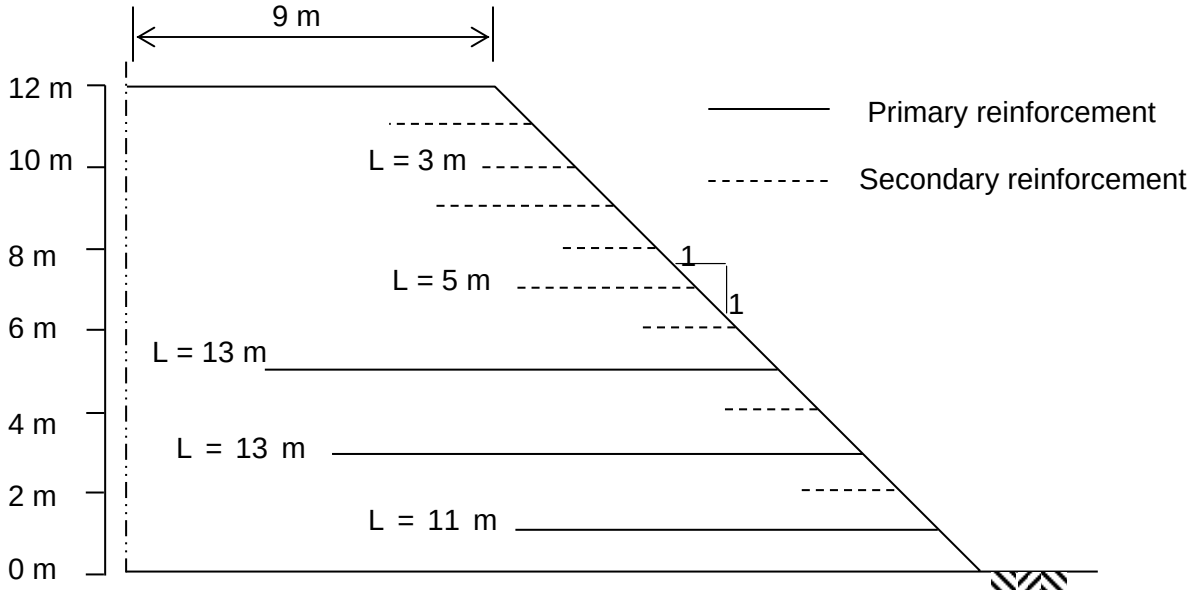

Figure 2.5 Geogrid layout in reinforced slope section (redrawn from Liu *et al.* 1994 with permission of Geosynthetics International, March 2, 2009)

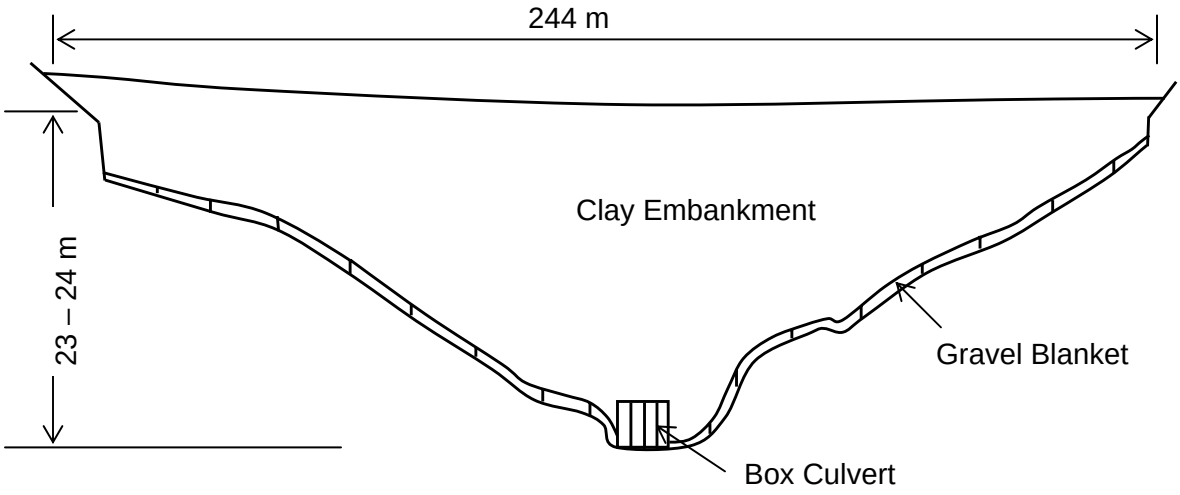

Figure 2.6 Centerline profile of highway 16 embankment (redrawn from Hayden *et al.* 1991 with permission of North American Geosynthetics Society, March 2, 2009)

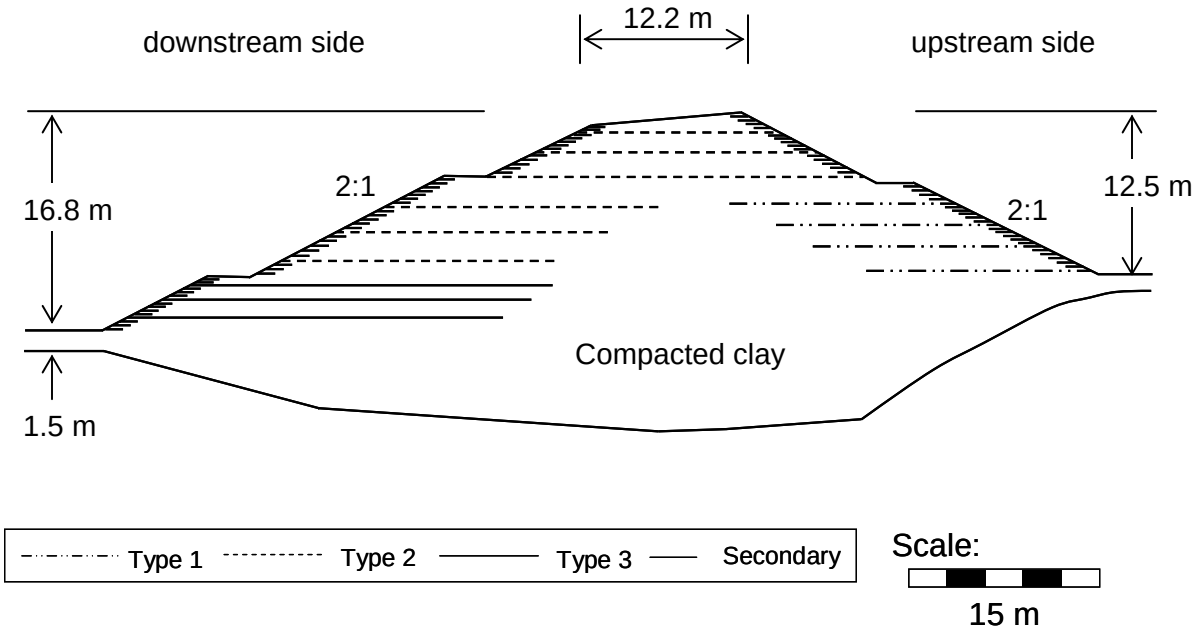

Figure 2.7 Reinforcement layout for embankment section at station 85+95 (redrawn from Hayden *et al.* 1991 with permission of North American Geosynthetics Society, March 2, 2009)

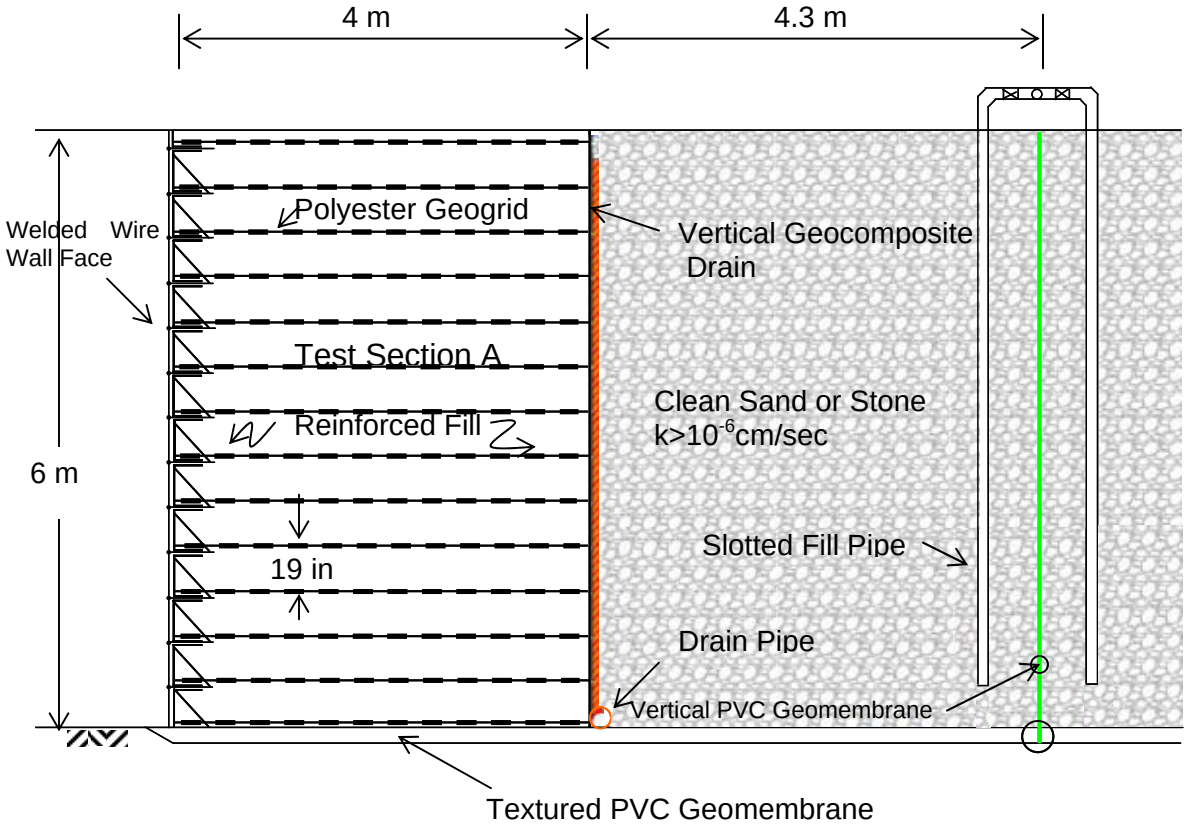

Figure 2.8 Typical reinforced test wall cross-section (redrawn from Stulgis 2005b with permission of North American Geosynthetics Society, March 2, 2009 and Geosynthetics Research Institute, March 10, 2009)

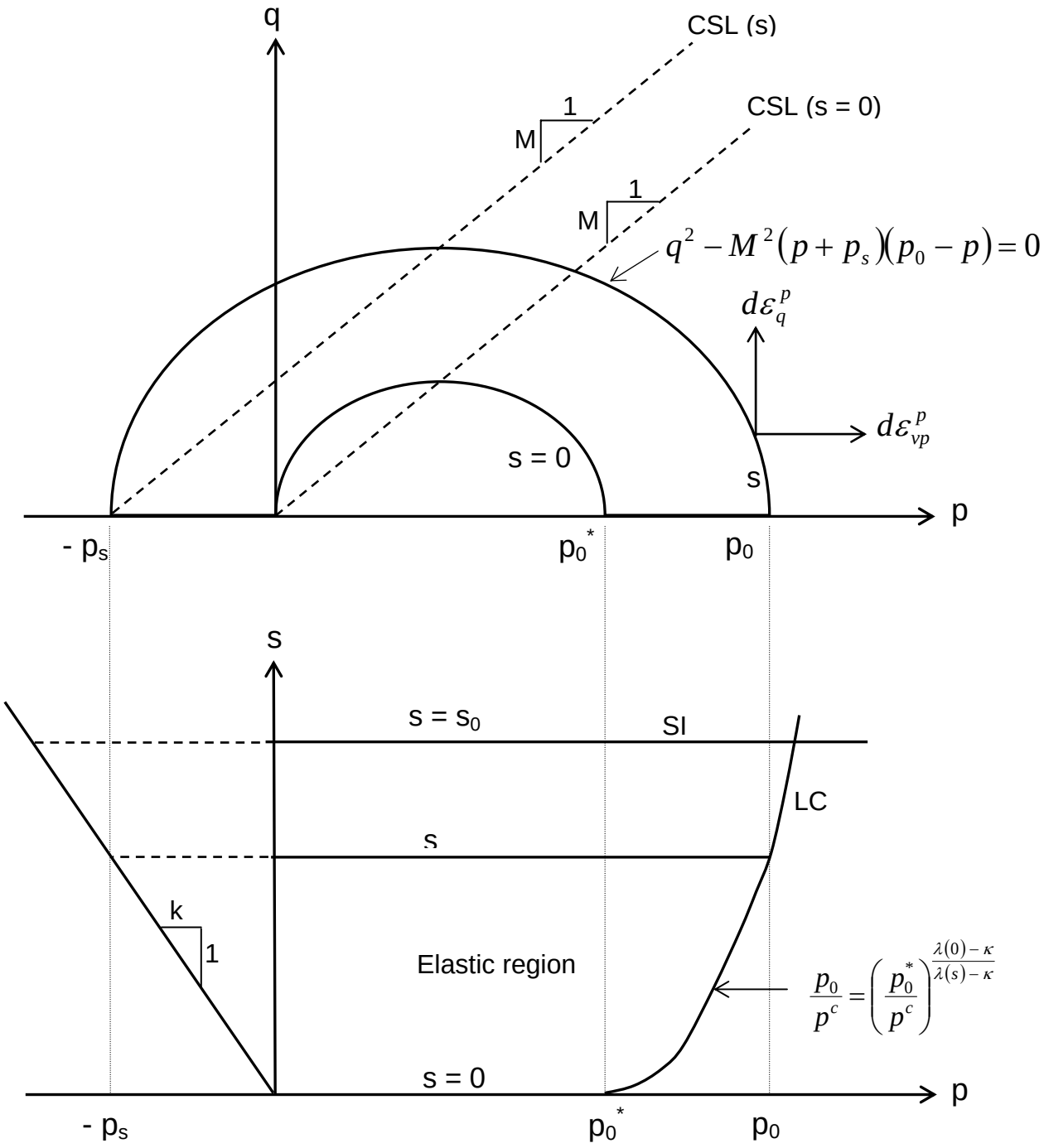

Figure 2.9 Barcelona Basic Model in p:q:s space (replotted from Alonso *et al*. 1990 with permission of Thomas Telford, February 27, 2009)

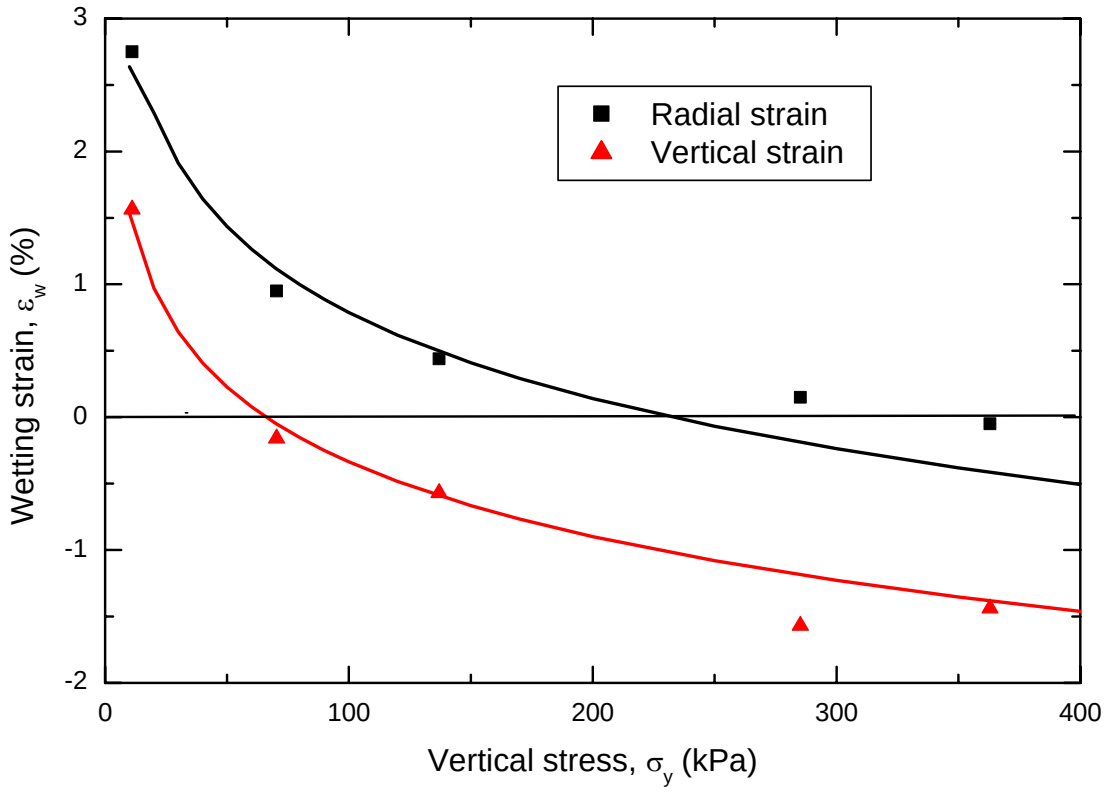

Figure 2.10 Wetting stress-strain relationship from triaxial wetting test (replotted from Noorany *et al.* 1999)

CHAPTER 3

LABORATORY TESTING PROGRAM

3.1 INTRODUCTION

This research designed a laboratory testing program to simulate environmental effects (wetting-drying cycles and freezing-thawing cycles). Locally available fine-grained soils (clay and silt) and commercially-available geogrid reinforcements were used. Geosynthetic-reinforced soil specimens were prepared by compacting soil at its optimum moisture-maximum dry density condition (Figure 3.1). This condition simulates the field placement moisture and density of soil in GRS structures. Geogrid reinforcement was placed at the middle elevation of the soil specimen during its preparation. The plane-strain condition, a prevailing condition in typical GRS structures, was physically modelled in the soil specimen by restraining deformations of specimen in the z-direction (that is, the soil strain in the z-direction, $\varepsilon_z = 0$). The prepared soil specimen was first loaded vertically and horizontally at its compacted condition up to a desired stress level. This condition is referred here as the *mechanical loading condition*. Both vertical pressure (σ_y) and horizontal pressure (σ_x) were applied independently to the soil specimen to simulate anisotropic field stress conditions. The mechanical loading condition represents the gravitational load as well as externally applied loading (if

any) on soil elements of GRS structures in the field. The mechanical loading condition was followed by *wetting-drying cycles* in reinforced swelling clay specimens, and *freezing-thawing cycles* in reinforced silt specimens under constant applied pressures. The introduction of wetting-drying cycles or freezing-thawing cycles represents the *environmental loading condition*. This represents part of the original contribution of the thesis.

Soil deformations and geosynthetic reinforcement strains were measured during the tests. Unlike the direct measurements of load in the reinforcement during loading of soil samples (Boyle 1995), reinforcement strains were measured in this research using strain gauges. The axial forces in the reinforcement were calculated based on the geogrid's in-air reinforcement stiffness and its measured strain. Tests with and without geosynthetic inclusions were performed in otherwise identical conditions for comparison purposes.

This chapter discusses the development of a new test apparatus and describes the test set-up for wetting-drying and freezing-thawing tests, soil and geogrid properties, testing programs, specimen preparation, test procedures and finally, the instrumentation and monitoring system.

3.2 TEST APPARATUS AND TEST SET-UP

A large-scale plane-strain test apparatus was developed and commissioned by the author at the University of Manitoba to study the behaviour of geosynthetic-

reinforced soils subjected to wetting-drying and freezing-thawing cycles (Pathak and Alfaro 2005a, 2005b). Figure 3.2 is a schematic of the test apparatus showing the layout and instrumentation. The test box consisted of rigid steel plates and plexiglass sidewalls, and a rigid steel plate at the bottom. The dimensions of the test box are 420 mm (wide) x 720 mm (long) x 600 mm (high). The geosynthetic-reinforced soil specimens, dimensions: 420 mm (W) x 430 mm (L) x 500 mm (H), were prepared and tested inside the test box. Lateral movement of the soil specimen was prevented across the plexiglass sidewalls (along z–direction). Bracing was provided to the plexiglass sidewalls using wooden planks and metal straps to reinforce the sidewalls against cross-plane movement of the soil specimen. Friction between the plexiglass sidewalls and the soil specimen was minimized by applying a lubrication layer consisting of a 0.5 mm thick latex membrane with silicon grease. This technique was developed at the University of Tokyo by Tatsuoka and his associates and has been used successfully in many tests for soil properties, both in reduced-scale model tests and full-scale tests (Tatsuoka *et al.* 1984, Wu 1992, Ling and Tatsuoka 1994).

Independent vertical and horizontal pressures were applied to the specimen. The specimen was allowed to deform in both vertical and lateral directions (y- and x-directions respectively) under constant applied pressures. The vertical pressure was applied on top of the soil specimen, and was sustained through a loading ram on top of a metal plate. The horizontal pressures were applied in the x-direction to both sides of the specimen through air bags. The interior of the

rubber air bags has 3 mm thick metal plates and movements of these plates were restrained to provide firm support to the soil specimen during compaction. This test set-up was an improvement of the test set-up used by Ketchart and Wu (2002) and Boyle (1995) in terms of applying anisotropic loadings to simulate construction induced stresses in GRS structures. The geosynthetic reinforcement strain, soil specimen deformations, soil temperature and soil suction were measured in the tests. All measurement data were recorded electronically via a data acquisition (DA) system. A photograph of the test apparatus and typical test set-up is shown in Figure 3.3.

3.3 WETTING-DRYING CYCLE

3.3.1 Introduction

An inherent practice with construction of reinforced soil slopes and embankments is to compact the soil fill at prescribed moisture-density conditions. Initially, compacted soil is generally unsaturated. Post-construction wetting (for example due to rain, drainage, irrigation, etc.) of swelling clay induces soil swelling, whereas post-construction drying (drying during hot summer weather) causes shrinkage of swelling clays. Such wetting and drying can cause vertical and lateral movements of the slopes and embankments. To simulate these environmental effects in geosynthetic-reinforced clay specimens, tests were conducted that involved wetting-drying cycles. The so-called “soaked-after-

loading" method (Lawton *et al.* 1992**)** was used in the tests. The specimens were first loaded then flooded with water to simulate wetting. The applied pressure remained constant throughout the tests. Once full swelling was achieved, excess water was drained from the specimen and test box. The specimens were then dried by supplying warm air at about 35°C from the bottom and top of the specimens. Porous stones were placed at the top and bottom of the soil specimen and between the rubber air bags and the soil specimen (Figure 3.2). This facilitates faster saturation and drying of soil specimen. In the wetting of the soil specimen, water was supplied from the bottom of the test box at 1 m of water head. During the drying, warm air was supplied through the top and bottom of the soil specimen via an air heating tank to dry the soil specimen during drying (Figure 3.3). Drying was continued until equilibrium of soil shrinkage was achieved. Originally, it was planned to repeat wetting-drying cycles until steady volume changes of the specimen were achieved. However, due to time constraints, only one wetting-drying cycle was performed in each test.

The tests carried out in this study examine the swelling-shrinkage behaviour of GRS structures under wetting-drying. Additional axial force developed in the reinforcement due to swelling-shrinkage of the specimens was evaluated. These tests were conducted on swelling clay, with and without geosynthetic reinforcement. Aside from comparing the results with reinforced soil specimens, unreinforced wetting tests were used to develop the constitutive relation between swelling strains of soil and confining pressure. The materials used in the test,

testing program, specimen preparation and test procedures and instrumentations are briefly discussed in the following sections.

3.3.2 Material Properties

3.3.2.1 Soil Properties

The soil used in the wetting-drying tests was locally-available Winnipeg clay taken from 1-2 m below the ground surface. Clays in Winnipeg are generally considered to be swelling clays due to their high content of montmorillonite. Organic materials were removed from the clay before oven drying and pulverizing the clay. A representative sample of the processed clay was then used for index property and standard Proctor tests. Figure 3.4 shows the grain size distribution curve of the soil from sieve and hydrometer analyses. The soil contains more than 95% of particles passing the No. 200 sieve and is classified as high plastic clay (CH) based on the Unified Soil Classification System (USCS). For the standard Proctor test, weighed batches of clay were mixed thoroughly with different amounts of water content and then cured at least three overnights in zip-locked plastic bags in a high humidity room to allow equal distribution of water within the soil mass. Subsequently, standard Proctor tests were carried out in the different batches of cured clay. Each compacted sample was divided into three layers and wax-density tests were performed for each layer to determine their density and water content. Figure 3.5 represents the dry unit weight-

moisture relationship from the standard Proctor compaction test. The density and water content values obtained for each layer from wax-density test were averaged for each Proctor sample. Table 3.1 summarizes the basic properties of soil.

Table 3.1 Basic properties of clay

Specific gravity (G_S)	2.72
Liquid limit, w_L (%)	96
Plastic limit, w_P (%)	35
Plasticity index, I_P (%)	61
Optimum moisture content, w_{opt} (%)	30
Maximum dry unit weight, γ_{dmax} (kN/m^3)	13.3

Further laboratory tests were carried out on the compacted clay samples prepared at optimum moisture-maximum dry density condition to determine their strength properties and stress-strain behaviour. Isotropically Consolidated Undrained (CIŪ) triaxial tests were performed on three samples (50 mm in diameter) at effective consolidation pressures (σ_c') = 50, 100 and 200 kPa. Pore water pressures were measured during shearing. All triaxial samples were back pressured until a Skempton's pore pressure parameter "B" (Skempton 1954) values of 98% were obtained. The samples were then consolidated using confining pressures. An axial strain rate of 0.01% per minute was used in the loading of samples. Figure 3.6 represents the stress versus strain and pore pressure change versus strain results. Figure 3.7 shows the deviator stress (q)

versus mean principal effective stress (p') results from the CIŪ tests during shearing. At the critical state failure condition, the slope (M) of the critical state line was about 0.7. This gives the equivalent internal angle of friction at critical state (ϕ'_{cs}) equal to 17.5°. Unconsolidated Undrained (UU) triaxial tests were also conducted on compacted clay at the compacted moisture condition. Tests were performed on three samples (50 mm diameter) at cell pressures (σ_c) = 50, 100, 200 kPa. The deviator stress versus strain results during shearing is shown in Figure 3.8. It was found from UU test results that the compacted clay has initial Young's modulus of elasticity (E) equal to 23 MPa at compacted moisture content and undrained shear strength (c_u) equal to 130 kPa.

A one-dimensional swell test was also performed on the compacted clay sample according to ASTM D 4546, Method C where the sample was maintained at constant height by making adjustments in the vertical pressures after the sample was inundated with water. The one-dimensional swell test result provided the past maximum mean pressure, p^*_0 equal to 200 kPa; slope of normal consolidation line, $\lambda(0)$ equal to 0.156 and slope of swelling line, κ equal to 0.01 (refer Figure 3.9).

3.3.2.2 Properties of Geosynthetic Reinforcement

A sheet of an extruded biaxial polypropylene geogrid designated as Tensar-BX1300 was used as specimen (dimensions: 420 mm x 430 mm) to evaluate the properties of the reinforcement. Table 3.2 summarizes the index properties of

virgin BX1300 obtained from the manufacturer. The virgin BX1300 was modified in this study to create a weaker reinforcement by removing alternate ribs (every other rib) in the cross- machine direction (XMD). This was done to ensure measurable strains in the geogrid during the wetting-drying cycle of the reinforced clay specimen. The cross-machine direction (XMD) was chosen here as the straining direction of the geogrid since it has longer ribs between junctions than the machine direction (MD). Longer ribs provided easier attachment of strain gauges.

Table 3.2 Geogrid index properties

	MD values	XMD values
Aperture dimensions, mm	46	64
Minimum rib thickness, mm	1.27	1.27
Tensile strength @ 2% strain, kN/m	5.5	9.5
Tensile strength @ 5% strain, kN/m	10.5	17.5
Ultimate tensile strength, kN/m	16.0	28.0

Strain gauges EA-13-250BF-350 from Micro-Measurement Division, Measurements Group, Inc. were used to measure geogrid strains (Figure 3.10). The strain gauge width approximately covers the entire rib width of the geogrid, thus the gauges were expected to measure the overall, local strain of a single rib quite accurately. A total of six strain gauges were attached on the geogrid specimen. M-bond AE-10 was used as adhesive to bond the strain gauges. The strain gauges were covered with wax and 3145 RTV epoxy for protection from

damage and water intrusion. Figure 3.11 shows the geogrid reinforcement after the strain gauges were installed with protection cover attached.

3.3.3 Wetting-Drying Testing Program

Tests for the effects of one wetting-drying cycle were performed at varying stress levels under working load conditions. For comparison, tests were conducted in the geogrid-reinforced and unreinforced clay specimens in otherwise identical conditions. Each test involved a mechanical loading stage that was followed by a wetting-drying cycle representing environmental loading. All together, five sets of wetting-drying tests (three in unreinforced specimens and two in geogrid-reinforced specimens) were performed. Horizontal pressure and vertical pressure were applied independently to the specimen with a coefficient of lateral earth pressure (K) equal to 0.7. This value has been calculated from Massarsch (1979) empirical equation for fine-grained normally consolidated soils, $K = 0.44 + 0.42 (I_p) = 0.69 \approx 0.7$, where I_p is plasticity index of clay with a value of 61%. Each test was given a unique designation. The first two letters correspond to reinforced specimen (RP) and unreinforced specimen (UP) respectively. The succeeding numbers in the test specimen designation correspond to the vertical and horizontal stresses respectively applied to the soil specimen. For example, RP20/14 was for the wetting-drying of a reinforced clay specimen at applied vertical and horizontal stresses of 20 kPa and 14 kPa respectively. Table 3.3 summarizes the testing program.

Table 3.3 Summary of wetting-drying testing program of clay specimens

Test condition	Reinforcement conditions	Test designation			Total number of tests
		Applied stresses (σ_y and σ_x), kPa			
		20 and 14	30 and 21	50 and 35	
Wetting-Drying cycle	without geogrid	UP20/14	UP30/21	UP50/35	5
	with geogrid	RP20/14	-	RP50/35	

3.3.4 Specimen Preparation and Test Procedures

The clay was oven dried and pulverized before it was weighed in batches. Each soil batche was mixed thoroughly with water in a mixer at 30% water content. Then, the soil batches were cured at least three overnights in zip-locked plastic bags inside a high humidity room to allow equal distribution of water within the soil mass. The test procedures are described as follows:

1) Rubber air bags for lateral pressure applications were positioned inside the test box. Metal plates of 3 mm in thickness were fixed inside the air bags to provide restraint during soil compaction. The flexibility of the side airbags to move both laterally and vertically can reduce friction between soil and porous stones.
2) A latex membrane with a thin layer of silicon grease was placed on the plexiglass sidewalls. Porous stones with filter papers were placed at the bottom and at the contact areas with the air bags.

3) Compaction of the clay was done in lifts (30 mm per lift) using a drop hammer (similar to Proctor compaction test) to achieve 13.3 kN/m^3 of dry unit weight. The top surface of each compaction lift was scratched to provide good bonding with the successive layer of compaction.
4) Instrumentation for example, psychrometers, tell-tales were installed inside the soil specimen at prescribed locations (see Figure 3.2). A geogrid specimen (with six strain gauges attached) was placed at the mid-height of the clay block during the soil specimen preparation (Figure 3.12). Two dummy strain gauges were attached in short pieces of geogrid rib that were placed inside the soil specimen at 20 mm above the geogrid reinforcement (Figure 3.13). The purpose of dummy strain gauges was to incorporate the effect of temperature on geogrid strain measurements. Miniature vertical drains were installed in the clay specimen to facilitate faster saturation and drying of the clay block. About 4 mm diameter holes were drilled in the clay specimens from top of lower half and upper half of the clay block during specimen preparation and geotextile was inserted into the holes as miniature vertical drains. Filter paper, a sand layer, a porous stone and the top metal plate were placed on top of the clay specimen.
5) All instrumentation, including spring-loaded linear position sensors (LPS), linear variable displacement transducers (LVDT), tell-tales, psychrometers, strain gauges, load cell and pressure transducer were connected to a data acquisition (DA) system and monitored periodically

throughout the test. Figure 3.14 shows a photo of the complete test set-up.

6) Before applying the vertical and horizontal pressures, the metal plates providing lateral restraint inside the air bags were released. The pressures were applied in increments for one hour until the desired stress levels were reached and then maintained constant during the test. Deformations were monitored until they reached equilibrium.
7) Under constant vertical and horizontal pressures, the wetting condition in the clay was simulated by flooding the clay with water from the bottom of test box under a head of 1 m. This simulates the wetting condition in the clay. Once full swell was achieved representing near full saturation, water was drained from the test box. The clay was then dried by supplying warm air (at about 35°C temperature) from the top and bottom of the soil specimen.

3.3.5 Instrumentation and Monitoring

The layout of instrumentation used in this study is shown in Figure 3.2. Four LPS were used to measure the lateral deformations of the clay block. Two tell-tales attached to LPS were placed inside the soil block along its mid-height to measure lateral strains. One LVDT was used at the top of the specimen to measure the vertical deformation of the soil block. Four psychrometers were installed inside the specimen at various locations to measure temperatures and suctions in the clay, and thus, the water content and saturation during testing. The vertical

pressure (load) was monitored via a load cell and the horizontal pressure was controlled via a pressure transducer. Six strain gauges were attached to the geogrid to measure reinforcement strains. All instrumentation was connected to a data acquisition (DA) system. The DA system consisted of a PC-based data readout module and a Labtech program to read and store data in the computer. All the instruments were calibrated before use. In the case of the suction measurements, psychrometers were connected to a Campbell Scientific CR7 data acquisition system. This was in turn connected to the PC-based data read out and storage program (Labtech).

3.4 FREEZING-THAWING CYCLE

3.4.1 Introduction

Freezing and thawing of soils are common in areas of cold climate, particularly in Western Canada. When geosynthetic-reinforced soil structures are constructed using frost susceptible soils in such areas, deformation of the soil structures as well as additional strains and stresses in the geosynthetic reinforcements are inevitable during seasonal freezing and thawing cycles. Freezing of frost susceptible soil produces expansion while thawing of soil produces consolidation. To simulate these environmental effects, tests with freezing-thawing cycles were conducted on frost susceptible silt specimens with and without geosynthetic reinforcement. The same test apparatus used in wetting-drying tests (described

in Section 3.2) was used for freezing-thawing tests. In this case, porous stones were not used at the top of soil specimen, as well as between the rubber air bags and the soil specimen (see Figure 3.15) to allow one dimensional flow of water in the soil from the bottom during freezing. The soil specimen dimensions were: 420 mm (W) x 450 mm (L) x 520 mm (H). A temperature-controlled environmental chamber in the Structures Laboratory at the University of Manitoba was used to house the test box for the freezing and thawing tests. The specimens were subjected to constant applied confining pressures, similar to those in wetting-drying tests. These were first applied with mechanical loading until equilibrium deformation was reached and then water was introduced for saturation. Saturation in silt specimens was quicker than in the clay specimens because of their relatively high permeability. Excess water was drained from the test box after saturation and the soil specimens were subjected to freezing temperatures (down to -25°C) in the environmental chamber. After 17 hours of freezing, the specimens were allowed to thaw under warm temperature (up to +23°C) for 19 hours. The freezing and thawing were repeated for several cycles. Note that for this test, excess water from the test box was removed prior to application of freezing temperatures; otherwise water would freeze in the rigid test box and might damage the test box. Materials used in the tests, the testing program, specimen preparation, test procedures and instrumentation are briefly explained in the following sections.

3.4.2 Material Properties

3.4.2.1 Soil Properties

The soil for the freezing-thawing tests was obtained from one of the construction sites of Manitoba Infrastructure and Transportation in Northern Manitoba. Figure 3.16 shows the grain size distribution curve of the soil. It is classified as sandy silt based on the Unified Soil Classification System (USCS); but for convenience it is referred here as silt. The specific gravity of the soil was found to be about 2.74. Figure 3.17 shows the dry unit weight-moisture content relationship from a standard Proctor compaction test. It indicates an optimum water content of 13% and maximum dry unit weight of 18.3 kN/m^3.

In order to determine the strength properties and stress-strain behaviour of the soil, Isotropically Consolidated Drained (CID) triaxial tests were conducted on compacted silt samples prepared at optimum water content and maximum dry density. The triaxial samples were prepared by applying suction during sample preparation to provide stability as they were positioned in place on the triaxial apparatus. An axial strain rate of 0.005 mm per minute was used in the CID tests to ensure drained conditions during loading. Prior to loading, the triaxial samples were back pressured until a "B" value of 98% was obtained. The samples were then consolidated using confining pressures (σ_c') = 50, 75 and 100 kPa. The resulting stress-strain and effective stress paths in q-p' space are shown in Figures 3.18 and 3.19, respectively. At critical state failure conditions the

compacted silt has slope (M) of critical state line equal to 1.25, which gives the equivalent internal angle of friction at critical state (ϕ'_{cs}) equal to 31°.

3.4.2.2 Properties of Geosynthetic Reinforcement

The geogrid materials used in freezing-thawing tests along with the instrumentation and sample preparation were broadly similar to those in the wetting-drying tests as discussed in Section 3.3.2.2. However, these will be briefly discussed in the following section as there were slight differences.

3.4.3 Freezing-Thawing Testing Program, Specimen Preparation and Instrumentation and Monitoring

Freezing-thawing cyclic tests were carried out in unreinforced and reinforced silt specimens, again in plane-strain and working load conditions. In the reinforced silt specimen, the geogrid was placed at the middle of soil specimen. The soil specimens were prepared by compaction of soil at optimum water content (13%) and maximum dry unit weight (18.3 kN/m^3). The process of soil specimen preparation was similar in wetting-drying tests as described in Section 3.3.4, except that there was no porous stone placed between air bags and soil specimen, no sand layer, and no porous stone on top of the soil specimen (Figure 3.15). Since silt has high permeability, no miniature vertical drains were installed in the specimens.

The geogrid specimen was laid-out at the mid-height of the silt block during the soil specimen preparation (Figure 3.20). Two tell-tales were installed at the same level for displacement measurements in the soil. Two dummy strain gauges were attached to short pieces of geogrid rib and placed inside the soil specimen at 20 mm above the geogrid reinforcement (Figure 3.21). The purpose of dummy strain gauges was to incorporate the effect of temperature on geogrid strain measurements. Thermocouples were also installed with the dummy strain gauges in the soil specimen. Four (4) thermocouples were placed in the silt specimen at four positions to measure the soil temperatures (Figure 3.15). The rest of the instrumentation and monitoring system were the same as those in wetting-drying tests as described in Section 3.3.5. The instrumentation such as LVDT, LPS, tell-tales, strain gauges and thermocouples were all connected to the DA system where all data were recorded electronically.

The testing box and soil specimen was placed inside the environmental chamber for the freezing-thawing simulation (Figure 3.22). Two unreinforced silt specimens namely UT-18°C/+23°C and UT-25°C/+23°C, and one geogrid-reinforced silt specimen namely RT-25°C/+23°C were tested. The first two letters of the each test designation again correspond to a reinforced specimen (RT) and unreinforced specimen (UT) respectively. The succeeding numbers in the test specimen designation correspond to freezing and thawing temperatures respectively. Freezing was simulated by subjecting the chamber to -18°C and -25°C temperatures. Thawing was simulated by subjecting the chamber

temperature to +23°C. The freezing and thawing cycles were done in 17 and 19 hours respectively. A vertical pressure of 20 kPa and horizontal pressure of 14 kPa were applied to each specimen, simulating anisotropic loading condition in the field. The specimens were loaded until equilibrium deformation was reached before they were flooded with water for about 20 hours for saturation. Excess water was removed from the testing box about 2 hours prior to applying the freezing temperature. However, the bottom of the soil specimen was connected with an outside water tank (water level in the tank was slightly above the bottom of soil specimen to maintain a low hydraulic gradient) to supply water during the freezing period. The water was supplied through an insulated pipe. However, the insulation was not adequate from preventing the water in the pipe to freeze. This blocked the flow of water to the specimen. To this effect, the upward flow of water in field conditions as the freezing front advances from the top was not well simulated in the tests. The tests can only provide the freezing and thawing of nearly saturated silts. Nevertheless, they can provide meaningful information on the soil-reinforcement interaction and deformation of reinforced silt specimens during freeze-thaw cycles.

3.5 SUMMARY

Development of a new test apparatus has been discussed and test conditions involving wetting-drying and freezing-thawing tests have been described. The following summarizes the content of this chapter:

1) A large-scale plane-strain test apparatus was developed and commissioned at the University of Manitoba to study the behaviour of geosynthetic-reinforced soils subjected to wetting-drying and freezing-thawing cycles. The geogrid-reinforced soil specimen, dimensions: 420 mm (wide) x 430 mm (long) x 500 mm (high) was prepared inside the test apparatus at optimum moisture-maximum dry density.
2) Independent vertical and horizontal pressures were applied to the soil specimen to simulate anisotropic field stress conditions. The soil specimen was allowed to deform laterally and vertically under plane-strain condition during the test. Soil deformations, geogrid strains, soil temperatures and soil suctions were measured.
3) Post-construction wetting-drying of swelling clay induces swelling-shrinkage in the soil mass. To evaluate the effects of wetting and drying, tests were performed in geogrid-reinforced and unreinforced clay specimens. Constant vertical and horizontal pressures were applied to the soil specimen before applying wetting until the soil reached equilibrium under the mechanical loading. Wetting was simulated by flooding the soil specimen with water. Once full swelling was achieved, excess water in the test box was drained from the specimen and test box. The soil specimen was then dried by supplying warm air at about 35°C from top and bottom of the specimen.
4) Freezing-thawing of frost susceptible soil induces heave and consolidation in the soil. To simulate these effects, tests with freezing-thawing cycles

were conducted on sandy silt specimens with and without geosynthetic-reinforcement. The test apparatus, including the specimen was kept inside a temperature-controlled environmental chamber to apply freezing-thawing temperatures. The specimen was first flooded with water for saturation and the excess water in the test box was removed prior to applying freezing. Then, the chamber temperature was set to -25°C temperature for 17 hours. This was followed by setting the chamber temperature at +23°C for 19 hours. Freezing and thawing of the specimens were repeated for several cycles. Vertical and horizontal soil specimen displacements, horizontal soil strains, geogrid strains and soil temperatures were measured during the test.

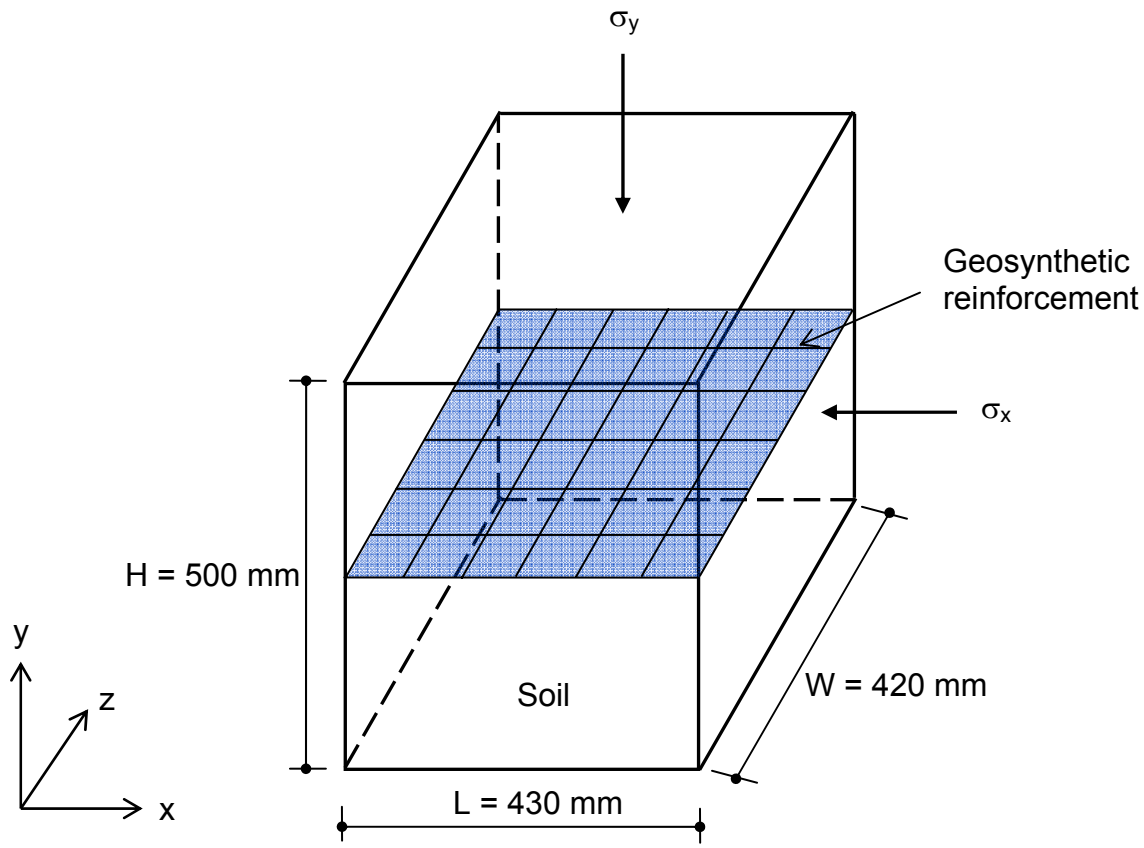

Figure 3.1 Schematic of plane-strain geosynthetic-reinforced soil specimen dimensions and testing principle ($\varepsilon_z = 0$)

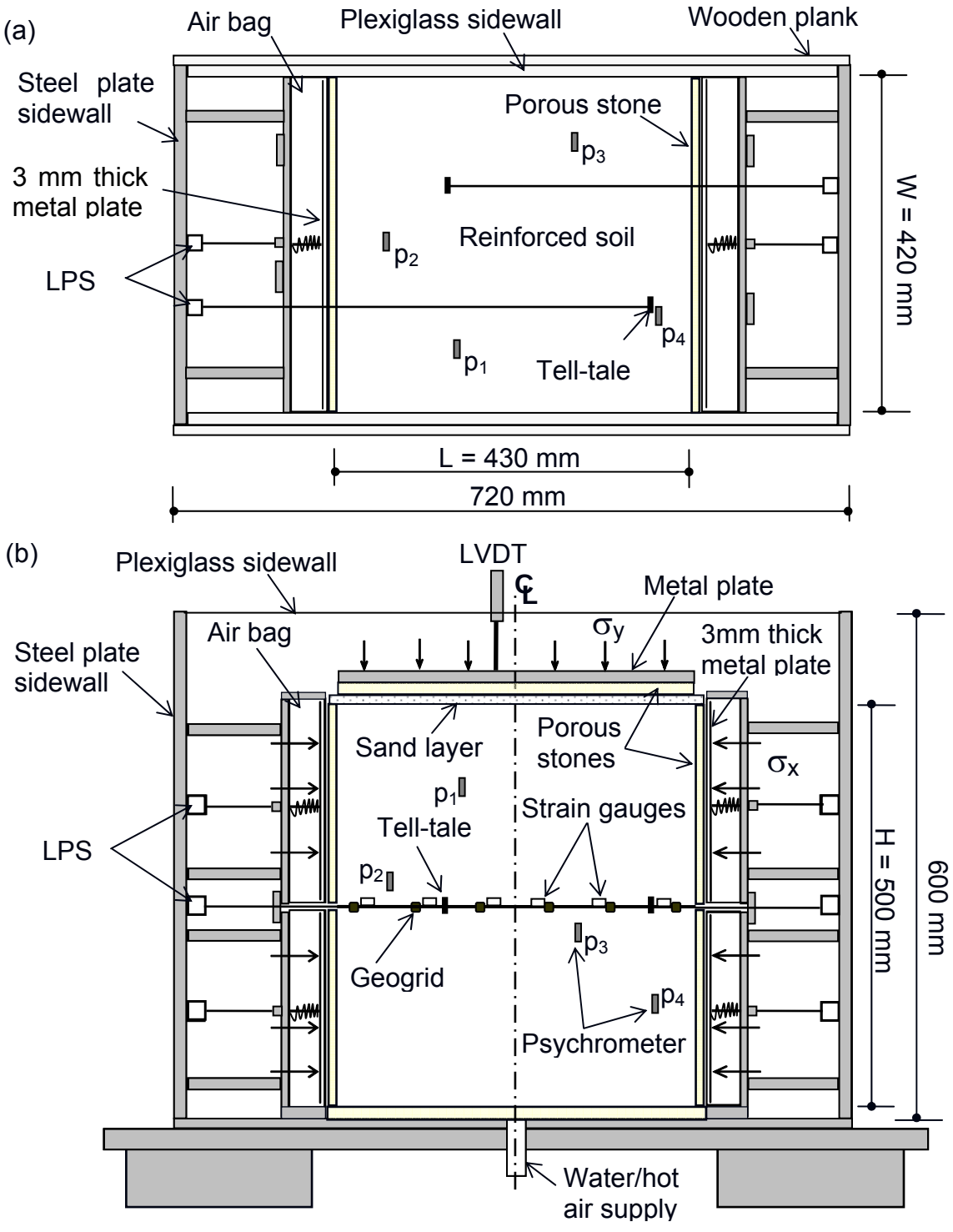

Figure 3.2 Schematic of plane-strain test apparatus and geogrid-reinforced clay specimen with layout of instrumentation: (a) plan view and (b) profile section

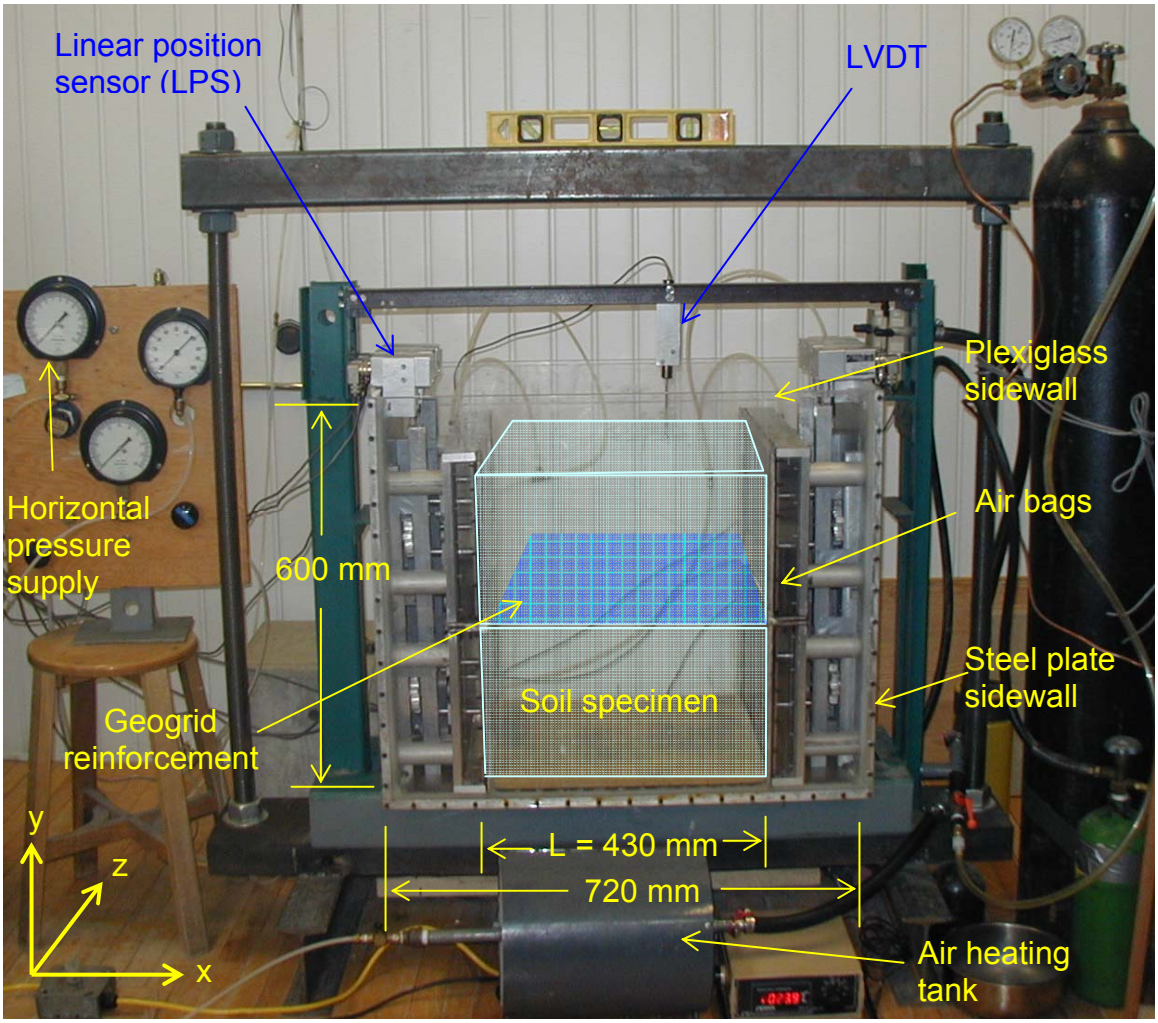

Figure 3.3 Photograph of plane-strain laboratory test apparatus and test set-up

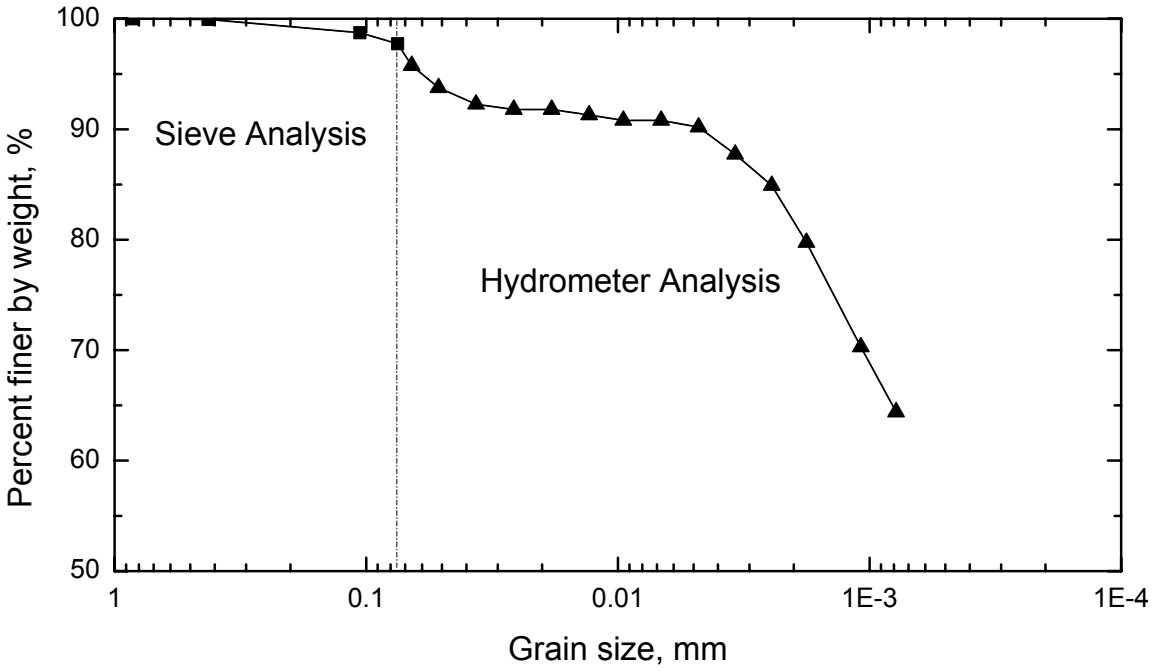

Figure 3.4 Grain size distribution of clay

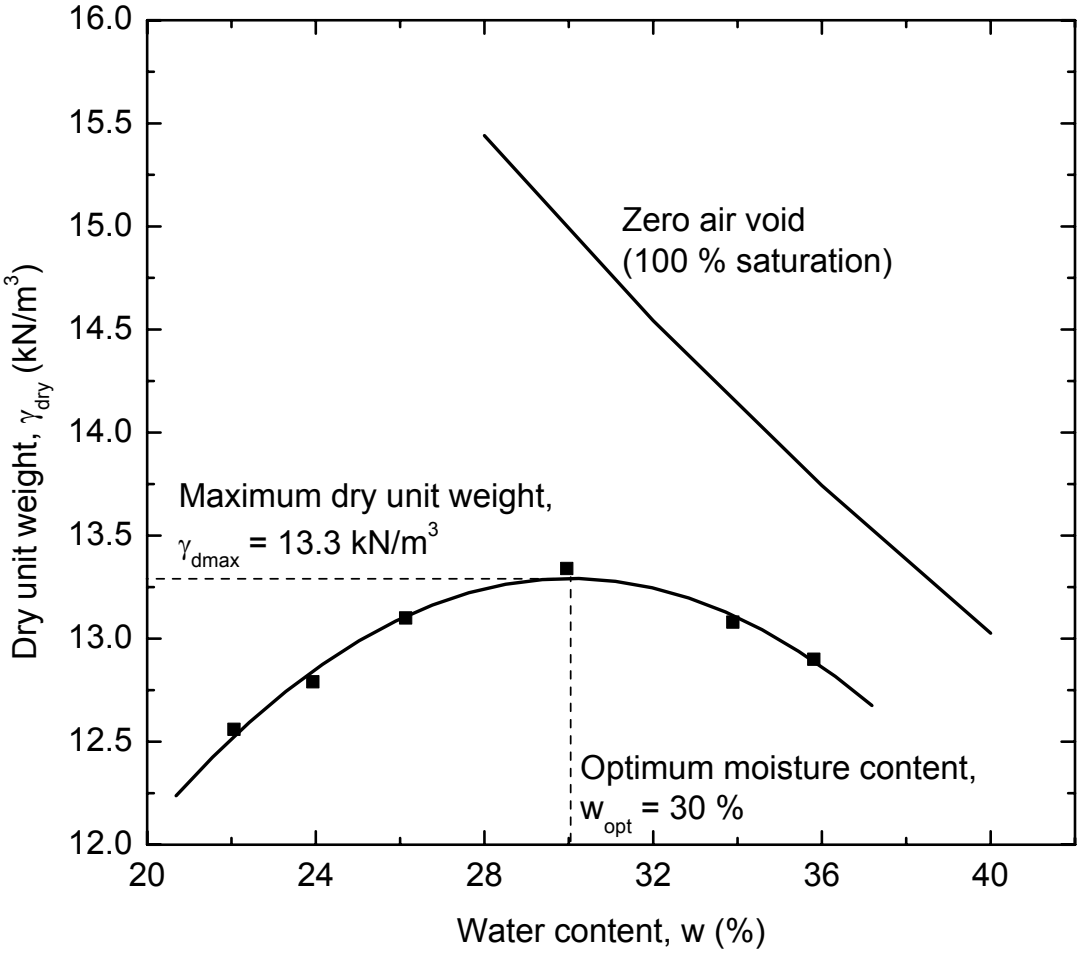

Figure 3.5 Dry unit weight - moisture relationship in clay soil from standard Proctor compaction test

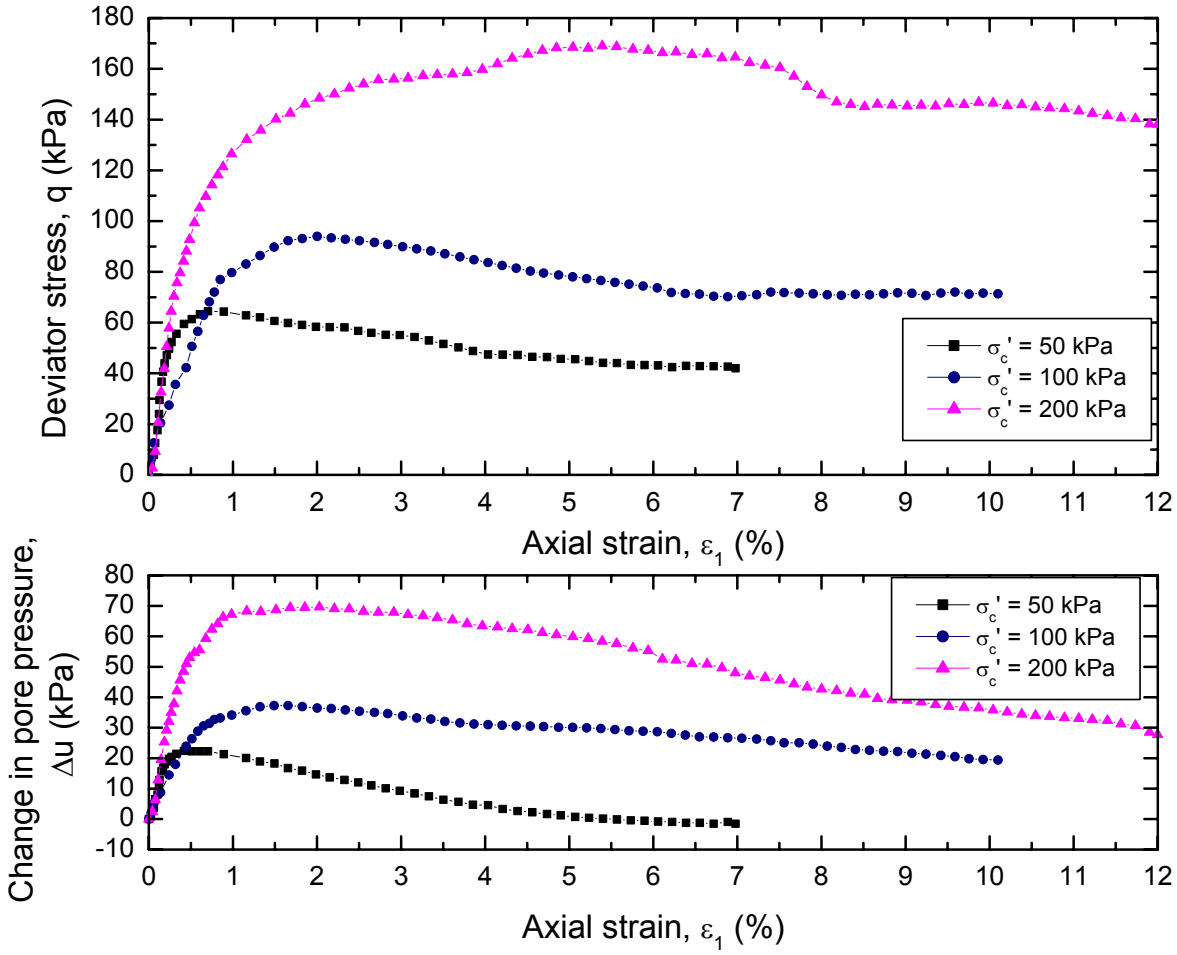

Figure 3.6 Stress-strain and change in pore water pressure curves of clay from isotropically consolidated undrained (CIŪ) triaxial test

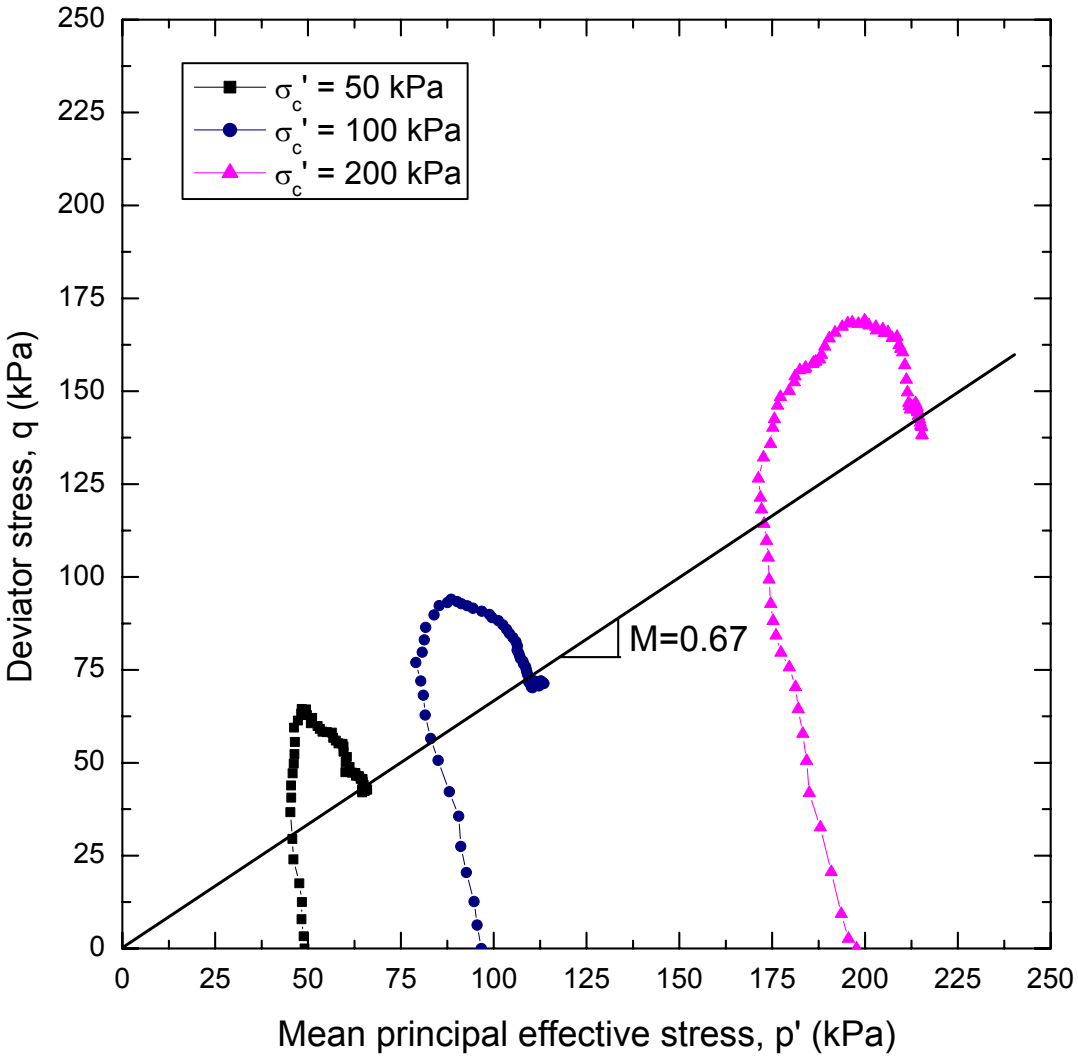

Figure 3.7 Effective stress path in q -p' space from CIŪ triaxial test of clay

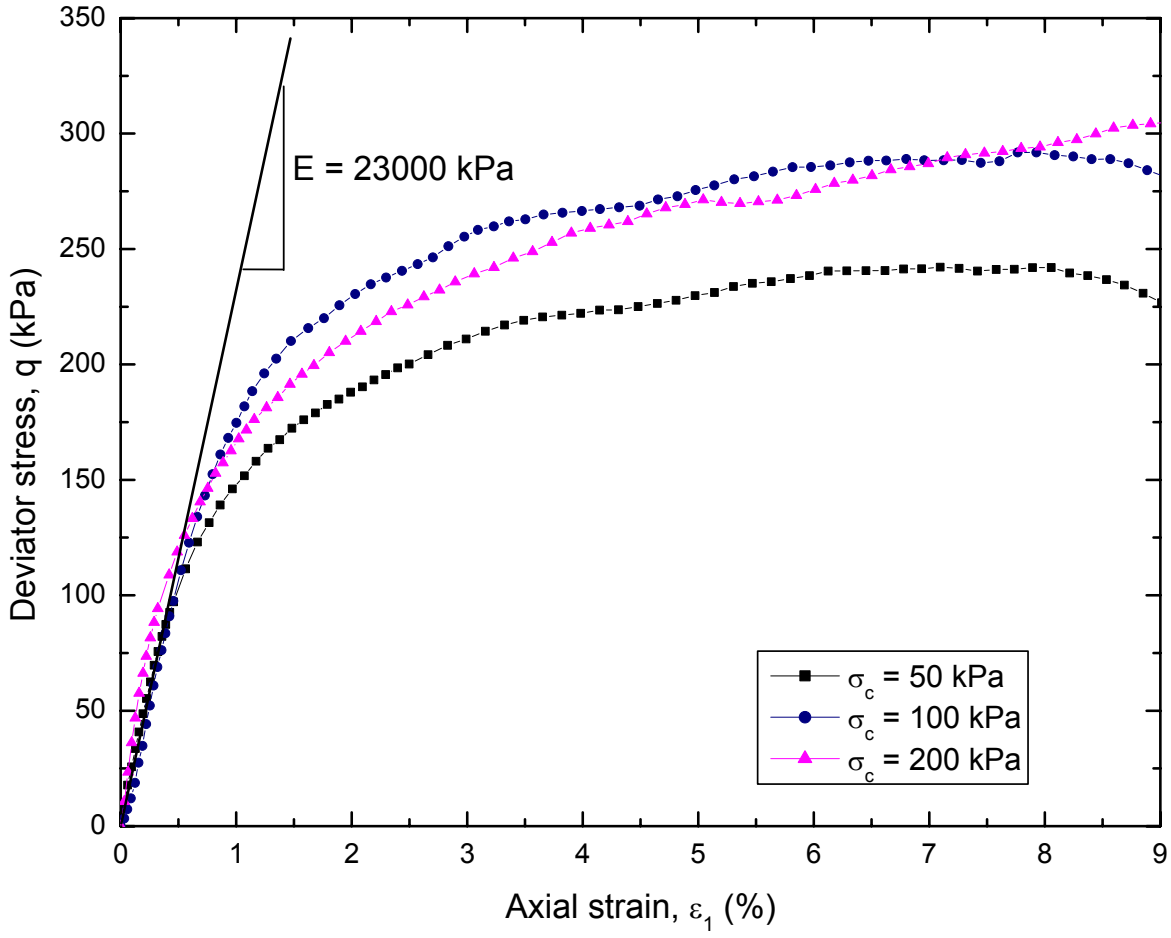

Figure 3.8 Stress-strain curves from unconsolidated undrained (UU) test of clay at unsaturated condition (compacted moisture content)

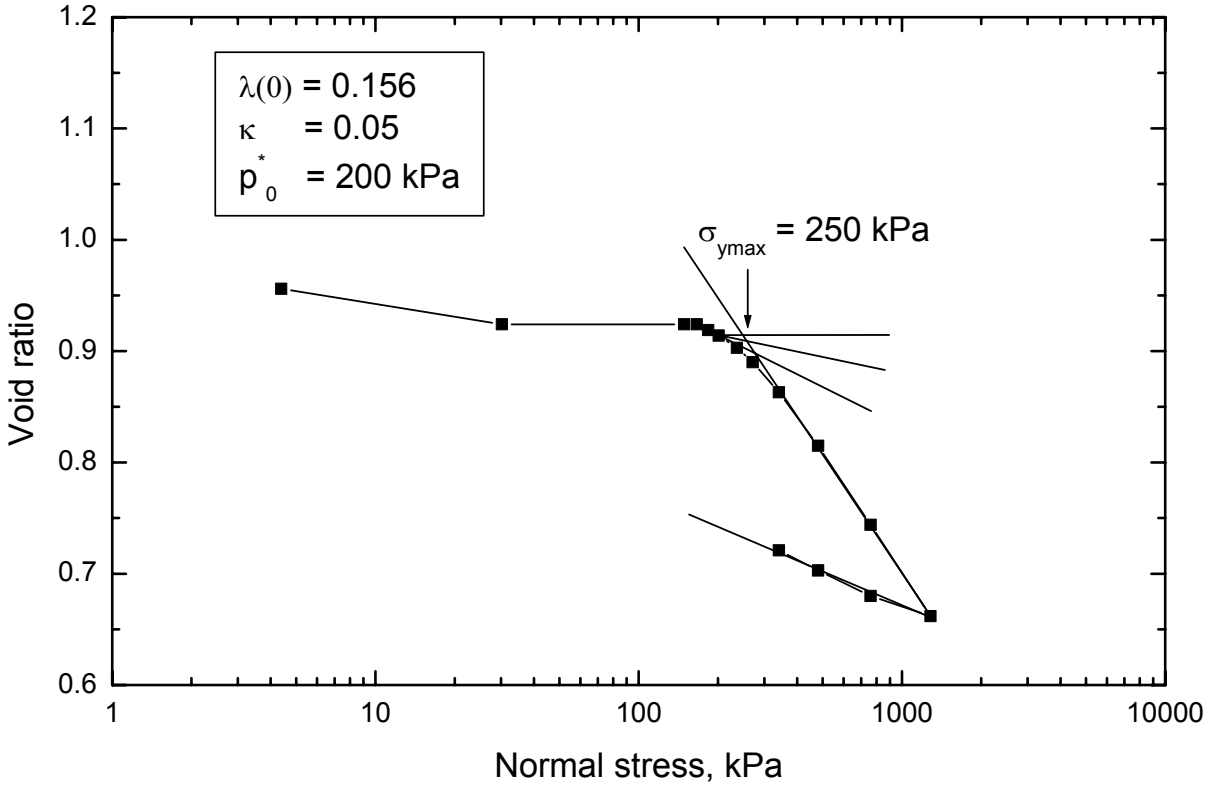

Figure 3.9 Void ratio-effective normal stress curve from one-dimensional swell test

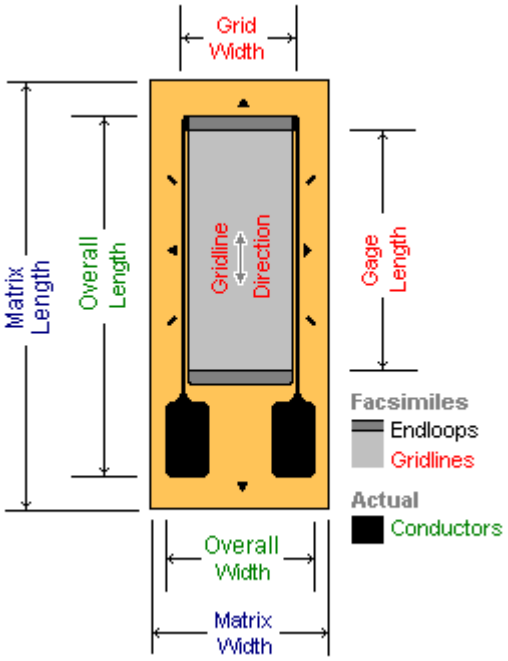

Dimensions	inch	mm
Gage Length	0.250	6.35
Overall Length	0.375	9.53
Grid Width	0.125	3.18
Overall Width	0.125	3.18
Matrix Length	0.52	13.2
Matrix Width	0.22	5.6

Figure 3.10 Strain gauge EA-13-250BF-350 dimensions

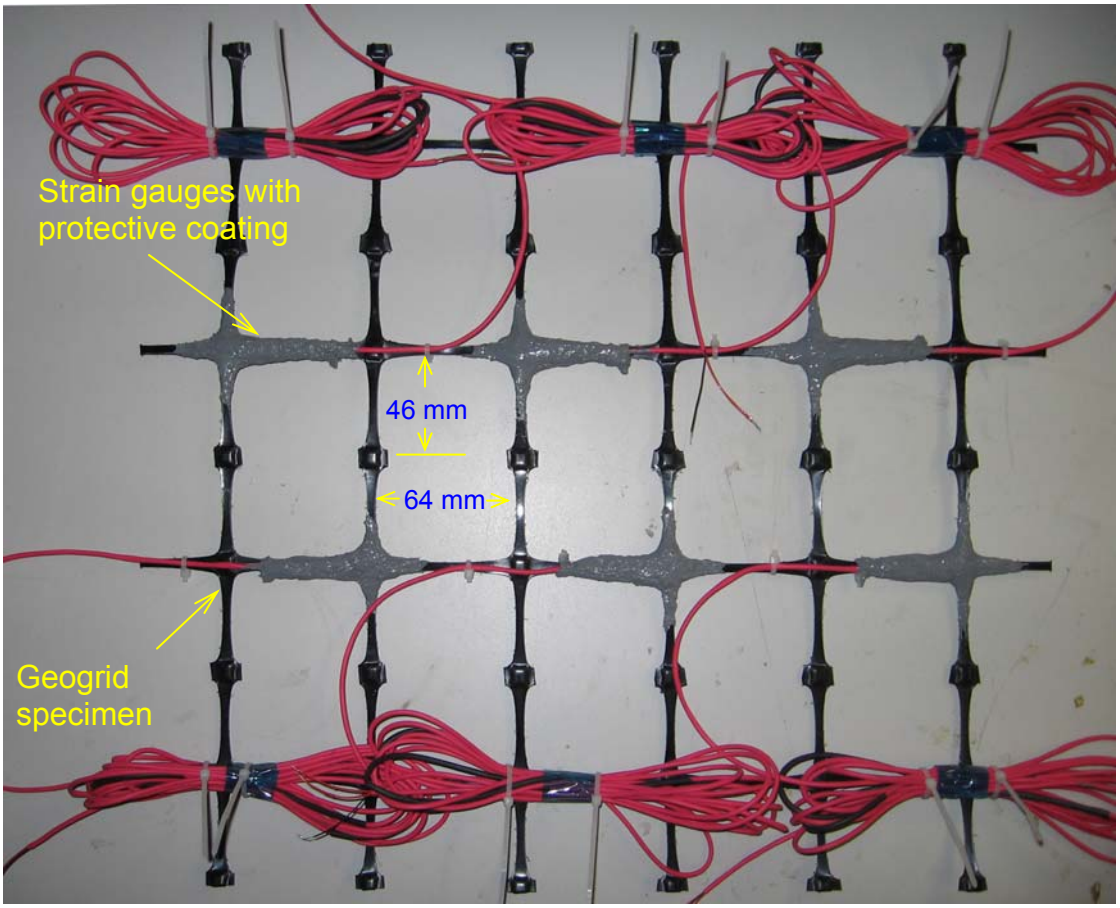

Figure 3.11 Photographs of geogrid reinforcement specimen after strain gauges attached

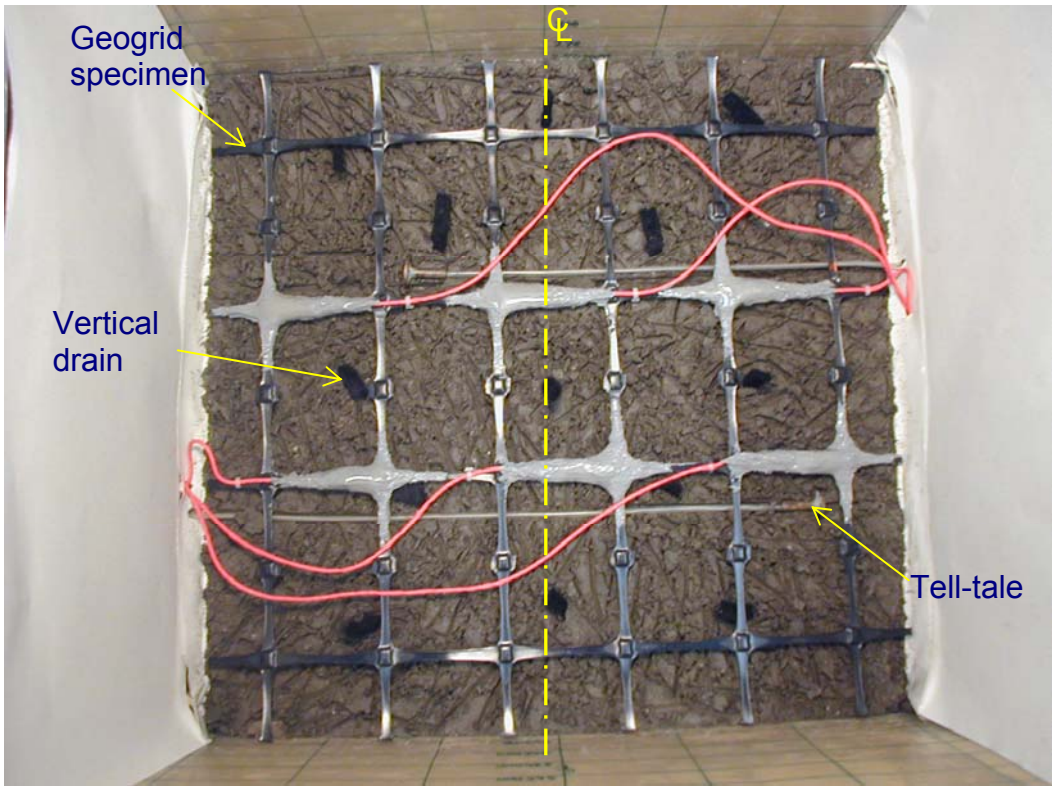

Figure 3.12 Photograph of geogrid reinforcement laid-out in the clay specimen

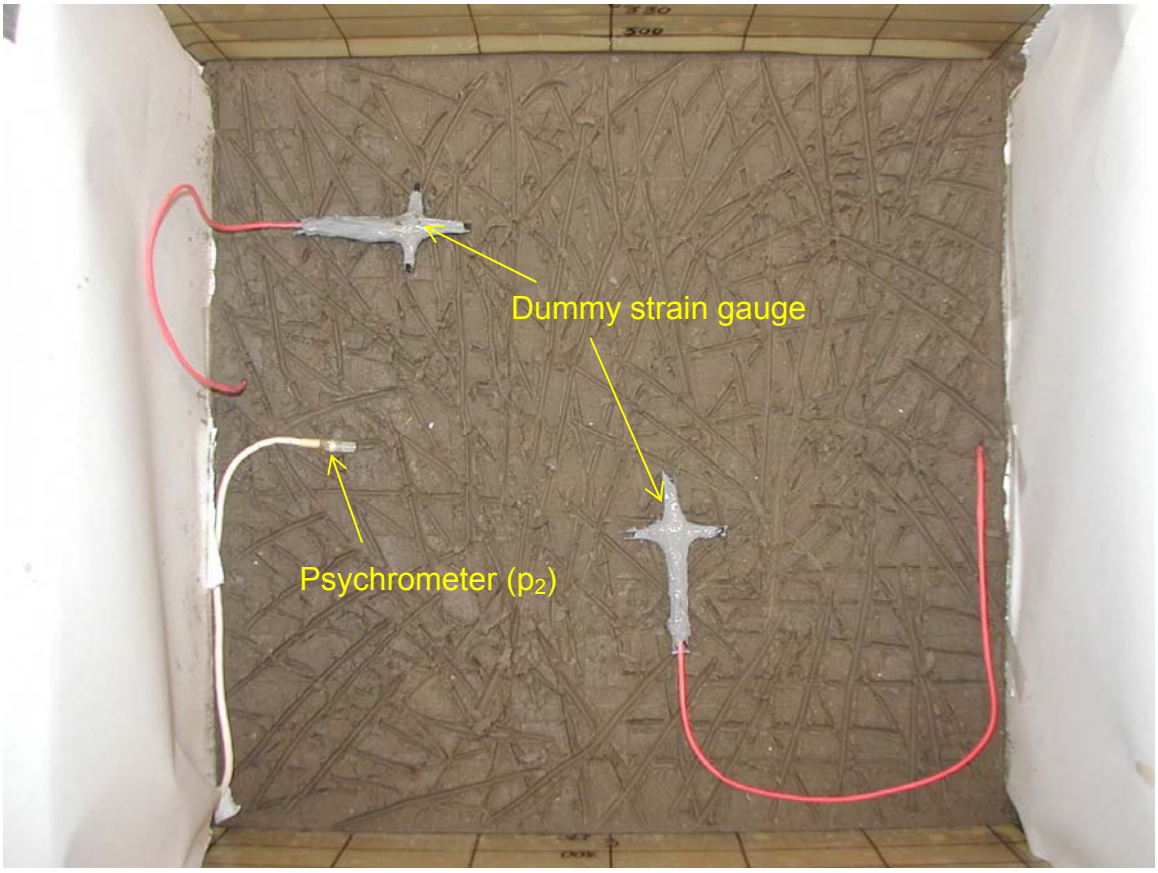

Figure 3.13 Photograph of dummy strain gauges and psychrometer laid-out in the reinforced clay specimen

Figure 3.14 Photograph of complete test set-up for wetting-drying of clay specimen

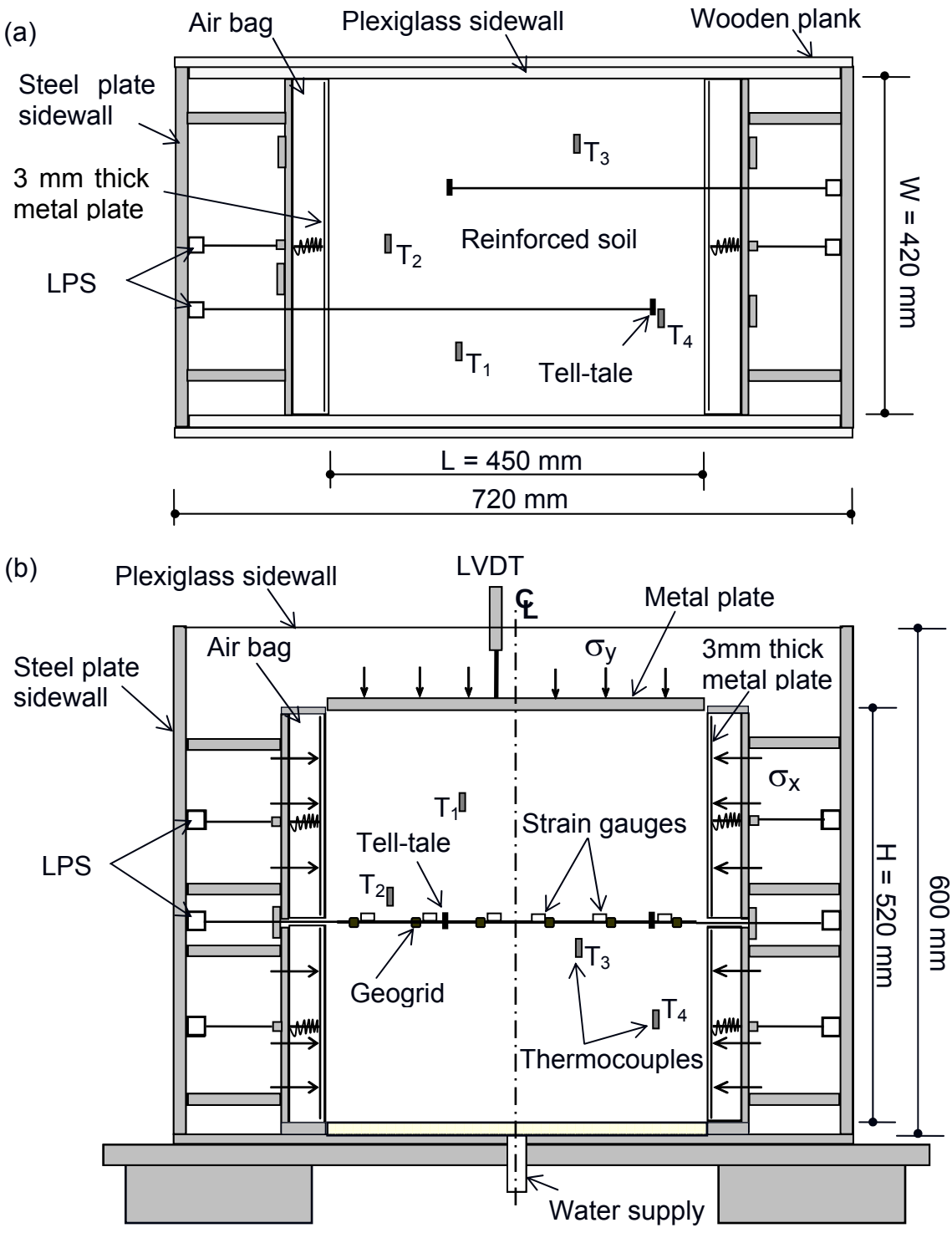

Figure 3.15 Schematic of plane-strain test apparatus and geogrid-reinforced silt specimen with layout of instrumentation: (a) plan view and (b) profile section

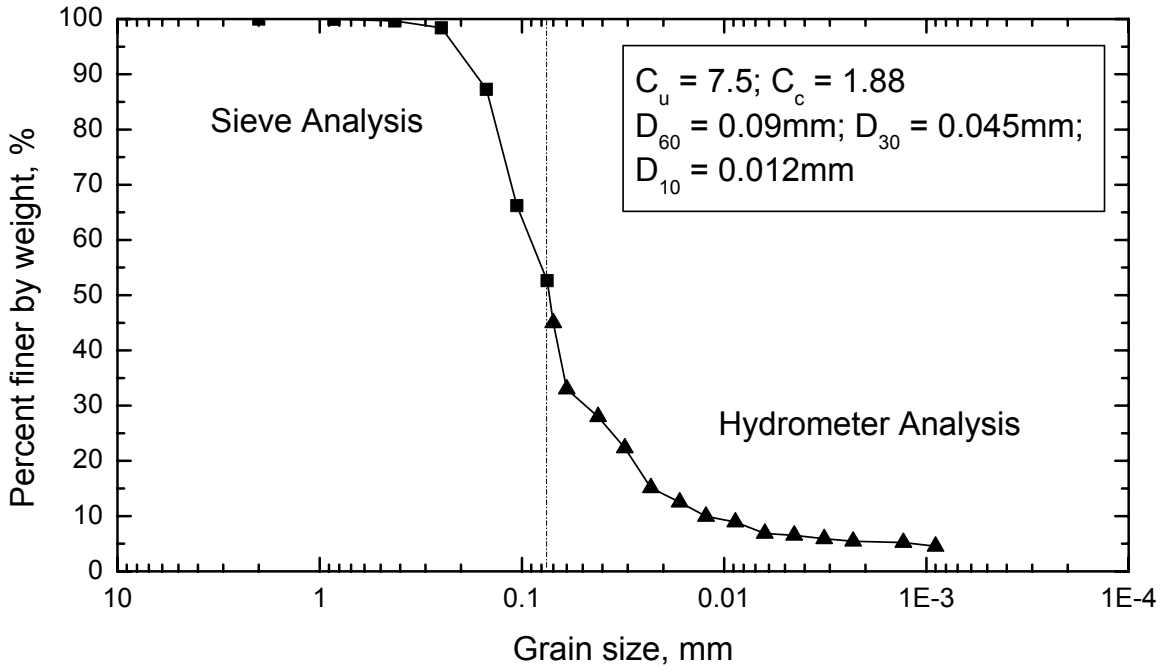

Figure 3.16 Grain size distribution of silt

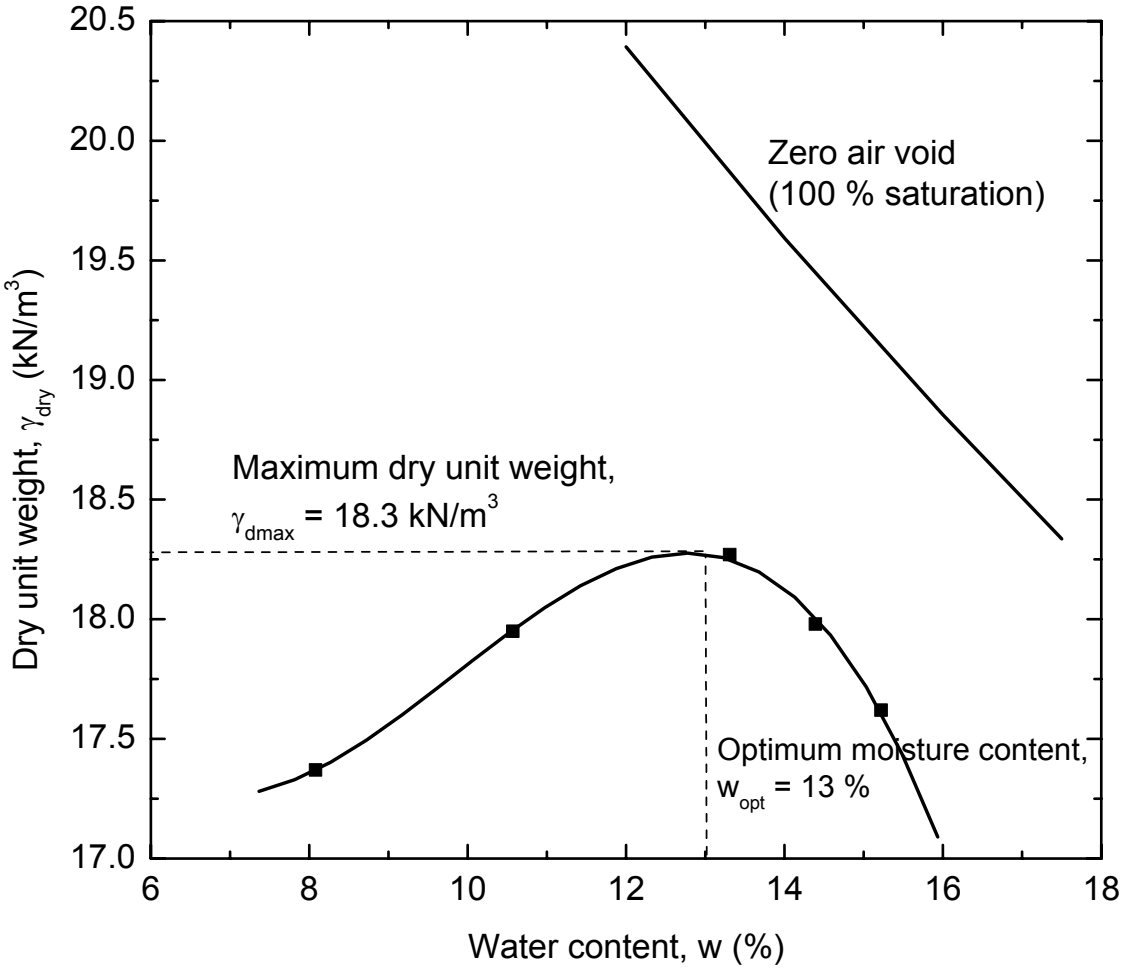

Figure 3.17 Dry unit weight - moisture relationship in silt from standard Proctor compaction test

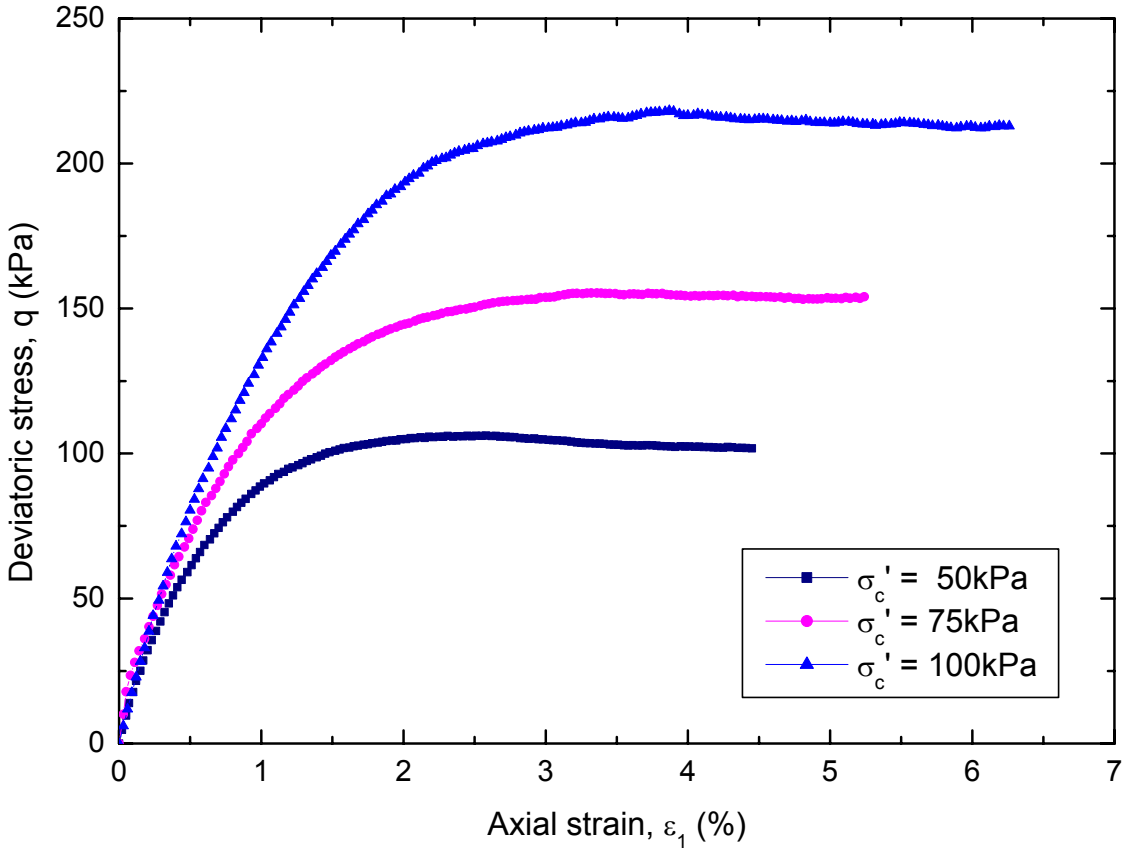

Figure 3.18 Stress-strain curves of silt from isotropically consolidated drained (CID) triaxial test

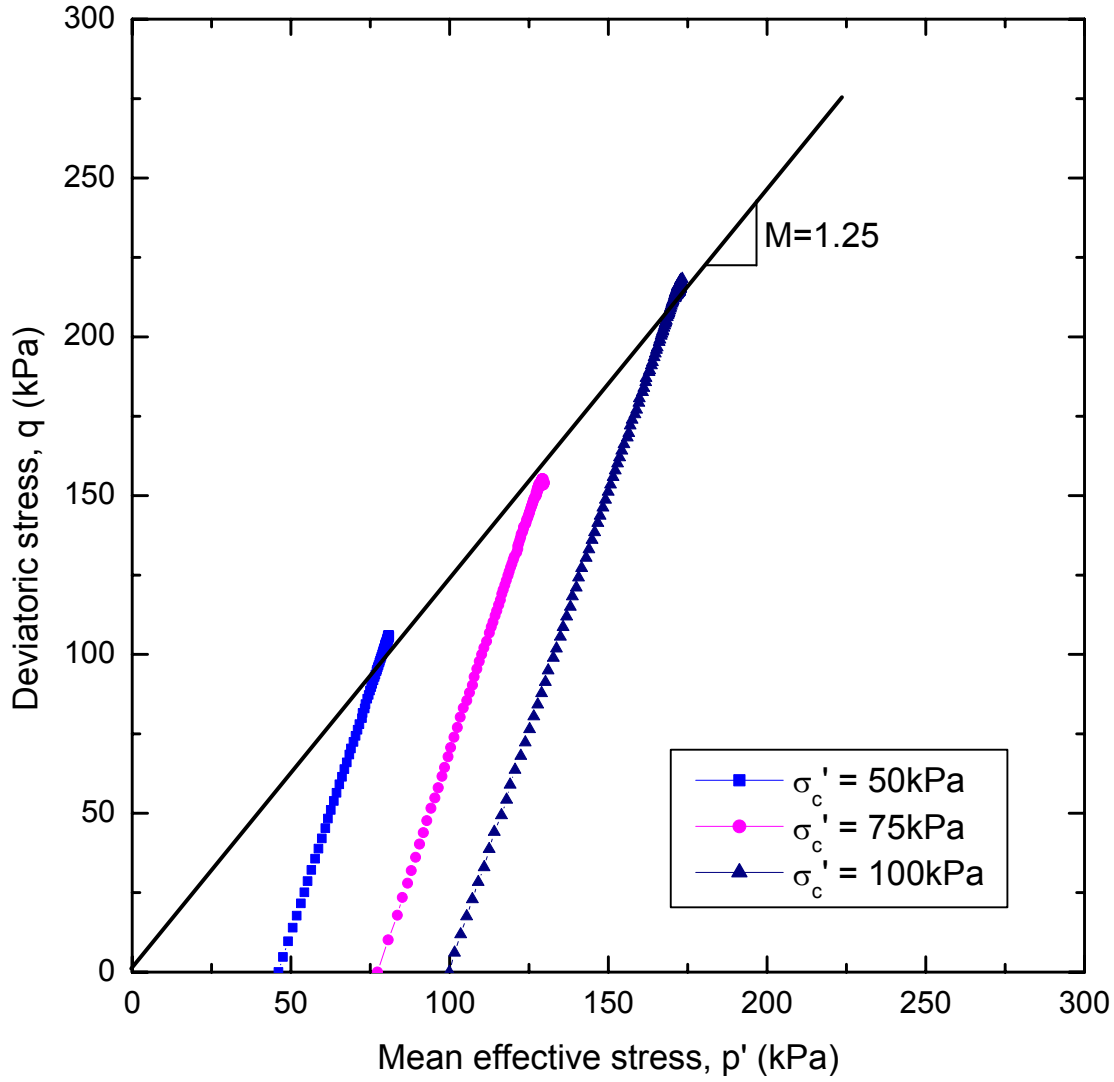

Figure 3.19 Effective stress path in q -p' space from CID triaxial test of silt

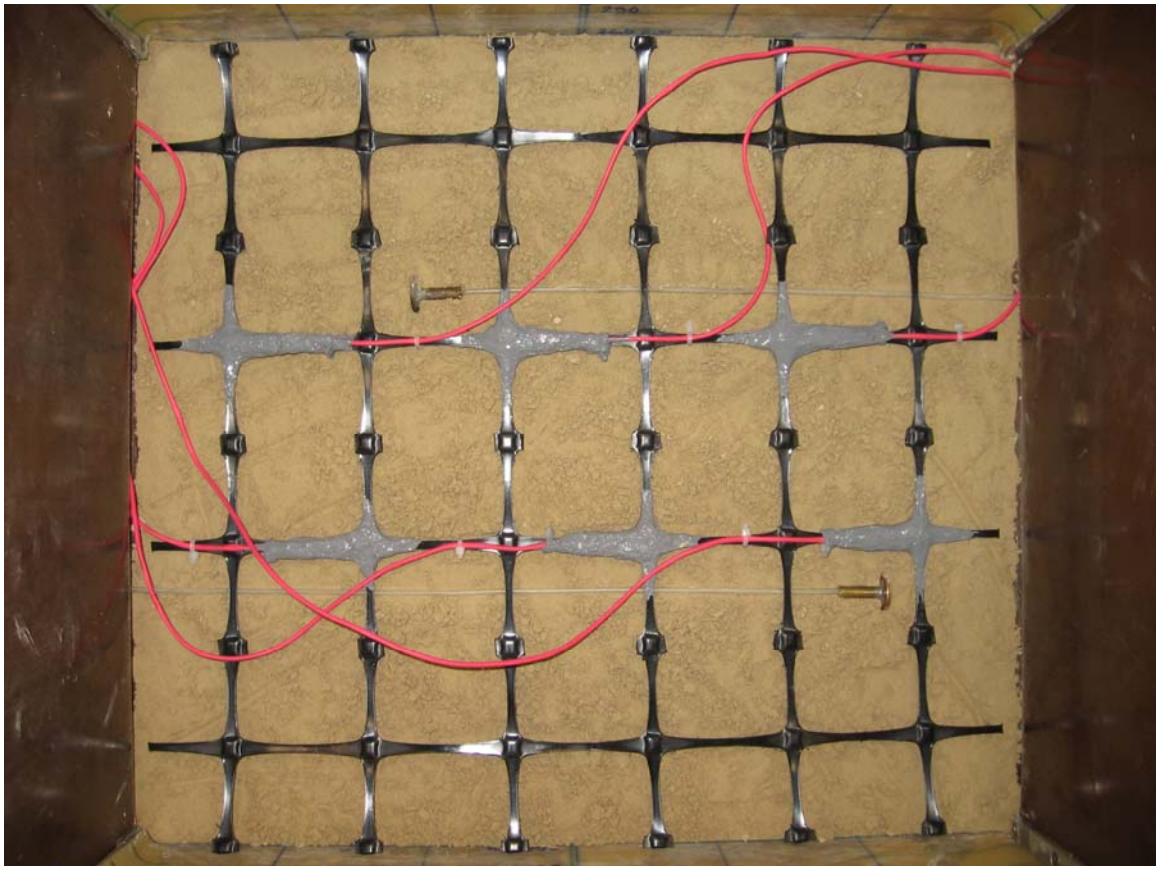

Figure 3.20 Photograph of geogrid reinforcement laid-out in the silt specimen

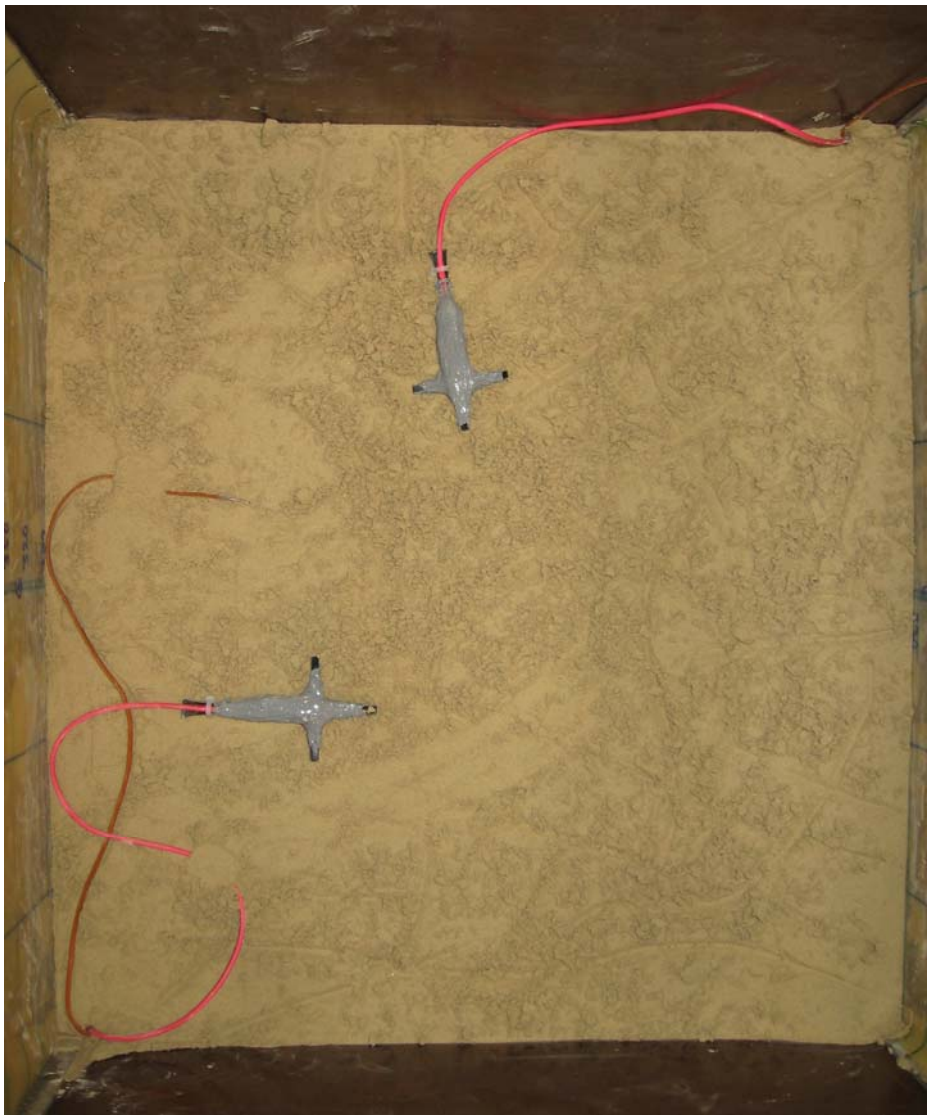

Figure 3.21 Photograph of dummy strain gauges and thermocouple laid-out in the reinforced silt specimen

Figure 3.22 Photograph of complete test set-up for freezing-thawing (test apparatus, including the soil specimen inside the environmental chamber)

CHAPTER 4

LABORATORY TEST RESULTS

4.1 INTRODUCTION

The laboratory testing program carried out in this study was divided into two parts: 1) wetting-drying tests of swelling clay fills, and 2) freezing-thawing tests of frost-susceptible silt fills. The testing program was discussed in Chapter 3. This chapter presents the laboratory test results and their interpretation in terms of geogrid strains, soil deformations, soil suctions and soil temperatures. Deformations of unreinforced and reinforced soil specimens that were subjected to wetting-drying cycles for clays and to freezing-thawing cycles for silts are discussed.

4.2 WETTING-DRYING TESTS RESULTS AND DISCUSSIONS

4.2.1 Introduction

Results form five sets of wetting-drying cycle tests (three in unreinforced and two in geogrid-reinforced specimens) are presented. The tests with and without

reinforcement were conducted in otherwise identical conditions for comparison purposes. They were performed at different applied pressure levels. In addition to comparing the results of unreinforced specimens with reinforced specimens, the test results on unreinforced clay specimens were used to develop the constitutive relation between swelling strains of clay and confining pressures. Deformations were measured using displacement transducers (LVDT, LPS) and tell-tales. The strains in the geogrid were measured using strain gauges, while soil suctions were measured by psychrometers. The results are presented and analyzed in the following sections.

4.2.2 Deformations of Soil Specimens

Figure 4.1(a) shows the locations of the instrumentation that will be discussed here. The measured deformations are presented in half-section only since they are expected to be symmetrical about the centreline. Horizontal displacements of the soil specimen are indicated as δ_{xt} and δ_{xb} for top and bottom, respectively. These are the average displacements measured on both sides of the specimen. Soil displacements measured by tell-tales at mid-height of the soil specimen are indicated as δ_{x1} and δ_{x2} while the vertical displacement is indicated as δ_{y}.

The sign convention that has been adopted is positive for soil expansion and reinforcement tension. This sign convention has been chosen to be consistent with the sign convention used in the numerical modelling but it is different from

the commonly used sign convention in geotechnical engineering. The numerical modelling will be presented in Chapter 5.

4.2.2.1 Mechanical Loading-Induced Deformations

Clay Specimens RP20/14 and UP20/14:

Geogrid-reinforced and unreinforced clay specimens were prepared at the same moisture-density condition and tested under identical loading condition. Each soil specimen was loaded with incremental pressures up to the desired stress level. The combination of vertical and horizontal pressures was chosen based on the stress ratio (K) = 0.7 discussed in Chapter 3. For this test series, the vertical pressure is 20 kPa and the horizontal pressure is 14 kPa. Soil specimens under these applied pressures are assigned as clay specimens RP20/14 and UP20/14 for reinforced and unreinforced clays, respectively. (Having established the usage, assigning of test specimens will be done similarly in subsequent sections.)

The applied pressures were kept constant until the soil deformation reached equilibrium. Figure 4.2 shows the applied pressure-time history of a reinforced soil specimen under the mechanical loading condition. It can be seen that the pressures were applied with very little variability with time. This is also true for other tests subjected to higher applied pressure levels (refer Figures A.1 and A.3 in Appendix A).

Figure 4.3 shows the displacement-time history for the reinforced specimen while Figure 4.4 shows results for the unreinforced specimen. Soil deformations are similar in both the reinforced and unreinforced specimens. This implies a negligible mobilization of tensile load in the reinforcement. The clay has been compressed vertically by about 1 mm and expanded laterally by about 0.73 mm on average. Soil deformations responded to the immediate application of pressures and then reached their constant values with time. Soil displacements (δ_{x1} and δ_{x2}) inside the soil specimen measured by tell-tales are very small and were considered unreliable measurements for such small amounts of deformation.

The total suctions in the soil measured by psychrometers during the mechanical loading in reinforced (RP20/14) and unreinforced clay (UP20/14) specimens are shown in Figures 4.5 and 4.6, respectively. The readings have been corrected for the effect of temperature. Soil suctions are fairly constant in the soil mass for both specimens, averaging to about 450 kPa. These results are also consistent for specimens with higher applied pressures as shown in Appendix A Figures A.2, A.4 and A.5.

Clay Specimen UP30/21:

In this particular test series, the specimens were applied vertical pressure of 30 kPa and horizontal pressure of 21 kPa. This was the first test conducted and

problems occurred related to wetting and drying of the specimens. There is no available reinforced specimen data and so there is no direct comparison between reinforced and unreinforced clay specimens under these particular applied pressures. However, the data under these pressure levels are used in developing wetting-induced strains and applied stress relationships that will be discussed in Chapter 5. The clay specimen (UP30/21) was also prepared in the same moisture-density condition as in clay specimens RP20/14 and UP20/14.

Figure 4.7 shows the displacement-time history for specimen UP30/21 indicating a vertical displacement (compression) of about 2.6 mm and expansion horizontally to about 0.52 mm on average. As expected, the vertical displacement is higher than that with applied vertical pressure of 20 kPa while the horizontal displacement is lower than that with horizontal pressure of 14 kPa. Soil deformations are also largely immediate and subsequently constant responding to the applied pressure-time history of the specimen. Soil displacements (δ_{x1} and δ_{x2}) inside the soil specimen are also very small.

Clay Specimens RP50/35 and UP50/35:

The test specimens were loaded with incremental pressures up to the desired level of 50 kPa in the vertical direction and 35 kPa in the horizontal direction (Specimens RP50/35 and UP50/35). Figures 4.8 and 4.9 show the displacement-time history for the reinforced and unreinforced specimens, respectively. Soil deformations are similar in both the reinforced and unreinforced clay specimens.

The specimens have been compressed vertically by about 3.3 mm but with negligible horizontal displacement. Relatively higher horizontal pressure of 35 kPa has restrained the horizontal movement of the clay. Soil displacements (δ_{x1} and δ_{x2}) inside the soil specimen are again very small.

In summary, vertical compression of the specimens increases with increase in applied vertical pressures, while the horizontal expansion of soil specimens decreases with increases in applied horizontal pressures. There is no noticeable difference in deformations with and without geogrid reinforcement, perhaps due to the low level of applied compressive stresses and the corresponding small deformations in the specimens that can be outside the resolution of the instrumentation used.

4.2.2.2 Wetting-Induced Deformations

Clay Specimen UP30/21:

As mentioned in the preceding section, this particular test on an unreinforced specimen was the first one that was conducted. No corresponding test was done on a reinforced specimen. The results for this unreinforced specimen are presented first instead of those for RP20/14 and UP20/14 that has been followed in the presentation sequence of the preceding section. This was done in an attempt to provide more coherent discussions.

In this particular test set-up, no porous stone was installed and no miniature vertical drains were installed in the clay specimen to facilitate faster saturation and drying. The clay specimen was flooded with water for wetting at constant applied vertical and horizontal pressures. Figure 4.10 shows the wetting-induced displacements in the clay specimen with time. The clay specimen swelled in both vertical and horizontal directions. Wetting-induced swelling of the clay specimen are as follows: δ_y = 2.8 mm, δ_{x3} = (δ_{xt} + δ_{xb})/2 = 3.1 mm, δ_{x1} = 1.5 mm and δ_{x2} = 2.36 mm. The value of δ_{x3} represents the average horizontal displacement of the top and bottom measurements of specimen. More than 50% of the total swelling occurred within a day after wetting and the rate of swelling decreased with time after the initial wetting. It took about 215 hours to reach equilibrium in swelling. This lengthy period limited the number of tests that could be completed.

Because the applied horizontal pressure was lower than the vertical pressure, it can be expected that the vertical displacement is lower than the horizontal displacement. Horizontal swelling at the bottom of the soil specimen (δ_{xb}) is higher than at the top of the soil specimen (δ_{xt}). Higher hydraulic head at the bottom of the specimen than at the top of specimen, and therefore higher saturation, can be the logical reason for the difference. As shown in Figure 4.11, suction measurements at the bottom of the specimen are relatively lower than those in the upper portion. Thus, for the rest of testing program, modifications were made by placing porous stones and miniature vertical drains for faster and relatively uniform saturation and drying.

Suction measurements were an indication of the amount of wetting or degree of saturation in the clay specimens during the wetting process. However, it is important to note that suctions measured by psychrometers during the wetting were not reliable for suction less than 100 kPa (Edil and Motan 1984). Psychrometers can operate successfully in a relatively wide range of suctions from 100 kPa to 7000 kPa (Briscoe 1984). The psychrometer was chosen to measure suction in this study because it is small in size and was the only available choice for low range suction measurements at the time of testing. Figure 4.11 shows the suction measured by psychrometers in the soil specimen UP30/21 during the wetting. Suctions in the soil are decreasing during wetting from its initial soil compaction moisture content suction (about 450 kPa). Suction at the top and middle of the soil specimen were found to be about 150 kPa. Psychrometer (p_4) shows zero suction within an hour of wetting. The results provided information whether or not suction decreased to about 100 kPa, indicating near full saturation of soil. One point to note is that wetting was continued until the rate of swelling was relatively constant after 200 hrs. Results of suction measurements for other stress conditions are given in Appendix A (Figures A.6 to A.8).

Clay Specimens RP20/14 and UP20/14:

Specimens RP20/14 and UP20/14 were flooded with water for wetting under constant applied vertical and horizontal pressures**.** Figures 4.12 and 4.13 show

the wetting-induced displacements in reinforced and unreinforced clay specimens, respectively. Both specimens show similar trends of swelling during wetting. More than 50% of the total swelling occurred within a day after wetting and the rate of swelling decreased with time. The test was stopped after 100 hours, approximately half the time compared to those on the earlier test set-up. This means that the porous stones and miniature vertical drains facilitated faster saturation of the specimens.

There is still a difference in horizontal deformations between lower and upper portions of the specimen, although it was reduced compared to the previous test set-up. The difference can be reduced or eliminated when the test set-up is similar to triaxial test where top and bottom of the specimen can both be supplied with the same pressure head of water. This was not possible in the test set-up used in this study.

Wetting-induced swelling measurements are summarized in Table 4.1, together with other test series that will be discussed in the following sub-sections. For this particular test series, the presence of geogrid reinforcement was found to reduce the swelling in the clay by about 20% compared to that in the unreinforced clay specimen. This reduction is smaller than the wetting test results of Vessely and Wu (2002) in reinforced and unreinforced swelling clay blocks. They observed about 30% reduction in horizontal strain in the reinforced clay block than in the unreinforced clay block. Larger swelling reduction of the clay specimen in the

wetting tests by Vessely and Wu (2002) is attributed to the free swelling condition of their test set-up. It can be expected therefore that the effect of reinforcement in their studies would be higher than what has been observed in my tests.

Variation of suction measured by psychrometers in the soil specimens RP20/14 during wetting is shown in Figure 4.14. Suction in the soil decreases from its initial soil compaction suction of about 450 kPa. Suctions were reduced to less than 100 kPa during wetting and remained constant until the end of the test. Suction measured values of 100 kPa or less implies near full saturation of soil.

Table 4.1 Wetting-induced swelling in clay specimens

	RP20/14	UP20/14	UP30/21	UP50/35	RP50/35
σ_y, kPa	20	20	30	50	50
σ_x, kPa	14	14	21	35	35
δ_y, mm	5.0	5.3	2.8	0.69	0.67
δ_{xt}, mm	3.4	4.26	2.3	1.6	1.43
δ_{xb}, mm	4.1	5.5	3.9	2.8	1.91
δ_{x1}, mm	1.42	1.81	1.5	1.12	0.9
δ_{x2}, mm	2.2	2.67	2.36	1.84	1.45
$\delta_{x3} = (\delta_{xt} + \delta_{xb})/2$, mm	3.75	4.88	3.1	2.2	1.67
Soil swelling reduction, %	19				20

Clay Specimens RP50/35 and UP50/35:

Figures 4.15 and 4.16 show the wetting-induced displacements in the geogrid-reinforced and unreinforced clay specimens at an applied vertical pressure of 50 kPa and horizontal pressure of 35 kPa. Swelling mostly occurred within a day after wetting and the rate of swelling decreased with time afterwards. Wetting-induced swelling of the clay specimens are also summarized in Table 4.1. Under the applied pressure level, the horizontal soil swelling was reduced by 20% on average due to the presence of geogrid reinforcement. This is consistent with the results found in the test series of RP20/14 and UP20/14.

Comparison with one-dimensional swell test:

One-dimensional (oedometer) swell tests were also performed at different vertical pressures for clay samples compacted at the same moisture-density condition as in the large plane-strain tests. Test samples were first loaded at desired vertical pressures at their compacted moisture condition until the deformation reached equilibrium. The samples were then given access to water and allowed to swell until equilibrium at constant seating vertical pressures. In this case, one-dimensional swelling strain represents the volumetric swelling strain.

Test results of wetting-induced swelling with applied vertical pressure from one-dimensional and plane-strain tests have been plotted in Figure 4.17. Volumetric swelling strain (ε_v) for plane-strain tests is the summation of vertical swelling

strain (ε_y = (δ_y/500) x 100 %) and average horizontal swelling strain (ε_{x3} = (δ_{x3}/215) x 100 %) of clay specimen with ε_z = 0. Plane-strain tests data presented here are for UP20/14, UP30/21 and UP50/35. Plane-strain tests have been conducted at constant *K = 0.7* (as derived from triaxial tests carried out in this study). It was thought that the swelling strains for plane-strain conditions might have lower values than one-dimensional condition based on the experimental observations that the upper portion of the specimen has lower degree of saturation. However, volumetric swelling strains from one-dimensional swell tests and plane-strain wetting tests were very similar and therefore provide confidence in the test results. As expected, clay swelling decreased with increase in applied pressures. These results will be used later in determining the parameters required in numerical analysis.

4.2.2.3 Wetting-Drying Induced Deformation

Clay Specimens UP30/21:

Water was drained from the test box for drying of the soil specimens after completion of first wetting process. In this test, drying was done at room temperature. It was found that the clay specimen subjected to room temperature for drying could not produce significant compression in the clay specimen (see Figure A.9). Also, suctions in the clay did not change from the suction values during wetting (Figure A.10). This indicates that the clay specimen was not being dried at room temperature. Thus, for the rest of tests, the apparatus was modified

so that warm air (35°C) could be supplied to the soil specimens from top and bottom to facilitate faster drying.

Clay Specimens RP20/14 and UP20/14:

These specimens were dried about 22.5 days by supplying warm air before they were again flooded with water for a second wetting. Full drying takes a long time and could not be achieved within the time constraint of this study. However, the observed deformations of the soil specimens indicated compression in both vertical and lateral directions during the drying process. Figure 4.18 shows the displacements induced during wetting-drying for both geogrid-reinforced and unreinforced clay specimens (RP20/14 and UP20/14). Both specimens show similar trends of soil shrinkage.

The clay specimen shrunk more in the RP20/14 than in the UP20/14 test set-up. This is mainly attributed to the different source of flow of warm air through the specimen. In the RP20/14, warm air was supplied from the top and bottom of the clay specimen whereas in the UP20/14, warm air was supplied only from the bottom of the clay specimen.

After drying, the wetting process was repeated until the swelling had reached equilibrium in both specimens. In this second wetting, both specimens swelled more than their first wetting in horizontal direction. Soil swelling is generally higher in UP20/14 specimen than in RP20/14 specimen.

At the end of the second wetting, water was drained from the test box. A soil sample was cored using sampling tube (63 mm inside diameter) from specimen UP20/14 to determine the final degree of saturation. Wax-density and moisture content determination tests were carried out in the cored sample and the results are converted to degree of saturation as shown in Figure 4.19. The soil specimen has degree of saturation of about 91% after the second wetting, indicating near full saturation.

Figure 4.20 shows the variation of soil suction in clay specimens RP20/14 during the wetting-drying-wetting cycles. Soil suctions at the end of drying are generally less than the suctions corresponding to that of compacted moisture content, with the exception of location of p_1 in the reinforced specimen where it is about 850 kPa. This implies that moisture content at the bottom ¾ of height of the specimen is higher than the initial compaction moisture content during drying process. Again, soil suctions are less than 100 kPa in both specimens during second wetting which indicates increased moisture content.

Clay Specimens RP50/35 and UP50/35:

Wetting-drying-wetting induced displacements in the clay specimens RP50/35 and UP50/35 are presented in Figure 4.21. The clay specimens were dried for about 24 days by supplying warm air from the top and bottom of the specimens. Similar compressions in vertical and horizontal strains were observed in both

specimens. However, less compression was observed in the clay specimen RP50/35 than in the clay specimen UP50/35.

In the second wetting, both clay specimens swelled slightly more than their first wetting in horizontal direction. This can be an indication that irrecoverable swelling strains were produced during the first wetting-drying process. Overall, the presence of geogrid reinforcement reduced the horizontal deformations of the swelling clay specimens during wetting-drying.

The variation of soil suction in clay specimens RP50/35 and UP50/35, respectively during wetting-drying cycle have the same trend (you may refer to Figures A.12 and A.13). Soil suctions at the end of drying are generally less than the suctions corresponding to that of compacted moisture content, with the exception of higher suction at location p_1.

Full drying of clay specimens could not be achieved in this study. However, the supply of warm air improved the drying process of the soil specimens. Geogrid reinforcement generally reduced the horizontal deformations induced by wetting-drying in the swelling clay.

4.2.3 Geogrid Strain and Soil-Geogrid Interaction during Wetting-Drying

As explained in Chapter 3, three pairs of strain gauges were attached in the geogrid specimen and covered with wax and 3145 RTV epoxy for protection.

Pairs of strain gauges were attached at top and bottom of geogrid for each location providing an average strain in one location. If one of the strain gauges in a location failed, the measured value was taken from the functioning one. The locations of strain gauges are shown in Figure 4.1(b). Points A, B and C are the locations of the strain gauges, Point A is nearest to the centerline.

The measured geogrid strains have been corrected to account for the effects of temperature through the installation of small dummy geogrid reinforcement with strain gauges. This is important because the stiffness of geogrid can be affected by operating temperatures.

Since the clay specimens were subjected to an air temperature of about 35°C to facilitate drying, there was a concern as to its effect on the stiffness of geogrid. The stiffness could be different from when the geogrid was tested under a room (base) temperature of 20°C to 25°C. Temperature measurements from psychrometers installed in the specimen indicated that its temperature did not exceed 25°C as shown in Figure 4.22. It was considered that the variation of temperature from 20°C to 25°C would not greatly affect the stiffness of geogrids.

Geogrid strains during the mechanical loading were very small. Figure 4.23 shows the geogrid strain-time history of specimen RP50/35 during mechanical loading. In the specimen RP50/35, the pair of strain gauges at Point C ceased to

function. Geogrid strain in the clay specimen RP20/14 has been omitted here due to very small measured values.

During wetting the measured geogrid strains are shown in Figure 4.24 for test specimens RP20/14 and RP50/35. In soil specimen RP20/14, one strain gauge out of six strain gauges attached on the geogrid did not function during the first wetting process. As expected, geogrid strains are higher near the centre line than those at the outer boundary.

The strains in the geogrid increased with time indicating a time-dependent swelling during wetting. The rate of increase in geogrid strain was higher during the first day of wetting and subsequently slowed down, consistent with the time-dependent swelling of clay during wetting. The maximum measured strain was about 0.75%. This was observed in specimen RP20/14. Wetting-induced geogrid strains are higher in the soil specimen RP20/14 than in the soil specimen RP50/35. This is consistent with the higher wetting-induced swelling in the soil specimen RP20/14 than in the soil specimen RP50/35.

The measured strains during the wetting-drying process are shown in Figure 4.25. It can be seen that the strains responded to some extent to the swelling and shrinkage of the specimen. The geogrid strains increased again in the second wetting. This is consistent with the behaviour of the clay specimen during the second wetting where the swelling was higher compared to the first wetting.

Some of the strain gauges failed to function at higher strains. This may be attributable to the failure of the gauge protection from wetting.

The geogrid strains and soil strains of the reinforced clay specimens were analyzed further at different intermediate times during wetting to understand the interaction between the clay and geogrid. The locations of soil strain measurements are shown in Figure 4.1 (c). Symbols ε_{x1}, ε_{x2} and ε_{x3} are the average soil strains between two strain measurement locations, such that $\varepsilon_{x1} = ((\delta_{x1}-0)/90) \times 100$ %, $\varepsilon_{x2} = ((\delta_{x2} - \delta_{x1})/75) \times 100$ %, and $\varepsilon_{x3} = ((\delta_{x3} - \delta_{x2})/50) \times 100$ %. Figure 4.26 shows strains in the geogrid and the soil during first wetting of soil specimen RP20/14. Strains are presented at 20, 60 and 95 hours after wetting. Soil strains are higher than the geogrid strains indicating relative movement between the geogrid and clay interface.

Looking at the results for specimen RP50/35 as in shown in Figure 4.27, the measured soil strains seemed to have the same trend as the geogrid strains. They are higher near the centreline and decrease towards the face of the specimen. In this test, the strain difference between soil and geogrid is lower than that of specimen RP20/14. This indicated reduction in relative movement which can be attributed to higher applied interface normal stress. The results indicated the necessity in numerical modelling to provide interface model elements between the soil and geogrid to properly model the clay-geogrid interaction particularly at low stress levels, which are generally found near the

face of reinforced slopes where clay swelling can be expected. It should be noted that most deformation analyses of geosynthetic-reinforced structures assume perfect bonding between soil and reinforcement.

The usual way of evaluating the interaction between soil and geogrid is to use pullout tests and direct shear tests. The University of Manitoba has large pullout test equipment that is also capable of conducting direct shear test. However, wetting and drying of clay is currently not possible in the pullout box. Modifications of the pullout test equipment to accommodate wetting and drying behaviour can be done in future studies.

4.3 FREEZING-THAWING TESTS RESULTS AND DISCUSSIONS

4.3.1 Introduction

Three sets of freezing-thawing tests (two unreinforced specimens: UT-18°C/+23°C and UT-25°C/+23°C; and one geogrid-reinforced specimen: RT-25°C/+23°C) were performed on silt specimens. The tests with and without geogrid reinforcement (RT-25°C/+23°C and UT-25°C/+23°C, respectively) were conducted under otherwise identical conditions for comparison purposes. All specimens were subjected to only one combination of stress level, namely a vertical pressure of 20 kPa and horizontal pressure 14 kPa (designated as specimen P20/14).

Soil deformations during freezing-thawing cycles were measured using displacement transducers (LVDT, LPS and tell-tales). The strains in the geogrid were measured using strain gauges, while soil temperatures were measured using thermocouples.

4.3.2 Deformations of Soil Specimens

Deformations and temperatures of the soil specimens were measured during the freezing-thawing cycles. Schematics of soil deformation measurements have been shown in Figure 4.28a. Horizontal displacements are represented as δ_{xt} and δ_{xb}. These are the average displacements measured on both sides of the specimen. Soil displacements measured by tell-tales at mid-height of the soil specimen are presented as δ_{x1} and δ_{x2}. Vertical displacement of the soil specimen is presented as δ_y. The sign convention is positive for expansion of the soil, as in the wetting-drying test series. Soil temperatures are presented as T_1, T_2, T_3 and T_4 which were measured by thermocouples at the locations shown in Figure 4.28a.

4.3.2.1 Deformations Induced by Mechanical Loading

All silt specimens were prepared at the same moisture and density. Each soil specimen was loaded with incremental pressures up to the desired stress level. Then, the applied pressures were kept constant until the soil deformation

reached equilibrium. Figure 4.29 shows the applied pressure-time history of the geogrid-reinforced silt specimen (RT-25°C/+23°C) during the mechanical loading.

Figure 4.30 depicts the corresponding displacement-time history of the specimen. The silt specimen has been compressed vertically by 0.42 mm and there is very small lateral deformation. Although results are not presented, soil deformations were found to be very small and there was no significant difference between unreinforced and reinforced silt specimens.

Figure 4.31 shows the soil temperature and environmental chamber temperature-time history during mechanical loading condition in the geogrid-reinforced silt specimen. Temperature readings T_1-T_4 are in-soil temperatures while T_5 is the environmental chamber temperature. Temperature readings T_2 and T_3 are located near the middle of the specimen where the geogrid is located. Soil and chamber temperatures are about +25°C during the mechanical loading. Figure 4.32 shows the soil temperature and chamber temperature in the unreinforced silt specimen UT-25°C/+23°C during mechanical loading. For specimen UT-25°C/+23°C chamber temperature is about +21°C and the soil temperatures are about +19°C. The soil temperature and environmental chamber temperature-time history in unreinforced silt specimen UT-18°C/+23°C during mechanical loading condition has been included in Appendix A, Figure A.14. Soil temperatures are essentially constant and close to the chamber temperature. It should be noted that the mechanical loading condition at room temperature was

conducted without the temperature control of the environmental chamber. There are therefore temperature differences between the unreinforced and reinforced specimens at the start of applying the initial mechanical loads. This is attributed to different weather conditions between two test times.

4.3.2.2 Freezing-Thawing Induced Deformations

Specimens were subjected to freezing-thawing cycles. Unlike the wetting-drying of swelling clays that required longer period of wetting and drying, the silt specimens only required shorter periods for each cycle. This allowed the specimens to be subjected to up to ten cycles. The results are presented in two parts: 1) the initial effect based on the first three cycles, and 2) for all ten cycles of freezing and thawing.

Silt Specimen UT-18°C/+23°C:

Figure 4.33 shows the temperature-time history of three freezing-thawing cycles. Before the initial freezing, soil and environmental chamber temperatures were at +20°C. Freezing and thawing were simulated by applying a constant chamber temperature of -18°C for 17 hours and +23°C for 19 hours. During the initial freezing, soil temperatures reduced gradually. About 11 hours after the first freezing, soil temperature at top of the soil specimen (T_1) decreased below 0°C. Soil at the bottom started to freeze in about 15 hours (T_4). During the initial freezing, soil temperatures reached a minimum -5°C at the top and just below -1°C at the bottom of soil specimen. At the middle of the soil specimen, soil

temperatures (T_2 and T_3) are near 0°C. Soil temperatures started to rise during thawing period. At the end of first thawing, soil temperatures reached maximum +14°C at the top and bottom; and +11°C at the middle of the soil specimen.

Soil temperatures during freezing started to respond in similar manner after the second freezing-thawing cycle. It can be seen later that soil temperatures during thawing decreased slightly with an increasing number of freezing-thawing cycles. Minimum soil temperatures during the freezing were -5.5°C and -2°C at the top and bottom of the soil specimen, respectively. The temperature was again zero at the middle of the soil specimen. Maximum soil temperatures during the thawing were +12.5°C at the top and bottom of the soil specimen and +10°C at the middle of the soil specimen. Soil temperatures reached minimum and maximum values (but not complete equilibrium) at the ends of freezing and thawing periods, respectively.

The corresponding soil displacements during 3-cycles of freezing-thawing are shown in Figure 4.34. The silt specimen expanded horizontally at top (δ_{xt}) and bottom (δ_{xb}) throughout the freezing-thawing cycles, except for a small amount of compression at the end of the third thawing cycle. Horizontal displacements were δ_{xt} = 0.27 mm and δ_{xb} = 0.56 mm during the initial freezing. At the end of 3-cycles of freezing-thawing, horizontal displacements were δ_{xt} = 0.33 mm and δ_{xb} = 1.17 mm. Higher horizontal expansion of the specimen at the bottom than at the top is attributed to the higher amount of water at the bottom than at the top of the soil

specimen. The bottom of the soil specimen was connected with the external water source to supply water during the freezing. Expansion of the specimen during freezing-thawing cycles depends on the amount of water available to the soil. Soil at the middle of the soil specimen is in compression horizontally during initial freezing. This implies that the inner portion of the soil for this particular test set-up was above sub-zero temperature while the outer portion of the soil specimen was subjected to a cold front. As the outer portion of the specimen expanded, the inner portion was compressed.

The specimen showed consistent vertical expansion and compression cycles in response to the freezing-thawing cycles. However, the values are relatively small compared with the horizontal displacements. This is due to the fact that the vertical pressure is higher than the horizontal pressure. Soil will expand in the direction of least resistance. It is also interesting to note that the horizontal displacements accumulated with freezing and thawing cycles, unlike the vertical displacements where there is a recoverable cycle of expansion and compression. The accumulation of horizontal displacements means that the specimen continued to expand laterally as it was compressive vertically during thawing.

Freezing and thawing were continued for ten cycles. Figure 4.35 shows the soil temperatures and chamber temperature during the time of testing. Again the specimen accumulated horizontal displacements during the cycles. The displacements at inner portion of the specimen showed consistent compression

and expansion (Figure 4.36), as the specimen experienced heaving and compression, respectively in the vertical direction. As mentioned earlier, this is the portion that has not been frozen and so responded in opposite deformation pattern from those of the outer portion.

Silt Specimen UT-25°C/+23°C:

Another freezing-thawing test was conducted in an identical specimen, that is, a second specimen under same loading, but with the freezing temperature in the environmental chamber reduced to -25°C from -18°C in an attempt to freeze the whole specimen. The thawing temperature was still at +23°C. Freezing was applied for 17 hours and thawing for 19 hours. Initially, the chamber and soil temperatures are +18°C as shown in Figure 4.37. At the initial freezing, soil temperatures gradually decreased and reached minimum values of -8°C and -4°C at the top and bottom of the soil specimen, respectively. The soil temperature at the middle of soil specimen reached 0°C. During the initial thawing, soil temperatures reached a maximum value of +10.5°C at the top and bottom of the soil specimen and +8°C at the middle of the soil specimen. Again longer period times would have produced better results.

In subsequent freezing-thawing cycles, soil temperatures decreased gradually until they reached -12°C, -9°C and -4°C at the top, bottom and middle of the soil specimen, respectively, during the third freezing cycle. The soil temperatures during thawing at this cycle were +9°C and +6.5°C at the top and bottom of the

soil specimen, respectively. After the second freezing-thawing cycle, soil temperatures at the inner portion of the specimen (T_1 and T_2) below sub-zero were found even during the thawing periods. This means that soil at the middle of the soil specimen remained frozen all the time after the second freezing-thawing cycle. This is the reverse of specimen UT-18°C/+23°C where the inner portion of the specimen remained unfrozen throughout the testing period. As expected, the extent of freezing in the soil also depends on the intensity and duration of freezing temperatures.

Figure 4.38 shows the corresponding soil displacements during 3-cycles of freezing-thawing in the unreinforced soil specimen UT-25°C/+23°C. The soil specimen again expanded horizontally and accumulated displacements in each freezing-thawing cycle. Horizontal expansion was larger at the bottom of the soil specimen than at the top of the soil specimen. This was also observed in the previous test set-up. Horizontal expansions, both at the top and bottom of the soil specimen, were higher in specimen UT-25°C/+23°C than in specimen UT-18°C/+23°C. The inner portion of the specimen compressed horizontally (δ_{x1} and δ_{x2}) until the end of second freezing cycle where it started to expand. The subsequent expansion at the inner portion of specimen after second freezing-thawing cycle was because the temperature reached below sub-zero in the inner portion of the specimen. The outer portion expanded more than the inner portion, as was also observed in the previous test set-up. The specimen also showed consistent vertical expansion and compression in response to freezing-thawing

cycles, although the measured vertical displacement was small compared to the horizontal displacement. As mentioned earlier, this is because the vertical pressure was higher than the horizontal pressure and so the specimen expanded more in the direction of least resistance.

Freezing-thawing cycles were continued for six cycles and then the specimen was thawed for a day and another six cycles of freezing-thawing was repeated (Figure 4.39). Soil temperatures decreased continuously and reached equilibrium in the fourth freezing-thawing cycle. Minimum soil temperatures during the freezing cycles were -12.5°C, -10°C and -8°C at the top, bottom and middle of the soil specimen, respectively. Maximum soil temperatures during thawing were +8°C at the top and +6.5°C at the bottom. After the day-long thawing, the soil showed similar temperature effects in subsequent freezing-thawing cycles as in the initial six freezing-thawing cycles. However, the specimen started to freeze more quickly at the beginning of the seventh cycle of freezing-thawing in comparison to first freezing-thawing cycle.

Figure 4.40 shows a clear trend in deformation behaviour during the freezing-thawing cycles. Accumulation of horizontal displacements is again observed as in the previous test. Interestingly, in this case, horizontal expansion at the inner portion of specimen (δ_{x1} and δ_{x2}) was higher than horizontal expansion at the outer portion (δ_{xt} and δ_{xb}). This observation can be attributed to the fact that the temperature in the inner portion was always below sub-zero (freezing) even

during the thawing periods. The next freezing cycle could have increased the extent of the frozen soil. A small volume of frozen soil about 120 mm cube in size was found at the centre of the soil specimen at the end of the test.

In summary, deformations of specimens were found mostly in the horizontal direction than the vertical direction. Horizontal displacements are accumulated with freezing and thawing cycles. The implication is that freezing-thawing of silt in unreinforced slopes could generate shallow sliding of slopes and embankments. Most of the research found in the literature for one-dimensional freezing-thawing tests may not be representative of the faces of slopes and embankments.

Silt Specimen RT-25°C/+23°C:

A geogrid-reinforced silt specimen was tested for comparison purposes in otherwise identical conditions to the unreinforced silt specimen UT-25°C/+23°C. A sheet of geogrid was placed at the middle of the soil specimen to reinforce the soil. Chamber temperatures were maintained to -25°C during freezing and +23°C during thawing simulations. Freezing was applied for 17 hours and thawing for 19 hours. Initially, the chamber temperature and soil temperature were +24°C (Figure 4.41). At the initial freezing, soil temperatures gradually decreased and reached minimum values of -10°C at the top and -4°C at the bottom of the specimen. The soil temperature at the middle of the soil specimen reached only 0°C. During the initial thawing, soil temperatures reached maximum +10°C at the top, +9°C at the bottom and +6°C at the middle of the specimen. In the

subsequent freezing-thawing cycles, soil temperatures decreased continuously. The soil temperatures at the end of second and third cycles are as shown in Figure 4.41. After the second freezing-thawing cycle, soil at the inner portion of the specimen was found to be below sub-zero temperature even during thawing period. This trend was also seen in the unreinforced specimen. This means that soil at the middle of the soil specimen remained frozen all the time. Soil temperatures after 3-cycles of freezing and thawing are similar for both the geogrid-reinforced specimen (RT-25°C/+23°C) and the corresponding unreinforced soil specimen (UT-25°C/+23°C).

Figure 4.42 shows the corresponding soil displacements during the 3-cycles of freezing-thawing in the geogrid-reinforced soil specimen (RT-25°C/+23°C). The soil specimen expanded horizontally both at top and bottom monitoring locations throughout the freezing-thawing cycles. The horizontal expansion was higher at the bottom of the soil specimen than at the top of the soil specimen. The middle of the specimen was in compression horizontally during freezing cycle and in expansion during thawing cycle. The soil specimen showed the same trend of expansion and compression as in other tests. The reinforced specimen (RT-25°C/+23°C) had slightly less horizontal deformation than the unreinforced soil specimen (UT-25°C/+23°C). However, soil displacements at the middle of the soil specimen were significantly reduced in the reinforced soil specimen compared with the corresponding unreinforced soil specimen (compare Figure

4.42 with Figure 4.38) particularly at the end of the third cycle. The presence of geogrid reinforcement reduced the horizontal deformation of the silt specimen.

Freezing-thawing cycles were continued for six cycles and then the specimen was thawed for a day and another six cycles of freezing-thawing was repeated (Figure 4.43). The reinforced soil specimen was subjected to similar freezing-thawing cycles as the unreinforced soil specimen UT-25°C/+23°C. Soil temperatures decreased continuously and reached equilibrium in the fourth freezing-thawing cycle. Minimum soil temperatures during freezing were -12.5°C, -10°C and -8.5°C at the top, bottom and middle of the soil specimen, respectively. Maximum soil temperatures during thawing were +8°C and +5°C at the top and bottom of the soil specimen, respectively.

The geogrid-reinforced specimen showed continuous horizontal expansion during freezing cycles (Figure 4.44). Very little horizontal deformation was observed during thawing cycles. This means that the lateral compression under lateral confining pressure is compensated with the lateral extension due to the vertical compression of the specimen. With an increasing number of cycles, the inner portion of the soil specimen showed generally continuous horizontal expansion as in the case of unreinforced specimen. Initially, the inner portions of the specimen showed horizontal compression and expansion (see displacements δ_{x1} and δ_{x2}) corresponding to vertical expansion and compression (δ_y) of the

specimen, respectively. This observation is similar to those seen in the other freezing-thawing tests.

Overall, the presence of geogrid reinforcement at -25°C/+23°C freezing-thawing cycles reduced the soil displacements (δ_{x1} and δ_{x2}) by 45% (compare Figure 4.44 with Figure 4.40).

4.3.3 Geogrid Strain and Soil-Geogrid Interaction during Freezing-Thawing

Geogrid strain was measured using strain gauges in the geogrid-reinforced silt specimen (RT-25°C/+23°C). Three pairs of strain gauges were attached to the geogrid specimen. Strain gauges in each pair were attached in symmetrical positions so that the average geogrid strain could be measured from the two points of measurements as a form of redundancy in case one failed from the pair (unless both failed to function). The location of the geogrid strain gauges in the reinforced soil specimen are shown in Figure 4.28b, where points A, B and C are the positions of strain gauges, position A being the nearest to the centreline. Geogrid strains are presented using the average values of strain gauges measured at two symmetrical points. An exception is at strain gauge B, where one of the strain gauges did not function after the tenth cycle. A single value was used thereafter at that location. Geogrid strain values are the corrected strain values after deducting the strain readings from dummy strain gauges.

Figure 4.45 shows the geogrid strain during 3-cycles of freezing-thawing. Progressive mobilization of tensile strains is observed during the 3-cycles, which is consistent with the accumulation of soil displacements δ_{x1} and δ_{x2} (see Figure 4.42). About 0.21% of geogrid strain was observed as the highest value at the end of the third freezing-thawing cycles. Extension of the geogrid increased with increasing freezing-thawing cycles. Geogrid strains were found to reflect that thawing is associated with lateral movements and so the reinforcement is restraining lateral movements. There was a slow reduction of strains as the soil starting to freeze, probably because the soil became stiffer. Therefore, the additional stresses (or strains) in reinforcements during freezing are lower than those during thawing. Although the additional stresses (or strains) in the reinforcements subjected to freezing-thawing cycles in this study were within the working stress levels for the type of reinforcement used, engineers need to understand that freezing-thawing cycles may accumulate tensile stresses in the reinforcements.

As expected, geogrid strains were higher near the centre line (strain gauge at position A) than at the outer boundary (strain gauge at position C), except at the transition of the second freezing-thawing cycle, when the geogrid strain at A is lower than the geogrid strain at B and C. This result can be supported with the higher compression of soil (δ_{x1} and δ_{x2}) at that time.

Figure 4.46 shows the geogrid strains for the whole test of twelve freezing-thawing cycles in the reinforced silt specimen. The highest value of geogrid strain is about 0.57% at the end of the test. There is a noticeable reduction in strains after the sixth cycle of freezing-thawing which coincides the additional 24 hours of thawing period. These are consistent with observed compression of soil at that period.

In further freezing-thawing cycles, it can be seen that soil displacements and geogrid strains are depend on the duration of thawing. Recall that soil temperatures at the inner portion of specimen were mostly below sub-zero even during the thawing period. An exception occurred with the sequence that allowed 24 hours for thawing. Here the soil temperatures reached +17°C (Figure 4.43) and the soil specimen as well as the geogrid showed compression (Figures 4.44 and 4.46). This indicates that eventually geogrid relaxes if soil gets enough time to thaw. The results in this study show that the 19 hrs of thawing in the general program were not sufficient.

The high values of geogrid extension during thawing in this study are associated with below sub-zero temperature of soil at the middle of the reinforced soil specimen. In other words, thawing time should be increased to have significant compression in the soil and reduction in the geogrid strains.

Geogrid strains and soil strains at the end of the different freezing-thawing cycles of the reinforced silt specimen were analyzed further to understand the soil-geogrid interaction. Figure 4.47 shows the geogrid strains and soil strains at the ends of first, sixth and twelfth freezing-thawing cycles. Geogrid strains and soil strains have been plotted against their position from centreline of the specimen. At the end of the first freezing-thawing cycle, geogrid strains and soil strains are close, except near the vertical face. Soil strains ε_{x1} and ε_{x2} are in compression and the geogrid is showing little extension. With an increased number of freezing-thawing cycles, the geogrid strains and the soil strains are both increasing. The soil strains are much higher than the geogrid strains. This indicates that relative movement has occurred between the soil and the geogrid. Again, modelling of the interaction between soil and geogrid requires simulating the interface behaviour. This requires different interface stiffness between thawed and frozen specimens.

4.4 SUMMARY

This chapter presented results from wetting-drying and freezing-thawing laboratory tests. Discussion in previous sections was based on geogrid strains, soil deformations, soil suctions, soil temperatures and soil-geogrid interaction induced by environmental loading. The main points of discussion are as follows:

1) Both reinforced and unreinforced clay specimens were loaded with mechanical pressure until equilibrium deformations were reached prior to wetting and drying. This represents the behaviour of unreinforced and

reinforced specimen under mechanical loading. There was no noticeable difference in specimen deformations with and without geogrid reinforcement, probably due to the small deformations involved. The applied pressures were relatively low, so the associated deformations were small and could not mobilize the reinforcement tensile force. As expected, the vertical compression of clay specimens increased with increasing applied vertical pressures while the horizontal expansion of the clay specimens decreased with increasing applied horizontal pressures.

2) Wetting-drying tests of both geogrid-reinforced and unreinforced clay specimens were performed at two different stress levels. It was observed that the reinforcement reduced the swelling of the clay during wetting by about 20%. Full drying of the clay specimens could not be achieved in this study. Only clay specimens RP50/35 and UP50/35 were dried until relatively high suction pressures. Test results indicated that there were no significant displacement differences between reinforced and unreinforced clay specimens. However, in the second wetting, geogrid-reinforced clay specimens swelled less than the unreinforced clay specimens. Overall, the geogrid reduced the swelling of clay specimen during wetting.

3) Swelling-shrinking of clay due to wetting and drying induced additional strains in the geogrid reinforcement. Measured geogrid strains during the test reached up to 0.75% due to wetting only. The reported working strains of geogrid reinforcements in actual reinforced structures are in the range from 1% to 2%. These are well below the rupture strains of geogrid

reinforcements available in the market. This means that the additional strains due to wetting and drying of swelling clay would have minimal effect on the design working load of the reinforcement. However, only one wetting-drying cycle was done in this study so accumulation of geogrid strains can not be confirmed.

4) The soil-geogrid interaction was analysed by comparing the soil and geogrid strains during wetting of reinforced clay specimens. It was observed that soil strains were higher than the geogrid strains. This indicates relative movement between the clay and geogrid interface during wetting particularly at low pressures. The difference in strains was found to be less at higher pressure levels. This results from an increased normal pressure at clay-geogrid interface.
5) Tests with freezing-thawing cycles were performed in both reinforced and unreinforced silt specimens. As with the clay specimens, the silt specimens were loaded mechanically until equilibrium deformations were reached. Freezing and thawing cycles were then applied. It was observed that the geogrid reduced the horizontal displacement of the silt specimens during freezing-thawing cycles. There was no noticeable difference in vertical displacement between reinforced and unreinforced silt specimens.
6) Freezing-thawing of the reinforced silt specimens induced additional strains in the reinforcement. Measured geogrid strains at the end of twelve freezing-thawing cycles were in the order of 0.57%. As with the wetting-drying of swelling clay specimens, the additional strains due to freezing

and thawing of frost susceptible silt specimens would have minimal effect on the design working load of the reinforcement. However, as the number of cycles increases, it was evident that geogrid strain increases. This has significant implications as the accumulated strains can overstrain the geogrid during freezing and thawing.

7) Increasing the freezing temperature from -18°C to -25°C in the unreinforced silt specimens, more than doubled the soil deformations. The soil deformations were observed to be mostly horizontal. This pattern of deformations during freezing-thawing of silt can result in shallow sliding at the face of slopes and embankments.
8) Soil-geogrid interaction was analysed by comparing the soil and geogrid strains during freezing-thawing cycles. As in reinforced clay specimen, the soil strains were higher than the geogrid strains which indicate relative movement between soil and reinforcement.

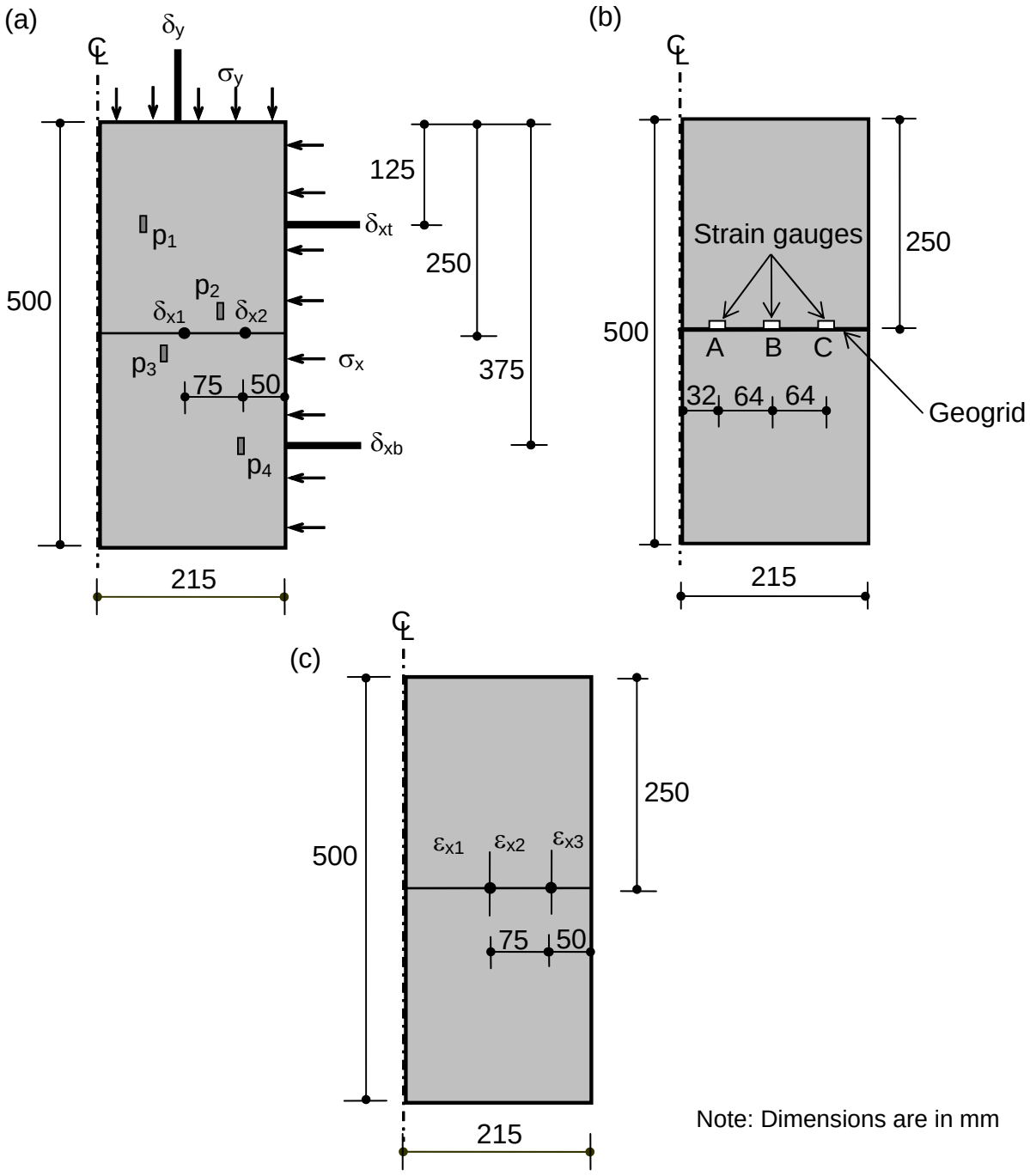

Figure 4.1 Schematic of (a) soil deformation and suction measurements, (b) geogrid strain measurement, and (c) soil strain measurement in clay specimen

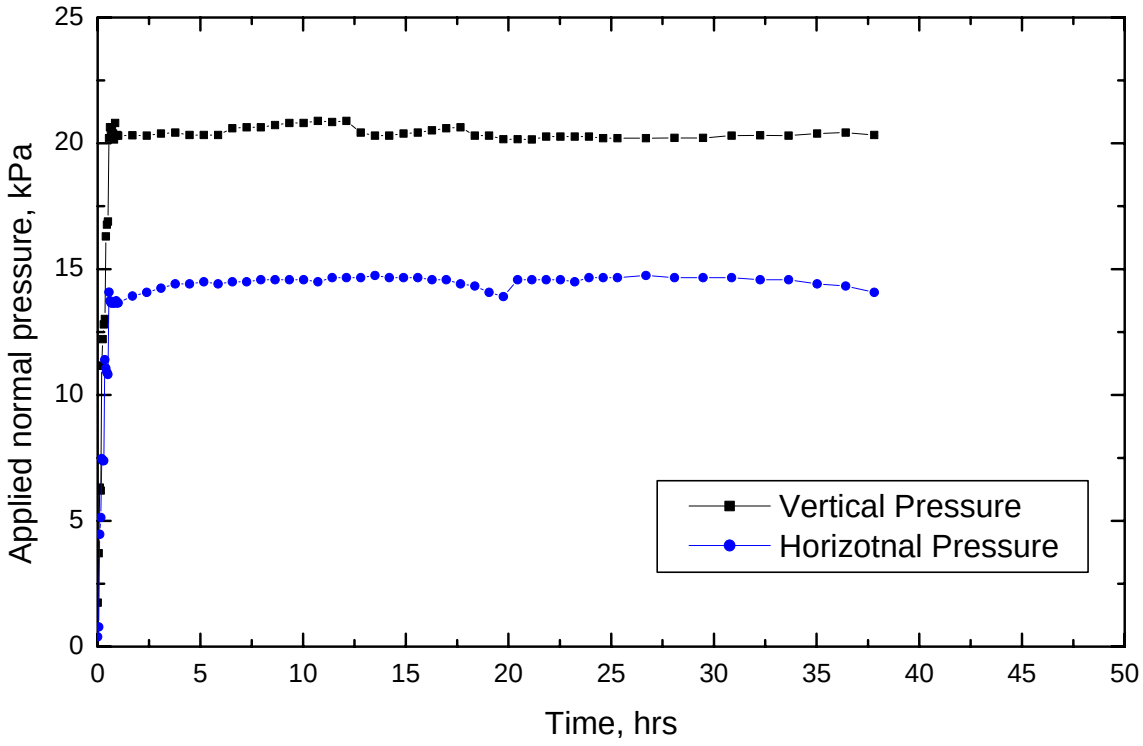

Figure 4.2 Applied pressure-time history of geogrid-reinforced clay specimen during mechanical loading (Specimen RP20/14)

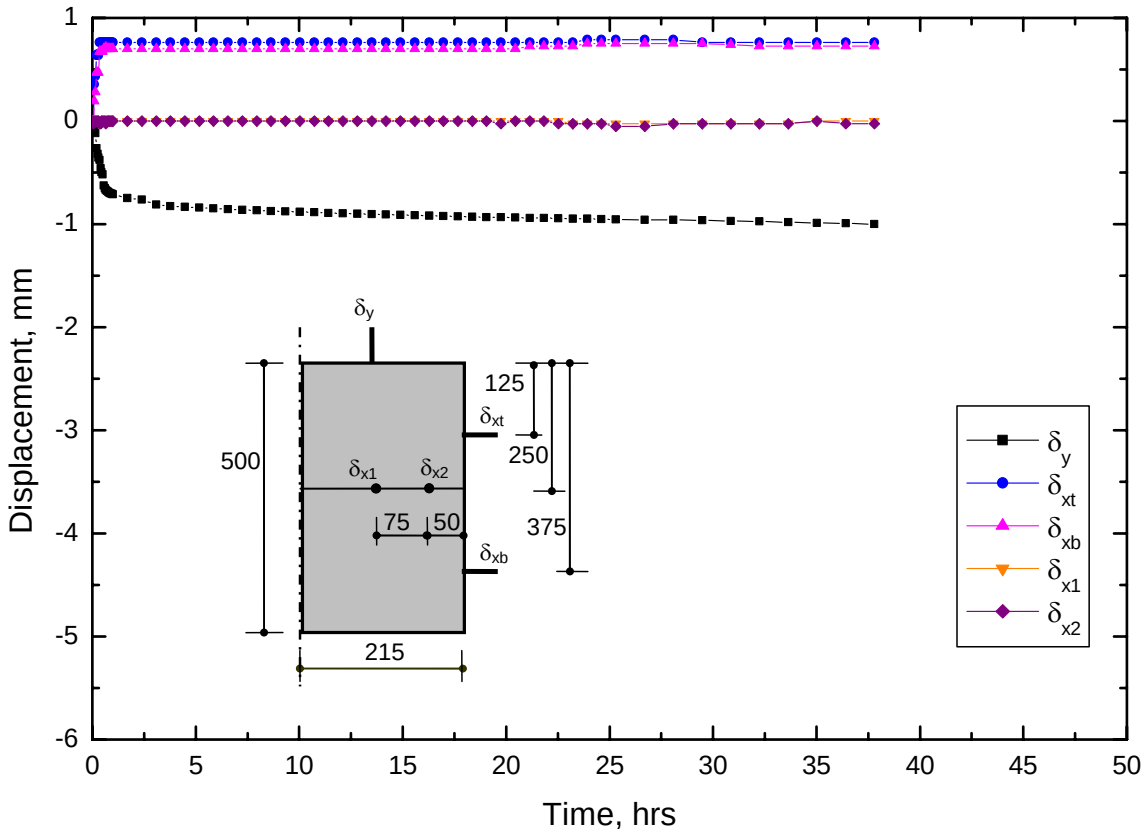

Figure 4.3 Displacement-time history for geogrid-reinforced clay specimen during mechanical loading at applied vertical pressure of 20 kPa and horizontal pressure of 14 kPa (Specimen RP20/14)

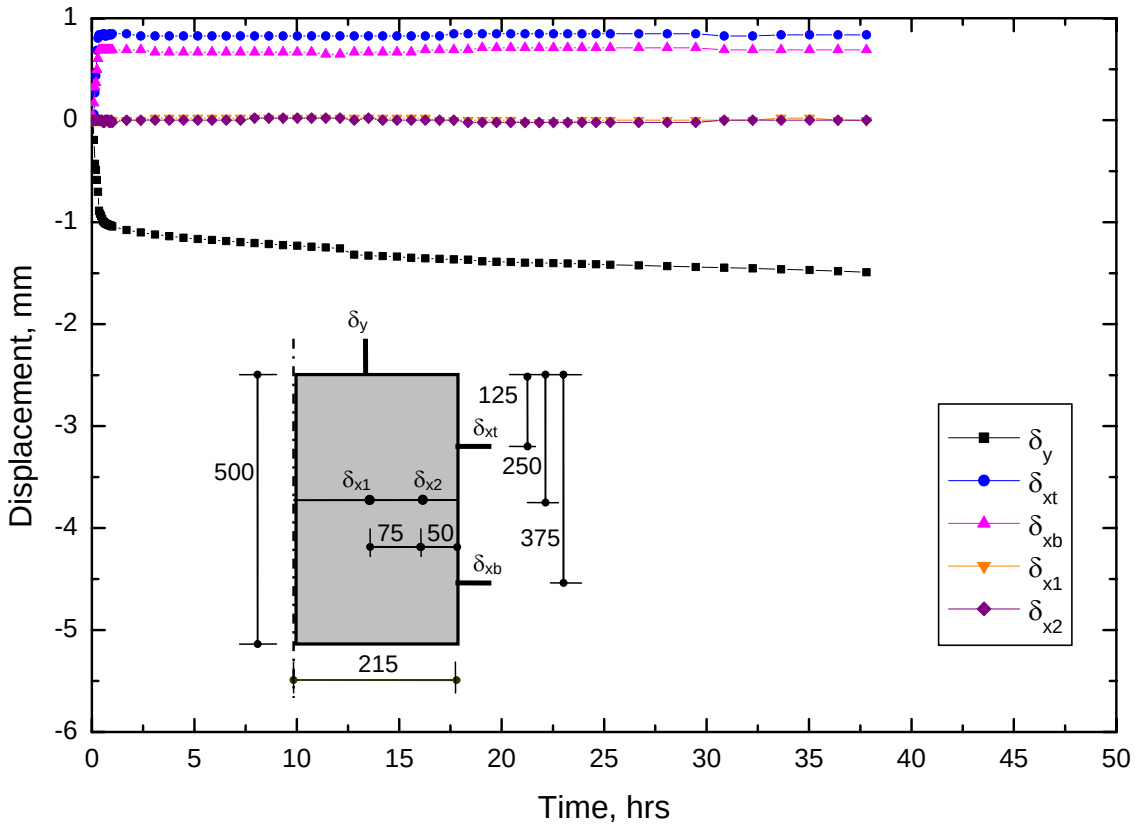

Figure 4.4 Displacement-time history for Specimen UP20/14 during mechanical loading

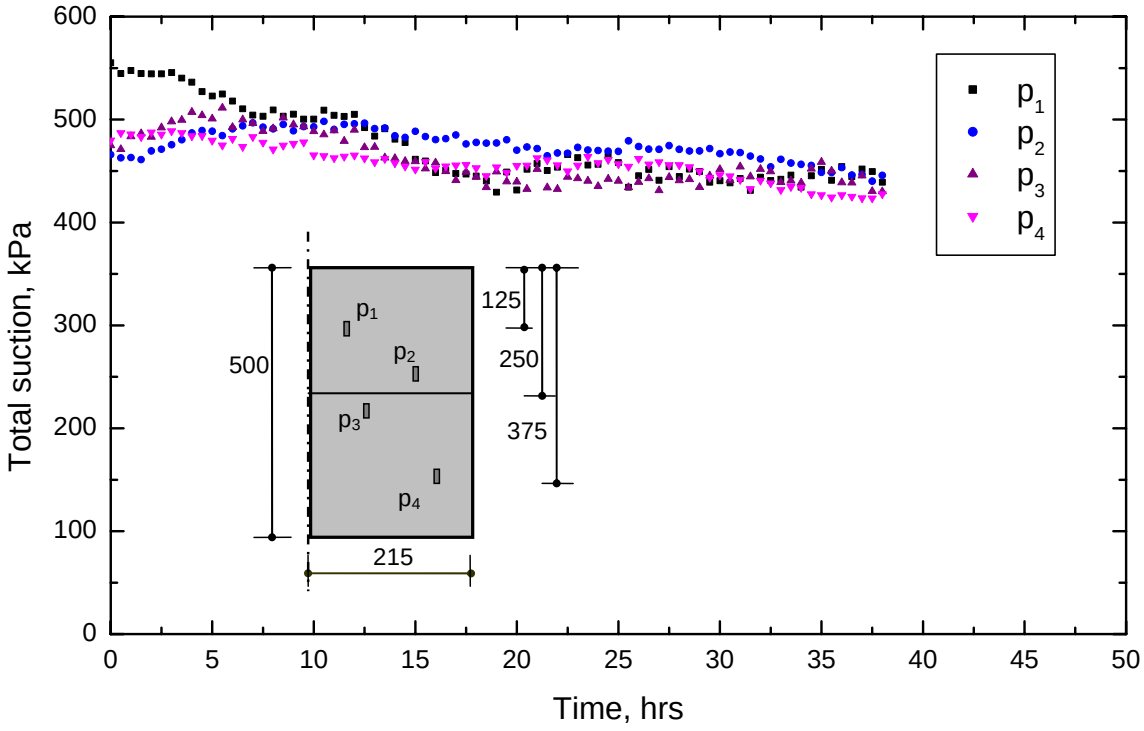

Figure 4.5 Variation of suction pressures for Specimen RP20/14 during mechanical loading

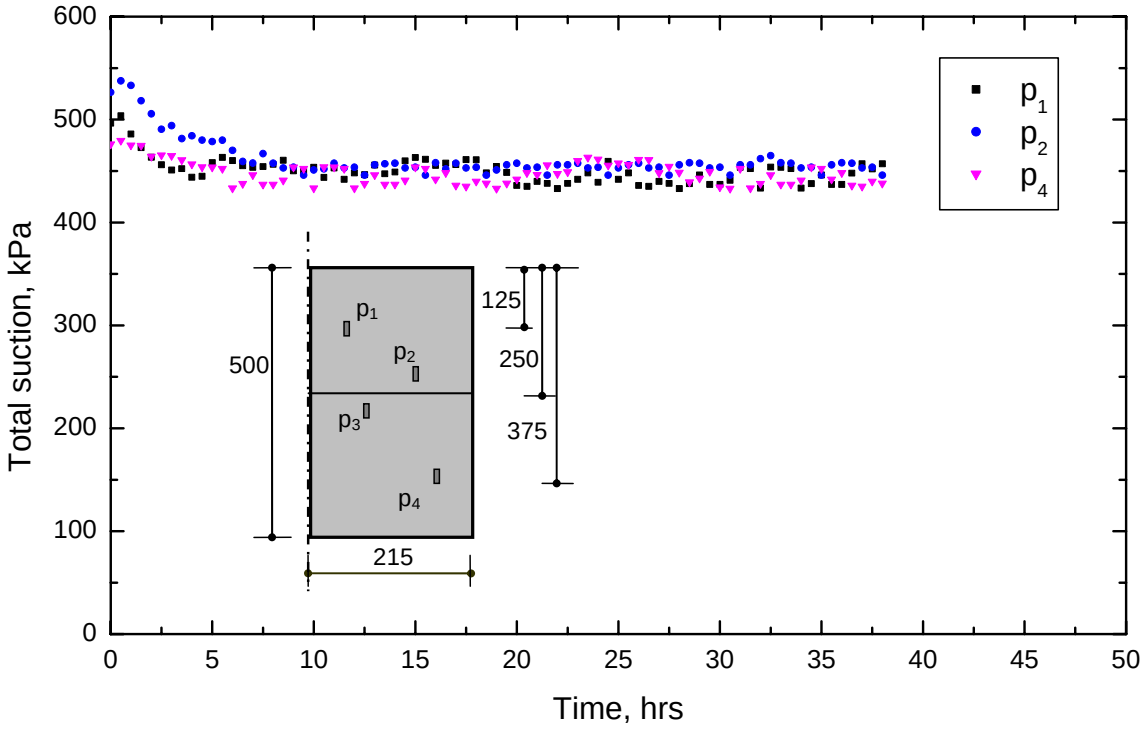

Figure 4.6 Variation of suction pressures for Specimen UP20/14 during mechanical loading

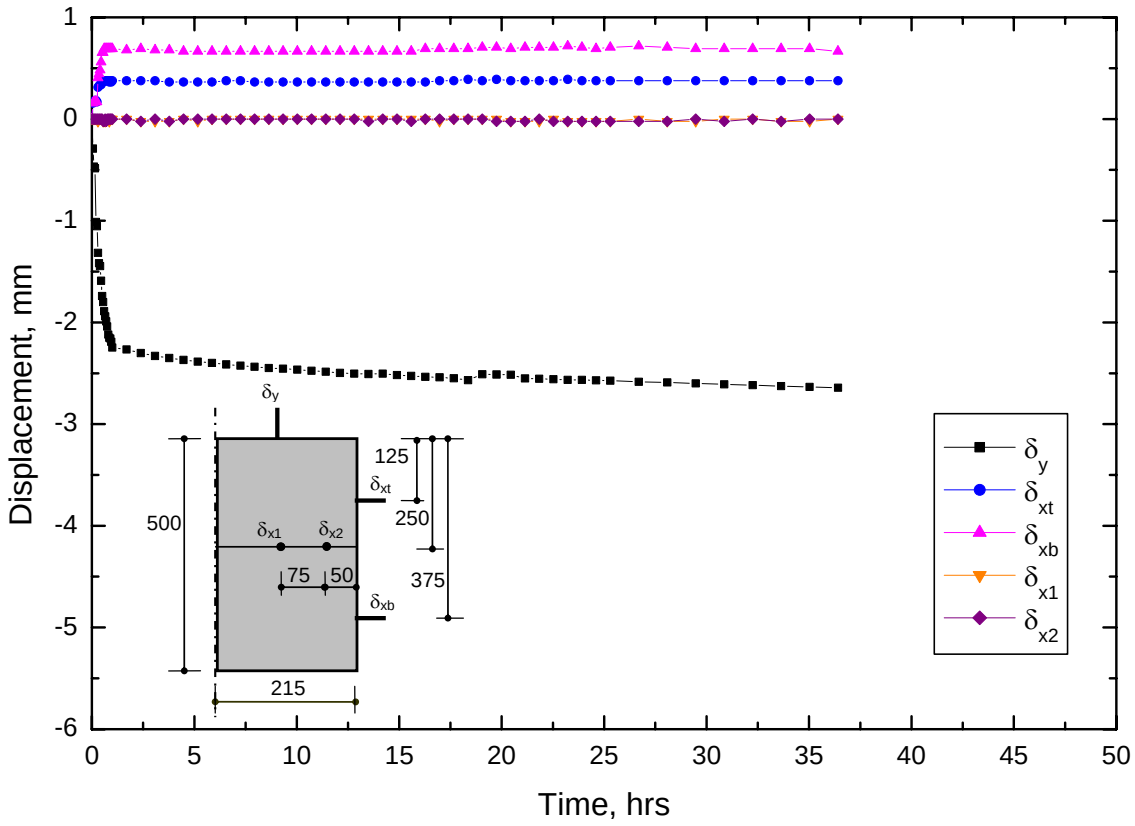

Figure 4.7 Displacement-time history for Specimen UP30/21 during mechanical loading

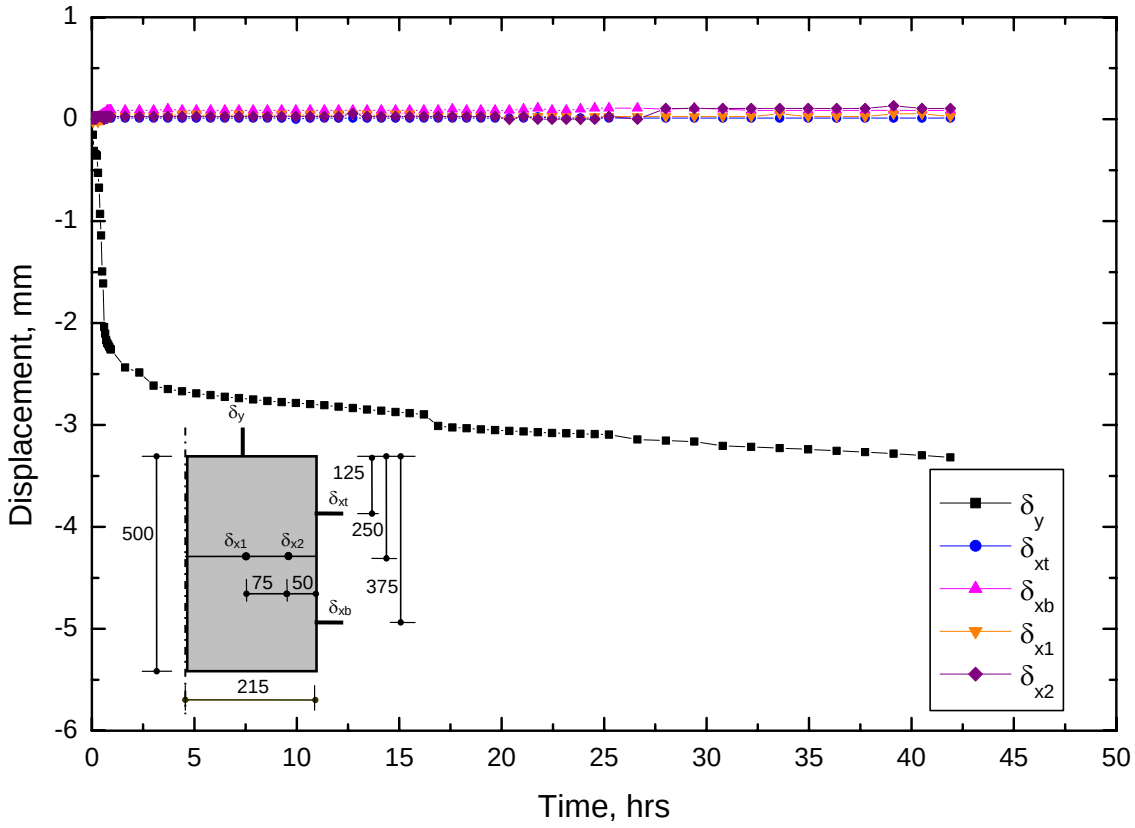

Figure 4.8 Displacement-time history for Specimen RP50/35 during mechanical loading

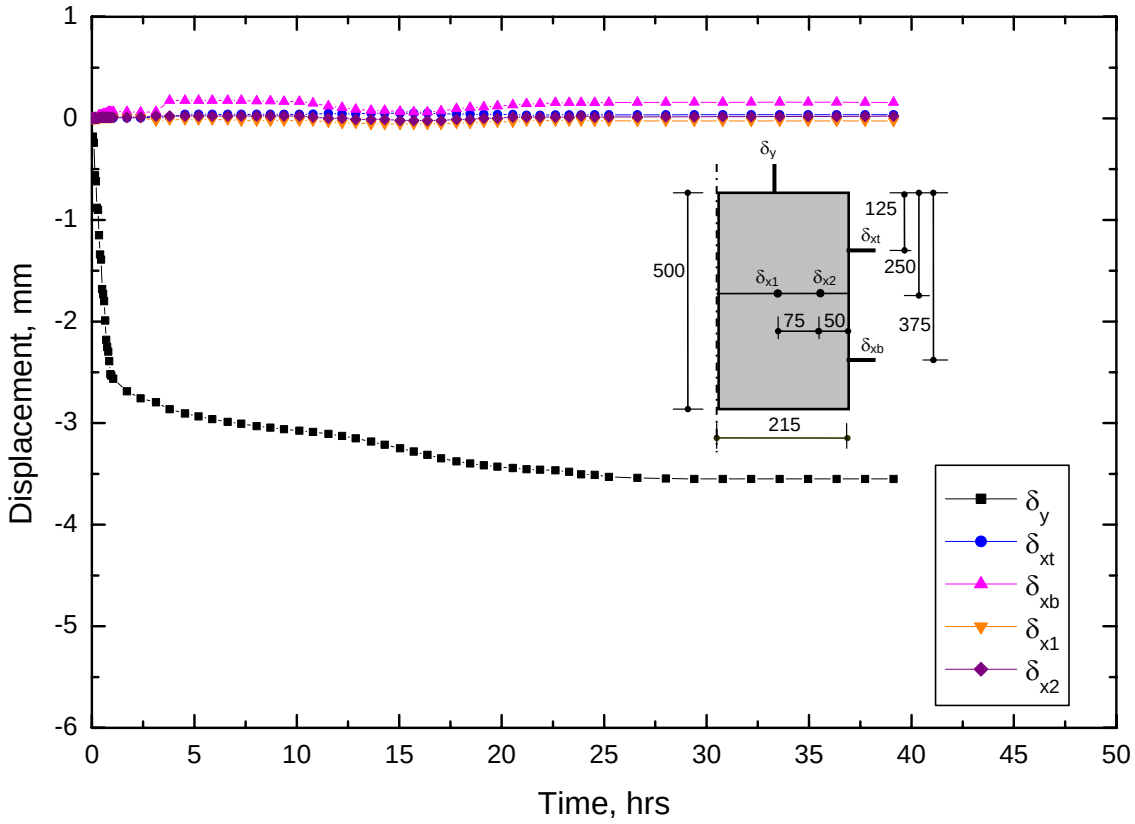

Figure 4.9 Displacement-time history for Specimen UP50/35 during mechanical loading

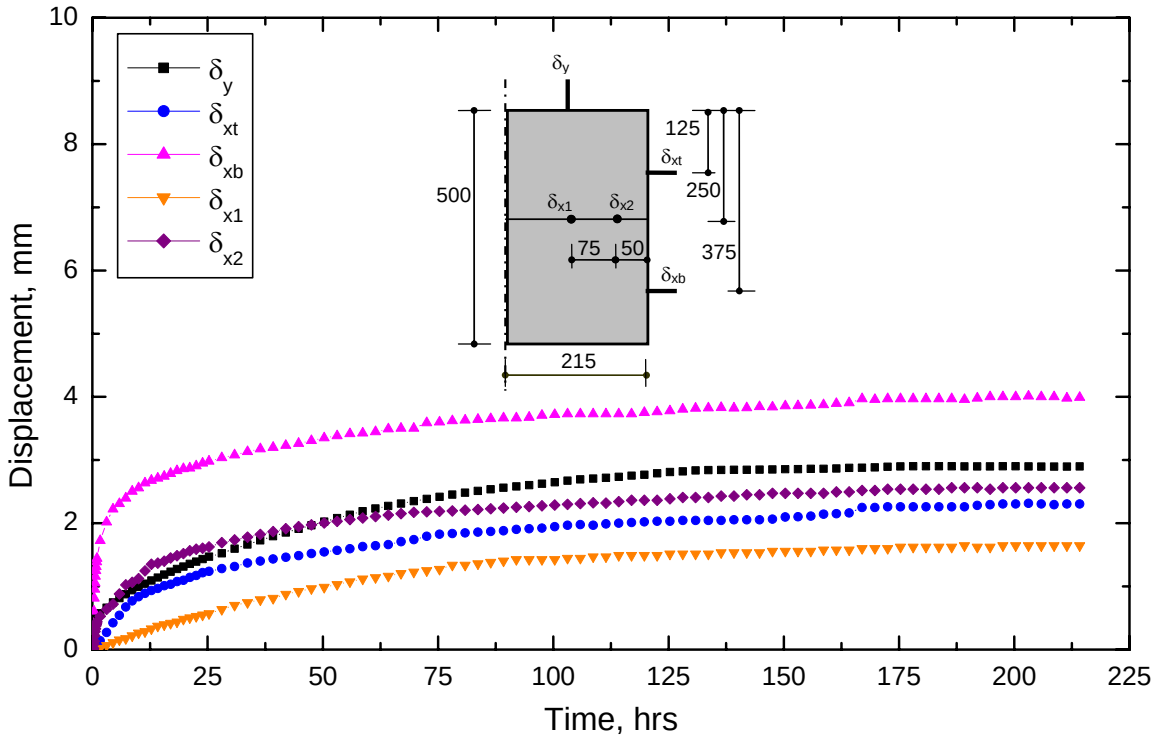

Figure 4.10 Wetting-induced swelling in Specimen UP30/21

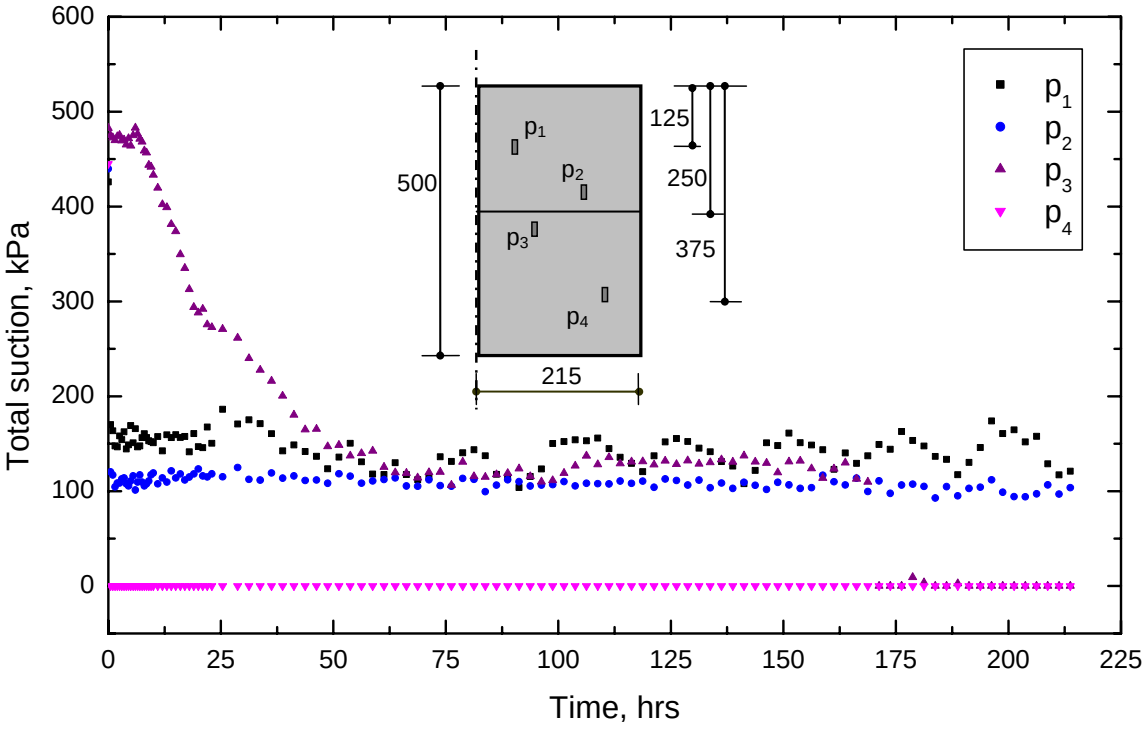

Figure 4.11 Suction pressures in Specimen UP30/21 during wetting

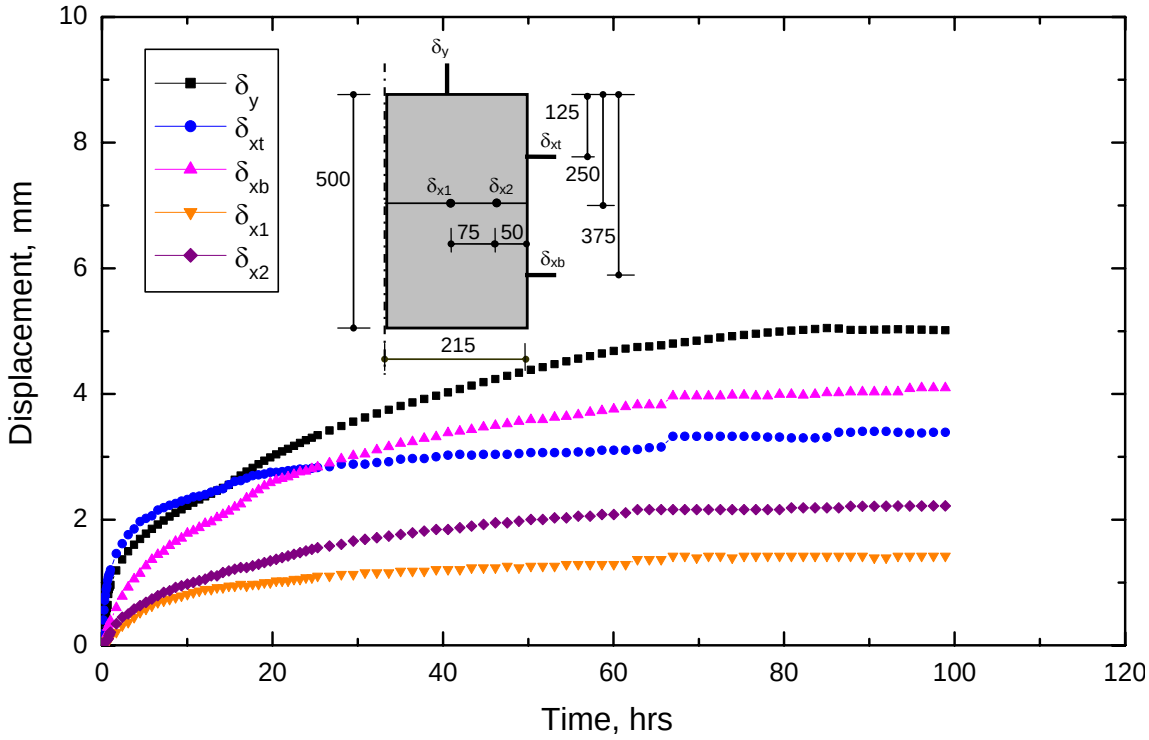

Figure 4.12 Wetting-induced swelling in Specimen RP20/14

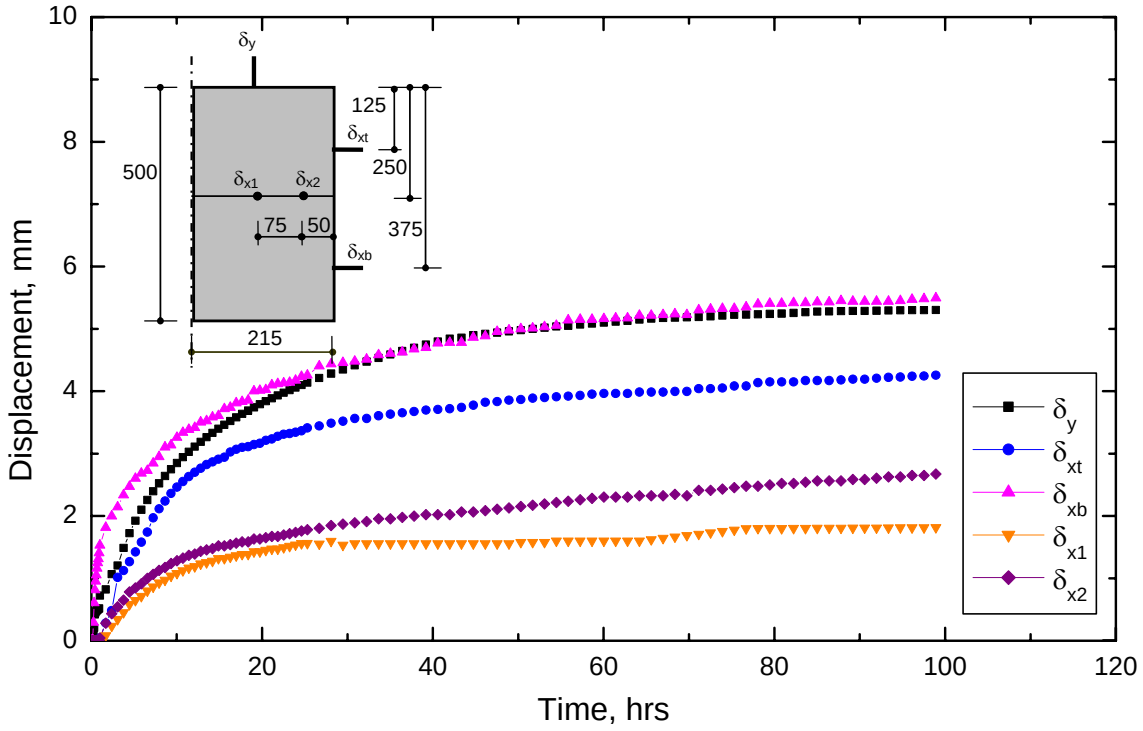

Figure 4.13 Wetting-induced swelling in Specimen UP20/14

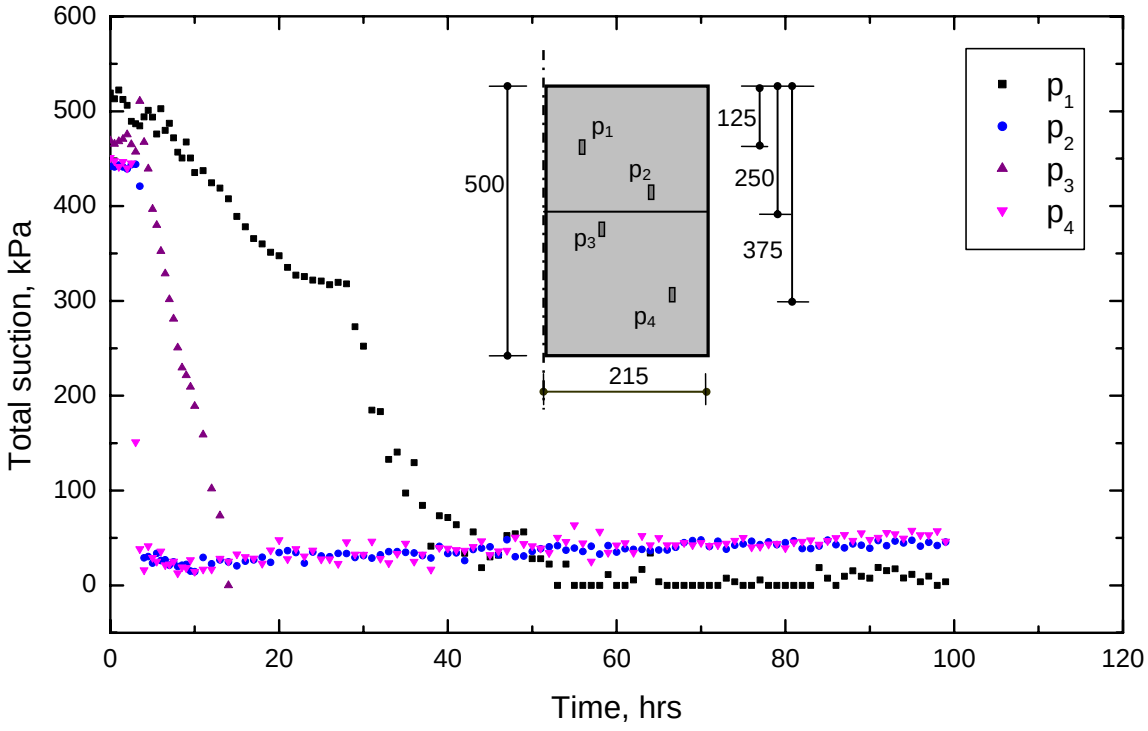

Figure 4.14 Suction pressures in Specimen RP20/14 during wetting

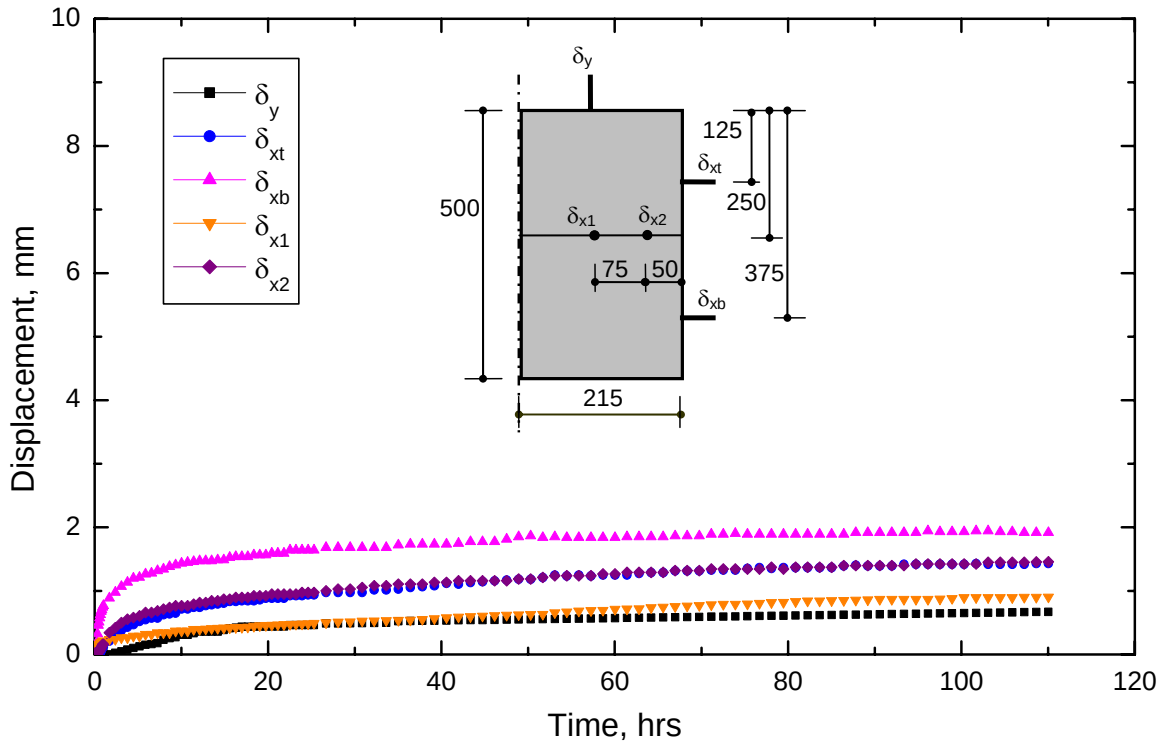

Figure 4.15 Wetting-induced swelling in Specimen RP50/35

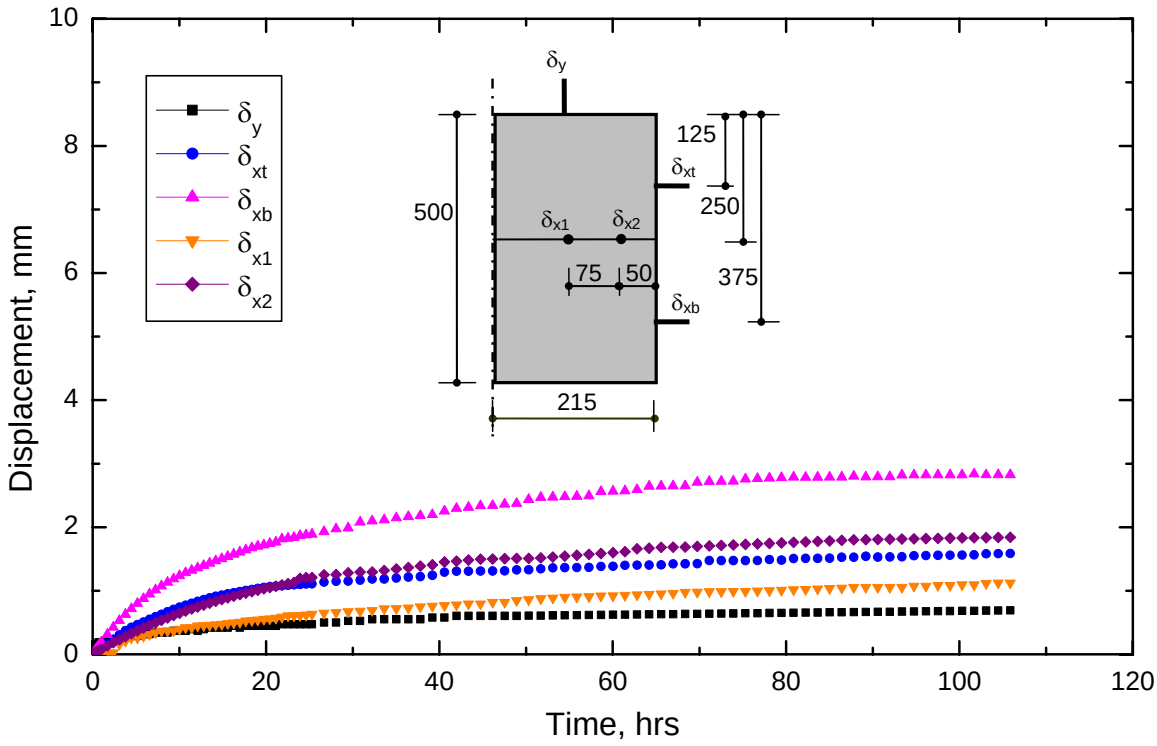

Figure 4.16 Wetting-induced swelling in Specimen UP50/35

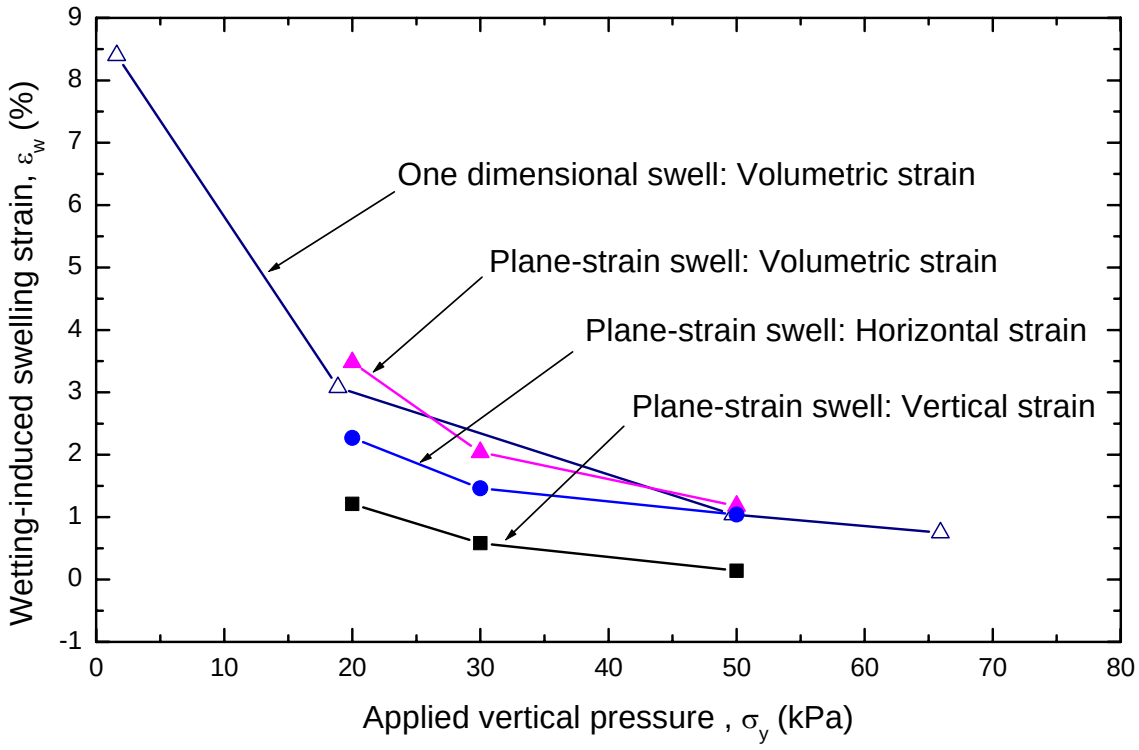

Figure 4.17 Wetting-induced swelling in unreinforced clay specimens at different applied vertical pressures tested in plane-strain condition and one-dimensional condition

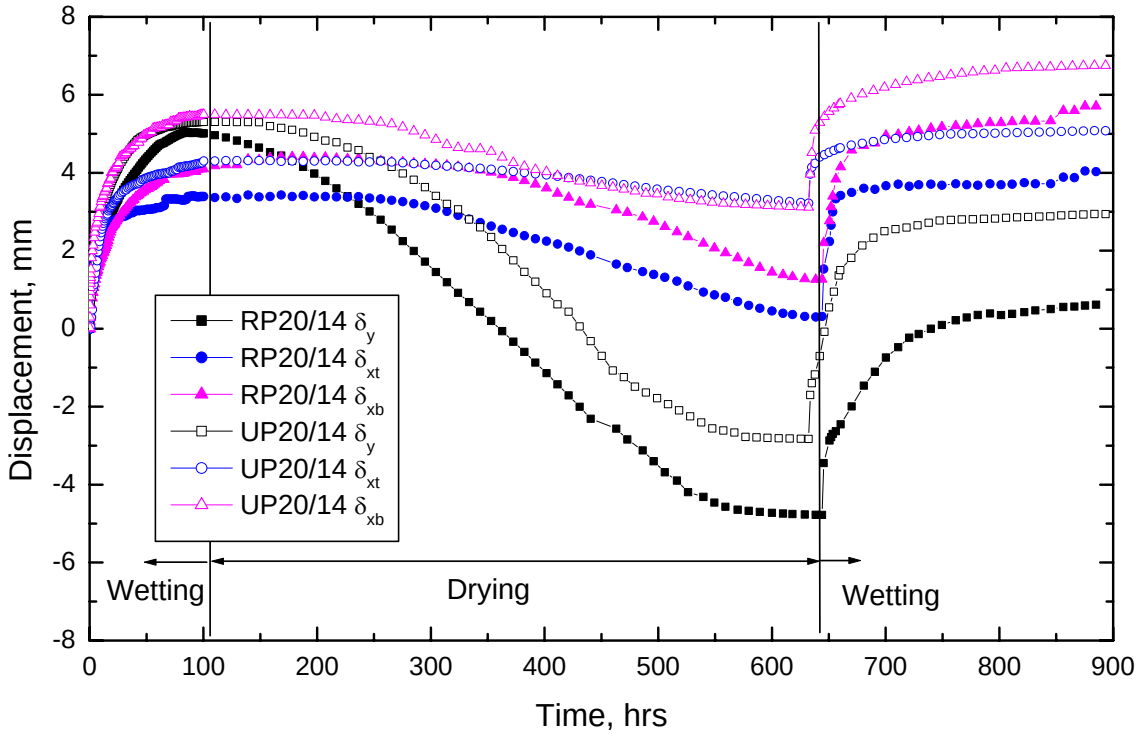

Figure 4.18 Wetting-drying induced displacements in geogrid-reinforced and unreinforced clay specimens RP20/14 and UP20/14

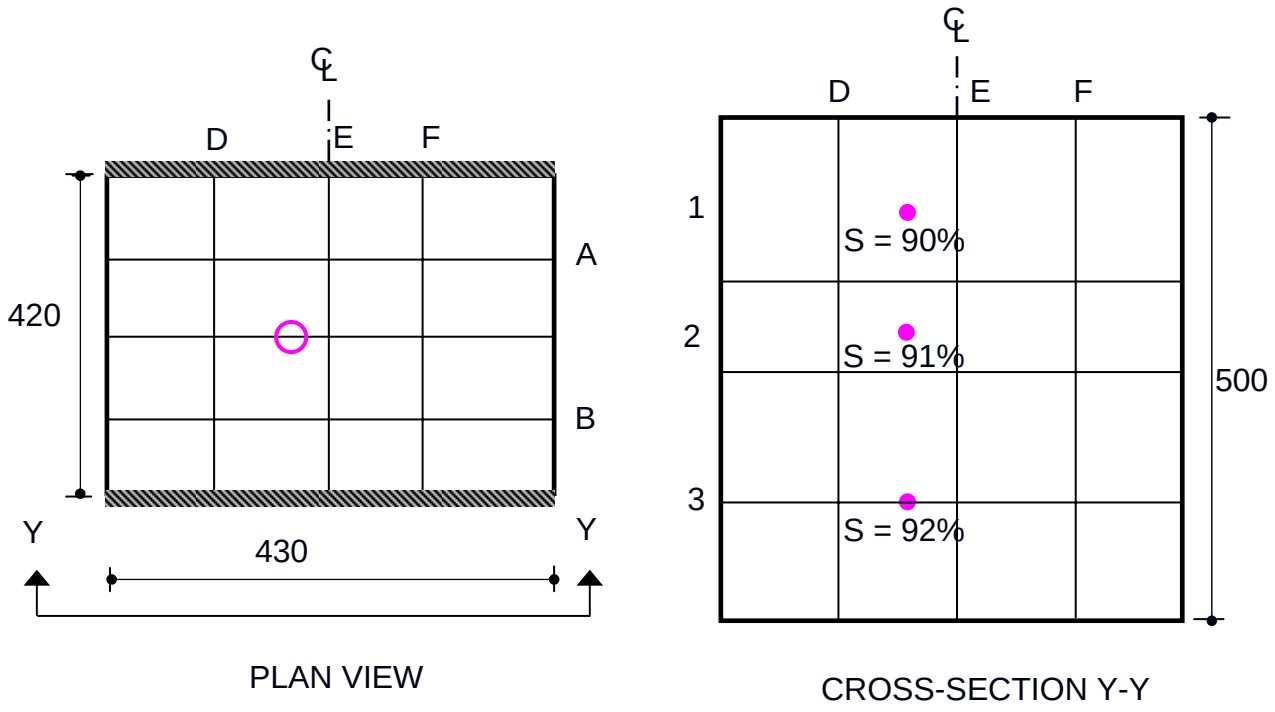

Figure 4.19 Degree of saturation at the end of second wetting in Specimen UP20/14

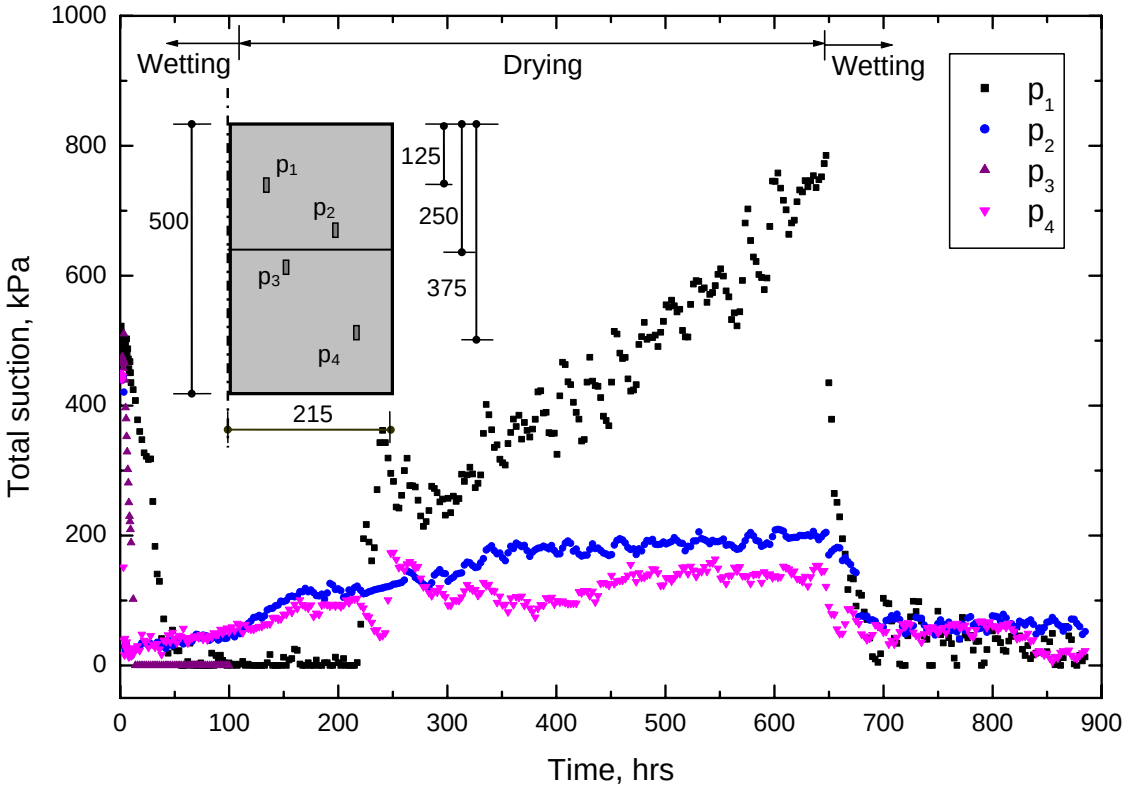

Figure 4.20 Suction pressures in geogrid-reinforced clay specimen RP20/14 during wetting-drying cycle

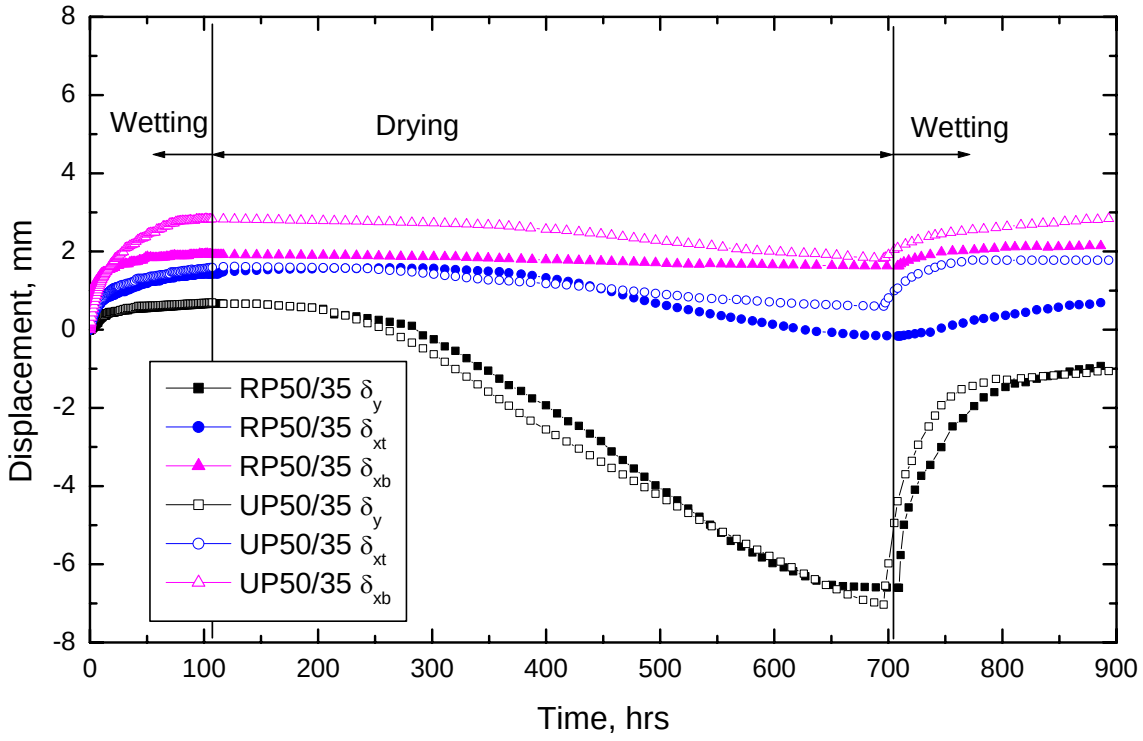

Figure 4.21 Wetting-drying induced displacement in geogrid-reinforced and unreinforced clay specimens RP50/35 and UP50/35

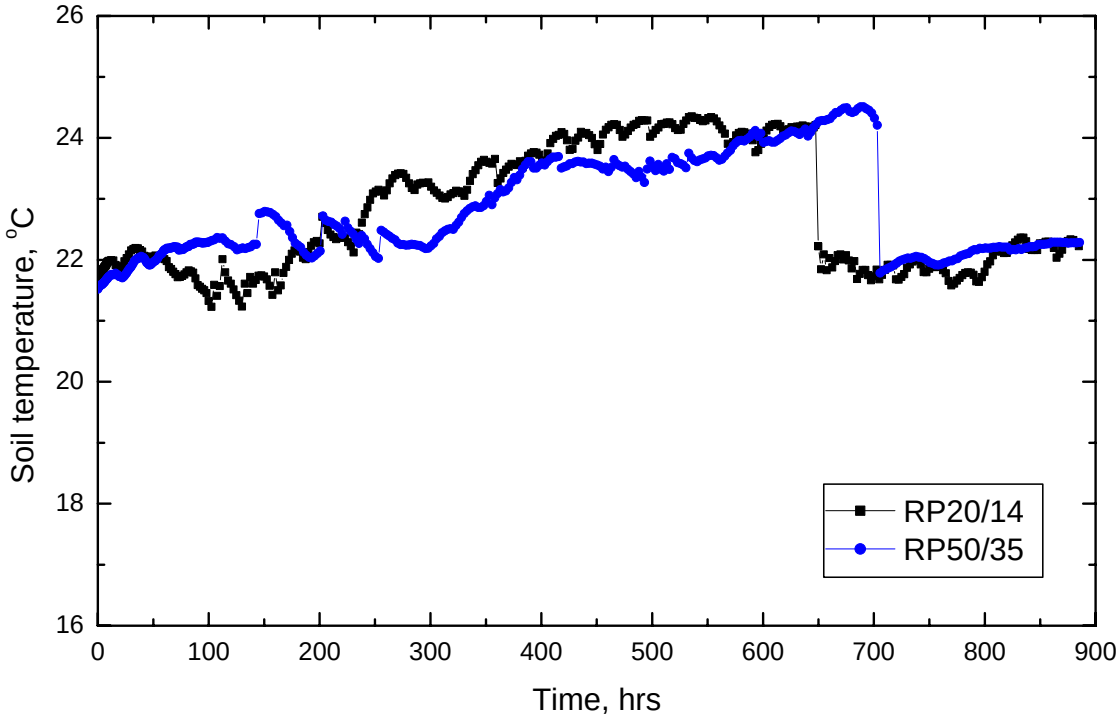

Figure 4.22 Soil temperature in the middle of geogrid-reinforced clay specimens RP20/14 and RP50/35 during wetting-drying cycle

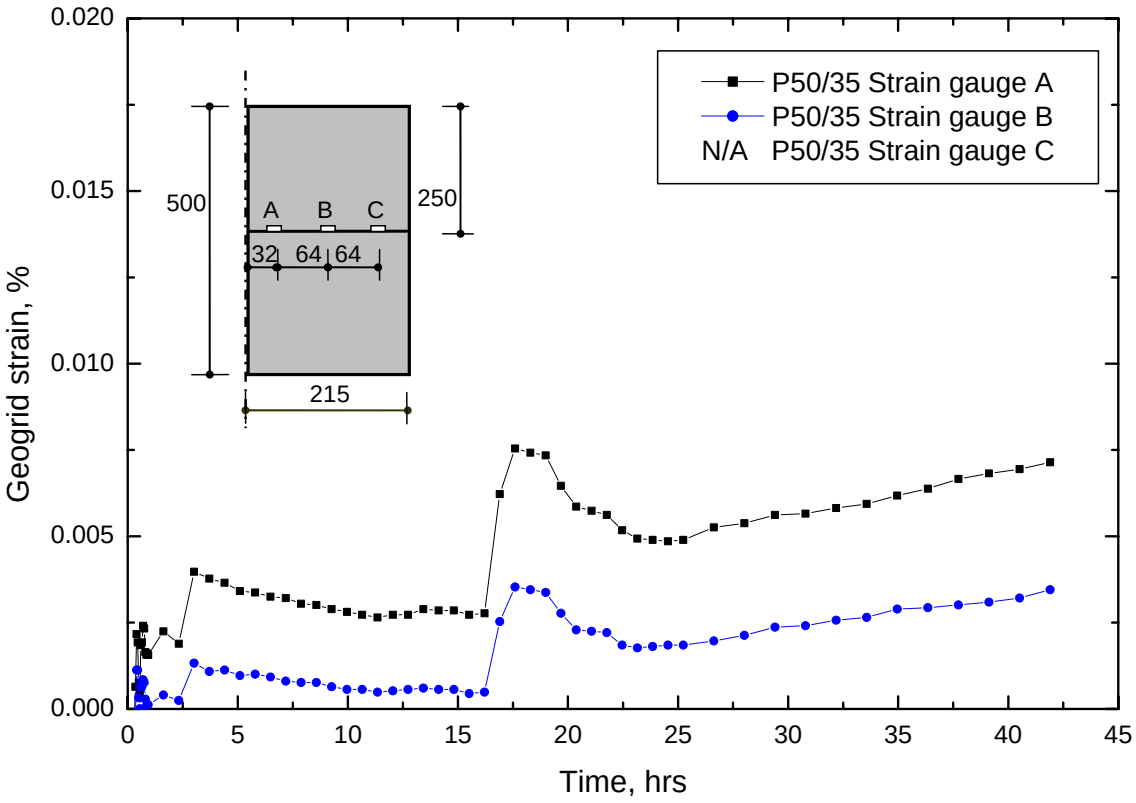

Figure 4.23 Geogrid strain-time history of reinforced clay specimen RP50/35 at mechanical loading condition

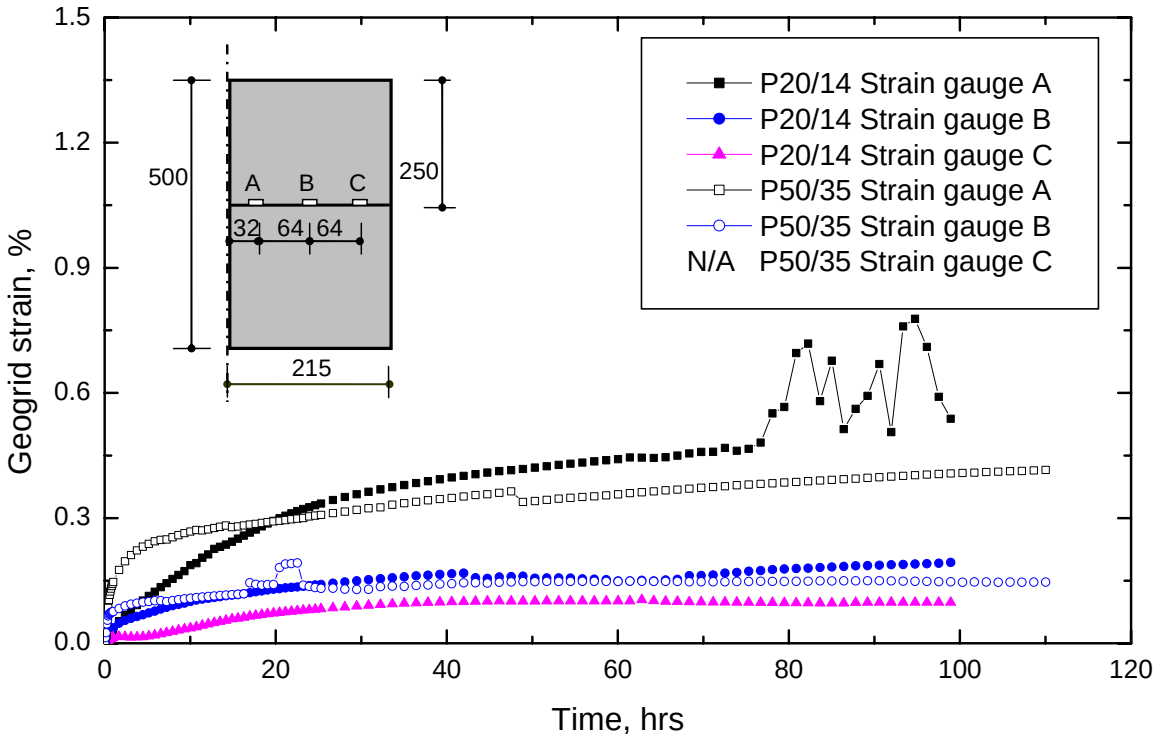

Figure 4.24 Geogrid strain-time history of reinforced clay specimens RP20/14 and RP50/35 during wetting

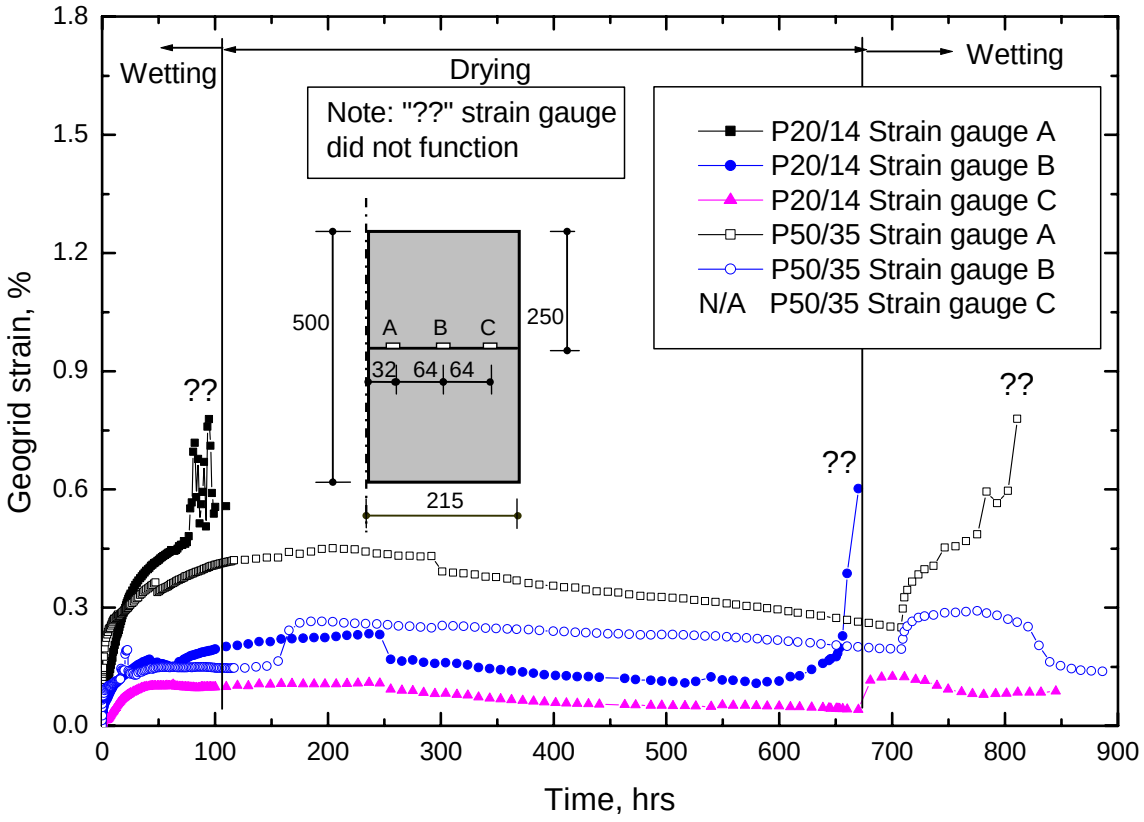

Figure 4.25 Geogrid strain-time history of reinforced clay specimens RP20/14 and RP50/35 during wetting-drying

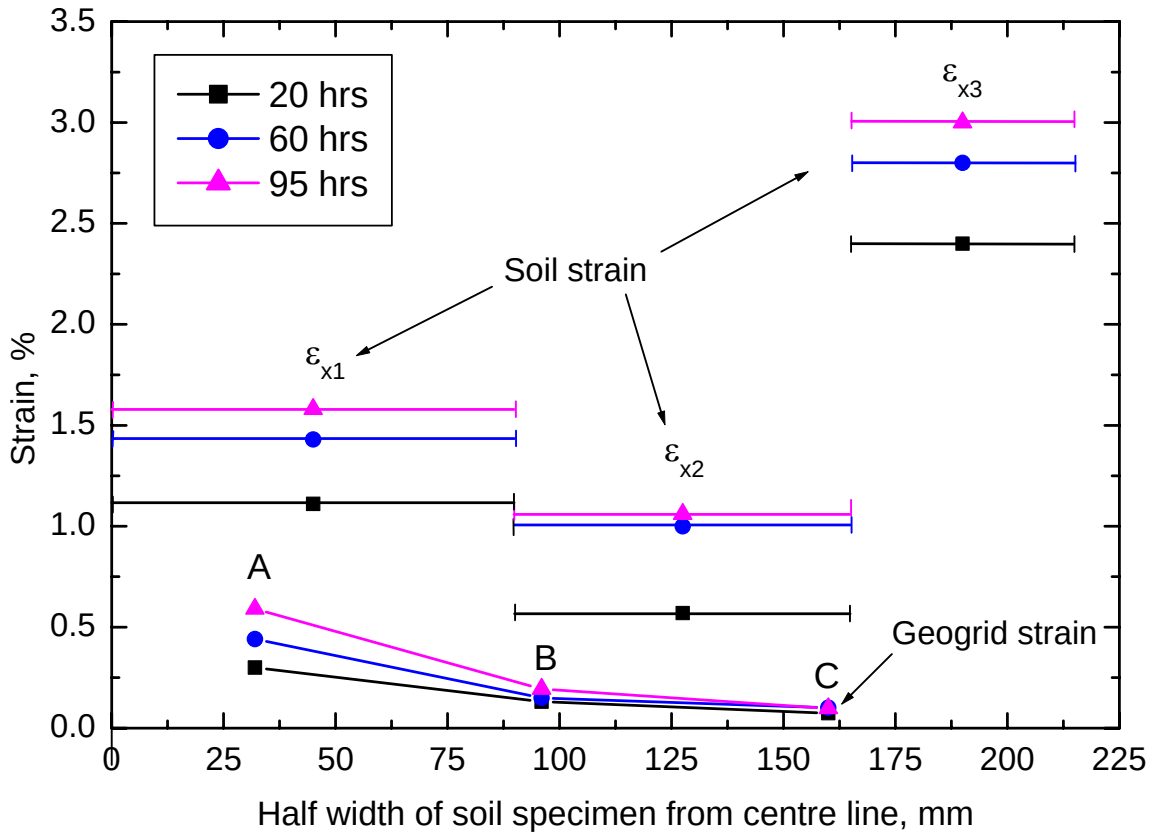

Figure 4.26 Wetting-induced strains in soil and geogrid in reinforced clay specimen RP20/14

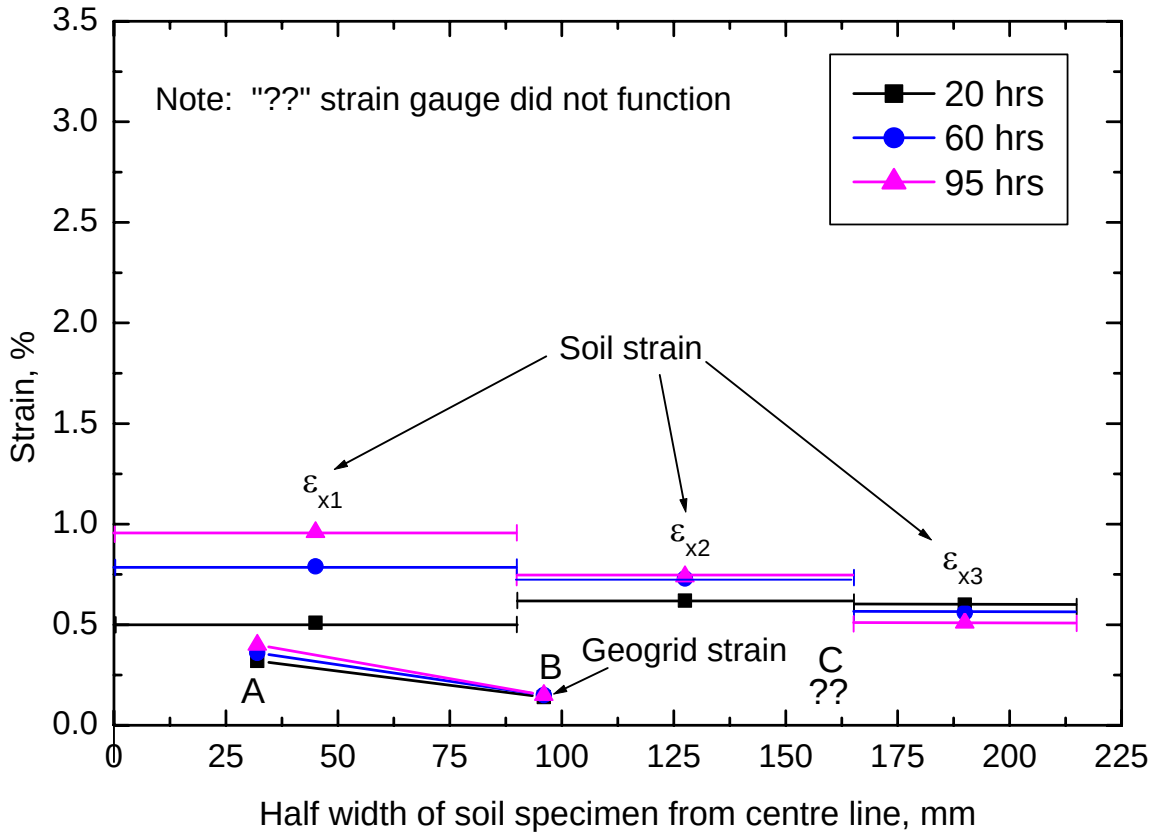

Figure 4.27 Wetting-induced strains in soil and geogrid in reinforced clay specimen RP50/35

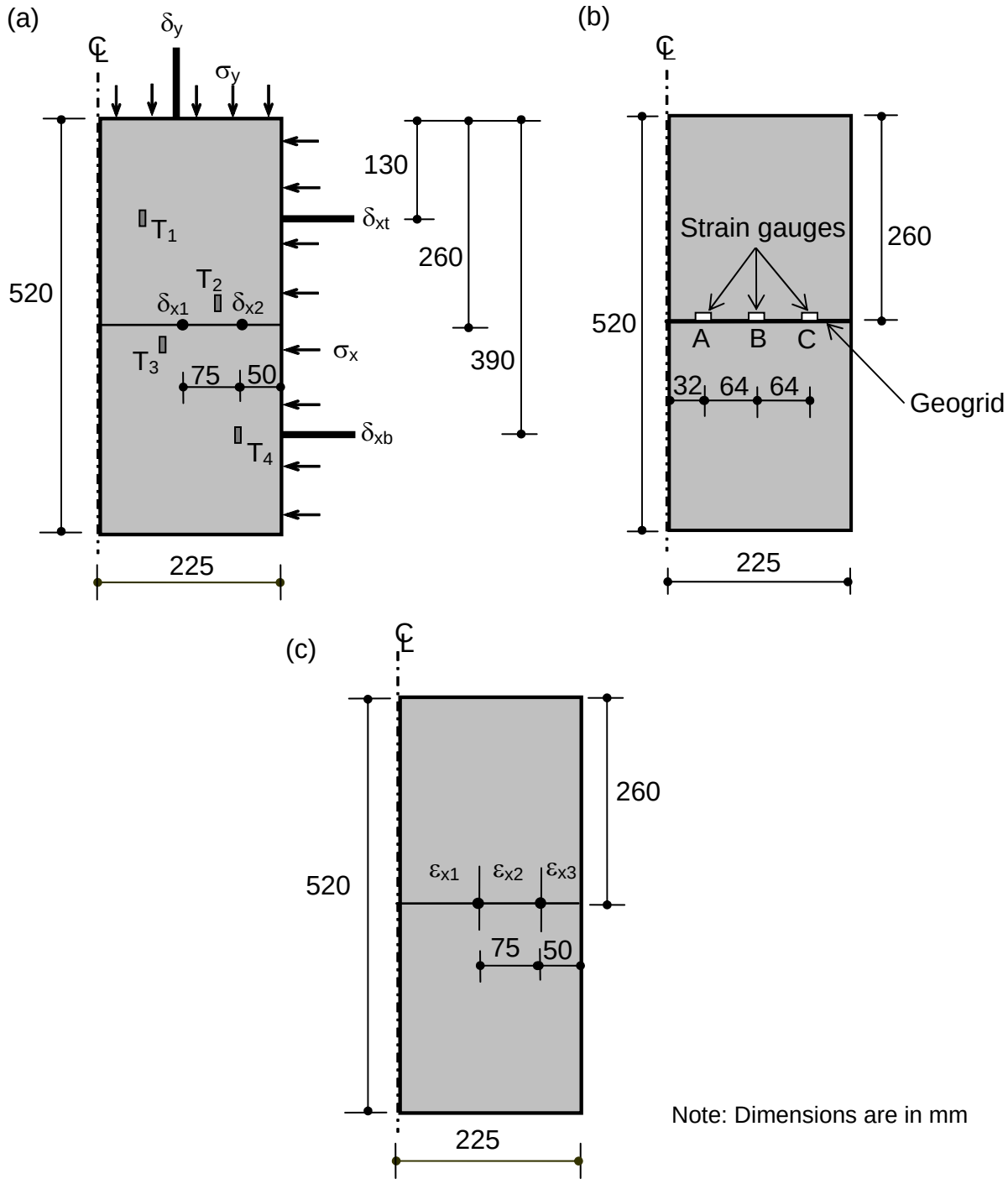

Figure 4.28 Schematic of (a) soil displacement and temperature measurements, (b) geogrid strain measurement, and (c) soil strain measurement in silt specimen

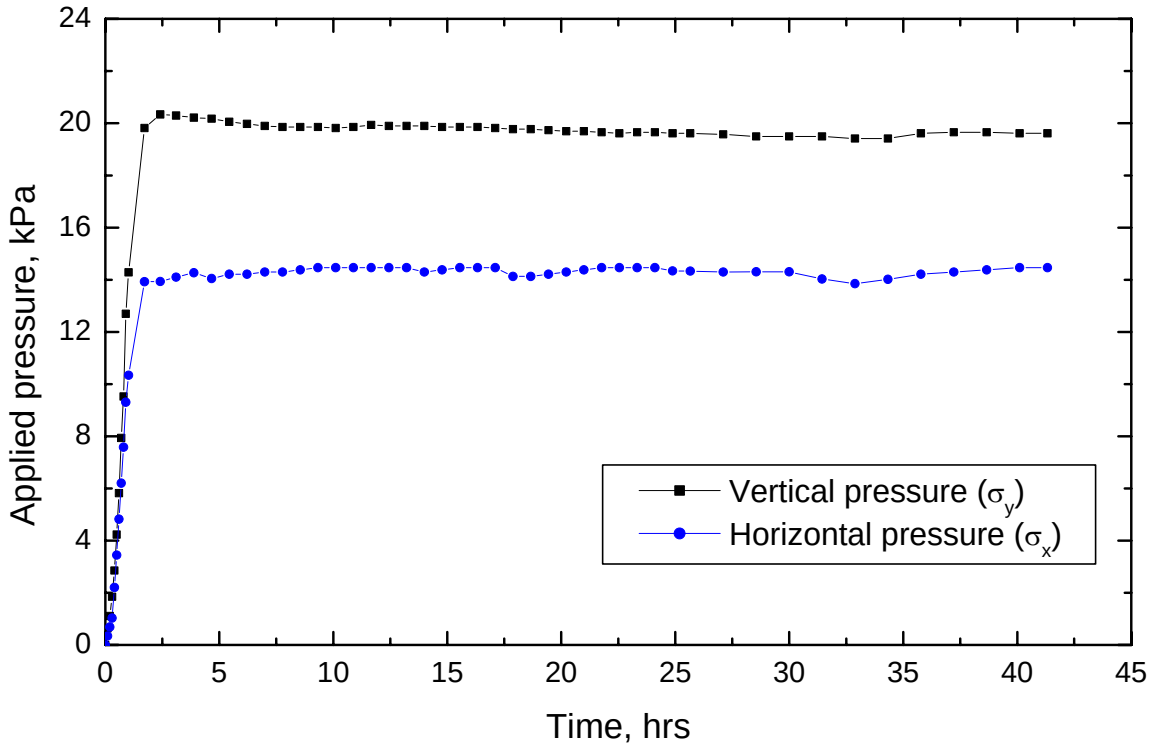

Figure 4.29 Applied pressure-time history of geogrid-reinforced silt specimen RT-25°C/+23°C during mechanical loading condition

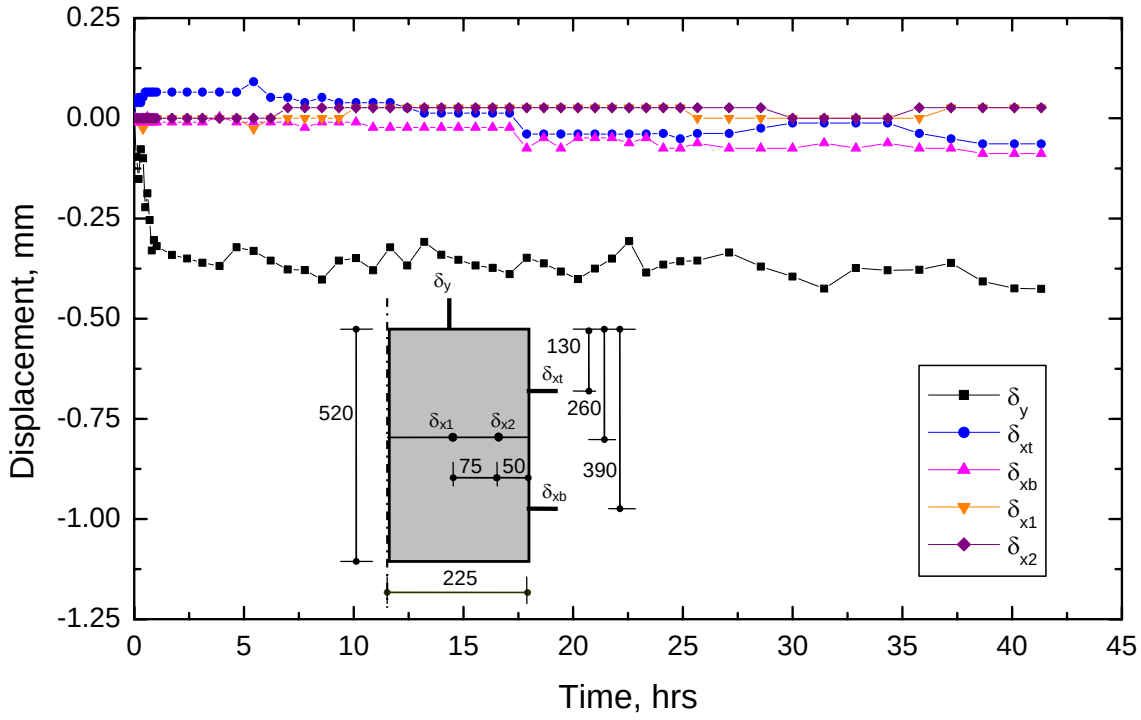

Figure 4.30 Displacement-time history for geogrid-reinforced silt specimen RT-25°C/+23°C during mechanical loading condition of 20 kPa vertical and 14 kPa horizontal pressure

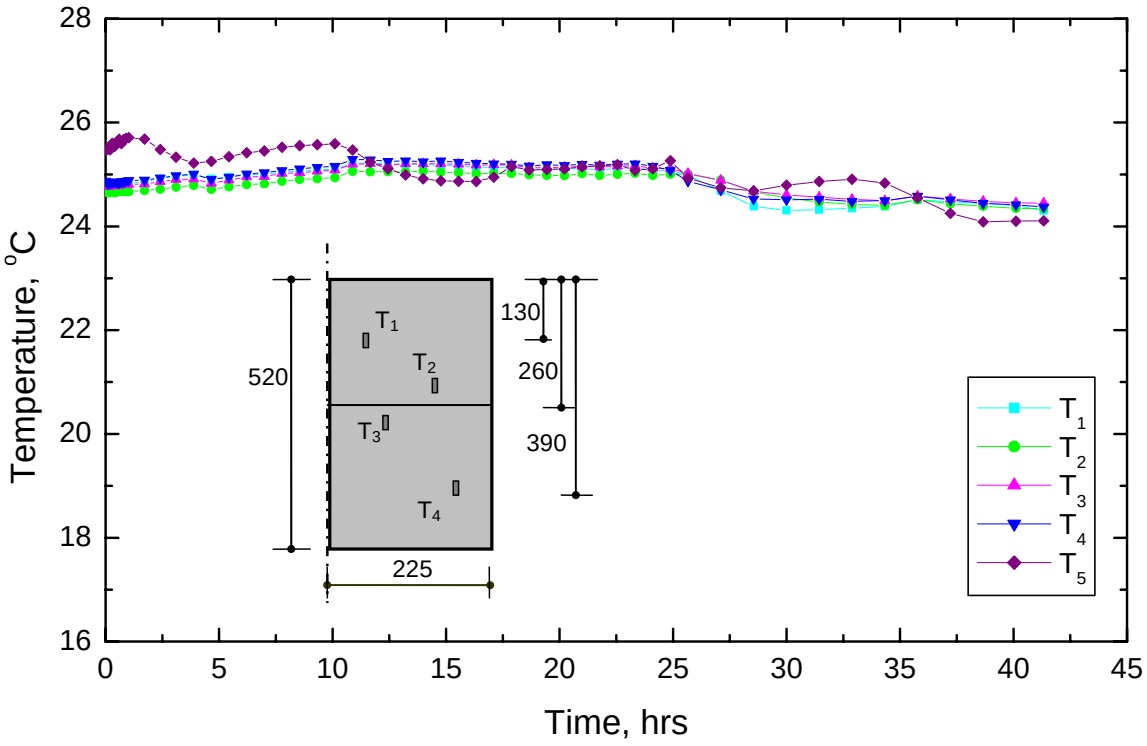

Figure 4.31 Soil temperature and environmental chamber temperature-time history in Specimen RT-25°C/+23°C during mechanical loading condition of 20 kPa vertical and 14 kPa horizontal pressure

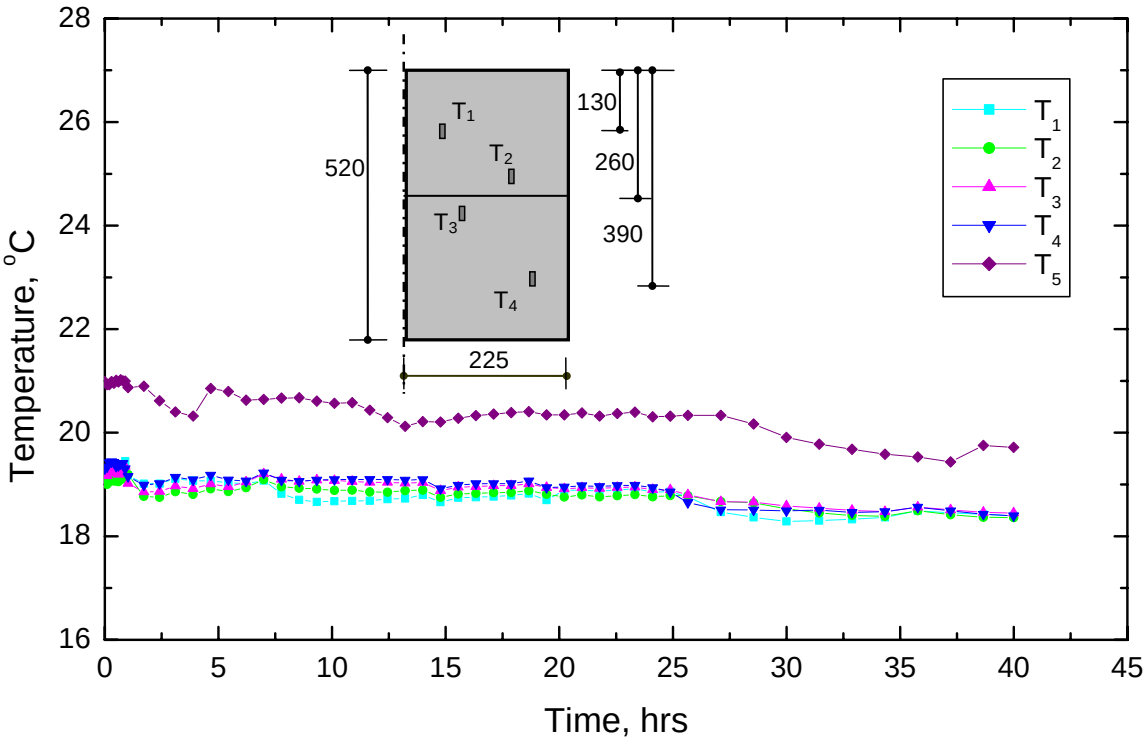

Figure 4.32 Soil temperature and environmental chamber temperature-time history in Specimen UT-25°C/ +23°C during mechanical loading condition of 20 kPa vertical and 14 kPa horizontal pressure

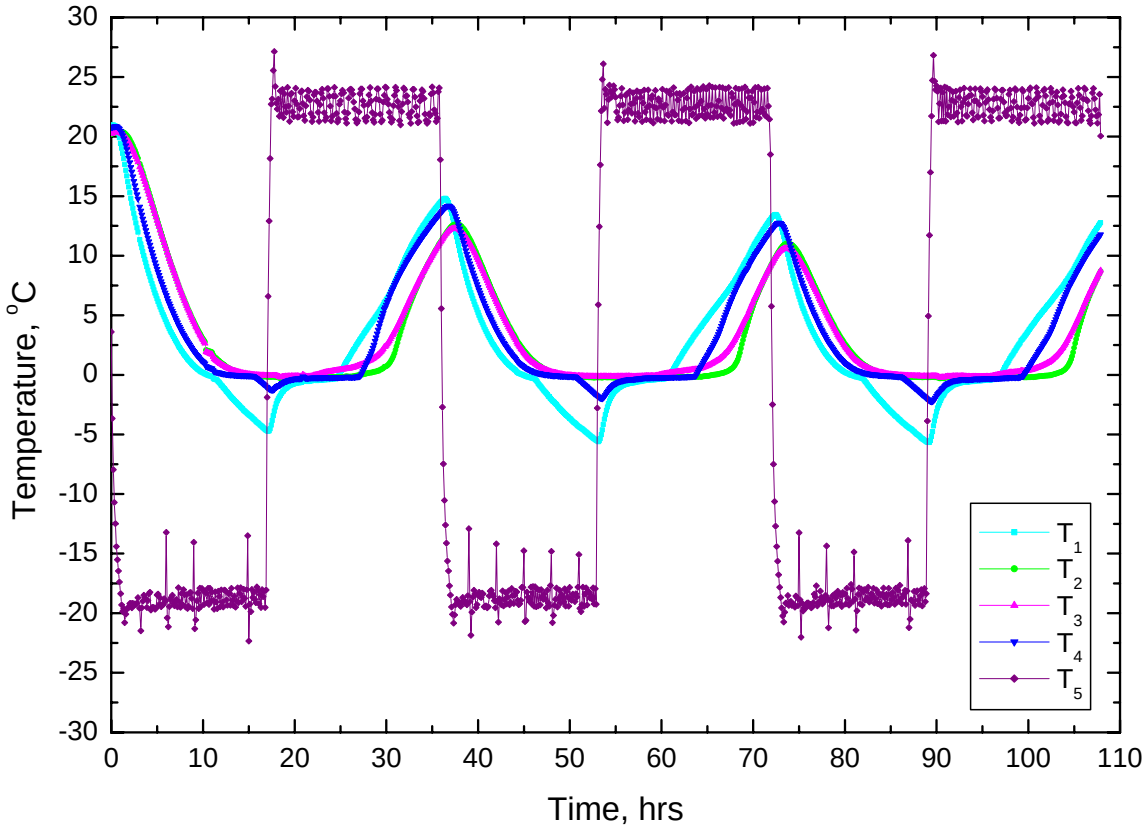

Figure 4.33 Temperature in unreinforced silt specimen UT-18°C/+23°C during three freezing-thawing cycles at environmental chamber temperature cycle -18°C/+23°C

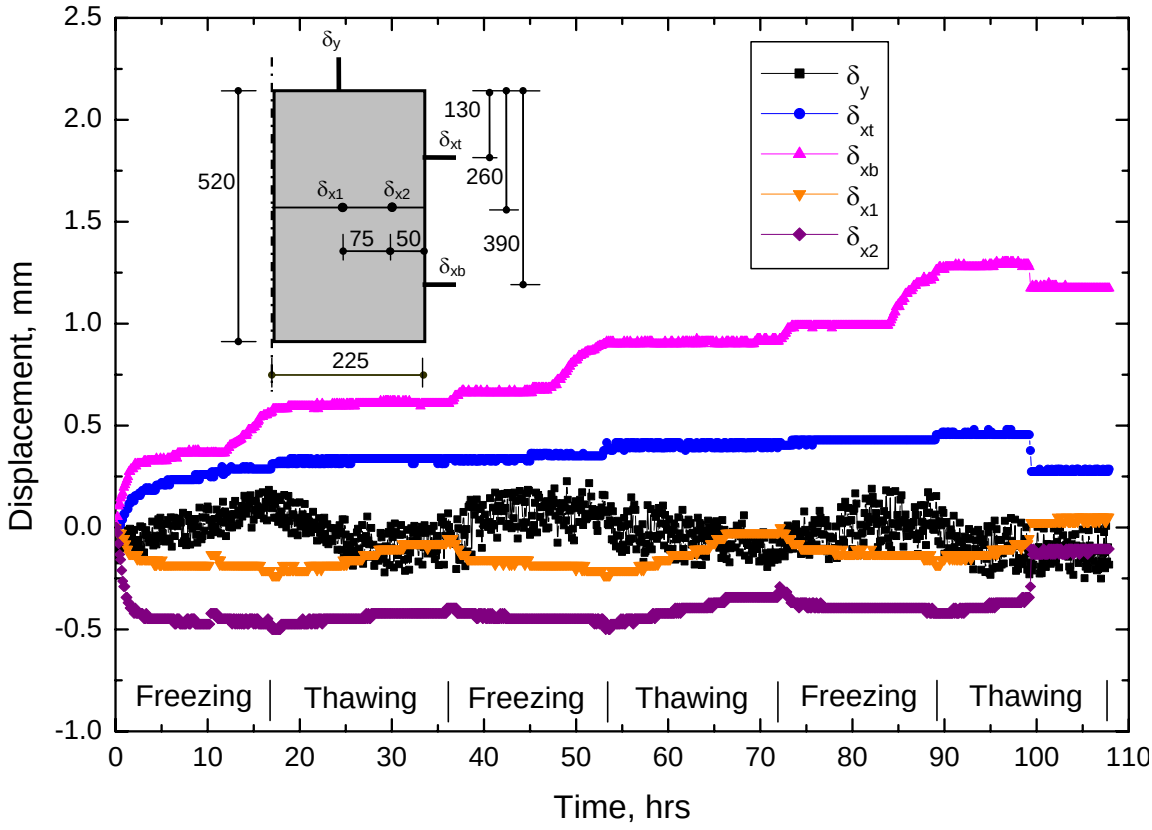

Figure 4.34 Soil displacement in unreinforced silt specimen UT-18°C/+23°C during three freezing-thawing cycles at environmental chamber temperature cycle -18°C/+23°C

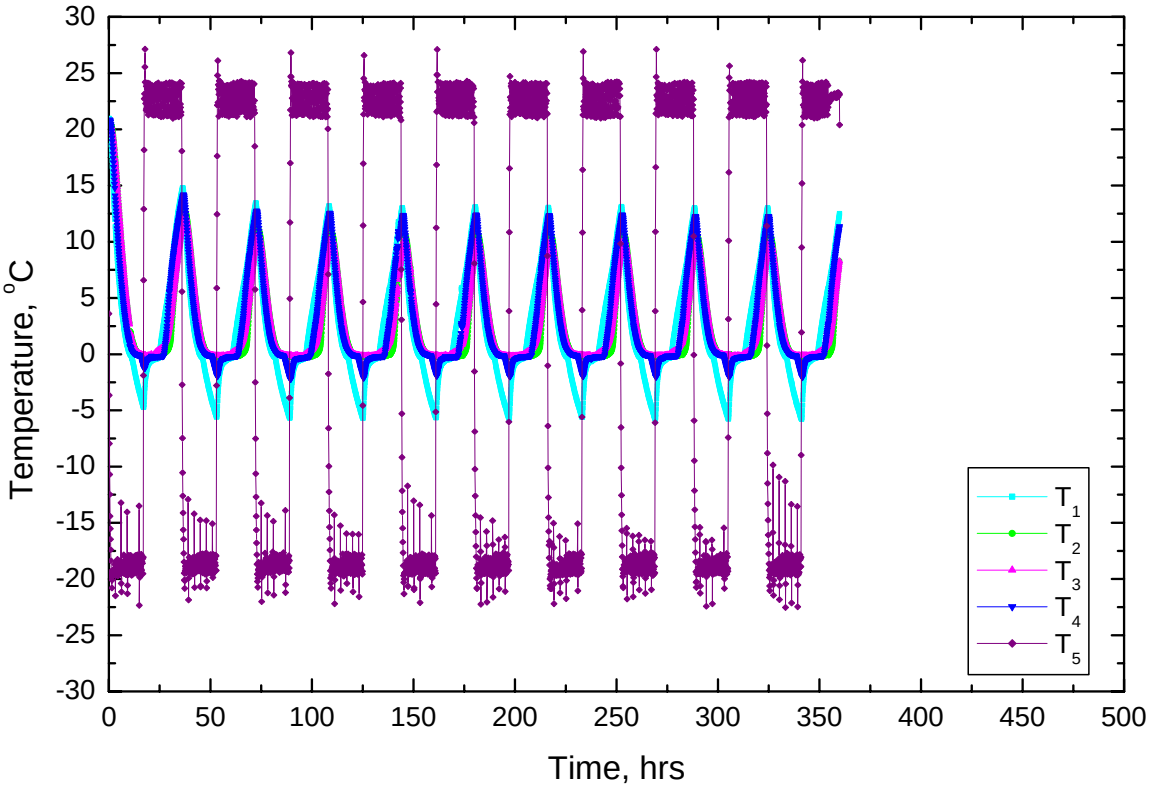

Figure 4.35 Temperature in unreinforced silt specimen UT-18°C/+23°C during freezing-thawing cycles at environmental chamber temperature cycle -18°C/+23°C

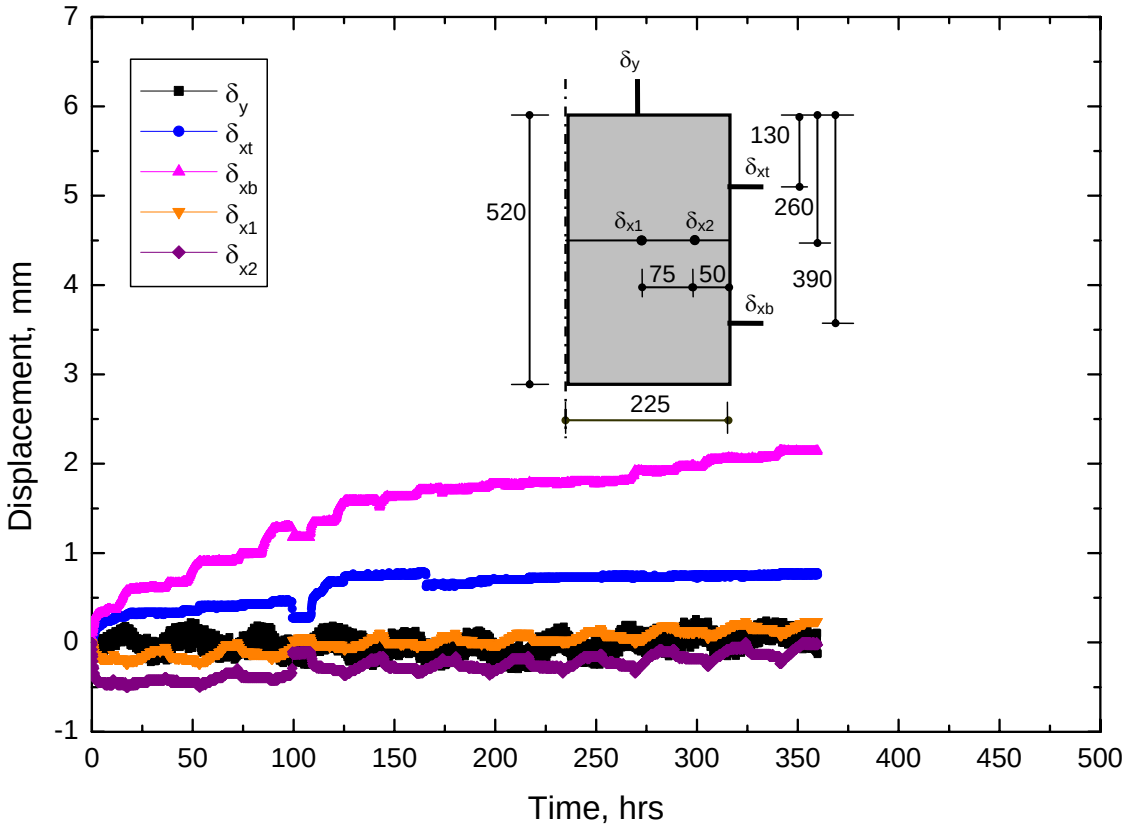

Figure 4.36 Soil displacement in unreinforced silt specimen UT-18°C/+23°C during freezing-thawing cycles at environmental chamber temperature cycle -18°C/+23°C

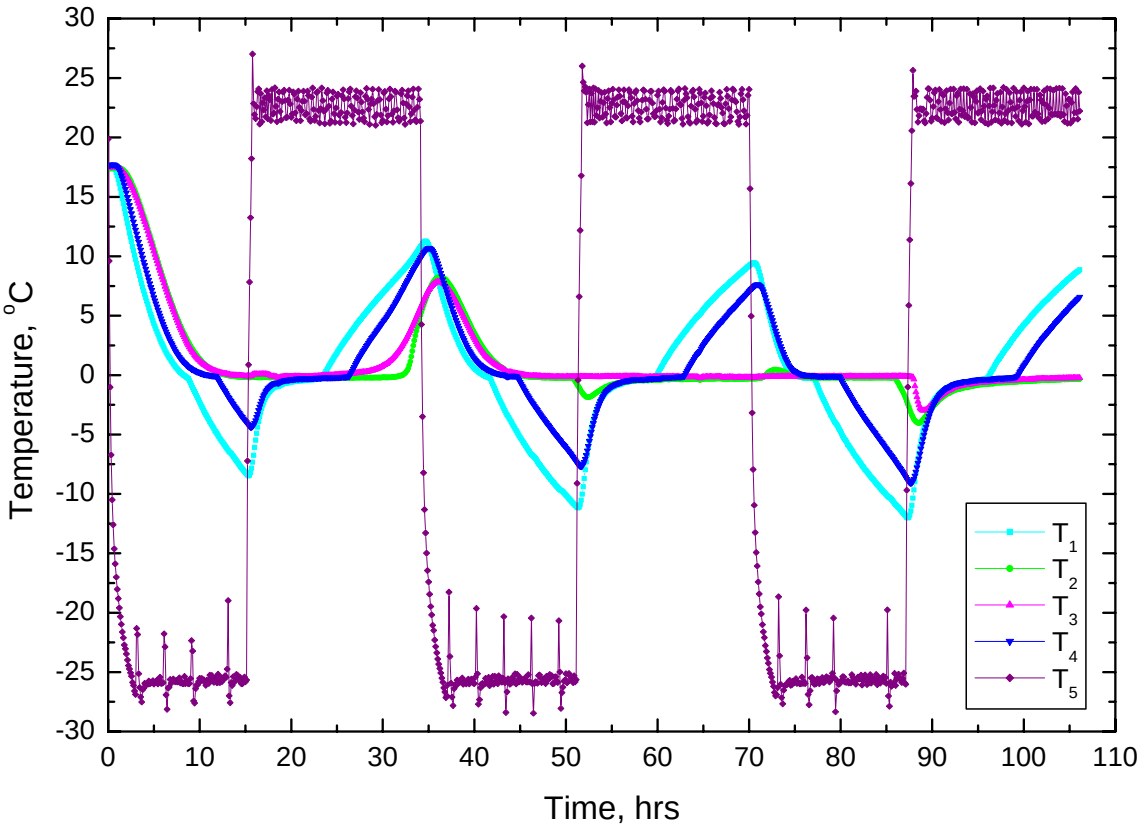

Figure 4.37 Temperature in unreinforced silt specimen UT-25°C/+23°C during three freezing-thawing cycles at environmental chamber temperature cycle -25°C/+23°C

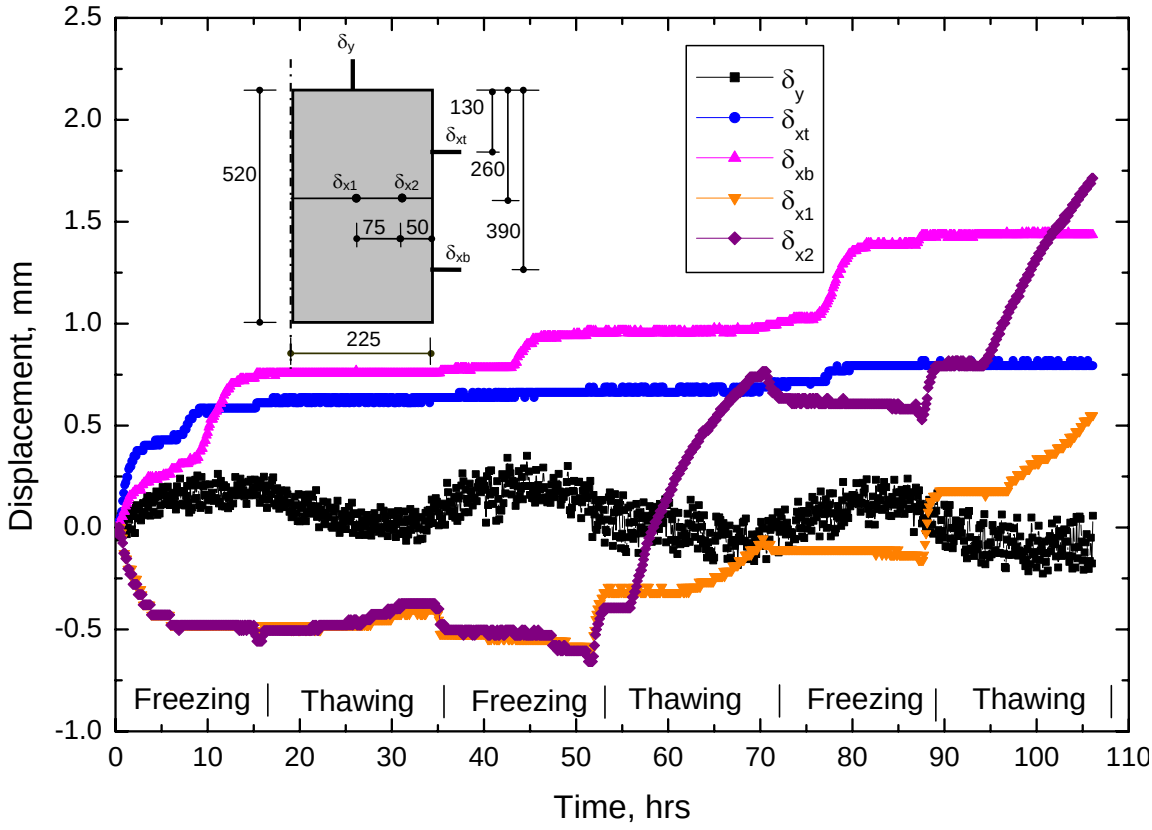

Figure 4.38 Soil displacement in unreinforced silt specimen UT-25°C/+23°C during three freezing-thawing cycles at environmental chamber temperature cycle -25°C/+23°C

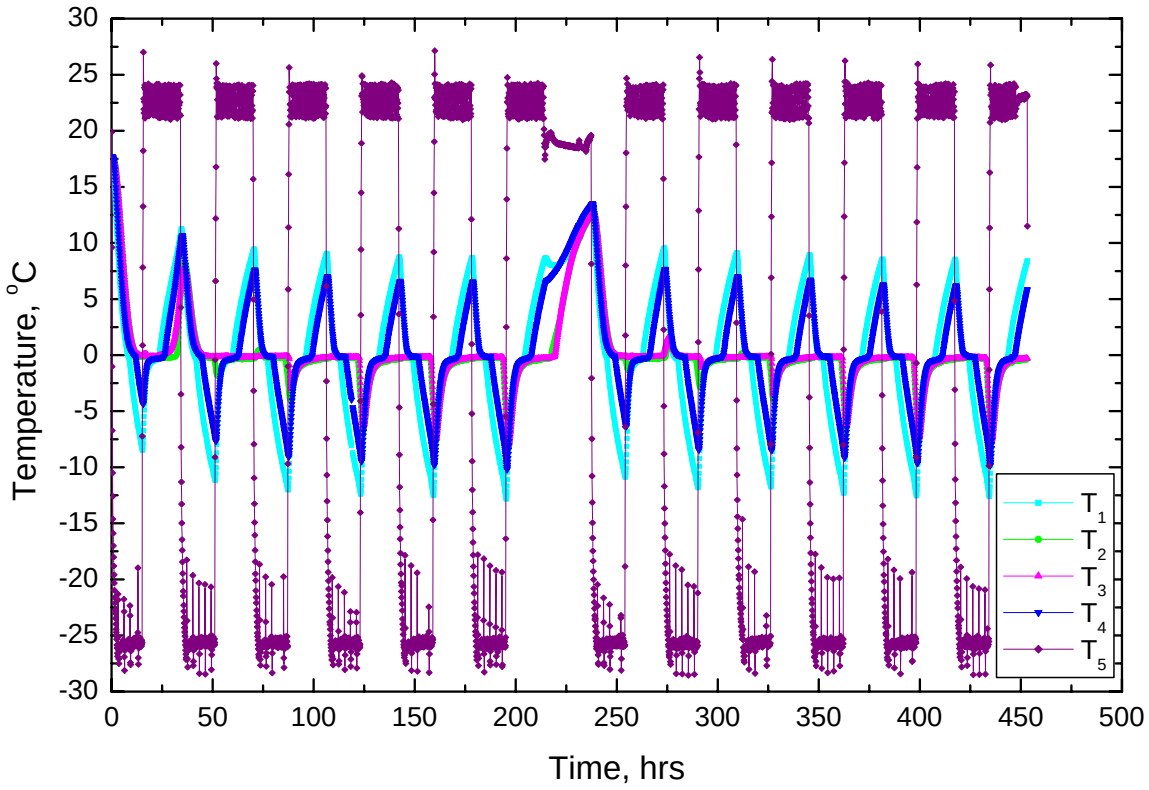

Figure 4.39 Temperature in unreinforced silt specimen UT-25°C/+23°C during freezing-thawing cycles at environmental chamber temperature cycle -25°C/+23°C

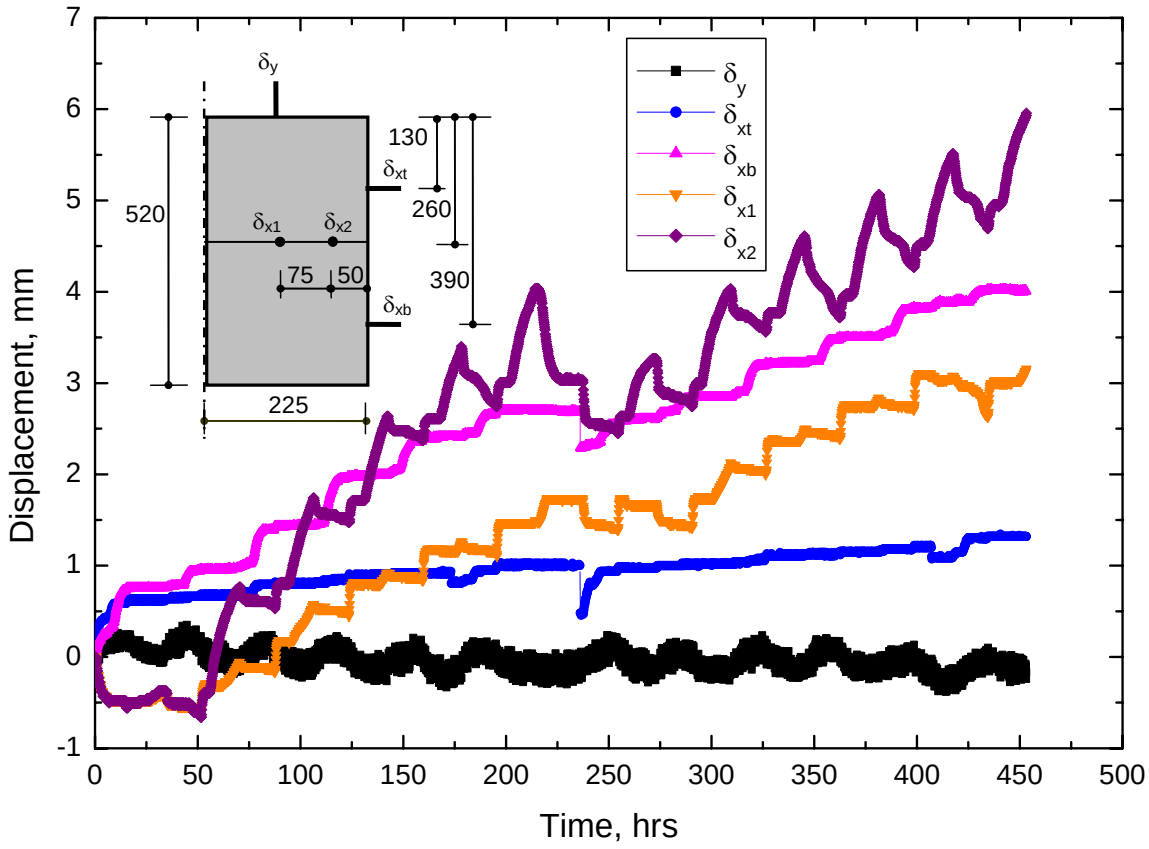

Figure 4.40 Soil displacement in unreinforced silt specimen UT-25°C/+23°C during freezing-thawing cycles at environmental chamber temperature cycle -25°C/+23°C

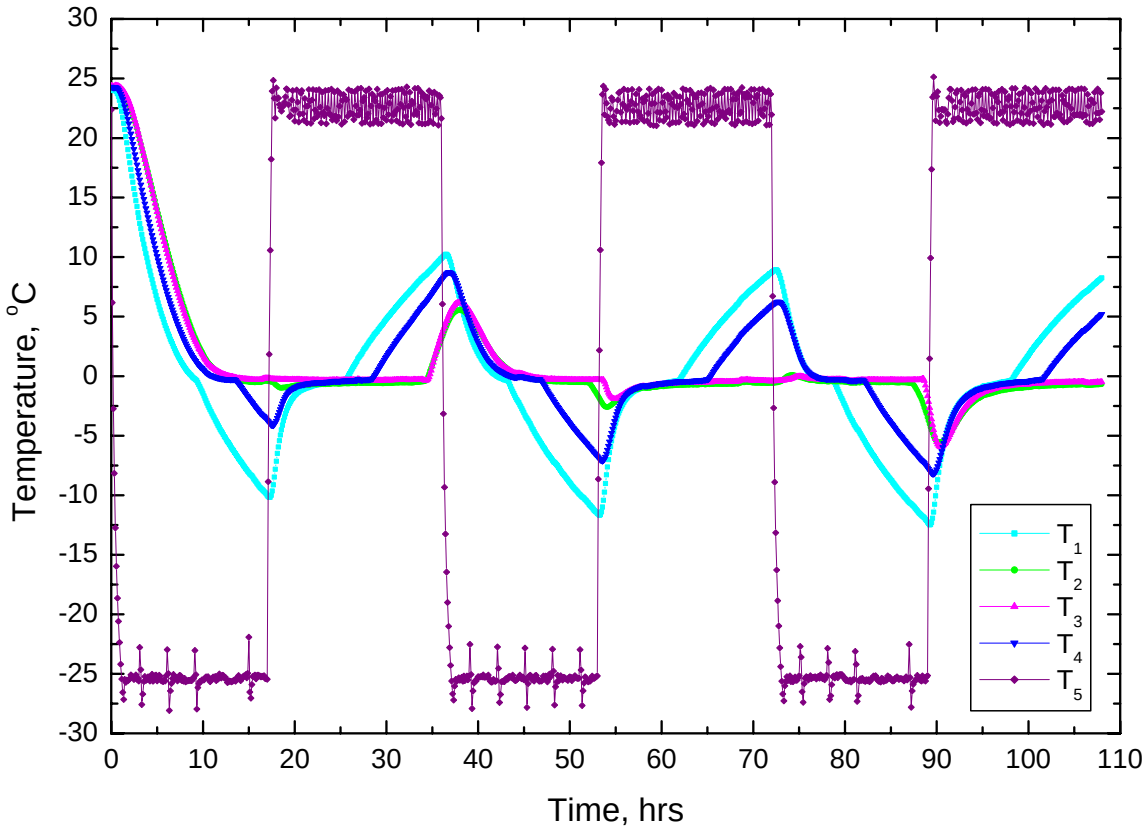

Figure 4.41 Temperature in geogrid-reinforced silt specimen RT-25°C/+23°C during three freezing-thawing cycles at environmental chamber temperature cycle -25°C/+23°C

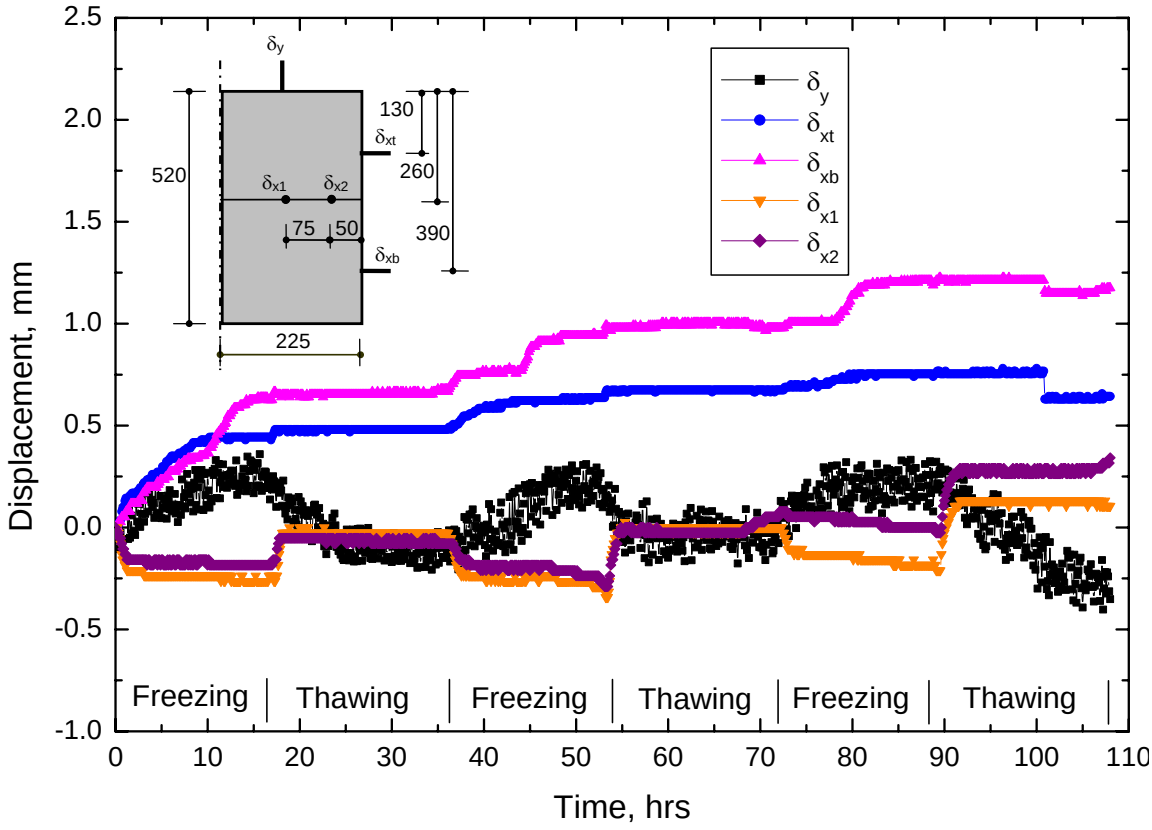

Figure 4.42 Soil displacement in geogrid-reinforced silt specimen RT-25°C/+23°C during three freezing-thawing cycles at environmental chamber temperature cycle -25°C/+23°C

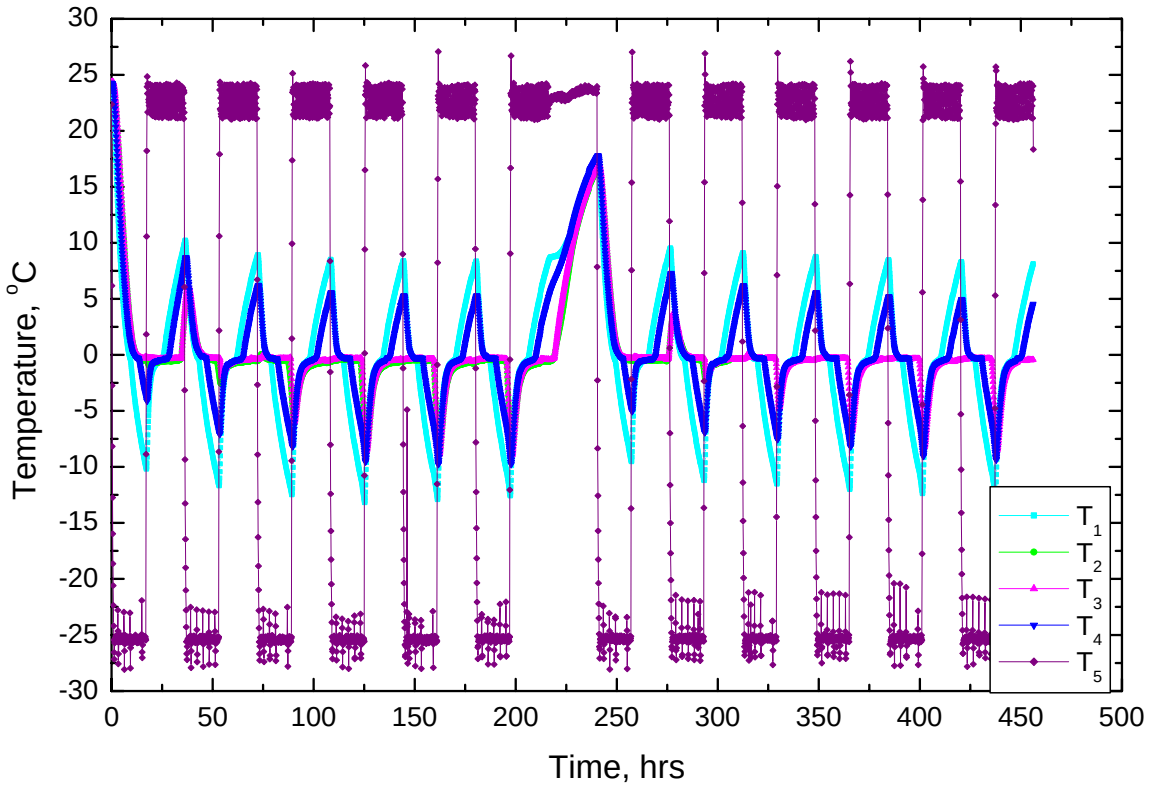

Figure 4.43 Temperature in geogrid-reinforced silt specimen RT-25°C/+23°C during freezing-thawing cycles at environmental chamber temperature cycle -25°C/+23°C

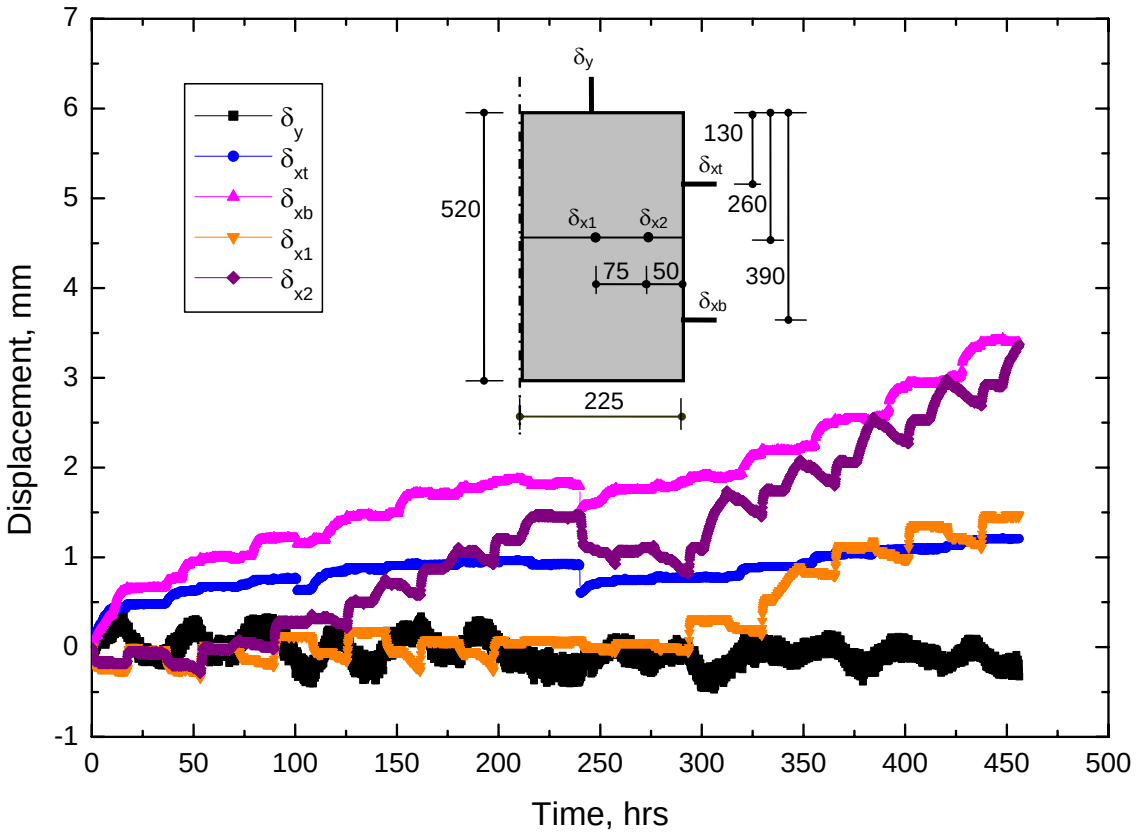

Figure 4.44 Soil displacement in geogrid-reinforced silt specimen RT-25°C/+23°C during freezing-thawing cycles at environmental chamber temperature cycle -25°C/+23°C

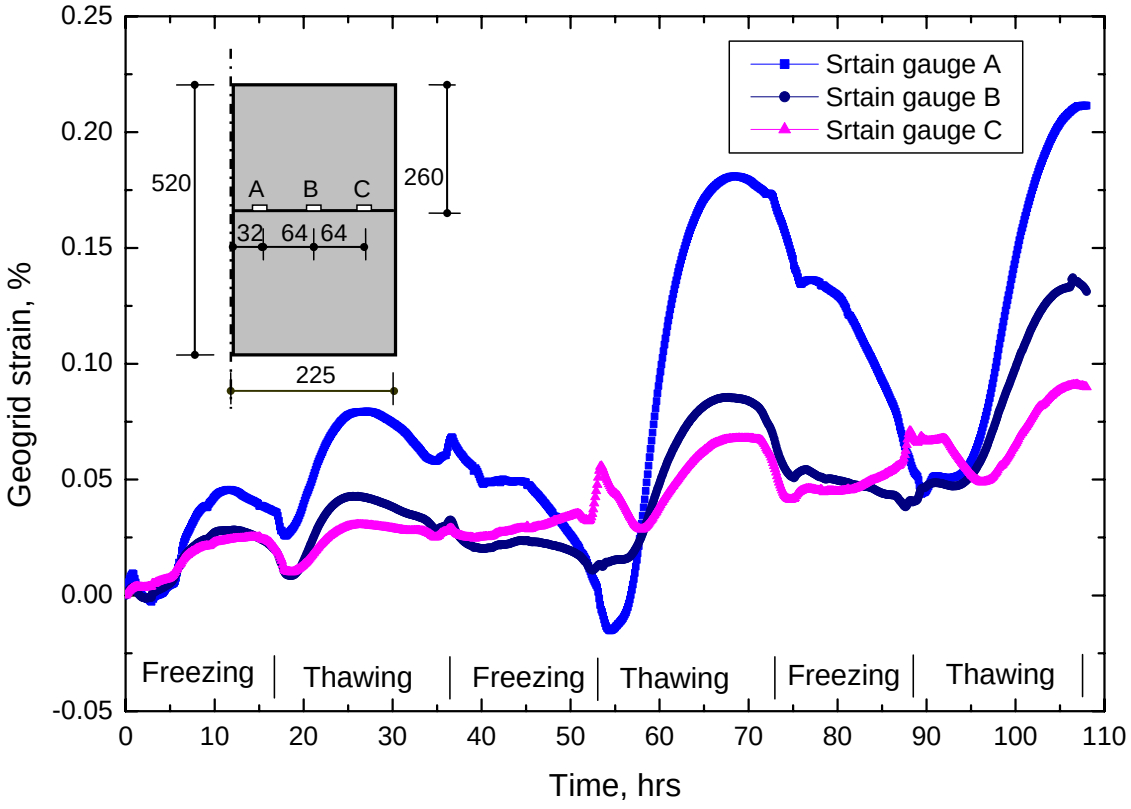

Figure 4.45 Geogrid strain in reinforced silt specimen RT-25°C/+23°C during three freezing-thawing cycles at environmental chamber temperature cycle -25°C/+23°C

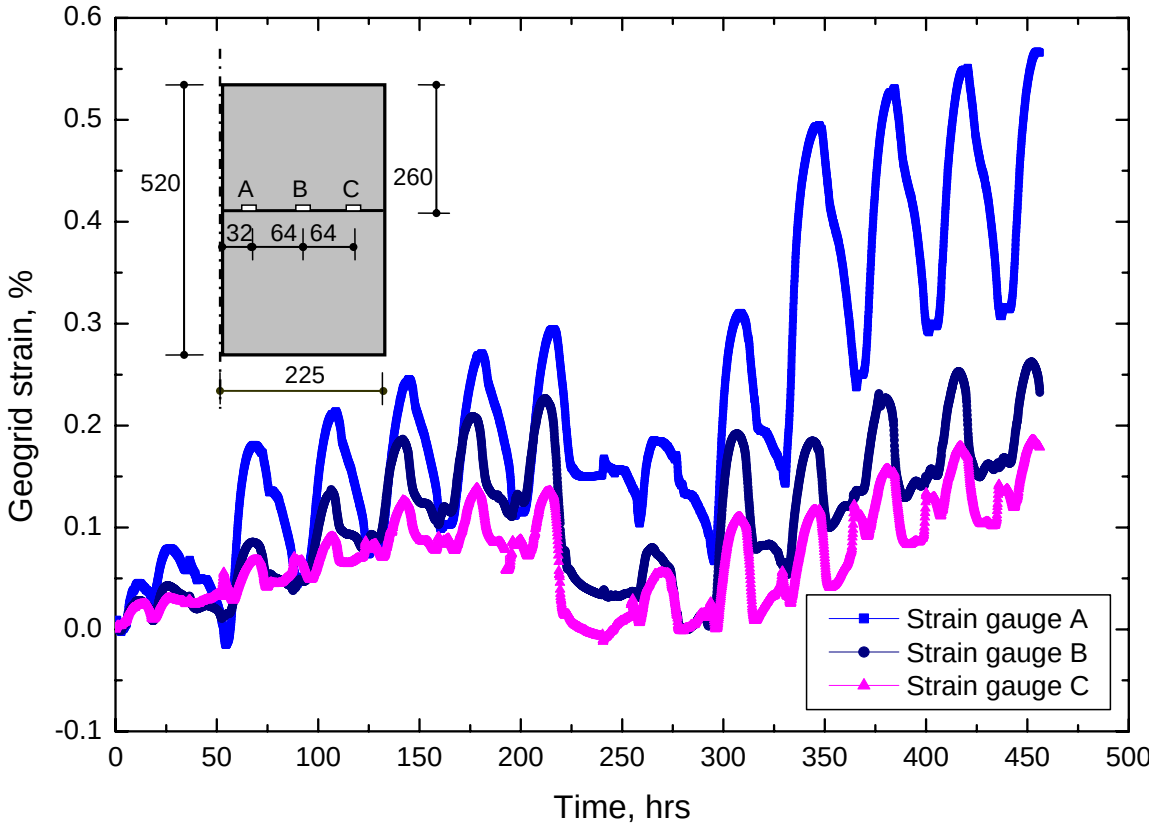

Figure 4.46 Geogrid strain in reinforced silt specimen RT-25°C/+23°C during freezing-thawing cycles at environmental chamber temperature cycle -25°C/+23°C

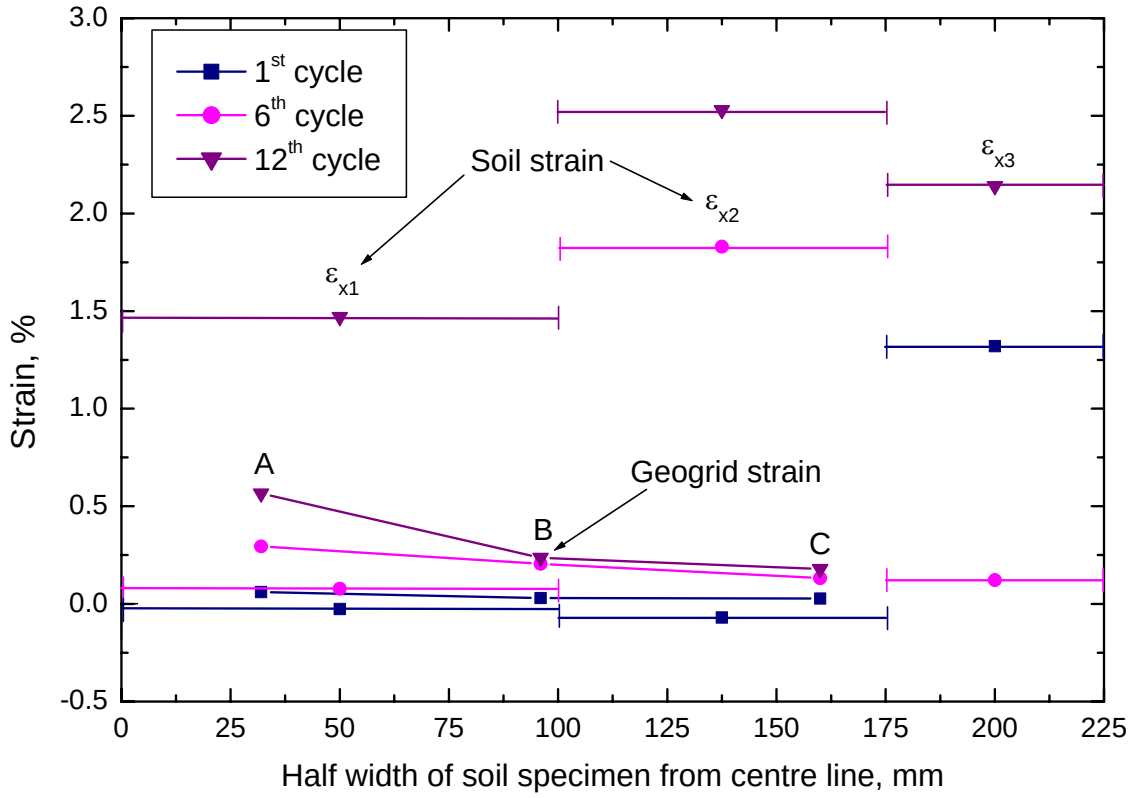

Figure 4.47 Soil-geogrid interaction in geogrid-reinforced silt specimen RT-25°C/+23°C during freezing-thawing cycles at environmental chamber temperature cycle -25°C/+23°C

CHAPTER 5

NUMERICAL MODELLING AND RESULTS

5.1 INTRODUCTION

Numerical modelling has been carried out in this study to develop an understanding of the deformation of GRS structures and reinforcement elements under environmental effects: wetting and freezing. There was no attempt to simulate wetting-drying cycles and freezing-thawing cycles due in part to the unavailability of constitutive models that can reasonably model these processes and in part, to associated parameters that are difficult to obtain from laboratory tests.

Wetting-drying cycles performed in the laboratory test set-up were not simulated because the established constitutive models (for example, Alonso *et al.* 1990) require many parameters and have to be obtained using advanced laboratory tests. As a result, only the wetting process is being simulated.

To the author's knowledge, there is no reliable constitutive model to simulate sequential coupling of soil expansion and compression due to freezing and

thawing, respectively. An add-in constitutive model for compression during thawing was just recently released in the 2007 version of GeoStudio 2007. The program does not take into account the frost heaving associated with freezing. Henry (1998) attempted to model the frost-induced heaves in pavements with capillary barriers using FROST and PC-Heave computer programs. Both programs are one-dimensional models and are based on basic equations of mass and heat transfer.

The author chose to use the finite difference based program, FLAC (Fast Lagrangian Analysis of Continua from Itasca Consulting Group 2001), as the modelling platform. FLAC provides the flexibility that user-defined constitutive models can be written and added into the program through the FISH functions. FISH is a programming language embedded within FLAC that enables the user to define new variables and functions. The constitutive models (BBM and Swell) described in the Literature Review were written by the author in the FLAC code as FISH functions to simulate the mechanical loading and wetting effects in swelling clays. Implementation of these models in FLAC is discussed in detail in the following sections.

The FLAC built-in thermal-elastic model has been used to simulate freezing in silt soil. Appropriate stress-strain characteristics of the soil, geosynthetics and their interface have been incorporated in the model. Individual modelling of each constituent (soil and reinforcement layer) of soil-reinforcement composite have

been done and then coupling terms (with their individual properties) have been added to take into account the interaction between the soil and the geosynthetics. The backfill soils were modelled with continuum elements and reinforcement layers were modelled with structural elements (cable).

This chapter deals with the development of numerical models to simulate wetting-induced expansion in swelling clays and freezing-induced expansion in frost susceptible silts in both the geogrid-reinforced and unreinforced soil specimens. The numerical models have been verified with the results of plane-strain tests. The models were then used in Chapter 6 to analyse the performance of geosynthetic-reinforced soil slopes with marginal soil backfills (clays and silts).

5.2 IMPLEMENTATION OF CONSTITUTIVE MODELS IN FLAC

5.2.1 Barcelona Basic Model (BBM)

Reinforced soil fills are compacted at prescribed moisture-density conditions. Initially compacted soil will usually be at an unsaturated state. In the case of swelling clay backfill, post-construction wetting-drying of the swelling clays can cause vertical and lateral movements of slopes and embankments. Alonso *et al.* (1990) proposed the constitutive model – BBM in the framework of hardening elasto-plasticity to describe the stress-strain behaviour of unsaturated expansive

soils. The theory behind the BBM has been described in the Chapter 2. Only the implementation of that model in the FLAC is presented here.

The model was written in FLAC by modifying the FISH function of modified Cam clay model. This was possible since the BBM extends the modified Cam clay model by including suction effects. The shear flow rule is assumed associated. The model assumes only constant suctions. The BBM has been used here to simulate the mechanical loading (gravity load and externally applied load if any) in swelling clays at constant suctions. The wetting effect has been decoupled from the BBM and a wetting-induced swelling has been modelled separately using the Swell model developed from the plane-strain laboratory test results. Although, the BBM can be used for various suction levels, that is, it can be used to determine the effects of wetting, the Swell model was used in this study for simulating wetting-induced swelling because of the simplicity in obtaining its modeling parameters. The BBM needs more parameters (κ_s, λ_s, s_0) to simulate the suction changes. This requires advanced laboratory testing and is beyond the scope of this study.

The FISH function developed to represent the BBM model in the FLAC has been provided in Appendix B.I as file “Alonso.fis”. The function is named **Alonso_cc** and requires the following parameters specified with the **PROPERTY** command:

m_g shear modulus, *G* (N/m^2)

m_k	maximum elastic bulk modulus, K_{max} (N/m^2)
m_kappa	slope of elastic swelling, κ
m_lambdas	slope of NCL or virgin line at s = const., $\lambda(s)$
m_m	slope of CSL, M
m_pcs	preconsolidation stress at s = const., p_0 (N/m^2)
m_poiss	Poisson's ratio, ν
m_p1	reference pressure, p_1 (N/m^2)
m_Ns	specific volume at reference pressure on NCL at s = const., $N(s)$
m_s	suction, $s = (u_a - u_w)$, N/m^2
m_ps	effect of suction on cohesion of soil (constant for s = const.), ps
m_v0	initial specific volume, v_0

These parameters default to zero if not specified.

In addition, the user has access to

m_e	total volumetric strain, e
m_ep	plastic volumetric strain, e^p
m_ind	state indicator:
	0 elastic
	1 plastic
	2 elastic now, but plastic in past

m_kc	current elastic bulk modulus, K
m_p	mean effective pressure, p
m_q	deviator stress, q
m_v	specific volume, V

As for the implementation of the BBM model in FLAC, the initial stress state is first established by function **set_v0**. Then, the elastic guess σ^{I}_{ij} is computed by adding it to the old stress components and increments calculated by the application of Hooke's law, and added to the total strain increment for a particular step. The principal stresses σ^{I}_{i}, $i = 1, 3$ (x, y) and the corresponding principal orientations are then evaluated. Elastic estimates for the mean pressure p^{I} and deviator stress q^{I} are calculated. If these stresses violate the yield criterion and $f(q^{I}, p^{I}) > 0$, plastic deformation takes place and the consolidation pressure changes. In this situation, a correction must be applied to the elastic estimate to give the new stress state.

The volumetric strain increment (Δe) and mean pressure (p) for the zone are computed as the average within an element (four triangles in a rectangular FLAC zone). The zonal volumetric strain (e) is incremented and the zone specific volume (V) is updated. In turn, a new zonal consolidation pressure is calculated and the tangential bulk modulus (K) is updated to reflect nonlinearity. If a nonzero value for the Poisson's ratio property is imposed, a new shear modulus is calculated from the expression $G = 1.5 (1 - 2 \nu) K / (1 + \nu)$. Otherwise, G is left

unchanged as long as the condition $0 \leq \nu \leq 0.5$ is satisfied; if it is not , G is assigned a value corresponding to $\nu = 0$ or $\nu = 0.5$, whatever is appropriate. The new values for the consolidation pressure, shear and bulk modulus are then stored for use in the next timestep.

The main aim for the BBM in this study is the reproduction of the general behaviour of unsaturated soil at constant suction. The model must predict saturated behaviour when the value of suction reduces to zero (s = 0). The yield curve (with shear) for a soil sample at constant suction (s = constant) is described by an ellipse which exhibits an isotropic preconsolidation stress given by Equation 2.5 which lies on the LC yield curve (Figure 2.9). In order to define the elliptical yield curve, it is also necessary to specify the failure state where the critical state line (CSL) for a saturated condition is parallel to the CSL at a given suction. The CSL at a given suction results the increased strength induced by suction.

5.2.2 Swell Model

The Swell model described in the Literature Review (Chapter 2) has been implemented and verified by Noorany *et al*. (1999) for use in the FLAC program. Their FISH function has been used with slight modifications to suit the plane-strain condition simulated in this study. Model parameters have been determined from plane-strain laboratory wetting tests conducted in unreinforced clay

specimens. The file “Swell.fis” given in Appendix B.II provides the FISH function of the Swell model in FLAC.

In the wetting-induced swelling modelling, relevant sets of properties of soil to be simulated are defined by the user. A wetting function number (1 for logarithmic, 2 for linear) and a property set number are then assigned to each zone in the domain. The wetting front is defined by a table of (x, y) values giving the coordinates of points on the wetting front in order of increasing x-values. The wetting front is assumed to vary linearly between points in the table and all elements with centroids above the wetting front are assumed to be wetted simultaneously. Wetting-induced strains are determined using logarithmic function based on equilibrium stress state prior to wetting. The corresponding wetting stresses are calculated using Equations 2.24 and 2.25. The wetting-induced strains and stresses are stored in extra grid variables. The wetting stresses are added to the stresses of elements with centers above the wetting front, and the system is cycled to equilibrium. The final state of the system provides the long-term stress state and displacements induced by wetting. Details of the Swell model implementation and verification are found in Noorany *et al.* (1999).

5.3 VERIFICATION OF BBM IN FLAC

Published data have been used to show the capability and the verification of the BBM model coded in FLAC in its finite-difference form. An example given by

Alonso *et al.* (1990) has been re-computed in this study using FLAC. The effects of loading on volumetric deformation of the reference 'soil' (Alonso *et al.* 1990) in the isotropic compression test sample has been selected for comparison purposes at constant suction. The model parameters for computation are as specified by Alonso *et al.* (1990) and are given in Table 5.1.

The initial net mean stress and suction are given by Alonso *et al.* (1990) as 150 kPa and 200 kPa respectively and in Figure 5.1a point A represents the initial condition. The initial position of the LC and SI yield curves are also shown in Figure 5.1a. The loading path AB at constant suction (s = 200 kPa) is of interest in this study, so only this path is modelled in FLAC using BBM. The FLAC simulation is carried out using a single zone of unit dimensions. The initial stress state is specified with $\sigma_x = \sigma_y = \sigma_z$ = -150 kPa. The velocity components are fixed in the x- and y-directions. A velocity of magnitude 0.5×10^{-5} m/steps is applied to the side and top of the model in the negative x- and y- directions respectively for at least 12000 steps to provide good results.

Table 5.1 BBM parameters for reference 'soil' (Alonso *et al.* 1990)

M	G MPa	$\lambda(0)$	κ	p^c kPa	p_0^* kPa	s kPa	v_0	r	β MPa^{-1}	k	$\lambda(s)$	p_0 kPa	p_s kPa	N(s)
1.0	10	0.2	.02	100	200	200	1.9	.75	12.5	0.6	.154	254	120	2.034

Figure 5.2 represents the author's numerical results plotted in terms of the specific volume (V) of the soil sample versus net mean stress (p). The compression path AB starts in the elastic region, so the first part of load path AB exhibits relatively little deformation followed by large plastic volumetric deformation after yielding. The numerical prediction is very close with the response presented by Alonso *et al.* (1990) (Figure 5.1b). This verifies that the numerical model reasonably predicts the unsaturated soil behaviour at constant suction. In view of the limited existing data available, this is the only example to verify the numerical model (BBM) implemented in FLAC.

5.4 VALIDATION OF BBM AND SWELL MODEL WITH LABORATORY PLANE-STRAIN WETTING TEST

Results from plane-strain laboratory tests conducted in this study are used to validate the numerical models. The BBM implemented in FLAC is validated with test results of clay specimens subjected to mechanical loading. The Swell model, also implemented in FLAC, is validated with test results of clay specimens subjected to wetting. Figure 5.3 shows the numerical mesh used for the unreinforced clay specimen in vertical symmetrical half-section. The bottom boundary of the specimen is fixed in both vertical and horizontal directions. The left side boundary is simulated with rollers to allow only vertical movement. The right side boundary is free in both the vertical and horizontal directions.

5.4.1 Model Parameters

The BBM parameters used in the numerical simulation for the clay in this study has been given in Table 5.2. Some parameters determined by other investigators on different types of clays are also tabulated for comparison purposes. The type of clay used in this study is referred to as “UMPAT”. Most of the UMPAT soil parameters were determined from the laboratory triaxial and one-dimensional swell tests that were described earlier in Chapter 3. The value of Poisson’s ratio (ν) was estimated equal to 0.44 using the following relation (Duncan *et al.* 1991):

$$\nu = \left(\frac{4 - 3\sin\phi'}{8 - 4\sin\phi'} \right) \tag{5.1}$$

However, the above relation is valid for ϕ’ = 25° to 40° only and the value of ν equal to 0.44 seems high for soft clay. So, ν equal to 0.35 has been used in the numerical simulation of mechanical loading in the unsaturated state. In the elastic range of material behaviour, the shear modulus (G) = 8 MPa and bulk modulus (K) = 25.5 MPa have been estimated from the values of E and ν. It should be mentioned that a tangent Young’s modulus has been used here. The estimated value of the shear modulus is within the range (G = 2.75 to 13.75 MPa) that Sabatini *et al.* (2002) recommended for soft clay. Matric suction (s) of about 200 kPa was taken from the plane-strain laboratory test during the mechanical loading condition, assuming the osmotic suction is about 250 kPa for Lake Agassiz clay (Fredlund 2005). Determination of the remaining parameters related

to unsaturated condition needs sophisticated laboratory tests that have not been performed in this study. That is why those parameters were determined using data available in the literature. The available data for low to moderate plastic clay (CK1 and CK2) and very high plastic clay-sand-bentonite buffer (DA-007) are given in Table 5.2. Using the available data, preconsolidation pressure (p_0) versus suction (s) graph can be drawn for soils CK1, CK2 and DA-007 (Figure 5.4). The p_0 versus s graph for UMPAT clay in Figure 5.4 was determined as the average of CK1, CK2 and DA-007. Then, r and β parameters in BBM for UMPAT clay were determined from a trial and error solution of Equations 2.5 and 2.6, setting a minimum error of a target value of 0.6. This k value falls between the corresponding values of CK1 and DA-007 (Figure 5.5).

Table 5.2 Basic soil properties and BBM parameters

Soil Properties	Low to moderate plastic clay		Highly plastic clay	
	CK1	CK2	UMPAT	DA-007
Basic soil properties				
w_L, %	38.7	37	96.0	230 - 250
w_P, %	26.9	9	35.0	30 - 50
I_P, %	11.8	28	61.0	200.0
% particles ≤ No.200 ASTM	95	-	95.0	-
USCS classification	ML	-	CH	CH
BBM parameters				
M	0.82	-	0.67	0.71
$\lambda(o)$	0.14	0.065	0.156	0.11
κ	0.015	0.011	0.05	0.005
p^c, kPa	43.0	10.0	100.0	10.0
p_o^*, kPa	55.0	40.0	200.0	500.0
G, kPa	3300.0	-	8000.0	200,000.0
s, kPa	10.0	-	200.0	35,000.0 – 45,000.0
V_0, initial specific volume	1.915	2.098	3.16	-
r (= $\lambda(s\rightarrow\infty)/\lambda(o)$)	0.26	0.75	0.489	0.68
β , MPa^{-1}	16.4	20.0	2.84	0.23
k	1.24	-	0.6	0.04
$\lambda(s)$	0.124	-	0.121	-
p_0, kPa	57.0	-	248.8	-
p_s (= k x s), kPa	12.4	-	120.0	-
N(s)	-	-	3.237	-

Note: CK1: Compacted kaolin (Alonso *et al.* 1990)
CK2: Compacted kaolin (Alonso *et al.* 1990)
DA-007: Sand-bentonite buffer (Priyanto *et al.* 2004)

The model parameters for the wetting analysis were determined from the plane-strain laboratory wetting tests conducted in unreinforced clay specimens (Figure 5.6). The plane-strain wetting tests were conducted at vertical pressures of 20, 30 and 50 kPa, with the horizontal pressure calculated from K = 0.7. Wetting-induced strain values for vertical pressures 1 kPa and 10 kPa were extrapolated based on one-dimensional swell test results (Figure 4.25). The clay used in this modeling study (UMPAT) follows the logarithmic function in wetting-induced strain represented by the Swell model. Table 5.3 tabulates the Swell model parameters. The elastic shear modulus and bulk modulus of UMPAT clay have been estimated from the E_{50} (secant modulus of elasticity at half of the maximum deviatric stress) from CIU traixial test of clay presented in Chapter 3 and an assumed Poisson' ratio (ν) equal to 0.3. Because soils exhibit nonlinear stress-strain behaviour, their moduli decrease with increasing strain levels. It has been assumed that swelling deformations reduce the stiffness of clay during wetting conditions.

Table 5.3 Swell model parameters for UMPAT clay

a_1	c_1	a_3	c_3	Max. swell at $\sigma_y = 0$		G (MPa)	K (MPa)
				ε_{yw}	ε_{xw}		
1.863	-0.0272	0.820	-0.0272	0.0475	0.057	3.5	8

5.4.2 Numerical Modelling Procedures and Results

The numerical simulations started with determining the initial stress state in the soil specimen. Initial stresses in its as-compacted condition were determined by gravity loading (locked-in stress). Compaction increases the lateral earth pressure in the fill so they become higher than normal at-rest values (gravity) (Duncan *et al.* 1991). However, in clay backfill, the high horizontal pressures induced by compaction tend to decrease over time to normal at-rest values. Duncan *et al.* (1991) suggests it is better to make at least a rough estimate of the horizontal pressures in clay backfills immediately after compaction. Thus, this was incorporated in the initial stress analysis using a higher value of horizontal stress (1.1 times the gravity stress). Then, the effect of loading on an unsaturated specimen was modelled with the BBM. Table 5.2, shown earlier, tabulates the model parameters used. The vertical (σ_y) and horizontal (σ_x) pressures were applied in increments at the top and right side boundaries of the specimen to simulate the loading conditions in the laboratory test. For example, in the case of test specimen UP20/14, a vertical pressure of 20 kPa on the top boundary and a horizontal pressure of 14 kPa on the right side boundary were applied as mechanical loading. The calculations were then cycled to equilibrium, after which wetting was modelled using the Swell model. Displacements determined in the mechanical loading condition were set to zero before invoking the Swell model for wetting simulation. This allowed delineation of displacements from those prior to wetting under the mechanical loading condition. Table 5.3 shows the Swell model parameters used. The calculations were again cycled to equilibrium.

Numerically predicted deformations of unreinforced clay specimens are summarized in Table 5.4 and will be discussed in following paragraphs.

Table 5.4 Numerically predicted deformations of reinforced and unreinforced clay specimens during mechanical loading and wetting condition

Test specimens	Mechanical loading conditions		Wetting conditions	
	Horizontal displacement, δ_x (mm)	Vertical displacement, δ_y (mm)	Horizontal displacement, δ_x (mm)	Vertical displacement, δ_y (mm)
UP20/14	0.6	- 2.6	4.5	5.1
RP20/14	0.6	- 2.6	4.2	5.3
UP30/21	0.43	- 2.75	3.3	3.0
UP50/35	0.1	- 3.0	2.1	0.28
RP50/35	0.1	- 3.0	2.0	0.3

Figure 5.7 shows the displacement vectors of unreinforced clay specimen in the mechanical loading condition simulated with the BBM at applied pressure of 20 kPa (vertical pressure on top boundary) and 14 kPa (horizontal pressure on right side boundary). The soil specimen has been compressed vertically and expanded laterally. Horizontal and vertical displacement contours are shown in Figures 5.8 and 5.9, respectively. The lateral expansion is about 0.6 mm while the vertical compression is about 2.6 mm. Comparing these results with the

measured values (see Table 5.5), the numerical analysis slightly under-predicted the measured horizontal displacement (0.73 mm), while over-predicting the vertical displacement (-1.0 mm). Given the small amounts of displacements, the numerical analysis can be considered satisfactory.

Table 5.5 Laboratory measured average deformations of plane-strain test specimens during mechanical loading and wetting of clay

Test specimens	Mechanical loading conditions		Wetting conditions	
	Horizontal displacement, δ_x (mm)	Vertical displacement, δ_y (mm)	Horizontal displacement, δ_x (mm)	Vertical displacement, δ_y (mm)
UP20/14	0.73	- 1.0	4.88	5.3
RP20/14	0.73	- 1.0	3.75	5.0
UP30/21	0.52	- 2.6	3.1	2.8
UP50/35	0.10	- 3.3	2.2	0.69
RP50/35	0.10	-3.15	1.67	0.67

During the numerical simulation, the soil deformation prior to wetting was set to zero. Figure 5.10 shows the predicted wetting-induced displacement of the same soil specimen UP20/14 at constant applied pressure. The results show that the specimen swelled both vertically and laterally. Figures 5.11 and 5.12 are the corresponding wetting-induced displacement contours. Horizontal swelling is

about 4.5 mm and the vertical swelling is 5.1 mm. Comparing with the laboratory measured values shown in Table 5.5, the numerical analysis slightly under-predicted swelling displacements measured vertically (5.3 mm) and horizontally (4.8 mm). Again, the numerical predictions can be considered in close agreement with the laboratory measured swelling displacements.

Similar numerical analyses were also performed for the other unreinforced clay specimens UP30/21 and UP50/35. Detailed results have been presented in Appendix C. For specimen UP30/21, the numerically predicted lateral expansion is 0.43 mm and vertical compression is -2.75 mm during the mechanical loading, while the predicted horizontal swelling is 3.3 mm and vertical swelling is 3.0 mm during wetting condition. The small discrepancies between numerically predicted displacement and laboratory measured displacement values (see Table 5.5) suggest the numerical predictions can be considered close to the laboratory measured deformations.

For the clay specimen UP50/35 during mechanical loading condition, the numerically predicted vertical compression is -3.0 mm and horizontal expansion is 0.1 mm. Comparing these results with the laboratory measured values (see Table 5.5), the numerical analysis slightly under-predicted the measured vertical displacement (-3.3 mm) while closely predicted the measured horizontal displacement (0.1 mm). The numerical prediction is that the clay specimen UP50/35 will swell both laterally and vertically during wetting condition. The

numerically predicted horizontal and vertical swelling displacements are 2.1 mm and 0.28 mm, respectively. Comparing these results with the measured values (see Table 5.5), the numerical analysis under-predicted the measured vertical displacement value (0.69 mm) while the horizontal displacement prediction closely agreed with the measured value (2.2 mm).

Comparison of experimentally measured and numerically simulated displacements in the three unreinforced clay specimens showed fairly good agreements. Given that some parameters were assumed and were based on values taken from literature, the verification provided reasonable confidence in the numerical models (BBM and Swell model) to simulate wetting induced deformations.

Further numerical simulations were carried out, this time on geogrid-reinforced clay specimens. This allowed determination of induced strains in the geogrid reinforcement and the deformation in the reinforced specimens associated with wetting. Numerical predictions and laboratory results were then compared. Figure 5.13 shows the numerical mesh used in FLAC. The modelling parameters for the soil in the geogrid-reinforced clay specimens were the same as for the unreinforced specimens. Geogrid reinforcements were modelled using two-noded linear elastic cable elements (structural elements). The following properties need to be specified for the cable elements:

Reinforcement properties:

Elastic modulus, E (MPa)

Tensile yield limit, yield (kN)

Compressive yield limit, ycomp (kN)

Cross-sectional area, A (m^2)

Exposed perimeter, peri (m)

Soil-cable interface properties:

Shear stiffness, K_b (kN/m/m)

Cohesive strength, S_b (kN/m)

Interface frictional angle, δ (^{o})

It was assumed that cable elements have an out-of-plane depth of unity. To convert the planar strength properties of the geogrid into an equivalent cable, 3 mm of in-soil thickness was assumed. Data supplied by the manufacturer were used to determine the geogrid strength properties. The tensile strength at less than 2% strain was used to determine the elastic modulus of the geogrid. The reinforcement strength of the geogrid was reduced by one-half to account for the removal of alternate strips from virgin geogrid. Soil-geogrid interface behaviour was modeled by using the cable grout utility in the FLAC program. Since clay-geogrid interface data (which could be determined by laboratory pullout test) were not available, slightly reduced shear properties of clay were used as the interface shear properties of the clay-geogrid. The clay-geogrid interface angle

was estimated two-third of the clay friction angle. Table 5.6 summarizes the input properties used to simulate the geogrid as cable elements in the numerical analysis. The rest of the modelling procedures were the same as those in the unreinforced specimen to simulate the behaviour under mechanical loading. The BBM was used to simulate mechanical loading, followed by the Swell model to simulate the wetting behaviour. Numerically predicted deformations of the reinforced clay specimens are also summarized in Table 5.4.

Table 5.6 Geogrid reinforcement and soil-geogrid interface properties

E (MPa)	yield (kN)	ycomp (kN)	A (m^2)	peri (m)	K_b (kN/m/m)	S_b (kN/m)	δ (^{o})
100.0	14.0	3.3	0.003	2.0	$2.34e^4$	10	11.5

Figure 5.14 shows numerically predicted displacement vectors of the geogrid-reinforced specimens RP20/14 in the mechanical loading condition. The soil specimen has been compressed vertically and expanded laterally in the RP20/14 specimen. The soil displacements are similar to those in the corresponding unreinforced clay specimen UP20/14. Axial stress and strain in the geogrids are very small so that the figures showing these results are omitted. The reinforcement strains are consistent with the small deformations of the soil specimen at low confining pressures. The predictions are again comparable with laboratory measured displacement values.

Figure 5.15 shows the displacement vectors of the geogrid-reinforced specimen RP20/14 during wetting. The specimen swells both in horizontal and vertical directions. Figures 5.16 and 5.17 are corresponding wetting-induced displacement contours in the horizontal and vertical directions respectively. The average horizontal swelling is about 4.2 mm and vertical swelling is about 5.3 mm, which are comparable with the laboratory measured values (3.75 mm horizontal swelling and 5.0 mm vertical swelling displacements). In comparing these results with those of the unreinforced clay specimen UP20/14, the presence of geogrid reinforcement (RP20/14) reduced the horizontal swelling only in the middle area (where geogrid was placed) by about 4%. This reduction has not been shown in the contour lines of Figure 5.16 but can be examined in the displacement values at that location. Interestingly, the vertical swelling has increased in the reinforced clay specimen compared with the unreinforced one. This is consistent with the laboratory test results conducted by Vessely and Wu (2002) in reinforced and unreinforced clay blocks. They observed higher vertical swelling in reinforced specimens than in corresponding unreinforced specimens.

The geogrid-reinforced clay specimen RP50/35 was also simulated numerically under mechanical and wetting conditions. The results are presented in Appendix C. The numerical prediction under mechanical loading resulted in vertical compression and insignificant horizontal displacement. During wetting, the same specimen showed horizontal swelling of about 2.0 mm and vertical swelling about

0.3 mm. Comparing these results with the laboratory measured values (see Table 5.5), the numerical analysis over-predicted the measured horizontal displacement (1.67 mm), while under-predicting the measured vertical displacement (0.67 mm). The numerical analysis can be considered satisfactory in this particular case. The geogrid reinforcement reduced the horizontal swelling in the middle area by about 5%. The vertical swelling has increased in reinforced clay specimen compared with the unreinforced specimen.

Figures 5.18 and 5.19 show the simulated axial forces and strains, respectively induced in the geogrid after wetting in clay specimen RP20/14. These are the axial forces and strains after wetting due to both mechanical loading and wetting effects. As discussed earlier, the geogrid forces and strains due to mechanical loading were very small compared with the strength of the geogrid. About 0.94% of geogrid strain was predicted due to wetting only, which is slightly above the 0.75% strain measured during the wetting of specimen RP20/14. Figures 5.20 and 5.21 show the numerically predicted axial forces and strains, respectively, induced in the geogrid after wetting in specimen RP50/35. The maximum value of the geogrid strain due to wetting only is about 0.6%. The corresponding laboratory measured geogrid strain is 0.45%.

Overall, results from the numerical modelling compared fairly well with the experimental results. These results provide further confidence in the validity of the numerical model, which can then be used for carrying out parametric studies

of engineered embankment slopes constructed with swelling clay backfill reinforced with geogrid and subjected to wetting.

5.5 MODELLING THE EFFECTS OF FREEZING ON LABORATORY TEST SPECIMENS

Seasonal soil freezing and thawing have potential to cause significant damage to roads, foundations, buried pipelines and other infrastructure in cold climates. Soil heaving occurs during freezing and settlement occurs during thawing. The process of soil freezing-thawing is a complex problem, which involves coupling between thermal, hydraulic and mechanical interactions. It involves at least three phases: water, ice and the soil matrix. During freezing-thawing, phase changes take place with in the water/ice, accompanying volumetric changes and release of latent heat.

To the author's knowledge, there is still no widely recognized numerical model that quantifies accurately the effects of freezing and thawing cycles on deformation of soils, let alone models that are embedded in commercially available computer programs. Three cycles of freezing and thawing have been simulated in this study. The analysis used the isotropic thermal-mechanical model in FLAC.

Laboratory test results presented in Chapter 4 showed that the horizontal displacements were constant during thawing. To simulate negligible deformations

during thawing, only the thermal model was used, without mechanical coupling for the thawing phase. This phenomenological modelling procedure is solely for the simulation of the laboratory test results. The procedure is not likely to simulate field conditions especially, near the slope surface where vertical and horizontal stresses are low. To simulate field conditions, the modelling procedure needs to be modified. This has not been done in this study. This is why only freezing simulations have been made in the analysis of the reinforced silt slopes discussed in Chapter 6.

Water was not explicitly accounted for in the model. Rather, its coefficient of linear expansion has been used to analyze freezing-induced deformations. In another words, the process of water/ice phase change has not been modelled. Conduction is assumed to be the mode of heat transfer in the soil. The soil is assumed to freeze at 0°C. Frozen and unfrozen soil regions are delineated through the built-in thermal analysis in FLAC. The soil's mechanical behaviour is represented as a Mohr-Coulomb model. Thermal and mechanical models are coupled to determine the effect of freezing in the soil.

The numerical model simulates the laboratory plane-strain reinforced and unreinforced silt specimens subjected to freezing as described in Chapter 4. First, an unreinforced silt specimen UT-25°C/+23°C was simulated in plane-strain in an applied freezing and thawing temperature cycle of -25°C and +23°C for 17 and 19 hours, respectively under the applied vertical pressure of 20 kPa and

horizontal pressure of 14 kPa. Using carefully selected parameters, the results were verified with the corresponding laboratory freezing-thawing test results. These soil parameters were then used to simulate the freezing-thawing effects in the reinforced silt specimen RT-25°C/+23°C at applied freezing and thawing temperature cycle of -25°C and +23°C, respectively under the applied vertical pressure of 20 kPa and horizontal pressure of 14 kPa.

Figure 5.22 shows the numerical mesh used for the unreinforced silt specimen. As in the case of the clay specimens, the soil has been modelled with continuum elements. The bottom boundary of the specimen is fixed in both the vertical and horizontal directions. The left side boundary is simulated with roller allowing vertical movement only and right side boundary is free to move in both directions.

5.5.1 Model Parameters

The mechanical properties of the silt soil were determined from laboratory tests as described in Chapter 3. Table 5.7 represents the mechanical properties of the silt used in the numerical modelling. No test was conducted to determine the thermal properties of the silt. These were selected from published data and empirical formulas.

The thermal conductivity of silt was determined using Kersten's (1949) empirical formula for the frozen state as follows:

For frozen fine grained soils:

$$k = (0.0833)\left[0.01\left(10^{0.022\gamma_d}\right) + 0.085\left(10^{0.008\gamma_d}\right)(w)\right] \quad (5.2)$$

where, k = thermal conductivity of soil (BTU/hr. ft^2. °F/ft)

w = soil moisture content (%)

γ_d = soil dry density (lb/ft^3)

Kersten (1949) conducted thermal conductivity tests on frozen fine grained soils (silt and clay). Five different silt and clay soils were tested for soil moisture contents of 7% or higher. Based on his test results, the empirical formula (Equation 5.2) for thermal conductivity was developed. To be consistent with the use of SI units, the unit of thermal conductivity BTU/hr.ft^2.°F/ft was converted into W/m°C by dividing the value of thermal conductivity by 0.5714 (TEMP/W Manual 2004).

The specific heat capacity of the silt was estimated using the following equation, where the air component has been neglected (Johnston *et al.* 1981, Andersland and Branko 2004):

$$C = C_s + C_w w_u + C_i w_f \quad (5.3)$$

where,

C = Specific heat capacity of soil (J/kg °C)

C_s = specific heat capacity of soil particle (J/kg °C)

C_w = specific heat capacity of water (J/kg °C)

C_i = specific heat capacity of ice (J/kg °C)

w_u = unfrozen water content expressed in % of dry unit weight of soil, and

w_f = frozen water content expressed in % of dry unit weight of soil.

Table 5.7 Mechanical and thermal properties of silt

Mechanical Properties of Soil	
Wet density, ρ_{wet} (kg/m^3)	2050
Dry unit weight, γ_{dry} (kN/m^3)	18.25
Bulk modulus, K (MPa)	15.25
Shear modulus, G (MPa)	7
Friction angle, ϕ (degree)	31
Cohesion, c (Pa)	100
Thermal Properties of Soil	
Specific heat capacity, C (J/kg°C)	1000
Thermal conductivity, k (W/m°C)	2.0
Coefficient of thermal expansion, α (/°C)	5 x 10^{-5}

Table 5.7 also summarizes the thermal properties of the silt. The coefficient of thermal expansion of the frozen soil has been assumed in this study to fit the displacement measured in the unreinforced laboratory test specimen. It is within the range of the reported properties of similar soils found in the literature. The value is less than the coefficient of thermal expansion of ice and greater than coefficient of thermal expansion of saturated sand as indicated by Andersland and Branko (2004).

5.5.2 Numerical Modelling: Processes and Results

Numerical simulation of an unreinforced silt specimen at temperatures -25°C and +23°C began with determining the initial stress state in the soil specimen. Initial stresses in the specimen at its compacted condition were determined by gravity loading (locked-in stresses). Compaction increases the lateral earth pressure in the fill that are higher than normal at-rest values (Duncan *et al.* 1991). In case of sand-like material (non plastic sandy silt in my study), compaction induced horizontal pressures do not change appreciably with time unless the wall on which they act moves towards or away from the backfill (Carder *et al.* 1977). Duncan *et al.* (1991) presented charts to estimate the compaction induced horizontal pressure in the backfill soils. From this work a higher value of horizontal stress (1.5 times of gravity stress) was estimated in the initial stress analysis of the unreinforced silt specimen UT-25°C/+23°C. Then, the vertical pressure (σ_y = 20 kPa) and horizontal pressure (σ_x = 14 kPa) were applied in increments on the top and right side boundary of the specimen, respectively,

after which the model was cycled to equilibrium. Displacements determined in the mechanical loading condition were set to zero before invoking the thermal model simulating for freezing. At the end of mechanical loading simulation, thermal-mechanical coupling was simulated using the thermal model (isotropic heat conduction) and Mohr-Coulomb model. Both are built-in models in FLAC. The model parameters that were used are given in Table 5.7.

Freezing-thawing cycles in the laboratory were simulated by applying 17 hrs of freezing and 19 hrs of thawing time. During the freezing, the temperatures applied to the soil specimen were as follows: -25°C at top surface of the model, -20°C at bottom surface of the model and -25°C to -20°C (linearly varied) top to bottom along the right side of the model. During the thawing, the applied temperatures were as follows: 23°C at the top surface of the model, 15°C at the bottom surface of the model and 23°C to 15°C (linearly varied) top to bottom along the right side of the model.

The temperatures applied at the different boundaries were carefully selected based on the possible temperatures that may have been experienced at each boundary. During the laboratory testing, insulation was provided through Styrofoam placed at the bottom of the testing box. It was found that complete insulation could not be achieved at the bottom. To account for the inefficiency of insulation used in the experiment, the applied temperature at the bottom of the soil model has been reduced in the numerical simulations. It was assumed that

the temperature varied linearly from top to bottom along the right side of the soil model. In the initial freezing, the soil temperature in the laboratory specimen was above sub-zero until 12 hrs. That is why the first 12 hrs of freezing was simulated in the numerical model without a thermal expansion coefficient (i.e., no deformation in the soil sample due to temperature change above 0°C). The thermal-mechanical coupling was only invoked thereafter. Laboratory test results presented in Chapter 4 showed that the horizontal displacements were constant during thawing. It was apparent that the thawing time (19 hrs) was too short to induce consolidation or compression in the laboratory specimen. To simulate the no deformation effect during thawing, only the thermal model was simulated, without mechanical coupling for thawing cycles. Numerically predicted temperatures and deformations of unreinforced and reinforced silt specimens during freezing-thawing cycles are summarized in Table 5.8 and will be discussed in the following sub-sections.

Unreinforced silt specimen (UT-25°C/+23°C)

Figure 5.23 shows temperature contours in the unreinforced silt specimen during first freezing. The soil temperatures vary from -8°C at the outer portion to -1°C at the inner portion of the unreinforced silt specimen. Numerically predicted temperatures are close to the laboratory measured values (-8°C at the outer portion and 0°C at the inner portion). Figure 5.24 shows freezing-induced displacement vectors that indicate expansion both vertically and laterally. Figures 5.25 and 5.26 are corresponding freezing-induced displacement contours in the

horizontal and vertical directions, respectively. The silt specimen expands horizontally by 0.3 mm and vertically by 0.25 mm.

Comparing these results with the laboratory measured values (refer Table 5.9), numerical analysis under predicted the measured horizontal displacement (0.6 mm) while slightly over predicting the measured vertical displacement (0.2 mm).

Table 5.8 Numerically predicted temperatures and deformations of reinforced and unreinforced silt specimens during freezing-thawing cycles

Test specimen	Temperatures (° C)			Displacement (mm)			
	First freezing-thawing cycle		Third freezing cycle	First freezing cycle		Third freezing cycle	
	Freezing	Thawing		δ_x	δ_y	δ_x	δ_y
UT-25°C/+23°C	- 8 (out)*	13 (out)	- 13 (out)	0.3	0.25	0.8	0.7
	- 1 (in)*	8 (in)	- 6 (in)				
RT-25°C/+23°C	- 8 (out)	14 (out)	- 13 (out)	0.25	0.25	0.8	0.7
	- 1 (in)	8 (in)	- 6 (in)				

Note: ' * ' out = outer portion of soil specimen, in = inner portion of soil specimen

Figure 5.27 shows the temperature contours during the first thawing. The soil temperatures vary from 13°C at the outside to 8°C at the inside. Numerical predictions are again close to the laboratory measured values (see Table 5.9).

Table 5.9 Laboratory measured average temperatures and deformations of plane-strain test specimens during freezing-thawing cycles of silt

Test specimen	Temperatures (° C)			Displacement (mm)			
	First freezing-thawing cycle		Third freezing cycle	First freezing cycle		Third freezing cycle	
	Freezing	Thawing		δ_x	δ_y	δ_x	δ_y
UT-25°C/+23°C	- 8 (out)*	10.5 (out)	- 12 (out)	0.6	0.2	1.1	0.25
	0 (in)*	8 (in)	- 4 (in)				
RT-25°C/+23°C	- 8 (out)	10 (out)	- 12 (out)	0.45	0.3	0.95	0.35
	0 (in)	6 (in)	- 4 (in)				

Note: ' * ' out = outer portion of soil specimen, in = inner portion of soil specimen

Freezing-thawing numerical simulations were also performed for subsequent cycles. Figure 5.28 shows the temperature contours in the soil sample during the third freezing cycle. Soil temperatures (refer Table 5.8) are comparable to the measured soil temperatures at the end of the third freezing cycle in the laboratory sample (see Table 5.9). Figures 5.29 and 5.30 show corresponding soil displacement contours in the horizontal and vertical directions respectively at the end of the third freezing cycle. The numerically predicted maximum horizontal and vertical displacements are 0.8 mm and 0.7 mm respectively. Comparing these results with the laboratory measured values (refer Table 5.9), the

numerical analysis under predicted the measured horizontal displacement (1.1 mm) while over predicting the measured vertical displacement (0.25 mm).

Reinforced silt specimen (RT-25°C/+23°C)

Numerical simulations were carried out for the geogrid-reinforced silt specimen to determine soil deformations and induced strains in the geogrid due to freezing. Numerical predictions and laboratory measured results were then compared. Figure 5.31 shows the numerical mesh used for FLAC.

Table 5.10 summarizes the input properties used to simulate the geogrid as cable elements in the numerical analysis. The silt-geogrid interface angle was estimated two-third of the silt friction angle. There was no attempt to use different stiffness of reinforcements between room and freezing temperatures. It should be noted that cold temperatures increases the stiffness of geogrid reinforcements. The rest of the modelling procedures were the same as those in the unreinforced specimen to simulate mechanical loading followed by freezing-thawing cycles. Similar to the unreinforced silt specimen, the thermal effect during thawing has not been coupled with the mechanical model in the geogrid-reinforced silt specimen. The laboratory measured deformations were constant during the thawing period.

Table 5.10 Geogrid reinforcement and silt-geogrid interface properties

E (MPa)	yield (kN)	ycomp (kN)	A (m^2)	peri (m)	K_b (kN/m/m)	S_b (kN/m)	δ (^{o})
100.0	14.0	3.3	0.003	2.0	$2.5e^4$	10	21

Figure 5.32 shows temperature contours in the reinforced silt specimen due to first freezing cycle. The soil temperatures are below sub-zero and vary from -8°C to -1°C from the outer to inner surface of the geogrid-reinforced silt specimen. Numerically predicted temperatures are close to the laboratory measured values (compare the values associated with contour colours and those in Table 5.9). As expected, there is no difference in soil temperatures with and without geogrid reinforcement. Figures 5.33 and 5.34 are corresponding freezing-induced displacement contours of the reinforced silt specimen in the horizontal and vertical directions, respectively. The reinforced silt specimen expands horizontally by 0.25 mm and vertically by 0.25 mm. Numerical predictions slightly underestimate the laboratory measured values (refer again to Table 5.9). In comparing the numerical results for the reinforced and unreinforced silt, the geogrid reduced the horizontal expansion only in the middle area of specimen (where the geogrid was placed) by about 5%. Vertical strains are the same in reinforced and unreinforced silt specimens.

Figures 5.35 and 5.36 show the axial force and strain induced in the geogrid due to the first freezing cycle. The geogrid axial force and strain values shown in the

figures are the combination of mechanical loading and first cycle of freezing. About 0.008% of geogrid strain was predicted due to first freezing only. The numerically predicted geogrid strain is lower than the measured geogrid strain (0.03%) during the first freezing of geogrid-reinforced silt specimen in the laboratory test (compare with Figure 4.45).

Figure 5.37 shows temperature contours in the reinforced silt specimen during first thawing cycle. The soil temperatures vary from 14°C at the outside surface to 8°C at inside. Numerical predictions are reasonably close to the laboratory measured values (see Table 5.9).

Figure 5.38 shows the temperature contours in the soil sample during the third freezing cycle. Soil temperatures (refer Table 5.8) are comparable to those measured at the end of the third freezing cycle(refer Table 5.9). Figures 5.39 and 5.40 show corresponding soil displacement contours in the horizontal and vertical directions respectively at the end of the third freezing cycle. The predicted maximum horizontal and vertical displacements of the reinforced silt specimen are 0.8 mm and 0.7 mm respectively at the end of the third freezing cycle. Comparing these results with the laboratory measured values (refer Table 5.9), the numerical predictions can be considered satisfactory.

Figures 5.41 and 5.42 show the numerically predicted axial force and strain induced in the geogrid during the third freezing cycle. The maximum value of the

geogrid strain is about 0.2% from the numerical prediction and corresponding laboratory measured geogrid strain is about 0.1%. Numerically predicted geogrid strains are also smaller than the 2% strain used for estimating the elastic modulus. Overall, the results from numerical analysis are in satisfactory agreement with the experimental results. The model can then be used for parametric studies of silt backfill geogrid-reinforced engineered embankment slopes which will be subjected to freezing.

5.6 SUMMARY

The main points covered in this chapter are summarised as follows:

1) The BBM and Swell model have been coded in FLAC to develop the numerical models. The BBM simulates the effects of mechanical loading (gravity load and externally applied load if any) in swelling clay at constant suction. The Swell model simulates the swelling of clays upon wetting. The numerical simulation based on BBM has been verified with published data and experimental results.
2) The models were verified with the results from laboratory tests. Unreinforced clay specimens were simulated for mechanical loading by BBM, and for wetting by the Swell model. The soil materials were simulated with continuum elements in the numerical model. Experimentally measured and numerically predicted displacements of the unreinforced clay specimens showed fairly good agreement both in mechanical and wetting conditions. This shows that both BBM and Swell

models can reasonably be applied for numerical analysis of actual structures.

3) Geogrid reinforcements were modelled as cable elements. The soil-geogrid interface behaviour was modelled by using the cable grout utility in the FLAC program. Numerically predicted soil displacements and geogrid strains are again fairly comparable with the laboratory measured values.

4) Freezing effects in the laboratory plane-strain tests of silt specimens were analysed using FLAC built-in isotropic thermal-mechanical models. The focus of the analysis was on thermal-mechanical responses during freezing. Conduction was assumed to be the model of heat transfer and water was not accounted for explicitly. There was no attempt to simulate the movement of water within the specimen as the freezing front moves from the top towards the bottom of the specimen. The soil was assumed to freeze at 0°C, and thermal analysis was used to separate between frozen and unfrozen soil regions. The thermal model was coupled with the mechanical model to determine thermal induced stresses and displacements in the soil during freezing. Unreinforced silt specimens were first analysed for three cycles of freezing. Comparison of experimentally measured and numerically predicted temperatures and displacements in the unreinforced silt specimens showed reasonable agreement.

5) Thermal-mechanical models were used to simulate freezing in the geogrid-reinforced silt specimen. The geogrid reinforcements were again modelled as cable elements, while the soil was modelled by continuum elements. Numerically predicted soil temperatures, displacements and geogrid strains are fairly comparable with the laboratory measured values.

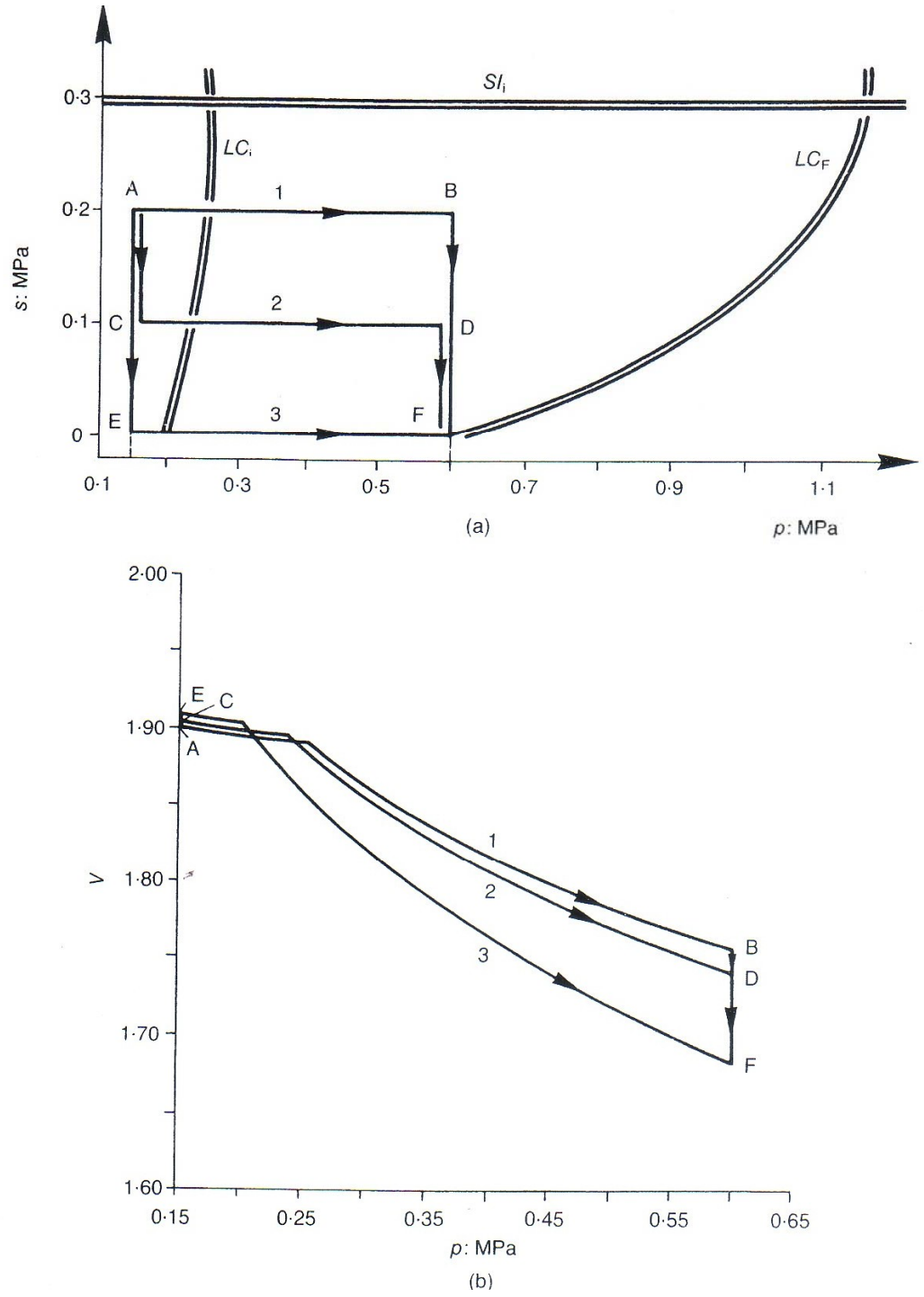

Figure 5.1 Response of Barcelona Basic Model to increments of net mean stress (p) and decreasing suction (wetting): (a) stress paths; (b) specific volume-net mean stress relationships (Alonso *et al.* 1990 – reproduced with permission of Thomas Telford, February 27, 2009)

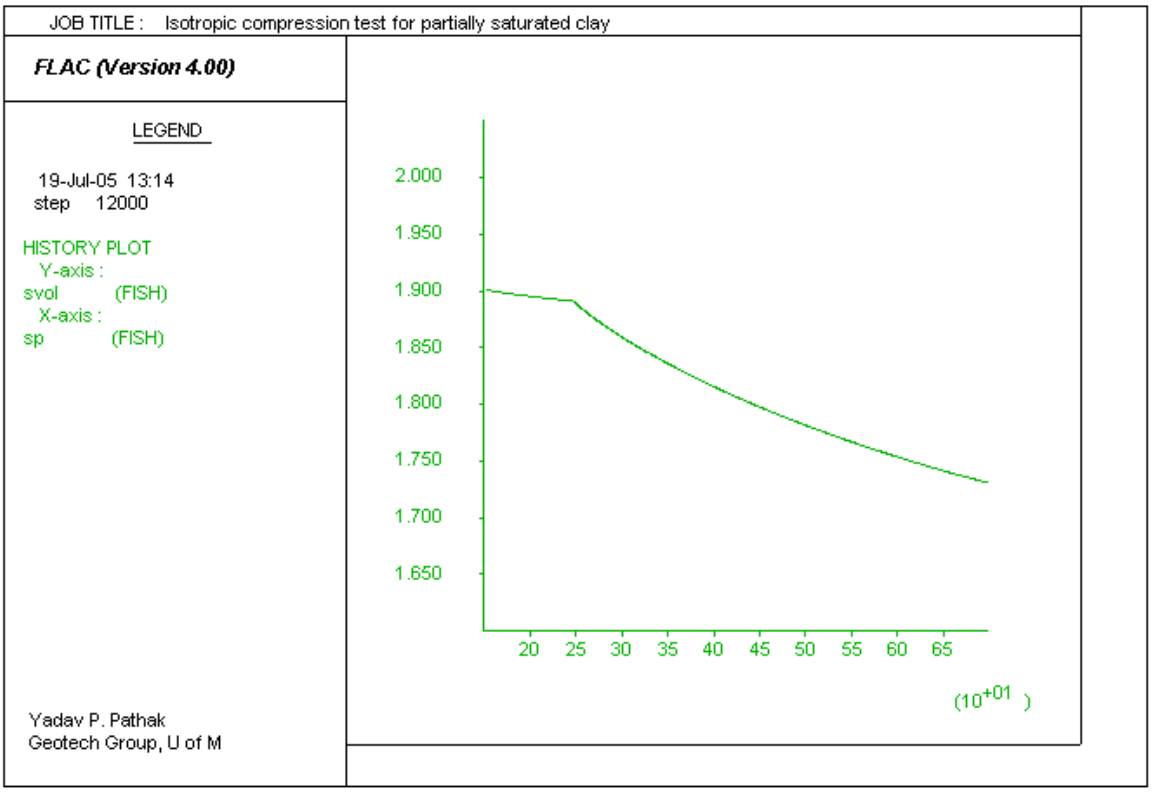

Figure 5.2 BBM prediction of specific volume (v) of the reference 'soil' (Alonso *et al.* 1990) sample versus net mean stress (p) in isotropic compression

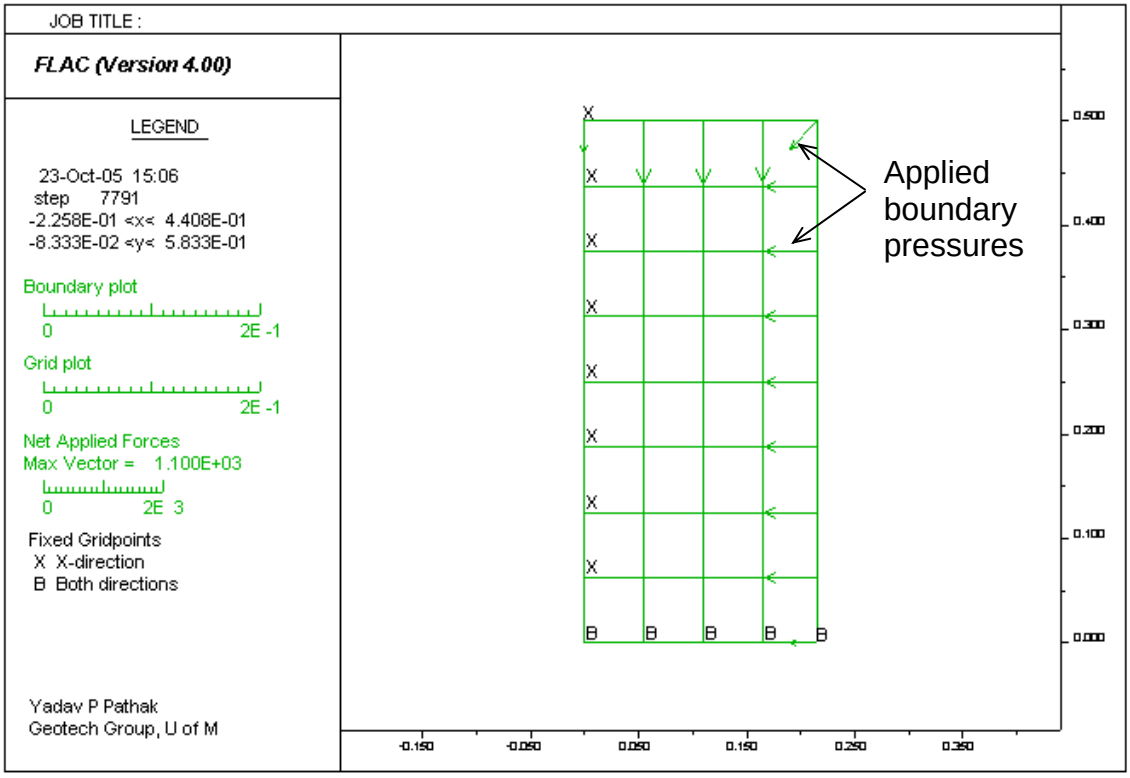

Figure 5.3 Numerical grid of unreinforced clay specimen

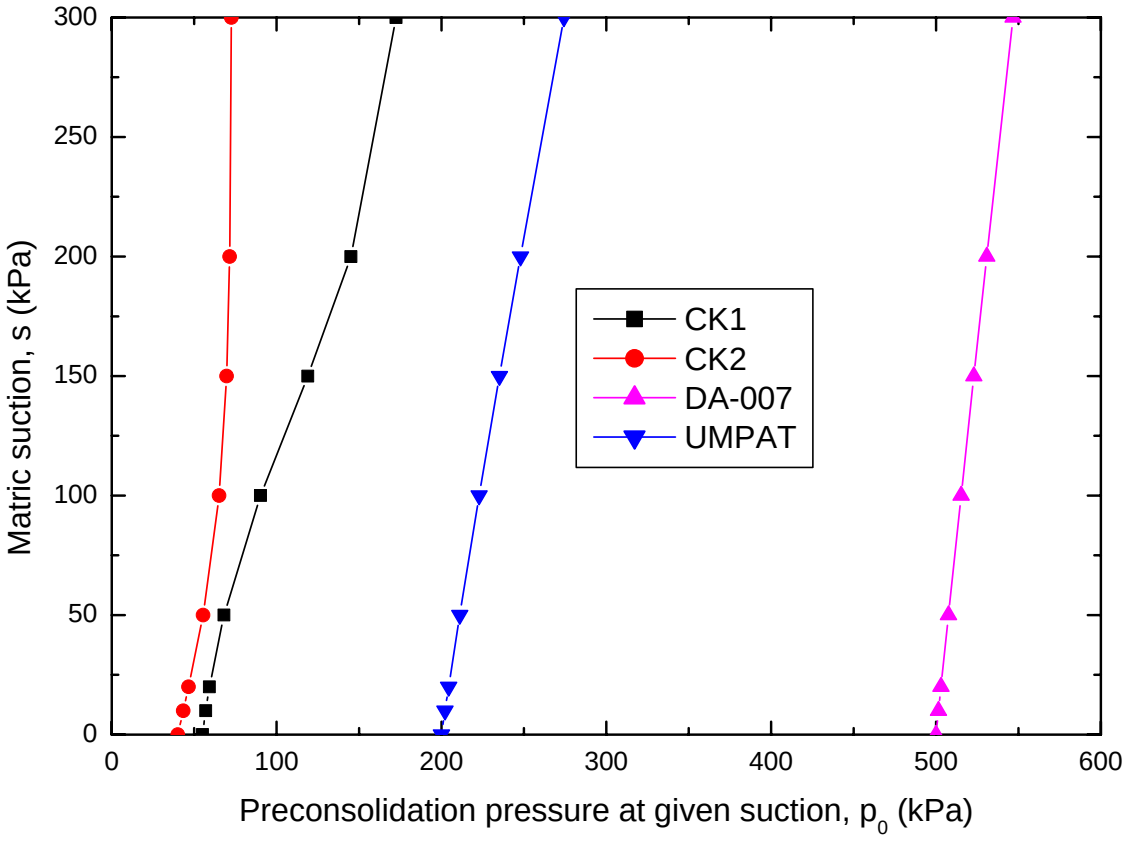

Figure 5.4 Preconsolidation pressure versus suction plot for different soils

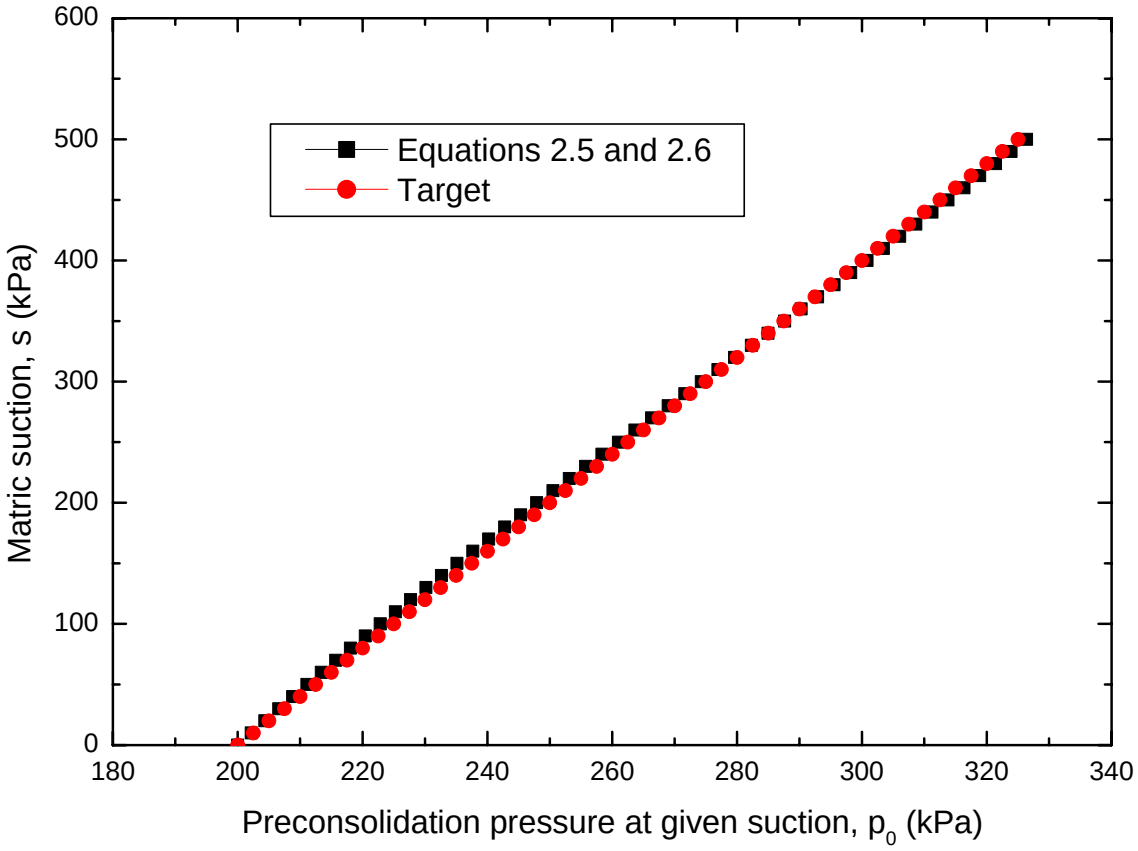

Figure 5.5 Preconsolidation pressure versus metric suction plot of UMPAT clay for estimation of r and β parameters

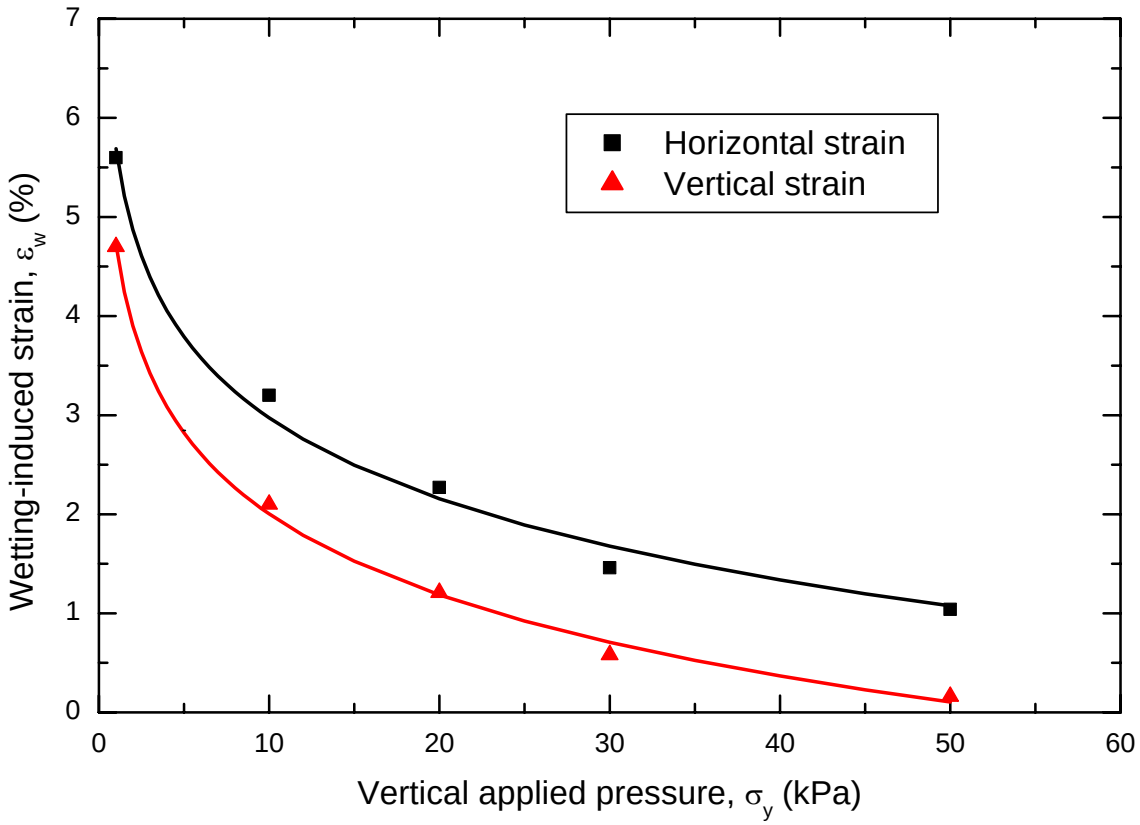

Figure 5.6 Wetting-induced strains and applied vertical pressure relationship from plane-strain test for UMPAT clay

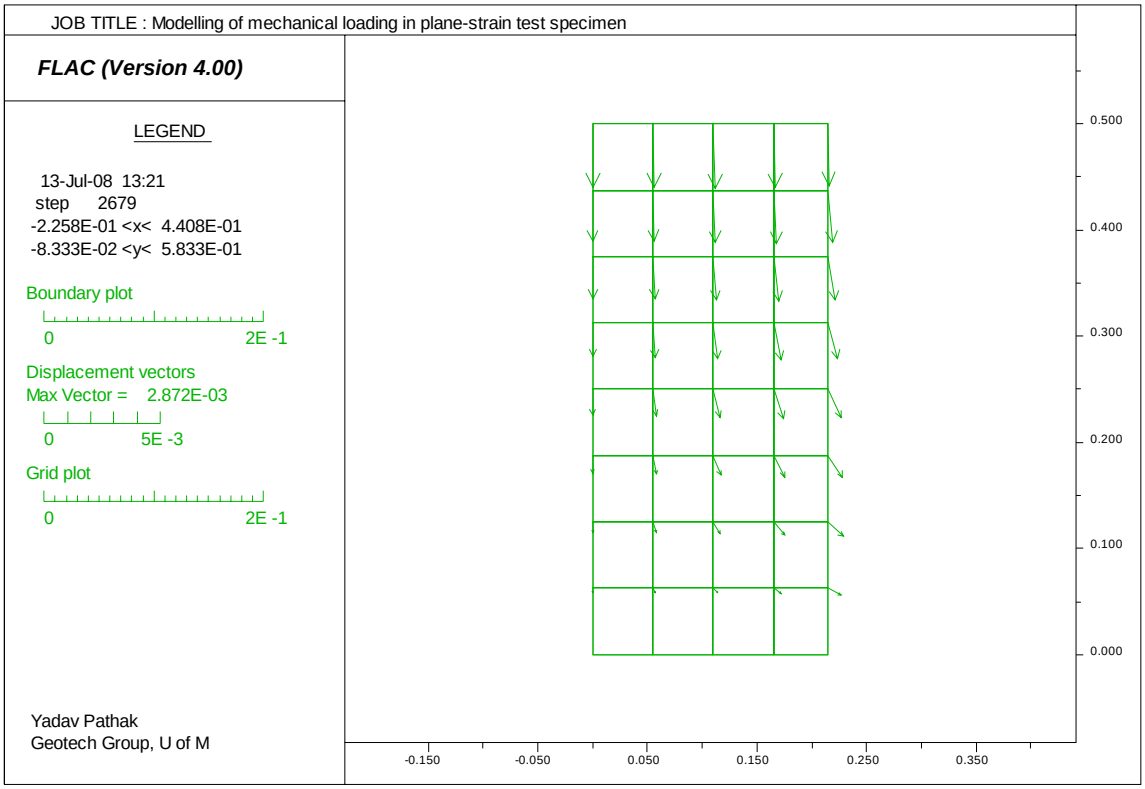

Figure 5.7 Displacement vectors in unreinforced clay specimen UP20/14 due to mechanical load

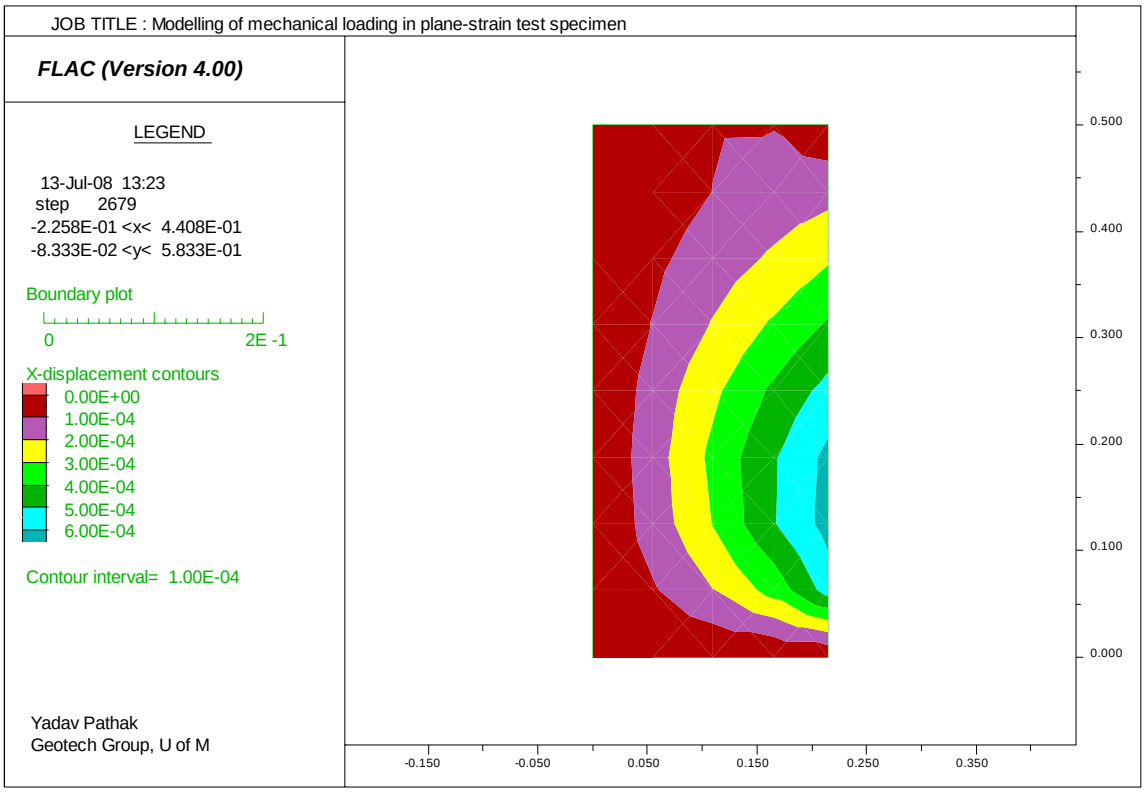

Figure 5.8 Horizontal displacement contours in unreinforced clay specimen UP20/14 due to mechanical load

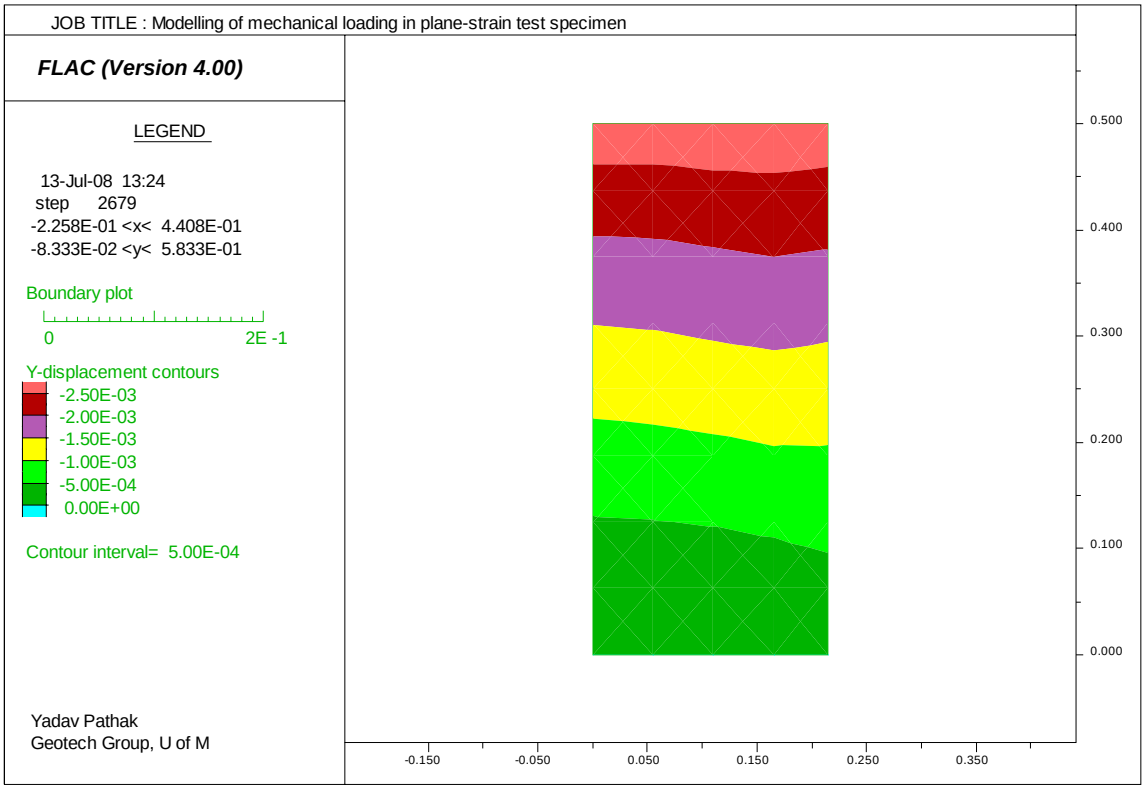

Figure 5.9 Vertical displacement contours in unreinforced clay specimen UP20/14 due to mechanical load

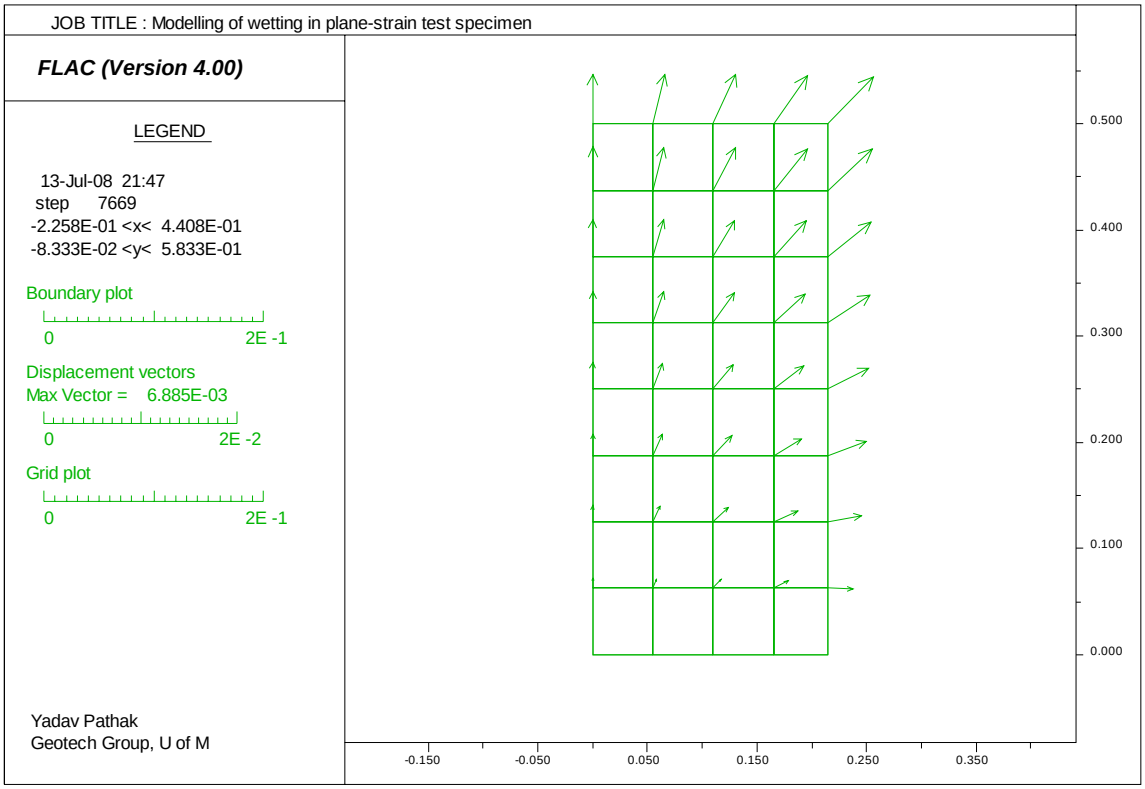

Figure 5.10 Wetting-induced displacement vectors in unreinforced clay specimen UP20/14

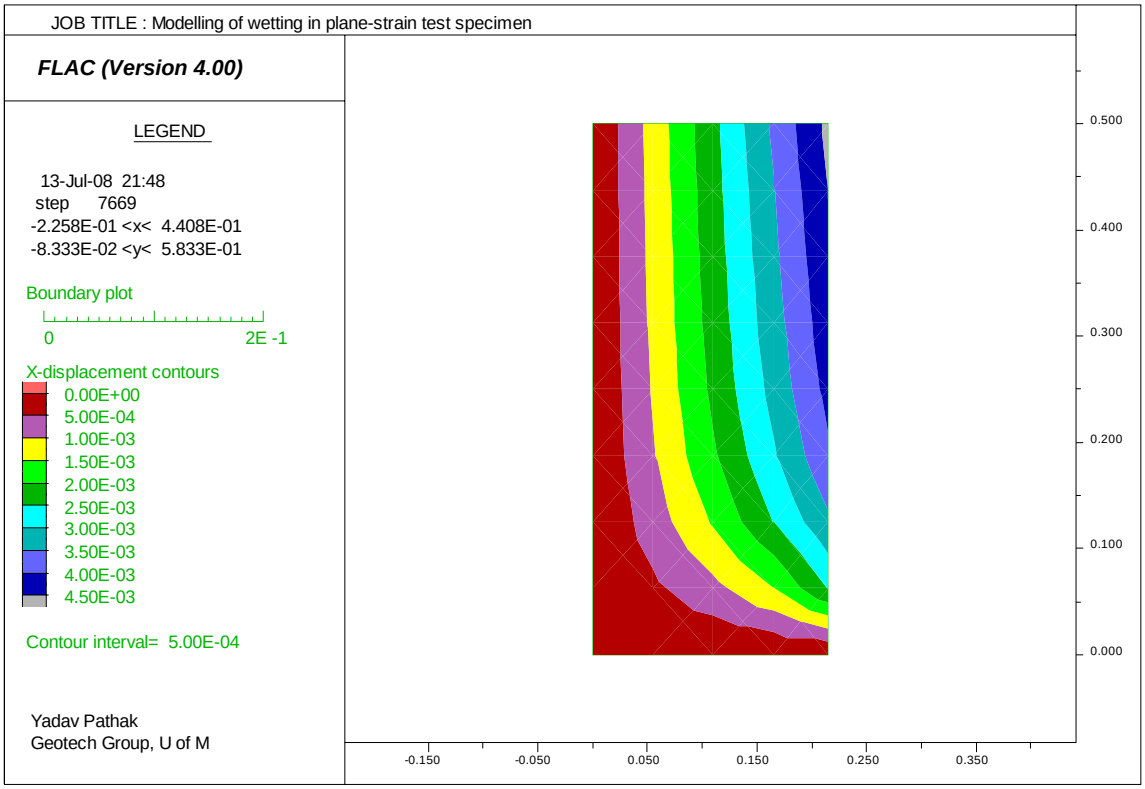

Figure 5.11 Wetting-induced horizontal displacement contours in unreinforced clay specimen UP20/14

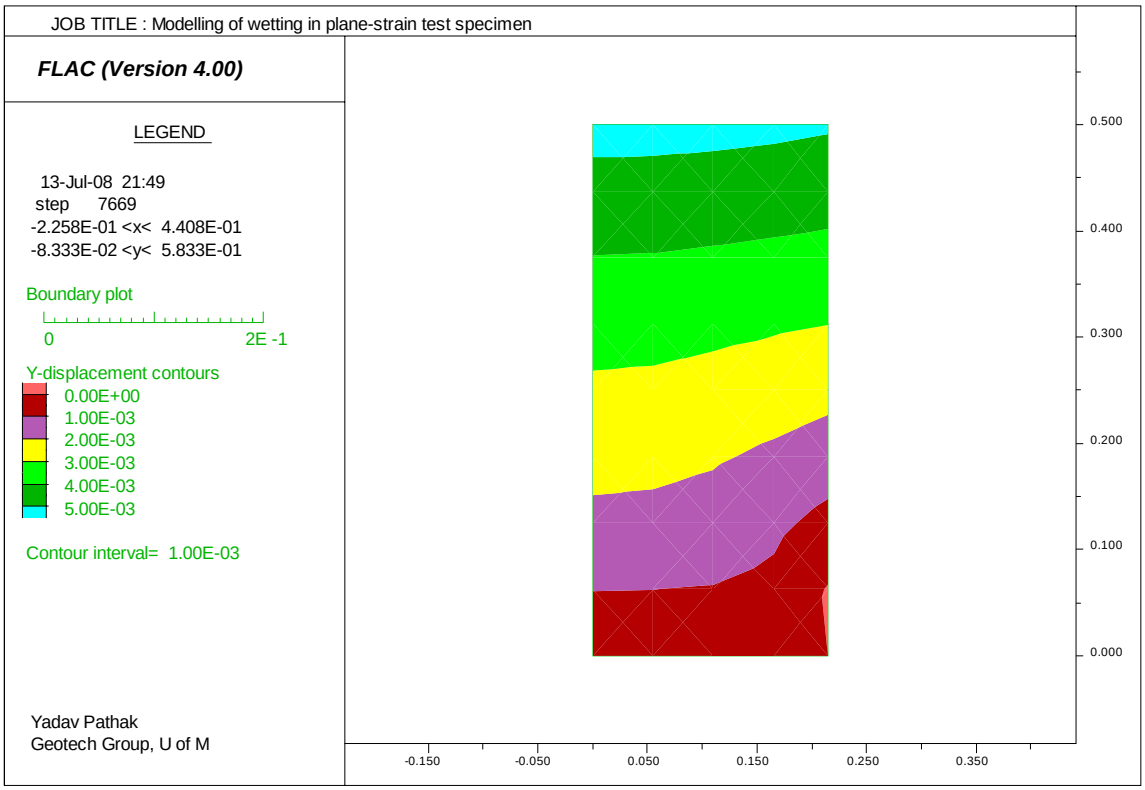

Figure 5.12 Wetting-induced vertical displacement contours in unreinforced clay specimen UP20/14

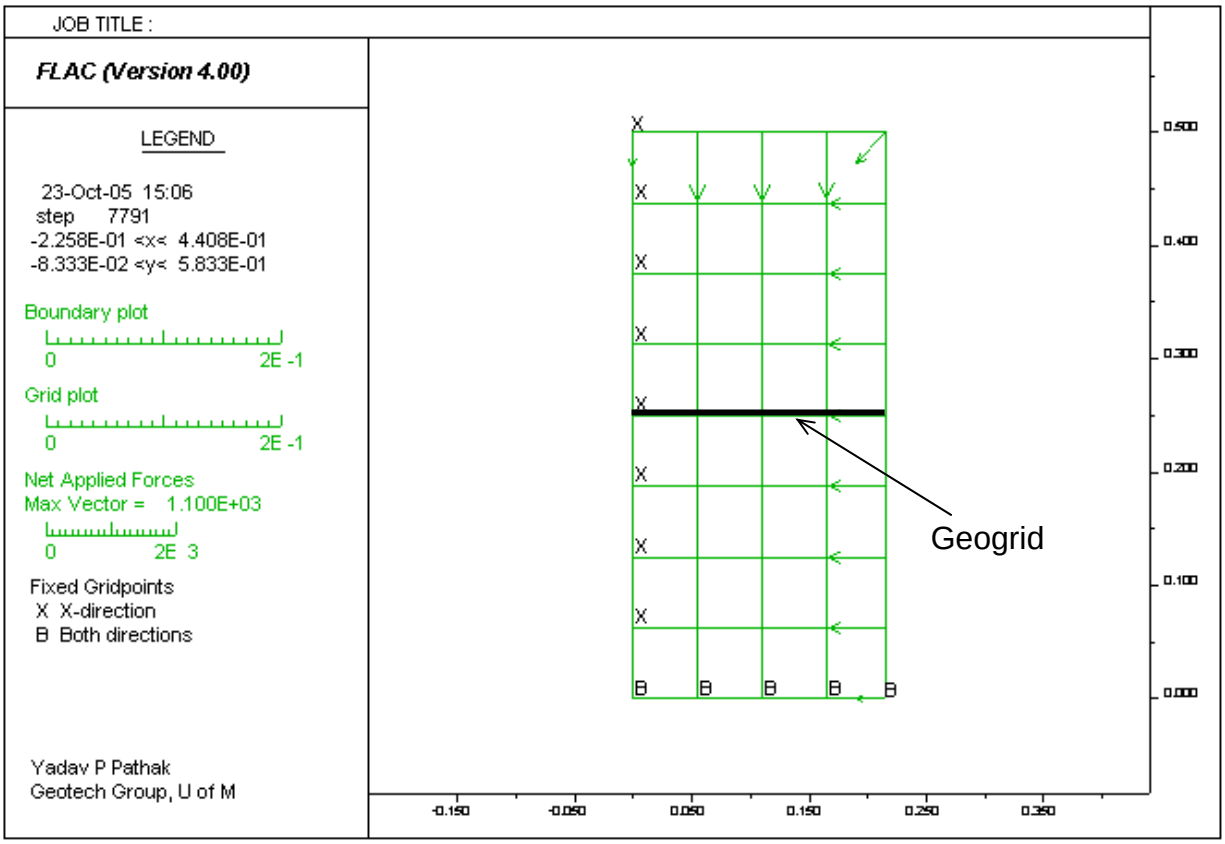

Figure 5.13 Numerical grid of geogrid-reinforced clay specimen

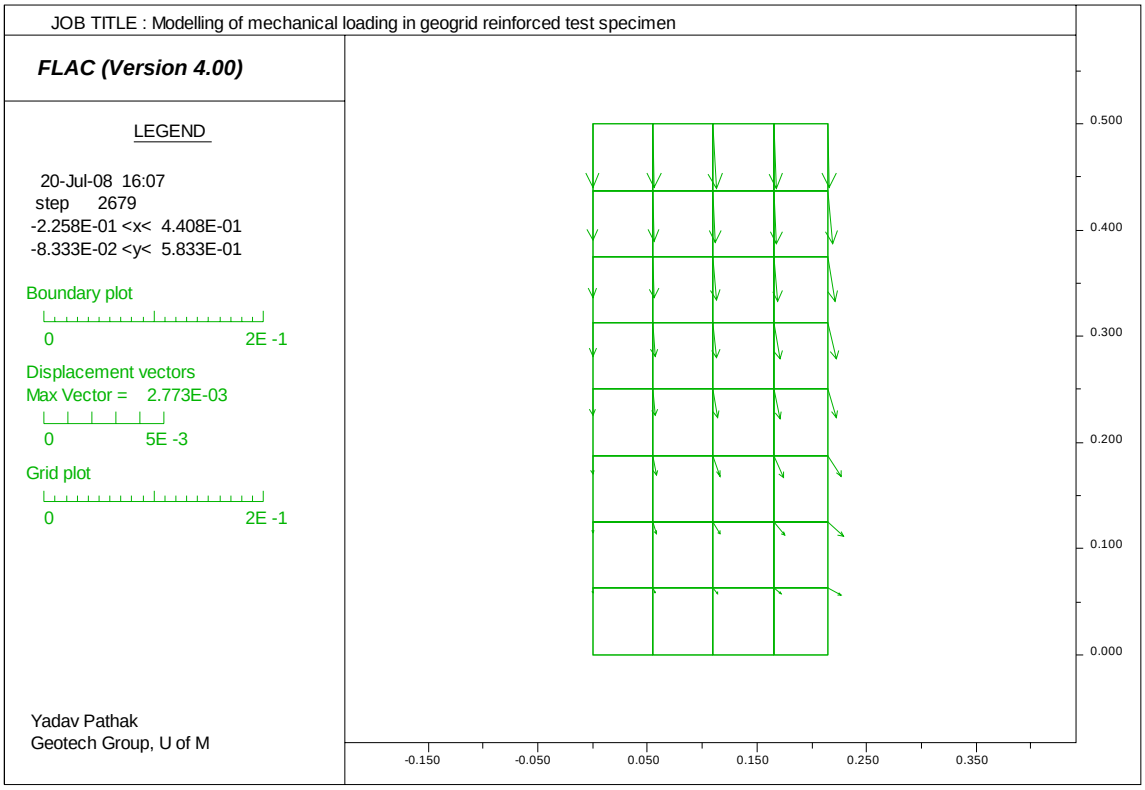

Figure 5.14 Displacement vectors in geogird-reinforced clay specimen RP20/14 due to mechanical load

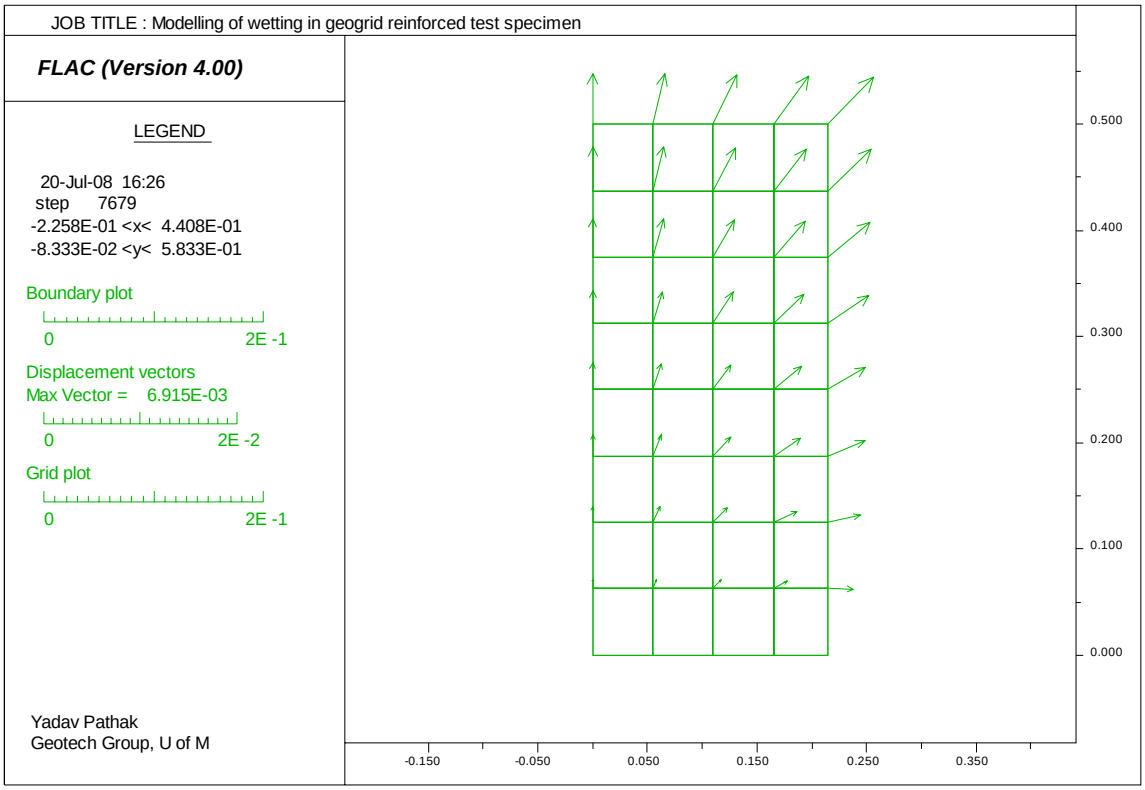

Figure 5.15 Wetting-induced displacement vectors in geogrid-reinforced clay specimen RP20/14

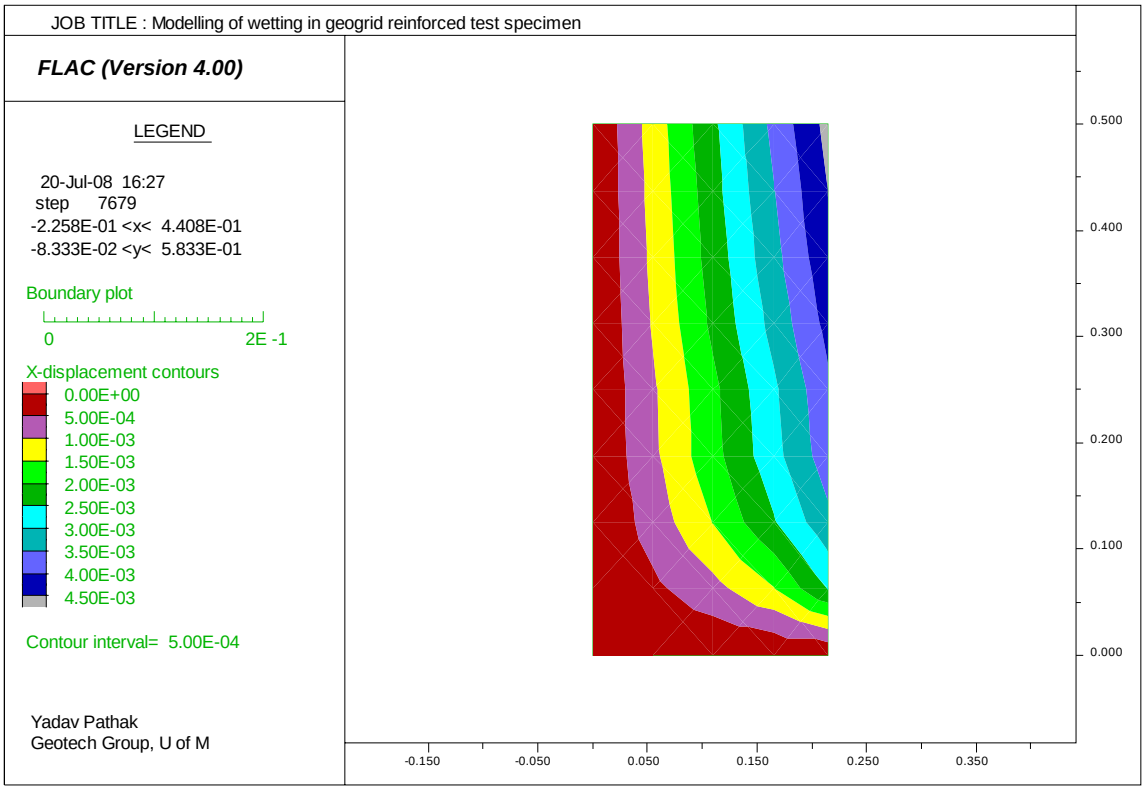

Figure 5.16 Wetting-induced horizontal displacement contours in geogrid-reinforced clay specimen RP20/14

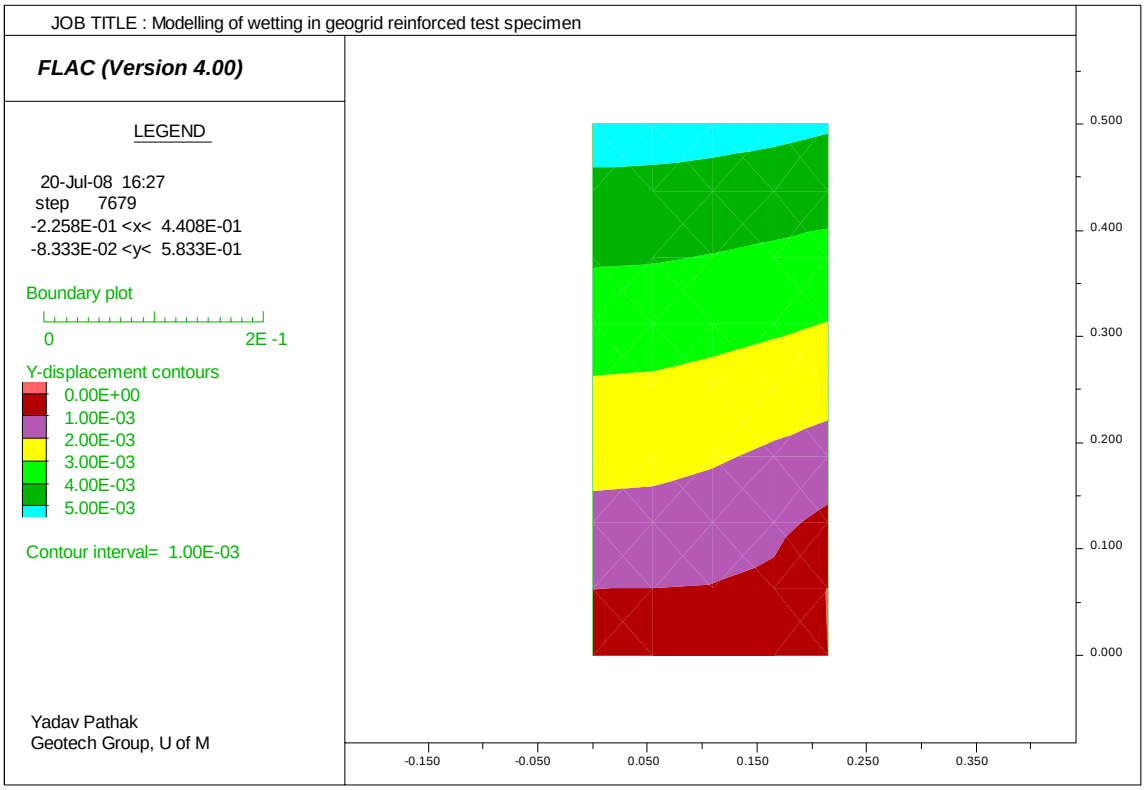

Figure 5.17 Wetting-induced vertical displacement contours in geogrid-reinforced clay specimen RP20/14

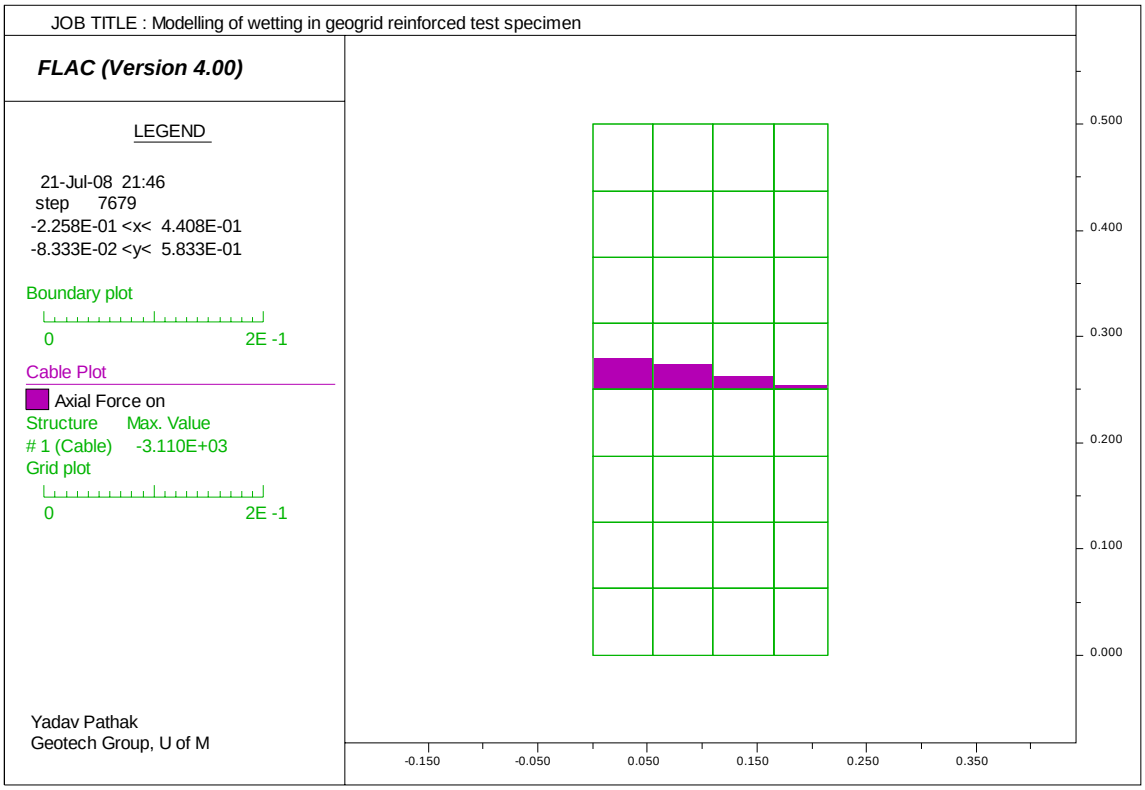

Figure 5.18 Axial force in geogrid after wetting of geogrid-reinforced clay specimen RP20/14

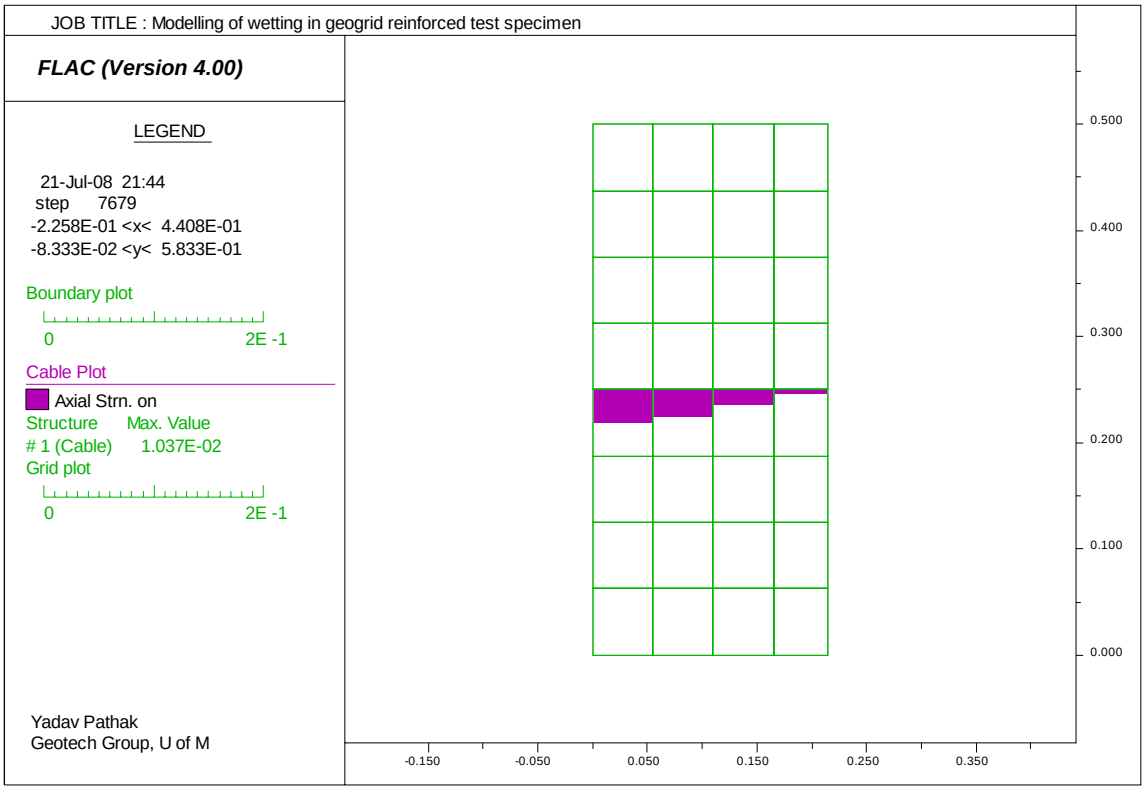

Figure 5.19 Axial strain in geogrid after wetting of geogrid-reinforced clay specimen RP20/14

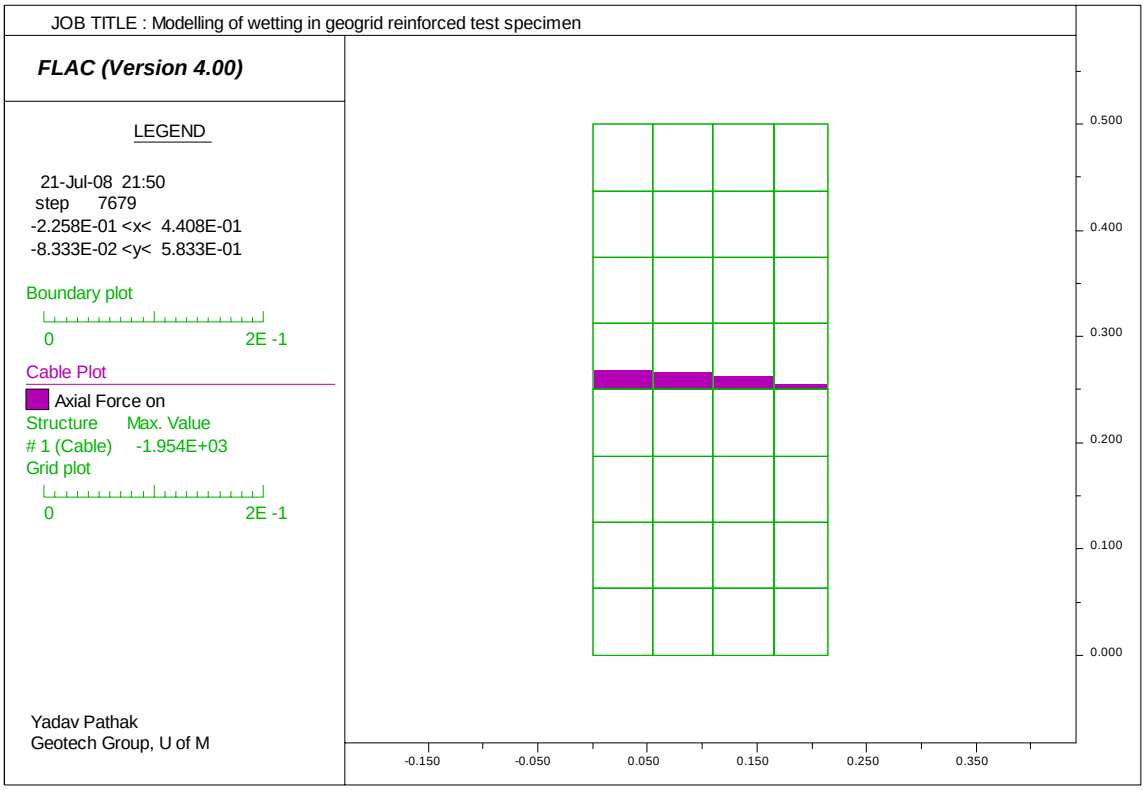

Figure 5.20 Axial force in geogrid after wetting of geogrid-reinforced clay specimen RP50/35

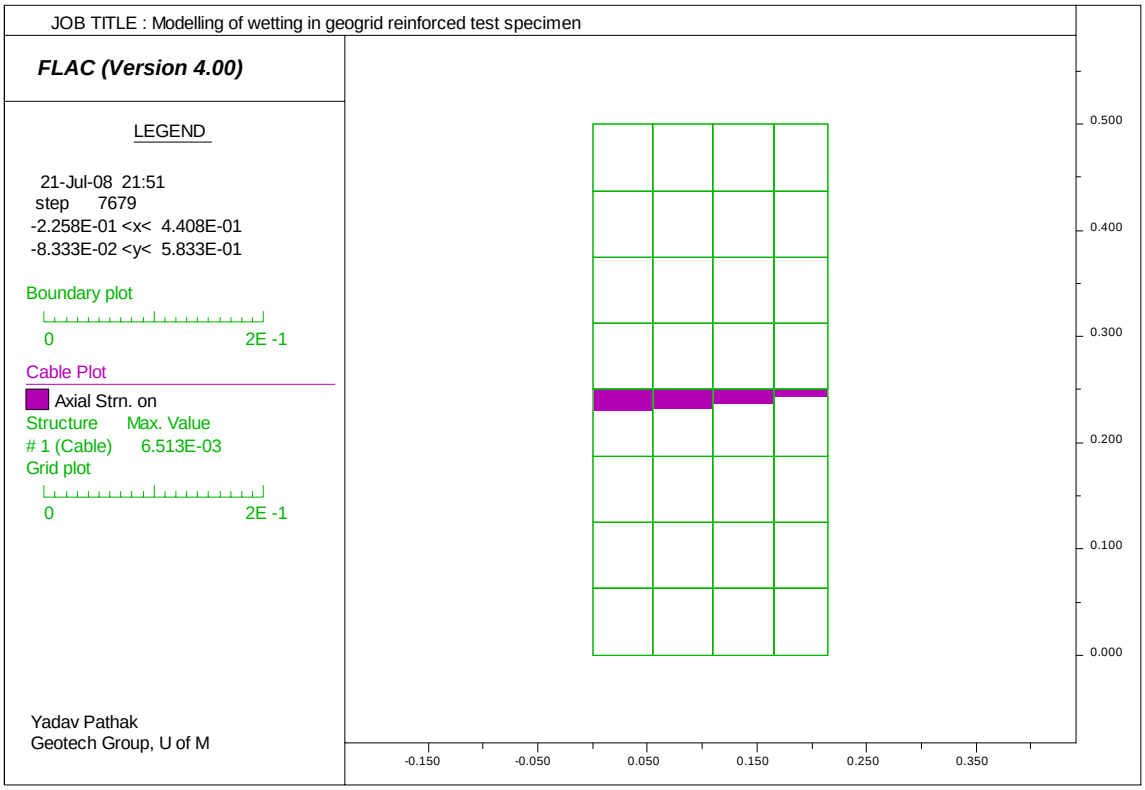

Figure 5.21 Axial strain in geogrid after wetting of geogrid-reinforced clay specimen RP50/35

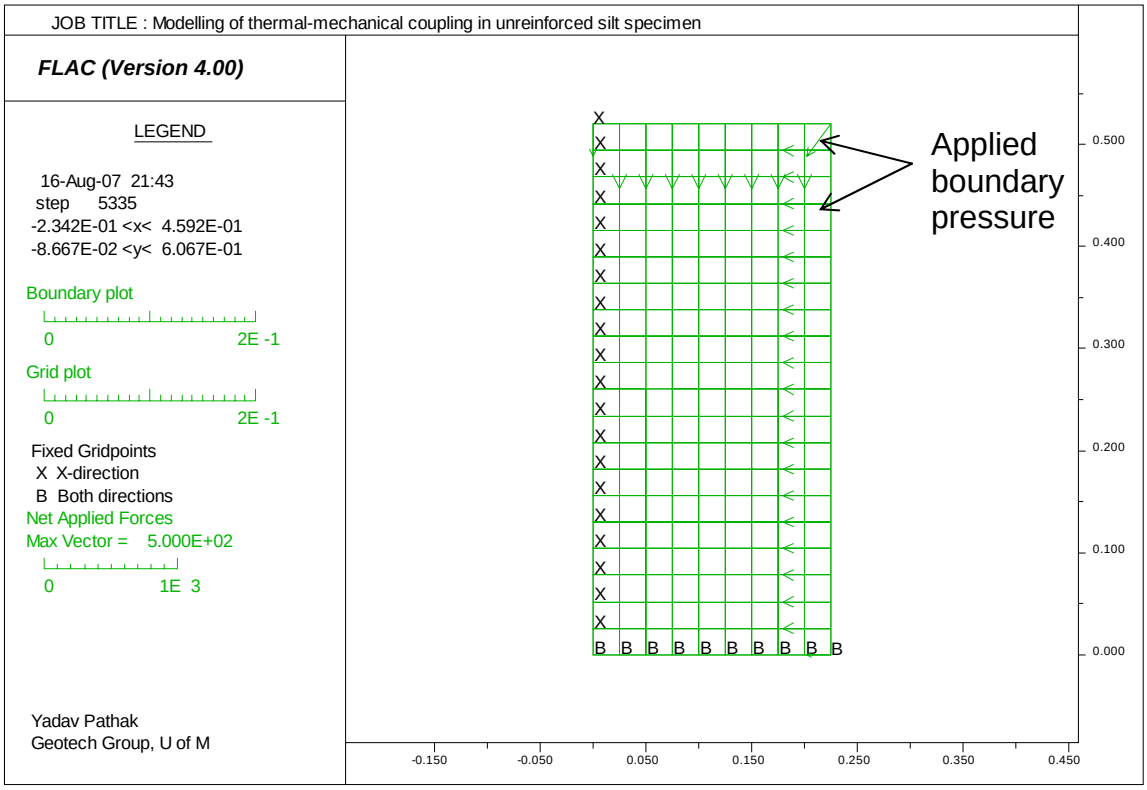

Figure 5.22 Numerical grid of unreinforced silt specimen UT-25°C/+23°C

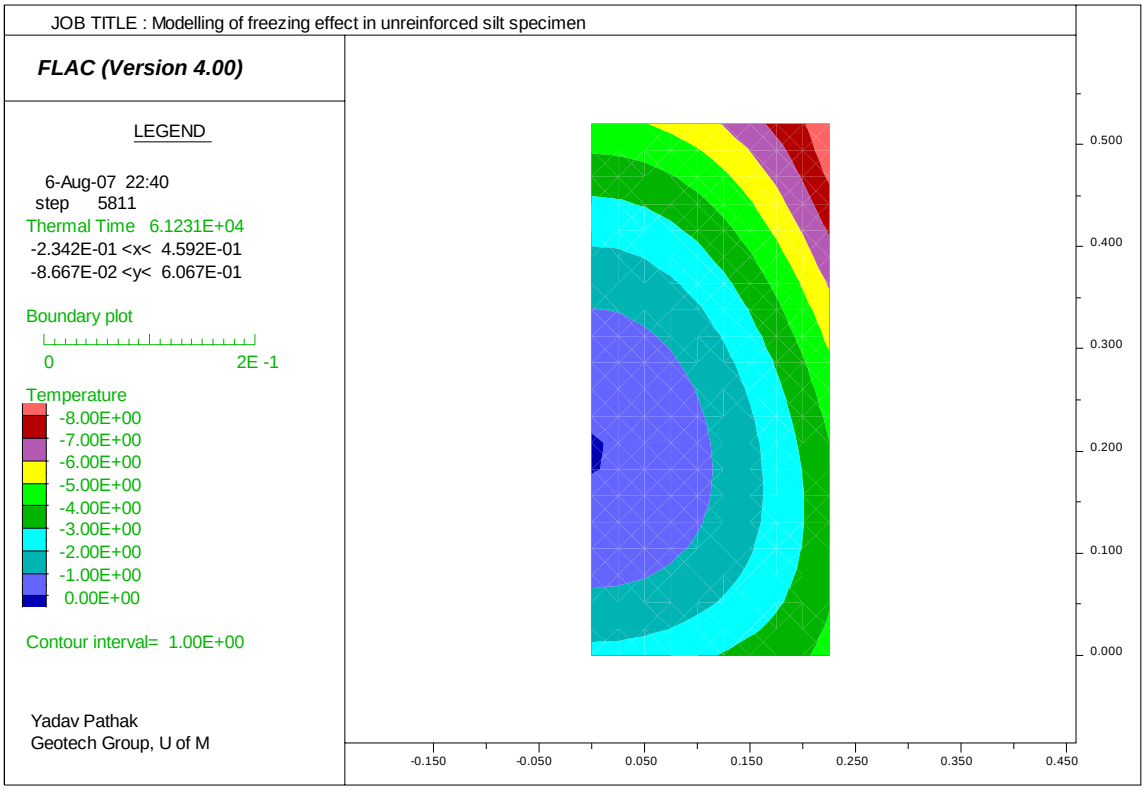

Figure 5.23 Temperature contours in unreinforced silt specimen UT-25°C/+23°C during first cycle of freezing

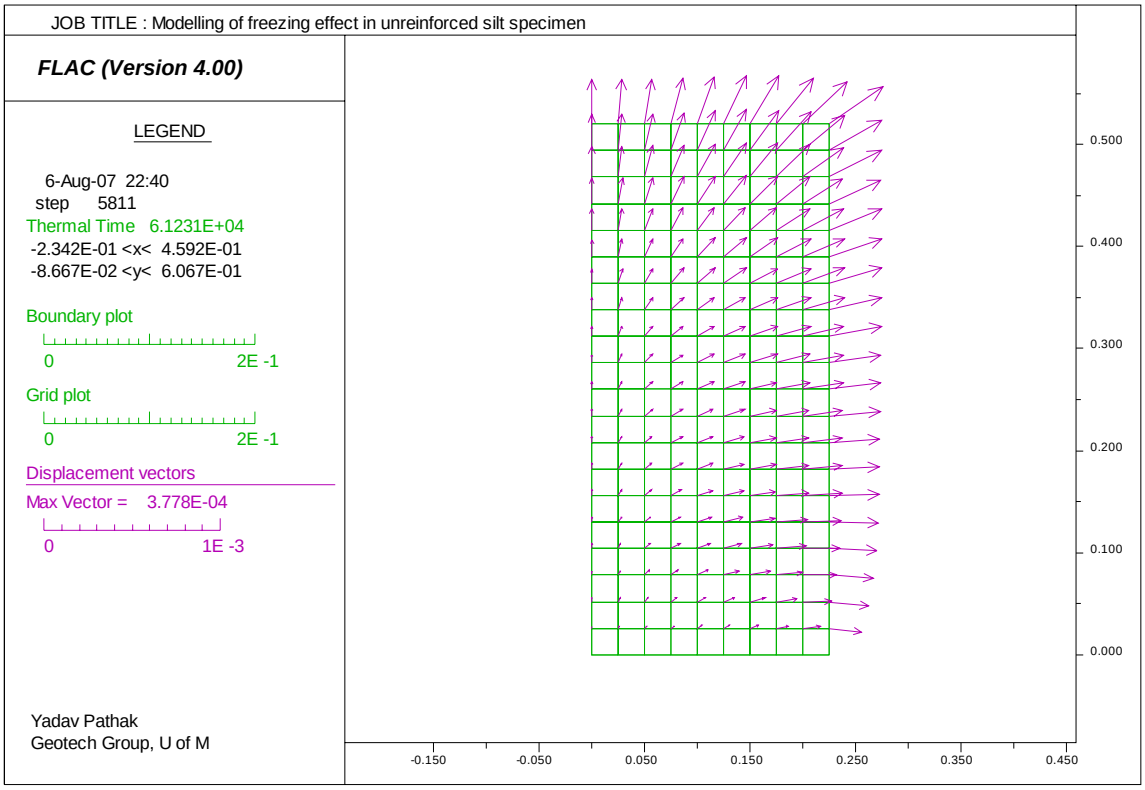

Figure 5.24 Displacement vectors in unreinforced silt specimen UT-25°C/+23°C during first cycle of freezing

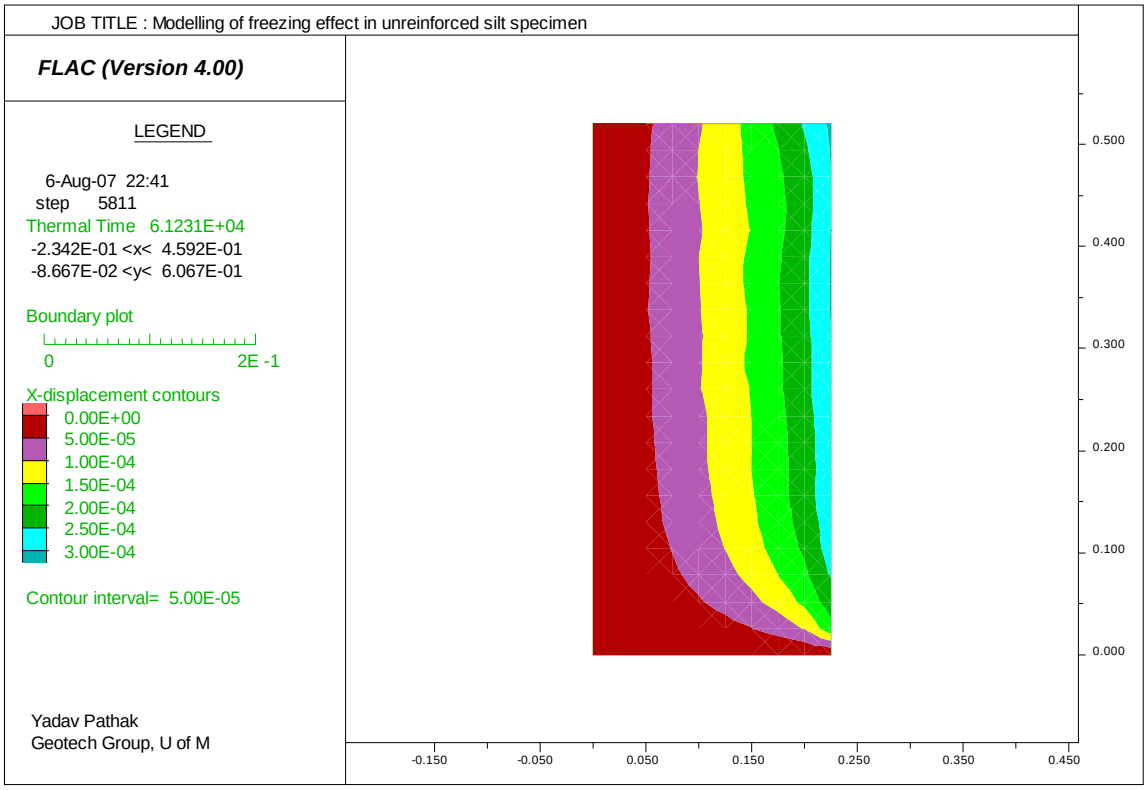

Figure 5.25 Horizontal displacement contours in unreinforced silt specimen UT-25°C/+23°C during first cycle of freezing

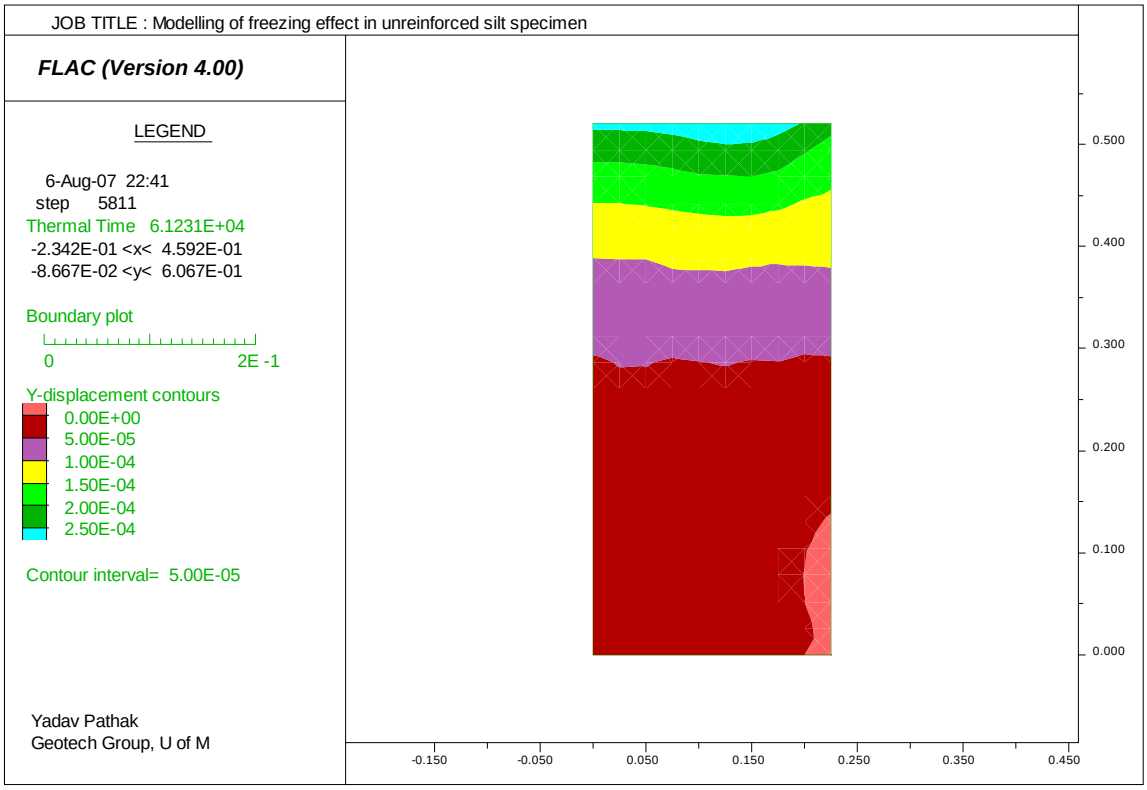

Figure 5.26 Vertical displacement contours in unreinforced silt specimen UT-25°C/+23°C during first cycle of freezing

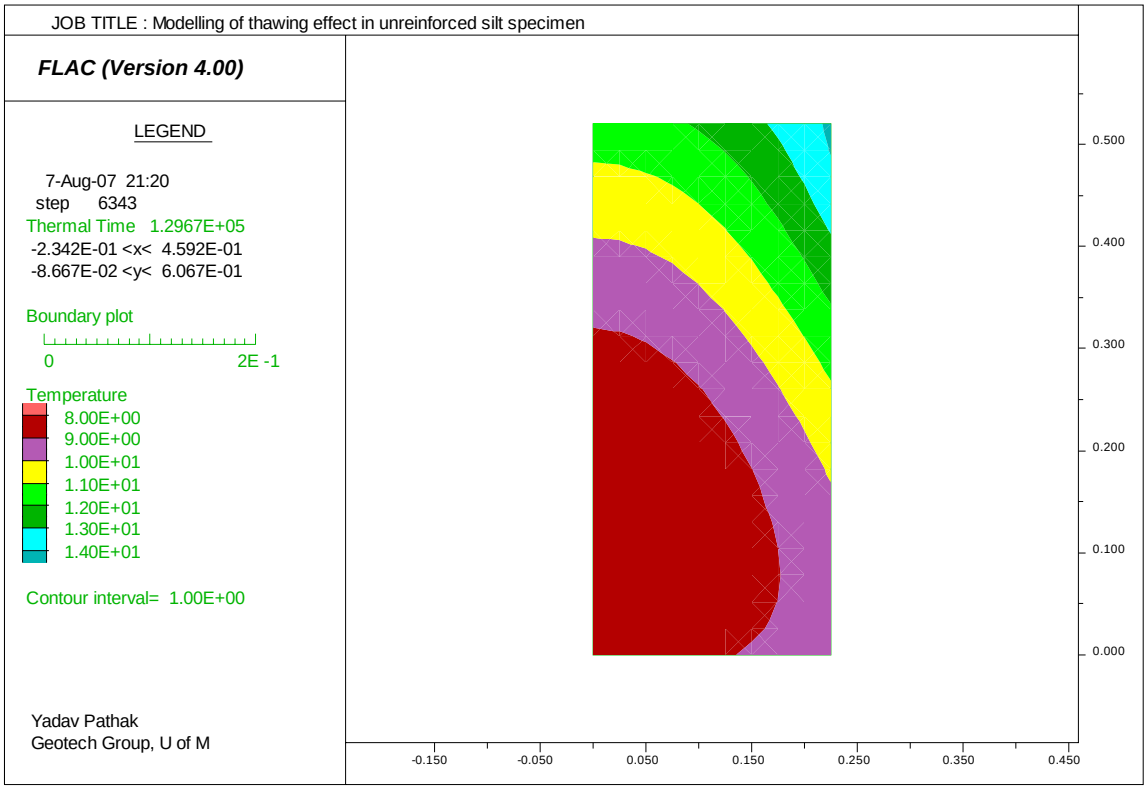

Figure 5.27 Temperature contours in unreinforced silt specimen UT-25°C/+23°C during first cycle of thawing

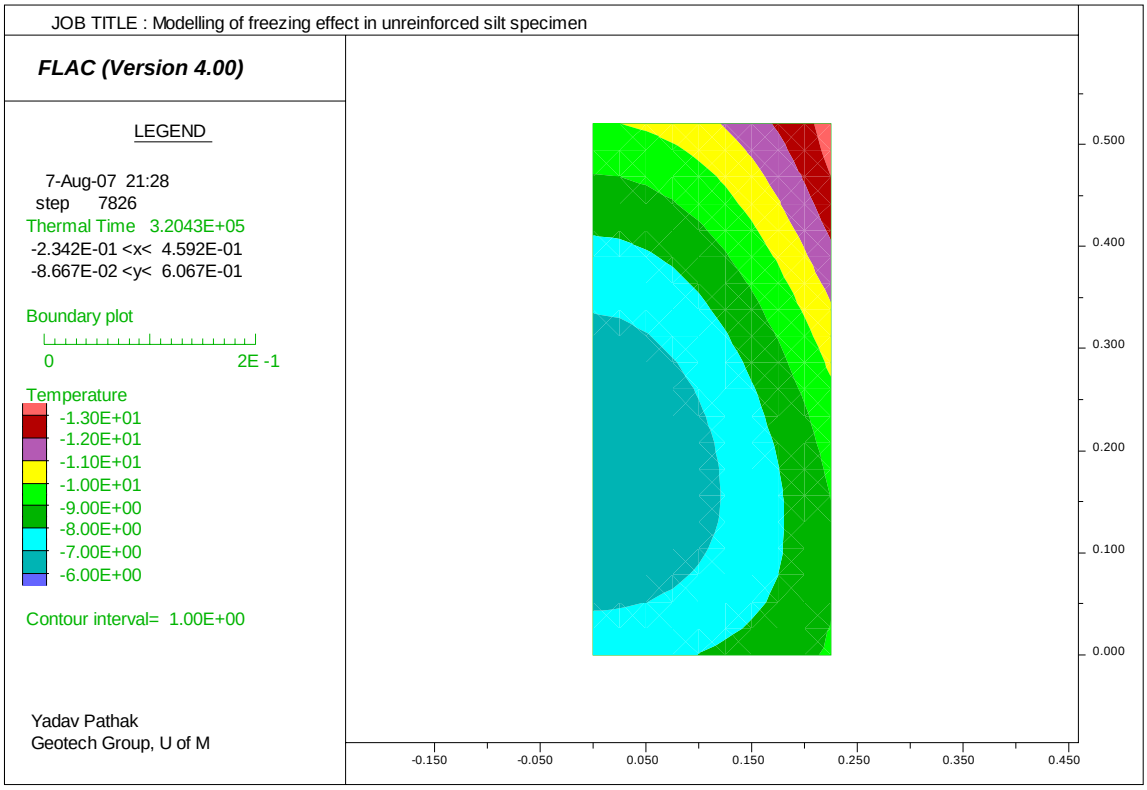

Figure 5.28 Temperature contours in unreinforced silt specimen UT-25°C/+23°C during third cycle of freezing

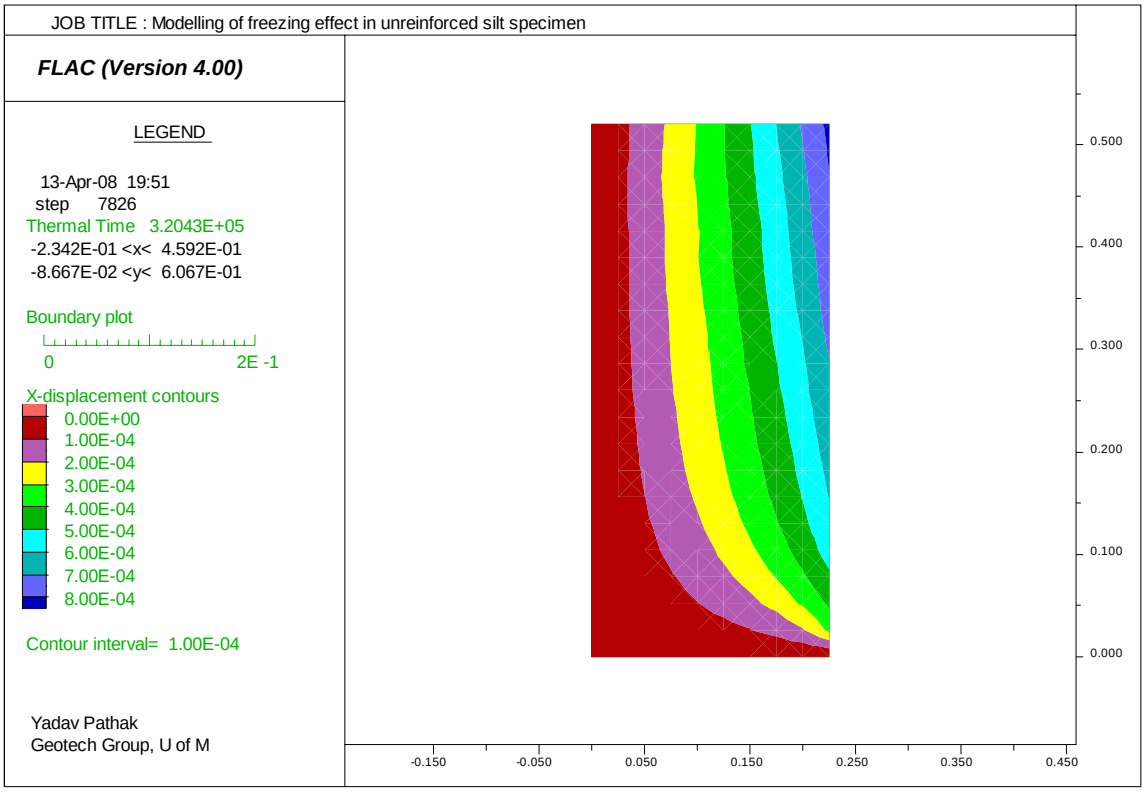

Figure 5.29 Horizontal displacement contours in unreinforced silt specimen UT-25°C/+23°C during third cycle of freezing

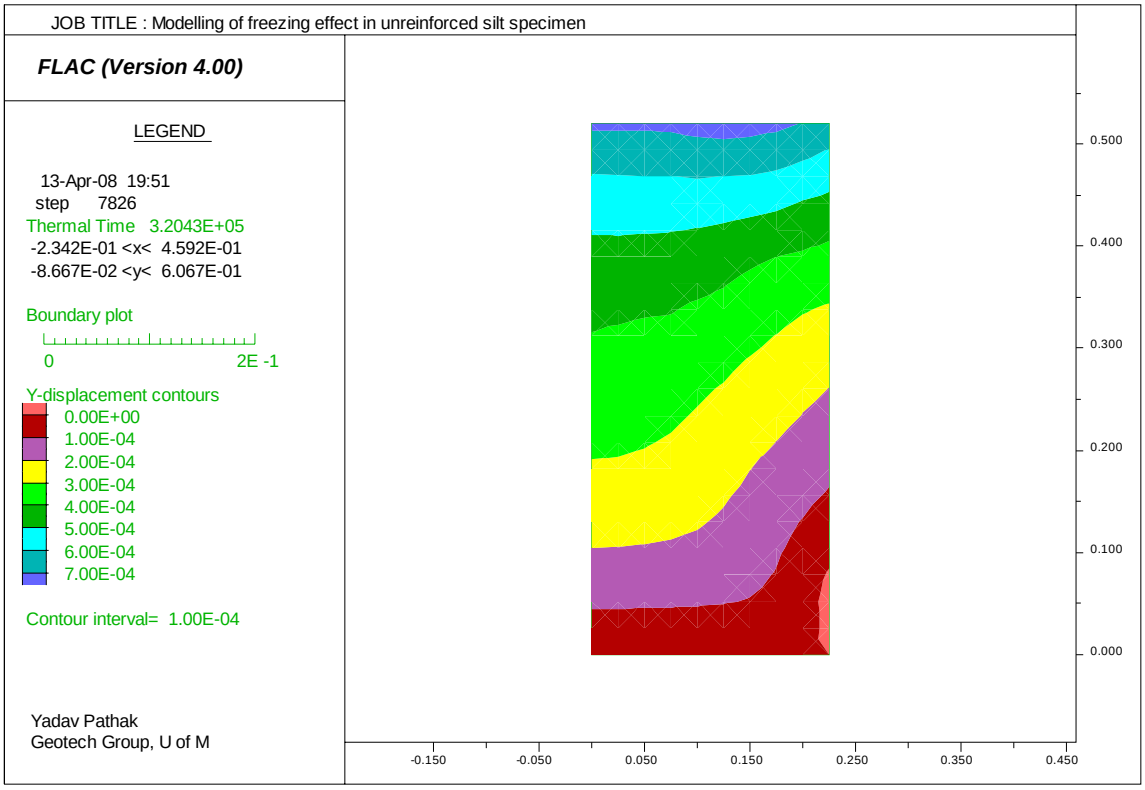

Figure 5.30 Vertical displacement contours in unreinforced silt specimen UT-25°C/+23°C during third cycle of freezing

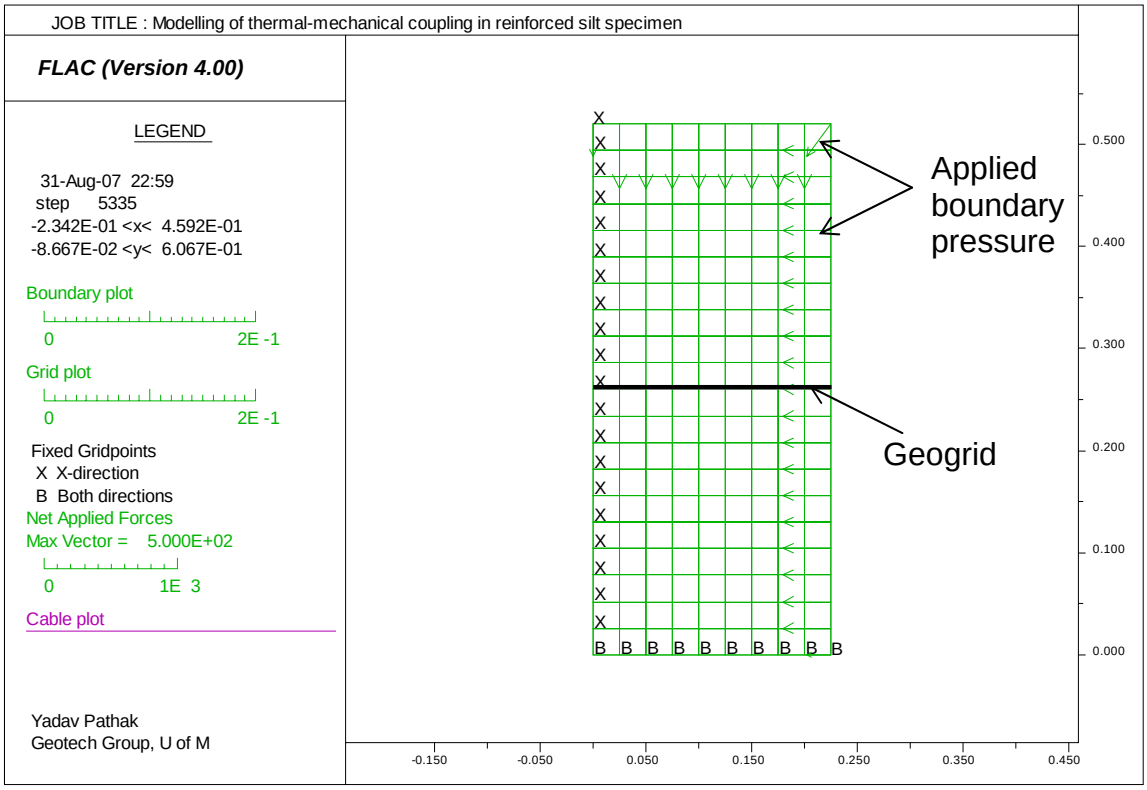

Figure 5.31 Numerical grid of geogrid-reinforced silt specimen RT-25°C/+23°C

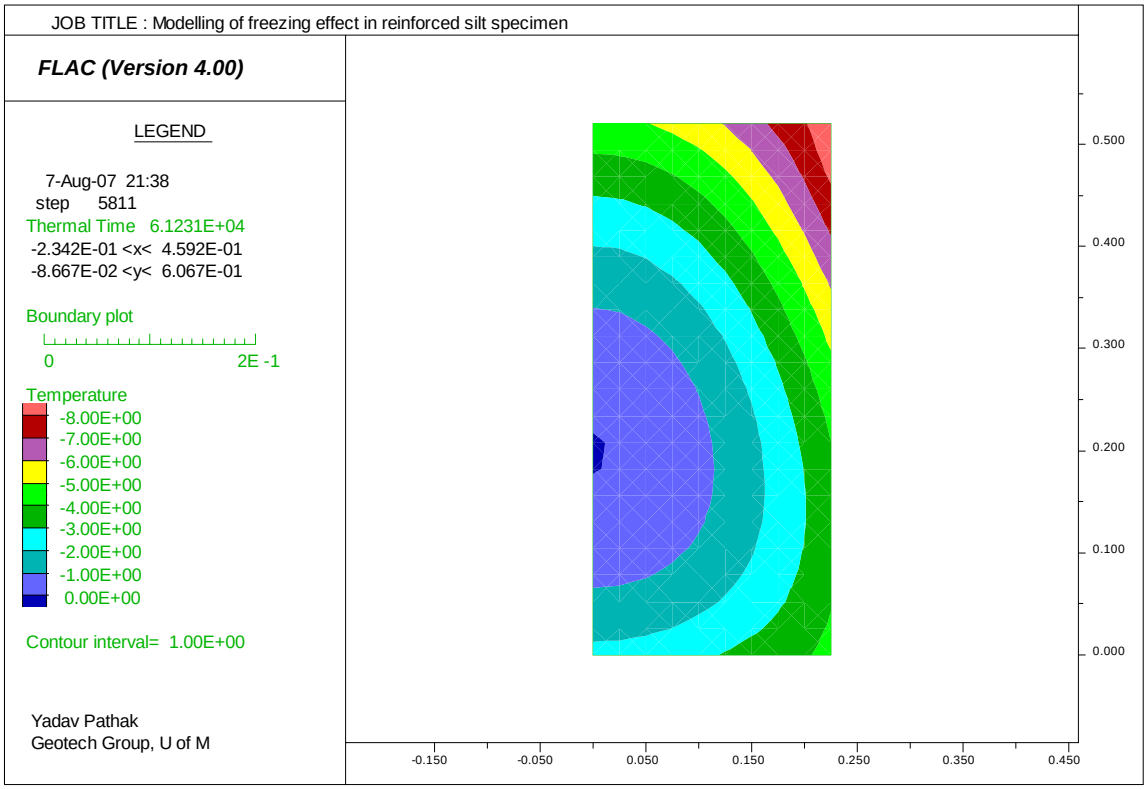

Figure 5.32 Temperature contours in geogrid-reinforced silt specimen RT-25°C/+23°C during first cycle of freezing

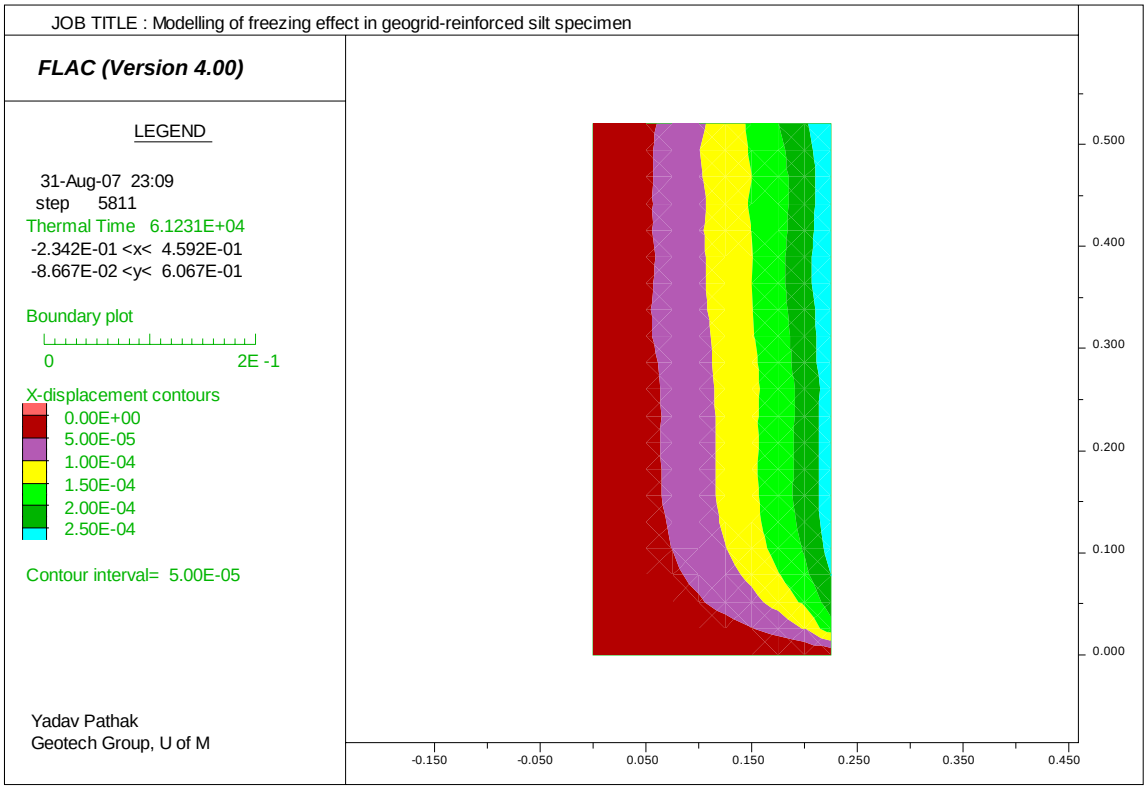

Figure 5.33 Horizontal displacement contours in geogrid-reinforced silt specimen RT-25°C/+23°C during first cycle of freezing

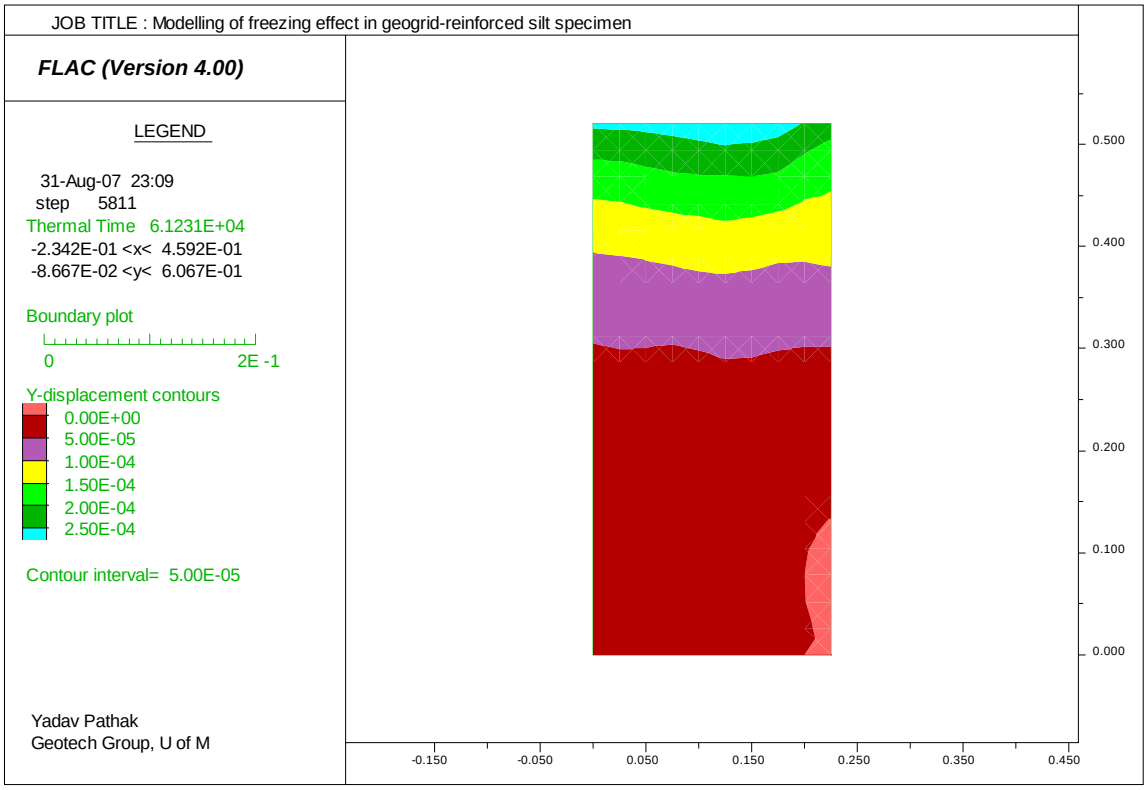

Figure 5.34 Vertical displacement contours in geogrid-reinforced silt specimen RT-25°C/+23°C during first cycle of freezing

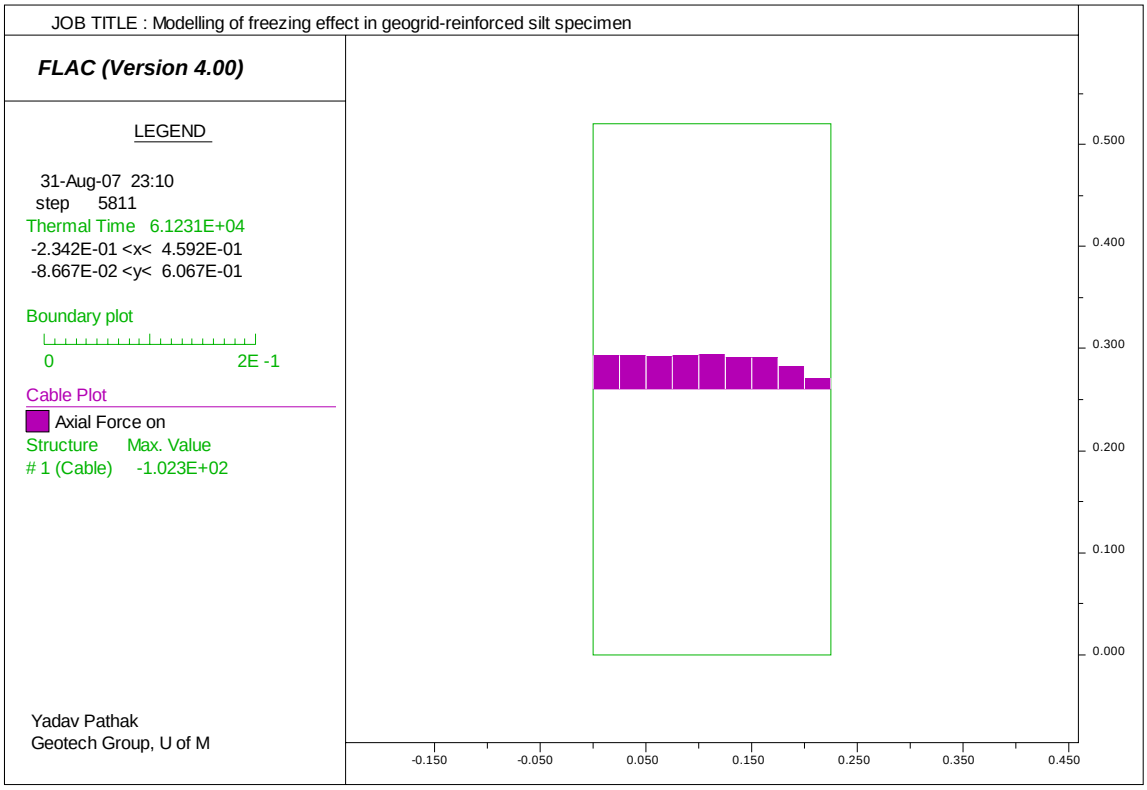

Figure 5.35 Axial force in geogrid reinforcement in geogrid-reinforced silt specimen RT-25°C/+23°C during first cycle of freezing

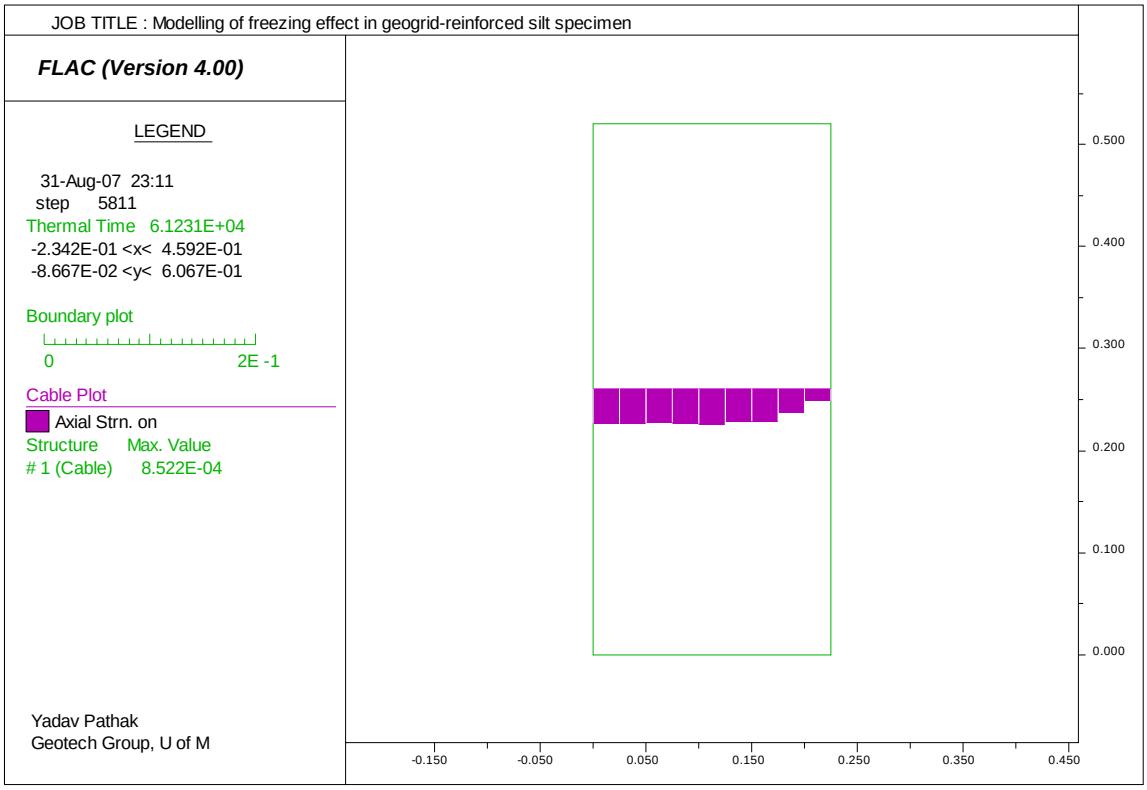

Figure 5.36 Axial strain in geogrid reinforcement in geogrid-reinforced silt specimen RT-25°C/+23°C during first cycle of freezing

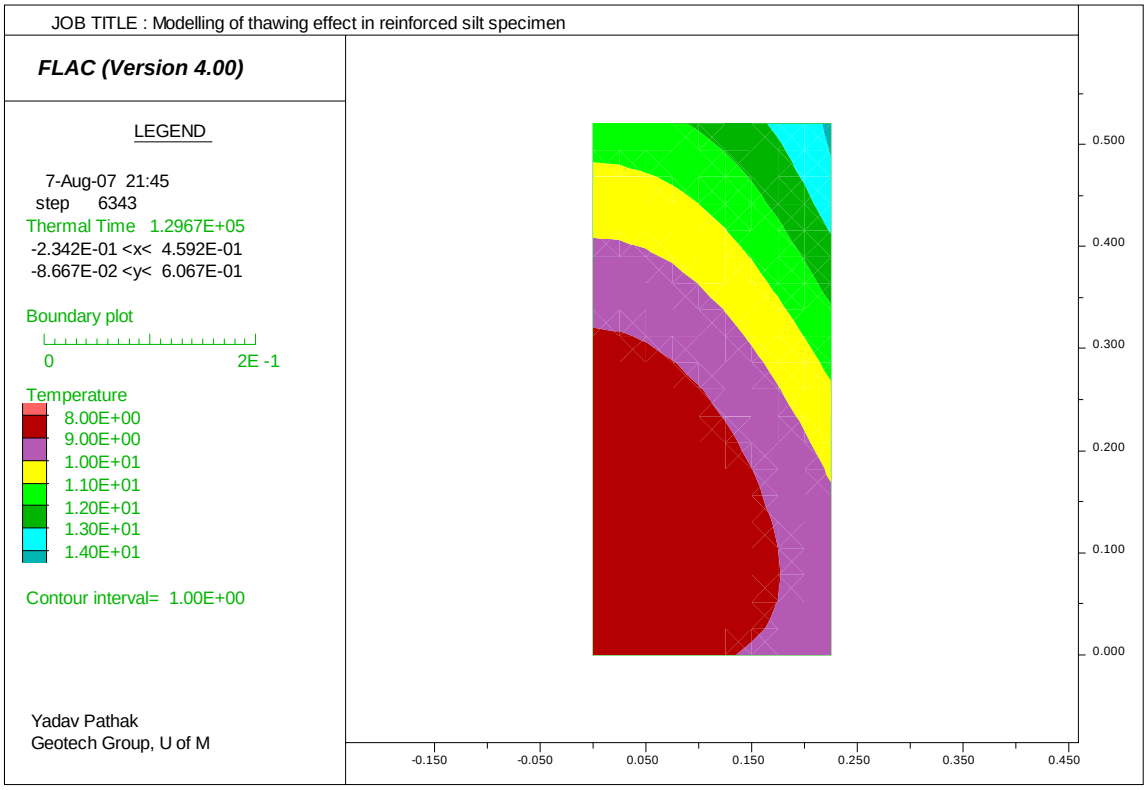

Figure 5.37 Temperature contours in geogrid-reinforced silt specimen RT-25°C/+23°C during first cycle of thawing

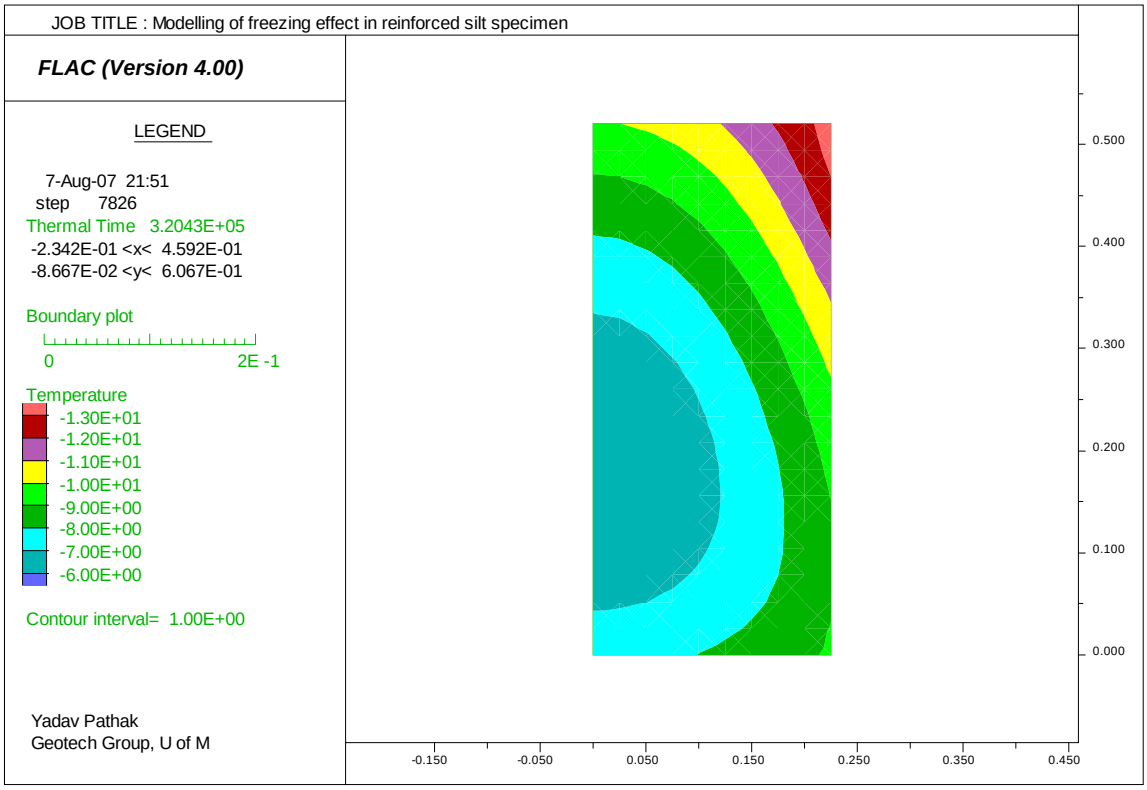

Figure 5.38 Temperature contours in geogrid-reinforced silt specimen RT-25°C/+23°C during third cycle of freezing

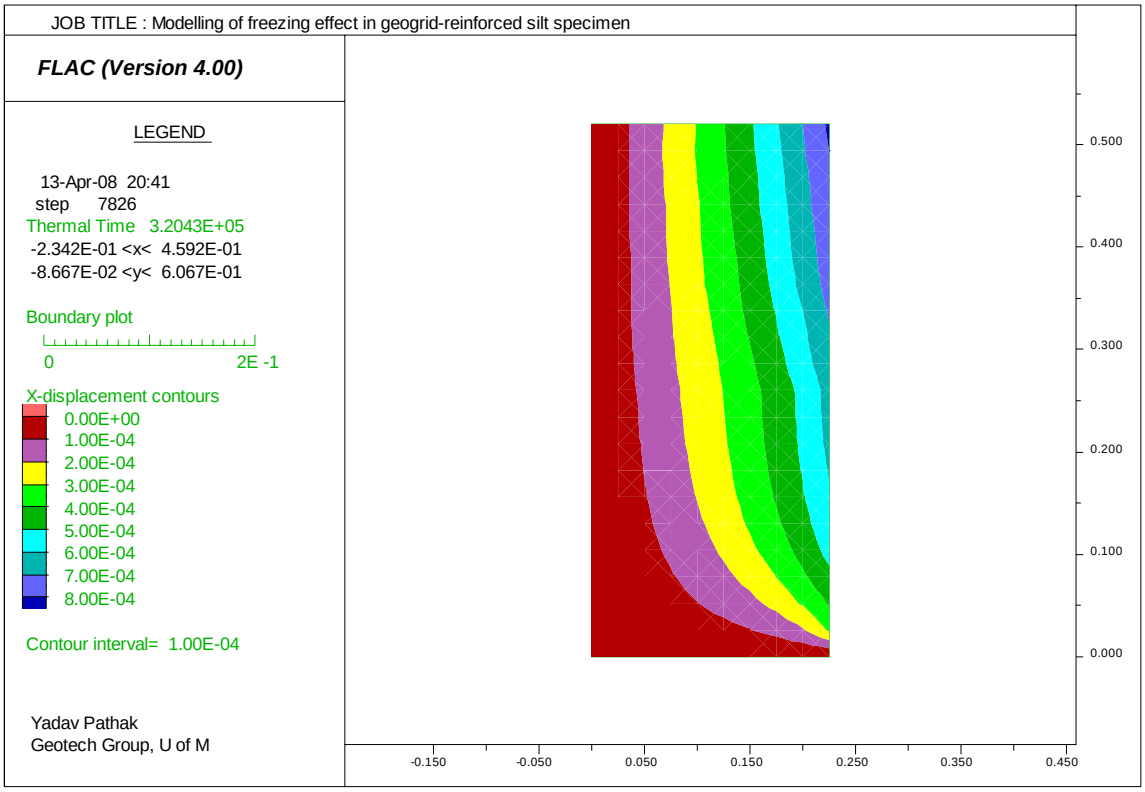

Figure 5.39 Horizontal displacement contours in geogrid-reinforced silt specimen RT-25°C/+23°C during third cycle of freezing

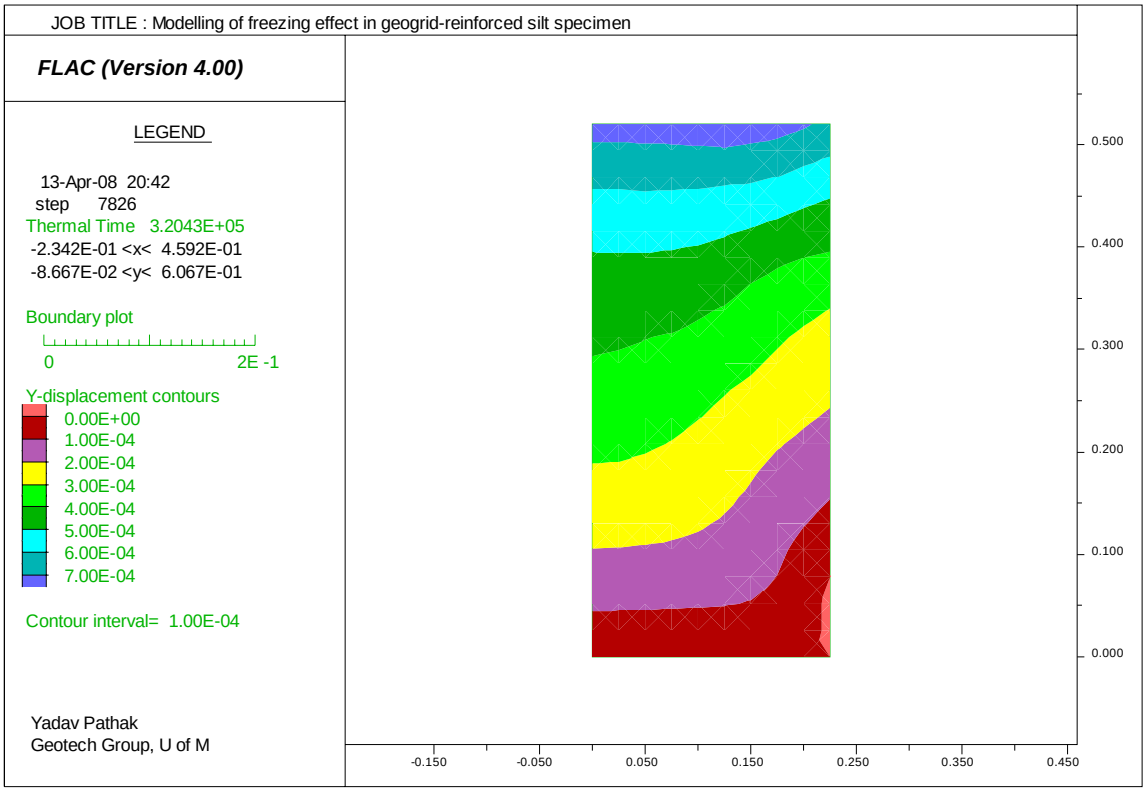

Figure 5.40 Vertical displacement contours in geogrid-reinforced silt specimen RT-25°C/+23°C during third cycle of freezing

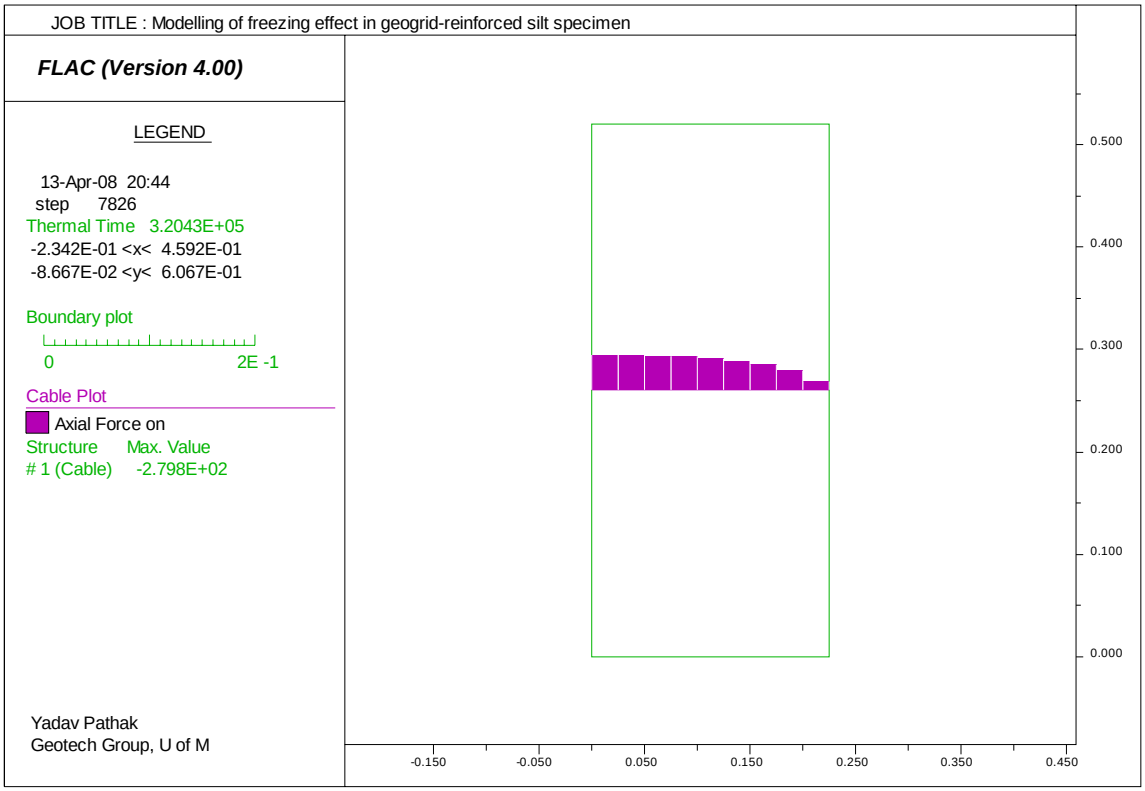

Figure 5.41 Axial force in geogrid reinforcement in geogrid-reinforced silt specimen RT-25°C/+23°C during third cycle of freezing

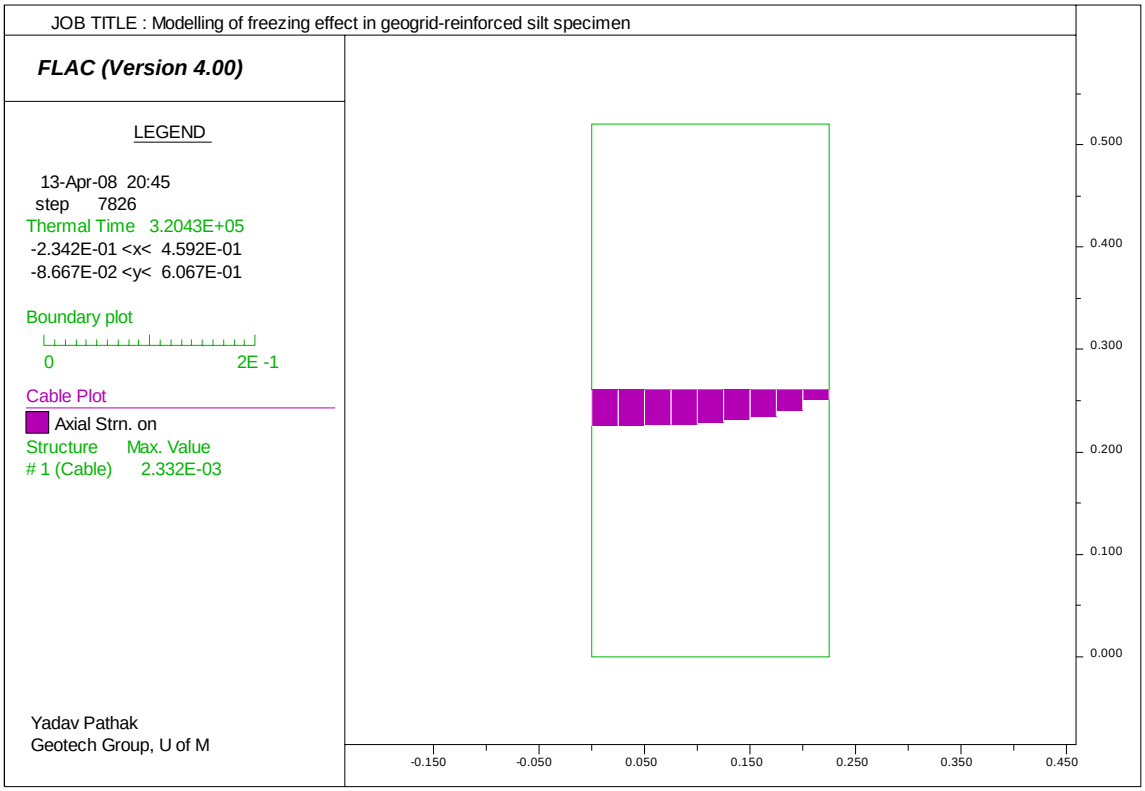

Figure 5.42 Axial strain in geogrid reinforcement in geogrid-reinforced silt specimen RT-25°C/+23°C during third cycle of freezing

CHAPTER 6

NUMERICAL ANALYSIS OF GEOSYNTHETIC-REINFORCED SLOPES

6.1 INTRODUCTION

Three numerical models (BBM, Swell model, and thermal-mechanical model) have been discussed in the Chapter 5. In this chapter, these models are used to analyse the performance of geosynthetic-reinforced clay or silt slopes under wetting or freezing conditions. The main objective of the analysis is to develop an understanding of the deformation of GRS structures and the generation of reinforcement loads under wetting- and freezing-induced loading in addition to mechanical loading. Soil deformations and reinforcement strains (and therefore loads) are evaluated. Both reinforced and unreinforced slopes are analyzed for comparison purposes. A parametric study is carried out to evaluate the most important mechanical, swelling, and temperature related parameters in the performance of reinforced slopes with marginal soils commonly found in Manitoba.

6.2 NUMERICAL ANALYSIS OF REINFORCED CLAY SLOPES

6.2.1 Slope Geometry and Material Properties

To develop an understanding of the performance of GRS structures under wetting-induced swelling, a generic clay slope was analyzed. Figure 6.1 shows the schematic of the slope and the soil profile used in the analysis. The slope has an inclination of 2H:1V and is 7 m high. The swelling clay is represented by the clay used in the laboratory test (identified as UMPAT in this study). The soil properties have been given in Tables 5.2 and 5.3 found in Chapter 5. The initial condition of the clay slope is assumed to be at unsaturated state. The foundation soil is assumed to be always saturated and therefore no subsequent swelling is expected. It is represented by a material that follows Mohr-Coulomb model and has the following properties: soil density (ρ) = 1978.5 kg/m^3, bulk modulus (K) = 29.3 MPa, shear modulus (G) = 22 MPa, cohesion (c) = 14.4 kPa and friction angle (ϕ) = 30°.

For modelling, layers of geogrid reinforcements 5.5 m long have been placed in the slope at 0.45 m vertical spacing. The slope face has geogrid reinforcement wrapped around into the slope to provide a flexible facing system. The chosen reinforcement properties are: Elastic Young's modulus (E) = 100 MPa, tensile yield limit (yield) = 28 kN, compressive yield limit (ycomp) = 3.3 kN, cross-sectional area (A) = 0.003 m^2 and perimeter (peri) = 2 m. These properties were taken from information provided by a supplier of geogrid reinforcement used in

such applications. Points A and B in Figure 6.1 are reference points used in the discussion of results from the numerical analysis.

6.2.2 Modelling Procedures

Figure 6.2 represents a numerical grid of the geogrid-reinforced slope used in FLAC. The bottom boundary is considered fixed in both vertical and horizontal directions. The left side boundary is represented with rollers. The right side boundary of foundation soil is also represented with rollers, while the slope face is free to deform in horizontal and vertical directions.

The zones occupied with soil are represented by solid elements while the reinforcements within the soil are cable (structural) elements. The wrapped-around portions of reinforcement at the slope face are represented by beam elements with negligible moment of inertia to minimize their bending stiffness. To take into account the interaction between soil and geogrid, an interface element is introduced and simulated by the cable grout utility in FLAC. Shear interface properties are estimated as follows: shear stiffness (K_b) = $6e^5$ kN/m/m, cohesive strength (S_b) = 20 kN/m and frictional angle (δ) =17°. In the absence of pullout test results in Manitoba clays, these values are estimations from the pullout test results in different type of clays (Bergado *et al.* 1994).

The first step of the analysis was to equilibrate the foundation soil under its own gravitational stresses. This allowed the *in-situ* stresses to be calculated. Then,

layers of fill materials and geogrids were placed and the calculation was stepped to equilibrium. The placement of layers of fill and the equilibration, were done until the desired height of the fill was reached. The FISH function invoking the BBM was activated to simulate the mechanical loading with 6.0 kPa of surcharge at the top surface of the fill and the calculation was again stepped to equilibrium. This completed the steps that determined the state of stresses and strains during the pre-wetting stage. The calculated displacements were then set to zero at this stage since they are small compared to the wetting-induced deformations. The next step was the application of the wetting front to the finite element domain. The wetting front was defined by a table of values in the coordinate system from the foundation level in the case of flooding (a case unique in Manitoba) or from the slope surface in the case of rainfall infiltration. It then moved vertically by assuming that all zones (elements) with centroid directly above or below the wetting front were wetted simultaneously. Finally, the FISH function invoking the Swell model was called to solve the stresses and deformations induced by wetting. The wetting-induced stresses were added to the stresses in the preceding step.

The same slope geometry was also analyzed without reinforcement for comparison purposes. The modelling procedures were the same as those in the reinforced slope, except there was no geogrid reinforcement in the fill. Analyses were performed when (a) all zones of the slope were saturated, and (b) when only the top portion of the slope was saturated (rainfall infiltration).

6.2.3 Results of Numerical Analysis

6.2.3.1 Fully Wetted Slope

Wetting was simulated for the full depth of the backfill soil. Figure 6.3 shows the displacement vectors of unreinforced clay slope after wetting. Displacements are expansive near the top surface of the fill and along the slope face. Vertical swelling generally occurred along the top surface of the fill. Along the slope, the displacement vectors are almost perpendicular to the slope face at the top half and tend to be directed horizontally at the bottom half. These deformation patterns are found consistent with those observed by Ng *et al.* (2003) on the field performance of unsaturated swelling clay slope subjected to rainfall infiltration. Ng *et al.* (2003) observed two distinct modes of slope deformations. The first mode was a cantilever deformation within the top 1.5 m at the mid-slope while the second mode was deep seated downward movement at the toe of the slope.

Displacement vectors for the reinforced clay slope are shown in Figure 6.4. The inclusion of geosynthetic reinforcement has reduced the maximum displacement vector by about 27% (from 187 mm to 137 mm). Other researchers (Al-Omari and Hamodi 1991, Vessely and Wu 2002) have also found reduction in deformations with the presence of reinforcements.

Deformation patterns for both reinforced and unreinforced slopes show decreasing swelling towards the inner and bottom portions of the slope that eventually lead to compression. The stress-strain relationship shown in Figure 5.6 in Chapter 5 helps to understand these deformation patterns. As the applied vertical pressure increases (in this case, due to overburden stress), the wetting strain decreases. Vertical compressions can occur during wetting at applied vertical pressures over 50 kPa for the type of swelling clay investigated in this study. The deformation patterns from numerical analysis results are consistent with those reported by Lawton *et al.* (1992) and Noorany *et al.* (1992). Post-construction wetting of clay fill was found to cause swelling in the near surface (at low stress levels) and compression in the deeper zones (at high stress levels) of the fill.

Figures 6.5 and 6.6 respectively show the horizontal and vertical displacement contours of the unreinforced slope due to wetting. In the upper half of the slope, and within 3 m from slope face in the interior, the horizontal swelling reached up to 55 mm. In the lower half of the slope, the horizontal swelling is higher and at greater extent than the upper half. The maximum horizontal displacement is about 175 mm located near the toe of the slope. The vertical displacements are within 1 m depth of the top surface of the fill with a maximum vertical swelling of 50 mm.

Figures 6.7 and 6.8 respectively show horizontal and vertical displacements of the reinforced slope. Not only are the horizontal displacements of the slope reduced, the extents of the areas of appreciable horizontal displacements are reduced as well. Large areas of appreciable displacements can have implications in the nature of slope failures. There is potential for deep seated failure in the unreinforced slopes as opposed to shallow failures in the reinforced slope (see also Figures 6.3 and 6.4 in terms of displacement vectors). Potential shallow slope failures can be easily remedied compared with deep seated slope failures. For example, the addition of secondary reinforcements can reduce near-surface deformations. Secondary reinforcements are much shorter than primary reinforcements, which require lengths and spacing that increase the factor of safety against overall instability of the slope under mechanical loading.

The presence of geosynthetic reinforcements did not reduce vertical swelling at the crest of the slope. On the contrary, vertical swelling at the crest of the reinforced slope is slightly higher than the unreinforced slope. This trend is the same as that shown by the results from laboratory model tests conducted in this study as well as the tests by Vessely and Wu (2002). The presence of reinforcement restricted the horizontal swelling but increased the vertical swelling, resulting in approximately the same volume of swelling as in the unreinforced condition.

With the geosynthetic reinforcements restricting the slope movements, the loads/strains in the reinforcement can be expected to increase. Figure 6.9 shows the reinforcement loads due to wetting-induced deformations. In this figure the reinforcement load is from a combination of mechanical and wetting-induced stresses. The distribution of reinforcement loads along the reinforcements is shown in terms of bar graphs. In the figure, cable number 1 is the bottom reinforcement layer while cable number 16 is the top layer.

Under pre-wetting conditions, only the mechanical loading (gravitational stress and externally applied pressure) is in effect. The axial forces and strains in the reinforcement at this condition are very small. The maximum force is 0.4 kN/m with corresponding maximum strain of 0.13%.

Axial loads induced in the reinforcements due to wetting alone were as high as 9.0 kN/m. The maximum reinforcement strain due to wetting alone is 2.5%. Higher reinforcement loads and strains are located near the slope surface. This is consistent with the simulated slope deformation patterns. The loads and strains decrease towards the interior of the slope.

6.2.3.2 Partially Wetted Slope

Numerical modelling was done on partial wetting of the fill. This simulates the case when rainfall infiltration can wet up the fill to a certain depth below the top surface and the sloping face of the fill. For the simulations, only the first 2 m

below the top and sloping surface of the fill was assumed to be saturated. A full transient seepage analysis was not performed.

Figures 6.10 and 6.11 show the displacement vectors of the unreinforced and reinforced slopes due to partial wetting of the fill. As expected, soil swelling of the unreinforced slope at partial wetting is less than that at full wetting. The deformation patterns are similar to those with full wetting. Horizontal and vertical displacement contours for unreinforced and reinforced slopes are given in Appendix D).

The vertical swelling of slope at the top of the fill is about 40 mm. This swelling can cause damage to overlying pavements, particularly when there are differential vertical movements along the length and cross-section of the pavement. The most common problems in roads and highways in Manitoba are longitudinal cracking and uneven pavement surfaces. The former results in differential wetting of the fill due to higher moisture increase near the shoulder than in the zones below the pavement. Therefore, there should be considerable efforts to prevent water infiltration into swelling clay fills. Provision of geosynthetic capillary breaks between sub-base drainage systems and the clay fill can also be used to allow egress of water from clay into the drainage system, thereby minimizing clay swelling. Geomembranes can also be used as seals to prevent rainfall infiltration into the clay subgrade. This is particularly important near the surface as reinforcements do not reduce vertical deformations that can cause

damage to pavements. Other techniques for reducing swelling in clays such as clay-cement or clay-lime mixtures can be used in clays below pavements.

Axial forces and strains along the reinforcements at different levels in the fill are shown in Figures 6.12 and 6.13, respectively. The loads in the reinforcements are mobilized closer to the slope face and are consistent with deformations of the slope. Since soil swelling at the slope face is similar, the maximum values of forces in the reinforcement in the fully wetted and partially wetted reinforced slopes are similar.

6.2.4 Parametric Study

Parametric studies were performed to evaluate the influences of design parameters such as soil swelling potential, reinforcement spacing, reinforcement stiffness and soil-reinforcement interface shear stiffness on the performance of geosynthetic-reinforced clay slopes under full wetting of the fill. These analyses were performed by varying only single parameters in turn while the other parameters remained unchanged. The results of the parametric study were analyzed in terms of slope deformations and additional loads induced in the reinforcements due to swelling of the clay. The two points A and B in Figure 6.1 near the top and bottom of the reinforced slope surface respectively, are of interest for discussion purposes.

6.2.4.1 Soil-Reinforcement Interface Shear Stiffness (K_b)

A parametric study was performed in the reinforced slope by varying shear stiffness of the soil-reinforcement interface during full wetting. The soil-reinforcement interface shear stiffness was chosen to vary by one order of magnitude, $6e^4$, $6e^5$ and $6e^6$ kN/m/m.

Figure 6.14 shows the influence of soil-reinforcement interface shear stiffness (K_b) on slope deformations and axial forces. Slope displacements are sensitive to the variation of the interface shear stiffness. Higher interface shear resistance derived from the interaction between soil and reinforcement is favourable to reducing wetting-induced deformations. This implies that the grid-type of geosynthetic reinforcements are preferable compared with planar type of geosynthetics. Due to its apertures, grid can exhibit higher bearing and frictional resistance with soil than planar surface. Another implication is that interface stiffness under wet and dry conditions should be determined from pullout or direct shear tests on both nearly saturated and less saturated clays.

As expected for large slope displacements, higher interface shear stiffness resulted to increase in reinforcement loads in both points A and B. It was shown that additional reinforcement load was not much of a concern during a single-event swelling of clay fill. However, this may not be the case for multiple wetting-drying cycles that were not investigated in this study due to the limitations of the numerical models.

6.2.4.2 Tensile Stiffness of Reinforcement (E)

Tensile stiffness of the reinforcement was varied to investigate its sensitivity to the performance of a reinforced clay slope during wetting. This parameter was varied from 50 MPa to 200 MPa.

Figure 6.15 shows the effects of varying the tensile stiffness of the reinforcement. The results indicate that increasing the stiffness of the reinforcement slightly decrease the slope displacements, which can be due to relative movement between clay and reinforcement at the interface as observed in the laboratory tests. On other hand, the reinforcement tension increased substantially as the reinforcement stiffness increased. Higher reinforcement tension is mobilized even with the smaller reinforcement strain when the reinforcement is stiffer. Therefore, the desirable reinforcements to be used are those with higher interface shear stiffness and with reasonable tensile stiffness.

6.2.4.3 Reinforcement Spacing

Three vertical spacing of reinforcement, namely 0.3 m, 0.45 m and 0.6 m were used in the parametric study. These are the typical vertical spacing used in practice. Figure 6.16 shows the influence of vertical spacing in the slope deformation and reinforcement tension. Slope deformations increased with increasing reinforcement spacing. The deformations increased more significantly

at the bottom of slope than at the top. In contrast, the tension in the reinforcement is virtually unchanged with the range of spacing analyzed in this study. The reinforcement tension is higher at the bottom of slope than at the top, which is consistent with the simulated deformations. This implies selecting 0.45 m spacing for practical and economical reasons, unless required by other factors. Providing secondary reinforcements can help reduce the near-surface swelling of slopes.

6.2.4.4 Swelling Potential of Clay

The swelling potential of clay is another important parameter that controls the slope deformation and reinforcement tension in the reinforced clay slope. The swelling potential of the clay fill was varied by increasing or decreasing its value for the reference clay (UMPAT clay given in Table 5.3) by 40%. As shown in Figure 6.17, increasing the swelling potential of clay cause both the slope deformations and mobilized tensions in the reinforcement increase very significantly. The same trends were found at the top and the bottom of the slope. Accurate determination of swelling potential of clay is undoubtedly important in achieving a reasonable prediction of field performance.

6.3 NUMERICAL ANALYSIS OF REINFORCED SILT SLOPES

6.3.1 Slope Geometry and Material Properties

A numerical analysis was carried out for a geogrid-reinforced slope in silt to develop an understanding of the slope's performance under freezing temperatures. A schematic of the slope geometry and the soil profile is shown in Figure 6.1, the same slope as was used previously in the swelling clay study, but this time with sandy silt backfill. The soil properties were given in Table 5.7 in Chapter 5. The fill was initially compacted at its optimum moisture and maximum dry density. At this initial stage, no freezing had been applied to the fill and foundation soil. The strength of the foundation soil was represented by a Mohr-Coulomb model with properties as follows: soil density (ρ) = 2100 kg/m^3, bulk modulus (K) = 29.3 MPa, shear modulus (G) = 22 MPa, cohesion (c) = 14.5 kPa and friction angle (ϕ) = 30°.

Layers of geogrid reinforcements (length = 5.5 m) at 0.45 m vertical spacing were placed in the fill to simulate actual construction. A wrapped-around facing system was employed at the slope face, similar to what was simulated for the reinforced clay slope discussed previously. The geogrid reinforcement properties are the same as those used in the reinforced clay: Elastic Young's modulus (E) = 100 MPa, tensile yield limit (yield) = 28 kN, compressive yield limit (ycomp) = 3.3 kN, cross-sectional area (A) = 0.003 m^2 and perimeter (peri) = 2 m. As in the reinforced clay slope, Points A and B in the Figure 6.1 are also the two points of

reference for the discussions on the results of numerical simulations of the reinforced silt slope.

6.3.2 Modelling Procedures

The initial steps in modelling the reinforced silt slope are the same as those for the reinforced clay slope except that freezing temperatures were applied at the appropriate boundaries of the silt slopes. Given the fact that frozen soil will have higher shear stiffness than unfrozen soil, the shear stiffness (K_b) of the silt-reinforcement interface has been assumed one order higher than the clay-reinforcement interface. The silt-reinforcement frictional angle (δ) was estimated to be 21°.

The next step was to simulate temperature and stress changes in the slope using the thermal-mechanical model built into the FLAC computer program. A uniform soil temperature was assumed to be 20°C in the soil prior to applying the freezing temperatures. Freezing was simulated by applying -25°C at the top and slope surface of the embankment, which approximates the actual temperatures at the site during the approximately 5 months of winter period in Manitoba. For the sake of simplicity in investigating the influence of freezing, the freezing temperature of -25°C was applied constantly for five months. The temperature changes were coupled with the mechanical model (Mohr-Coulomb model) via the coefficient of thermal expansion. The freezing-induced stresses were added to the zonal stress state before application of the constitutive law (mechanical model).

6.3.3 Results of Numerical Analysis

Figure 6.18 shows temperature contours in the unreinforced slope after freezing. About 4 m depth of embankment fill soil was frozen. The depth of frozen soil is greater along the slope face than below the top surface, most likely due to penetration of the freezing front both from the top and slope surfaces.

Figure 6.19 shows the corresponding soil displacement vectors in the unreinforced silt slope due to freezing. The displacement vectors are mostly directed perpendicular to the top and slope surfaces, with maximum displacement of about 46 mm. This displacement pattern is somewhat different from that of the wetted clay slope where compression was observed during wetting at higher overburden pressures. The displacement vectors for the reinforced silt slope shown in Figure 6.20 indicate marginal reduction of the slope displacements. The same patterns of horizontal and vertical deformations were produced for both unreinforced and reinforced silt slopes (refer Figures D.5 – D.8).

The reinforcement loads during the mechanical loading are shown by bar graphs in Figure 6.21. The cable numbering is the same as that of the reinforced clay slope where cable 1 is for the bottom reinforcement layer. The reinforcement loads under the combination of mechanical loading (gravitational stress and externally applied pressure) and freezing-induced stresses are shown in Figure

6.22. Reinforcement loads during pre-freezing are very small. The maximum force and strain in the reinforcement are 0.35 kN/m and 0.13% respectively prior to freezing. Reinforcement loads induced in the reinforcements due to freezing alone accounted for about 1.35 kN/m. The maximum reinforcement strain due to freezing alone is 0.6%. As in the reinforced clay slope, higher values of loads are located near the slope surface, which are consistent with the slope deformations. The loads decrease towards the deeper inner zone of the slope. Placement of secondary reinforcements can reduce the near surface deformation depending on the extent of frozen fill. The predicted axial force and strain in the reinforcement due to freezing are not significant in this case because the soil displacements are not significant. Caution must be considered because accumulations of tensile strains during freezing and thawing cycles were observed in the laboratory tests. This can impact the long-term tensile load of the reinforcements.

6.3.4 Parametric Study

Parametric studies were performed to evaluate the influences of design parameters such as reinforcement spacing, reinforcement stiffness and soil-reinforcement interface shear stiffness on the performance of geosynthetic-reinforced silt slopes under freezing conditions. As in the reinforced clay slopes, results of Points A and B in Figure 6.1 located near the top and bottom of the reinforced silt slope surface are selected for discussions.

6.3.4.1 Soil-Reinforcement Interface Shear Stiffness (K_b)

A parametric study was performed in the reinforced slope by varying the soil-reinforcement interface shear stiffness during freezing. The soil-reinforcement interface shear stiffness was chosen to vary by one order of magnitude, $6e^5$, $6e^6$ and $6e^7$ kN/m/m.

Figure 6.23 shows the influence of soil-reinforcement interface shear stiffness (K_b) on the slope deformations and reinforcement loads. As expected, the slope displacements decreased with increasing interface shear stiffness. The decrease is more significant at Point B and is due to less slippage at the higher stress levels in the lower part of slope. There is no significant change in the reinforcement loads with respect to interface shear stiffness change. Again, a grid-type of geosynthetic reinforcements is recommended rather than planar type of geosynthetic for this application.

6.3.4.2 Tensile Stiffness of Reinforcement (E)

The tensile stiffness of the reinforcement was varied to investigate its sensitivity to the performance of a reinforced silt slope during freezing. This parameter was varied from 50 MPa to 200 MPa.

Figure 6.24 shows the effects of varying the tensile stiffness of the reinforcement. The result indicates that increasing the reinforcement stiffness decreases the slope deformation. However, the slope deformation is slightly changed at Point A

with respect to change of tensile stiffness of reinforcement. The same trend was produced in the silt slope as in the reinforced clay slope, both in terms of deformations and reinforcement loads.

6.3.4.3 Reinforcement Spacing

Figure 6.25 shows the influence of reinforcement spacing on slope deformations and reinforcement tension in the reinforced silt slope as a result of freezing. Slope deformations as well as reinforcement tensions increase with increasing reinforcement spacing. However, the change in reinforcement tension is not significant for the typical range of reinforcement spacing analyzed in this study. Selecting a 0.45 m vertical spacing is an optimal design in case of reinforced silt slope which is the same design recommendation for reinforced clay slope under wetting conditions.

6.4 SUMMARY

The numerical models described in Chapter 5 were used to evaluate the performance of geosynthetic-reinforced soil slopes under wetting and freezing conditions. The aim is to acquire improved understanding of the deformation behaviour of GRS structures and reinforcement loads under environmental loading. Both reinforced and unreinforced slopes were analyzed. The main points covered in this chapter are as follows:

1) Swelling of a generic geosynthetic-reinforced clay slope subjected to wetting was evaluated. The BBM model was used to simulate the behaviour under mechanical loading. The Swell model was used to simulate the swelling behaviour during wetting. The analyses were performed for fully wetted and partially wetted slopes.
2) Slope displacements have two distinct modes. Displacement vectors are almost perpendicular to the slope face at the top half and tend to be directed horizontally at the bottom half.
3) Geosynthetic reinforcement reduces the horizontal swelling of the reinforced slope compared with the unreinforced slope. Soil swelling induces axial forces and strains in the reinforcement. Higher values of reinforcement loads and strains are predicted near the slope surface and are consistent with the predicted deformations; the reinforcement loads decrease towards the deeper portion of the slope.
4) Additional loads induced in the reinforcement are predicted, with values up to 9 kN/m and corresponding reinforcement strains of 2.5%. A level of 2.5% reinforcement strains are beyond the range of working strains (1-2%) commonly used in design practice. Taking into accounts the additional loads will be necessary for effective design of geosynthetic-reinforced soil structures with swelling clay backfill. Secondary reinforcements can reduce surficial slope deformations.
5) Effects of freezing in silt backfill geosynthetic-reinforced slopes were evaluated using FLAC. Built-in thermal-mechanical models were used to

simulate freezing temperatures in the soil, displacements in the reinforced soil and reinforcement loads. Freezing was simulated by applying -25°C temperature on outer surface of slope.

6) Frost heave occurs on top of the fill and along the slope face. Geosynthetic reinforcements reduce the horizontal expansion of the reinforced slope.
7) Frost heave induces additional loading in the reinforcement. Higher values are located near the slope face and are consistent with the slope deformation patterns.
8) The predicted additional loads are relatively small. The small load transfer is due to small soil displacements. Considerable soil displacements are necessary to mobilize the reinforcement loads.
9) Based on the parametric study, it is recommended that grid-type reinforcements, as opposed to planar reinforcements should be used. Due to their apertures, geogrids can exhibit superior interface shear resistance because of combined bearing and frictional resistance. Primary reinforcement spacing of 0.45 m and secondary reinforcement in between appear to be an acceptable reinforcement layout.

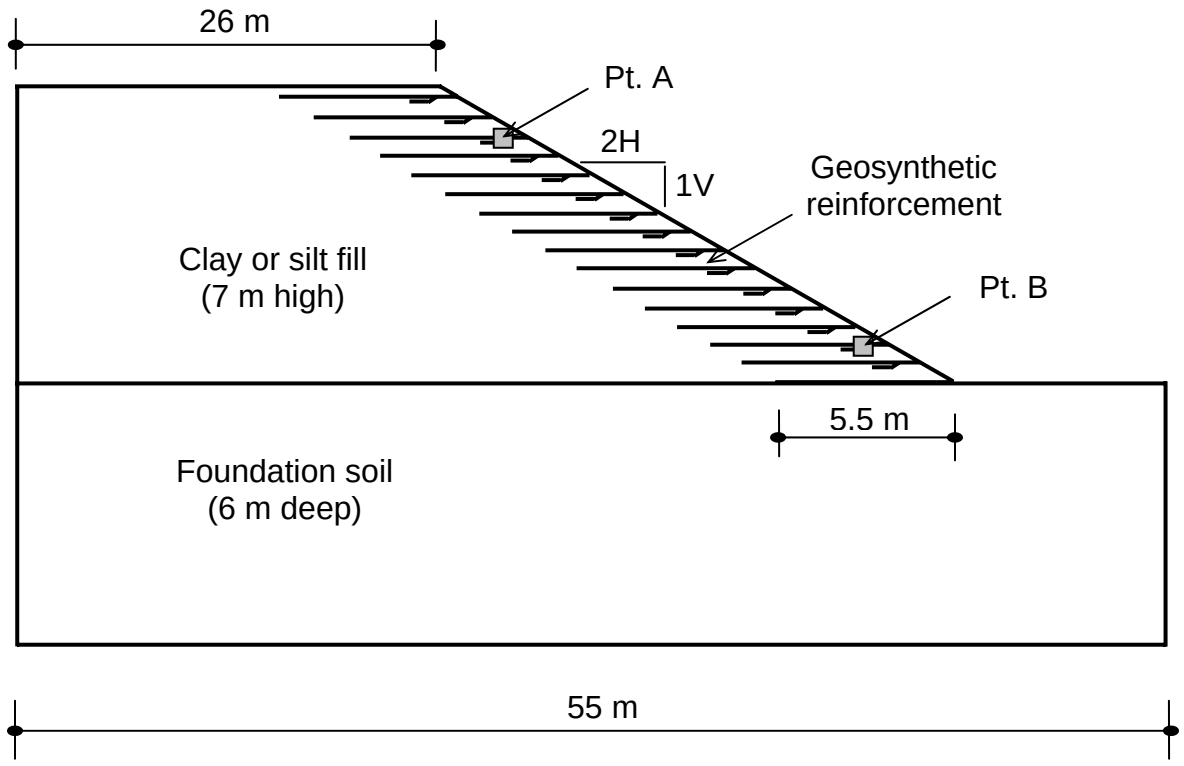

Figure 6.1 Schematic of geosynthetic-reinforced clay/silt slope geometry and soil profile

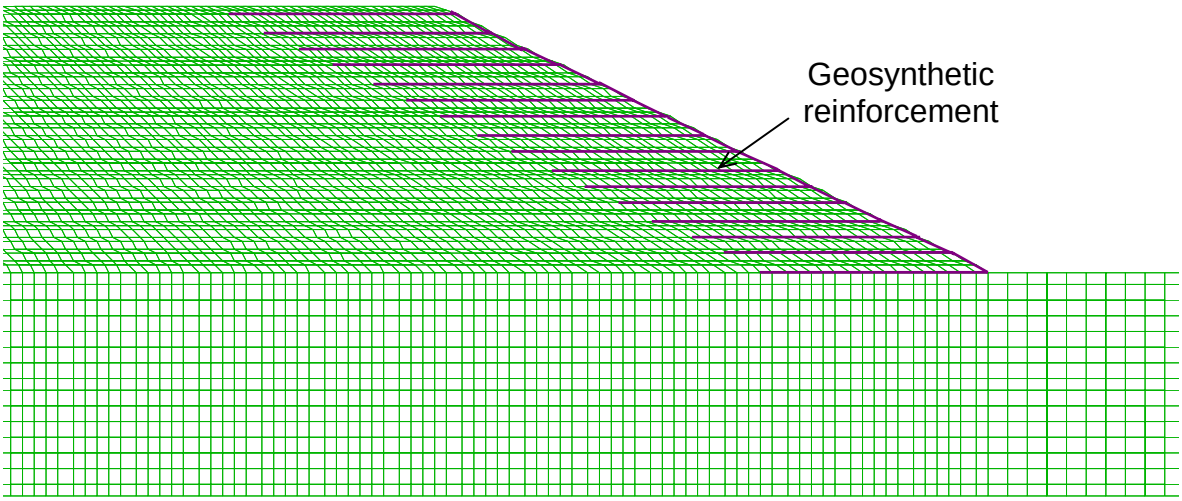

Figure 6.2 Numerical grid of geosynthetic-reinforced clay/silt slope

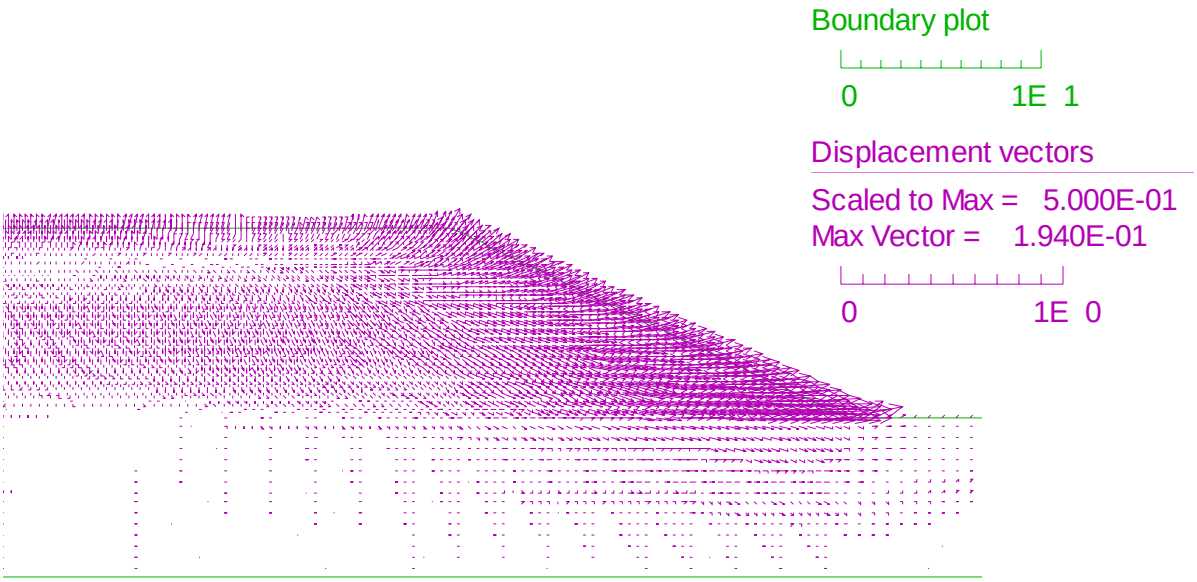

Figure 6.3 Wetting-induced displacement vectors of unreinforced clay slope in full wetting of fill

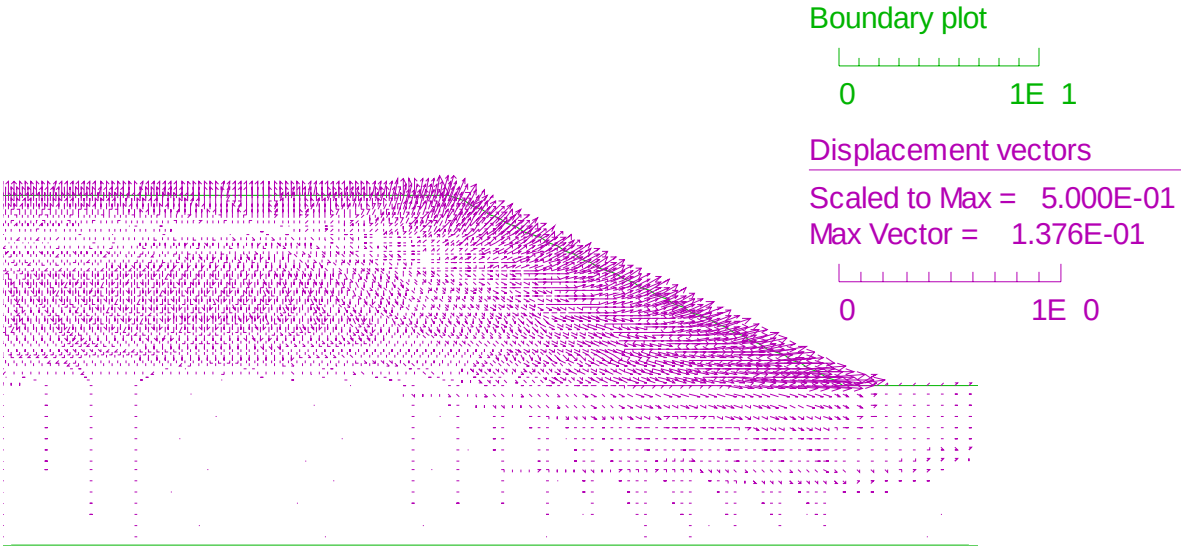

Figure 6.4 Wetting-induced displacement vectors of geosynthetic-reinforced clay slope in full wetting of fill

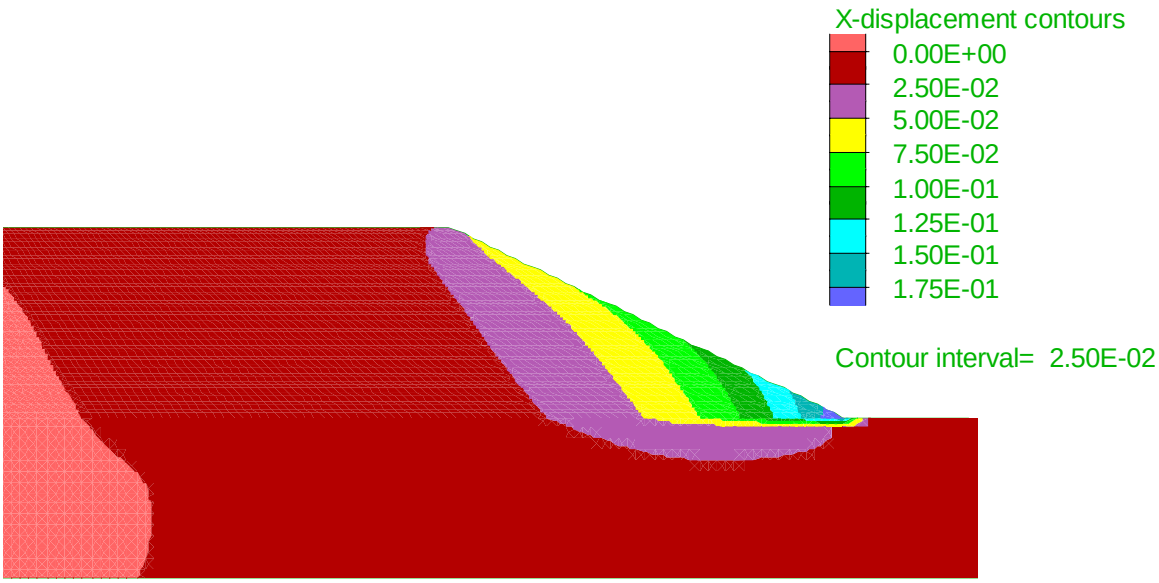

Figure 6.5 Wetting-induced horizontal displacement contours of unreinforced clay slope in full wetting of fill

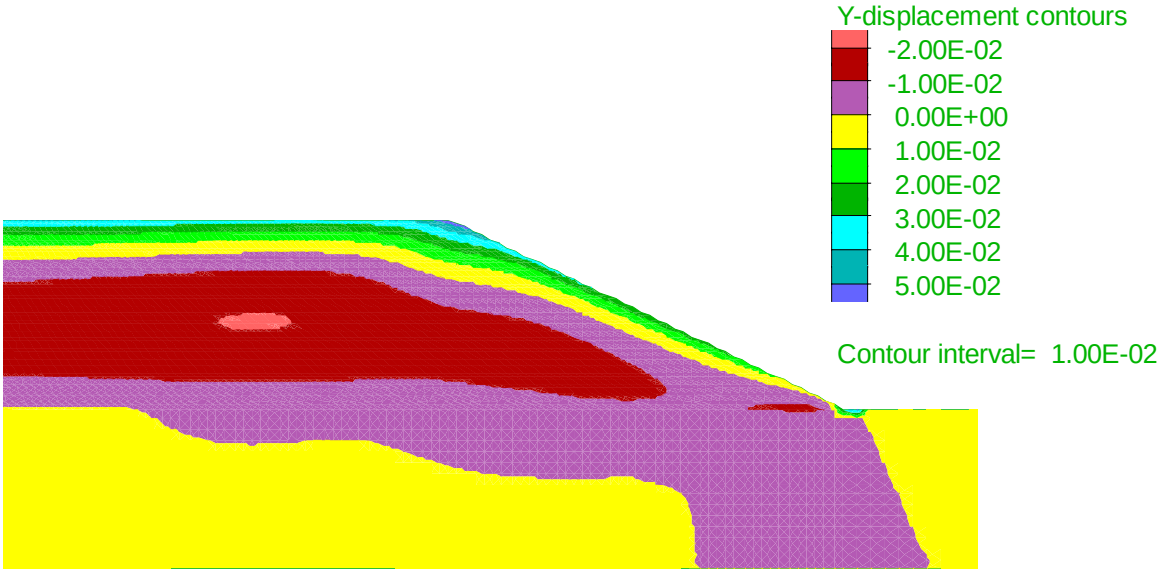

Figure 6.6 Wetting-induced vertical displacement contours of unreinforced clay slope in full wetting of fill

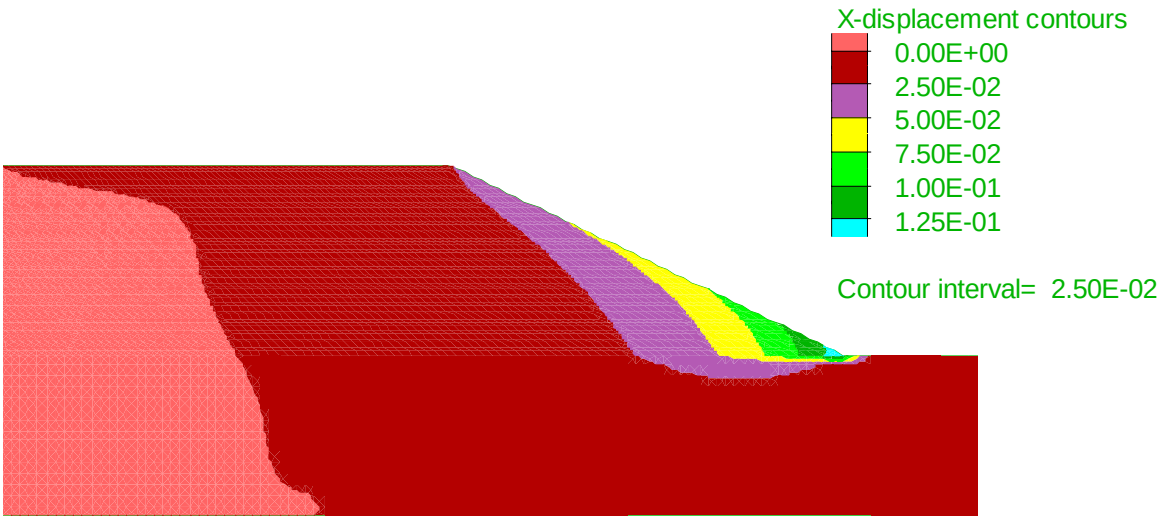

Figure 6.7 Wetting-induced horizontal displacement contours of geosynthetic-reinforced clay slope in full wetting of fill

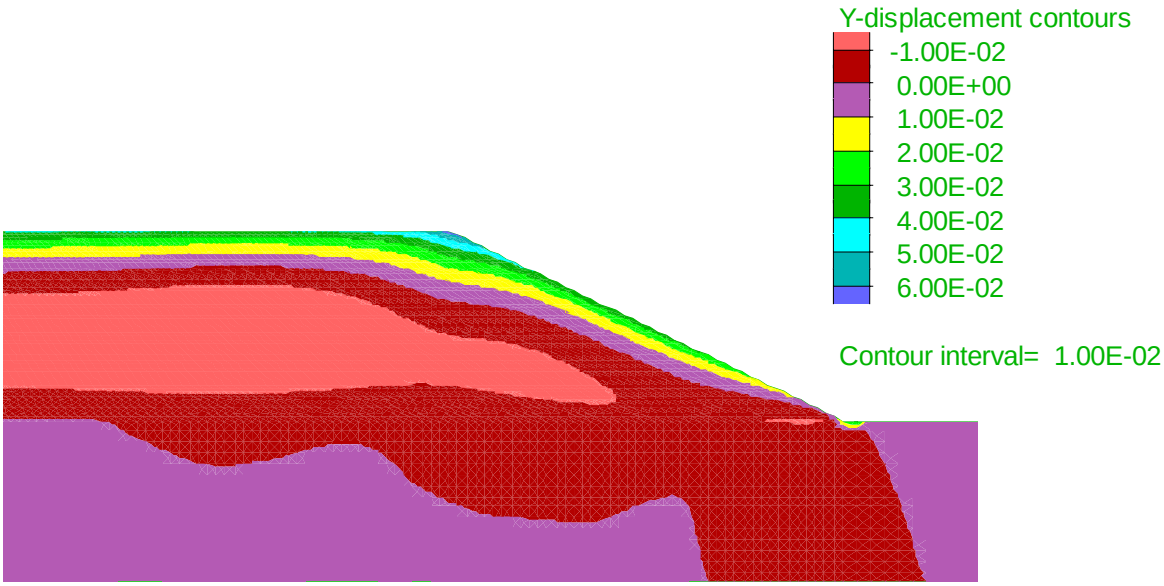

Figure 6.8 Wetting-induced vertical displacement contours of geosynthetic-reinforced clay slope in full wetting of fill

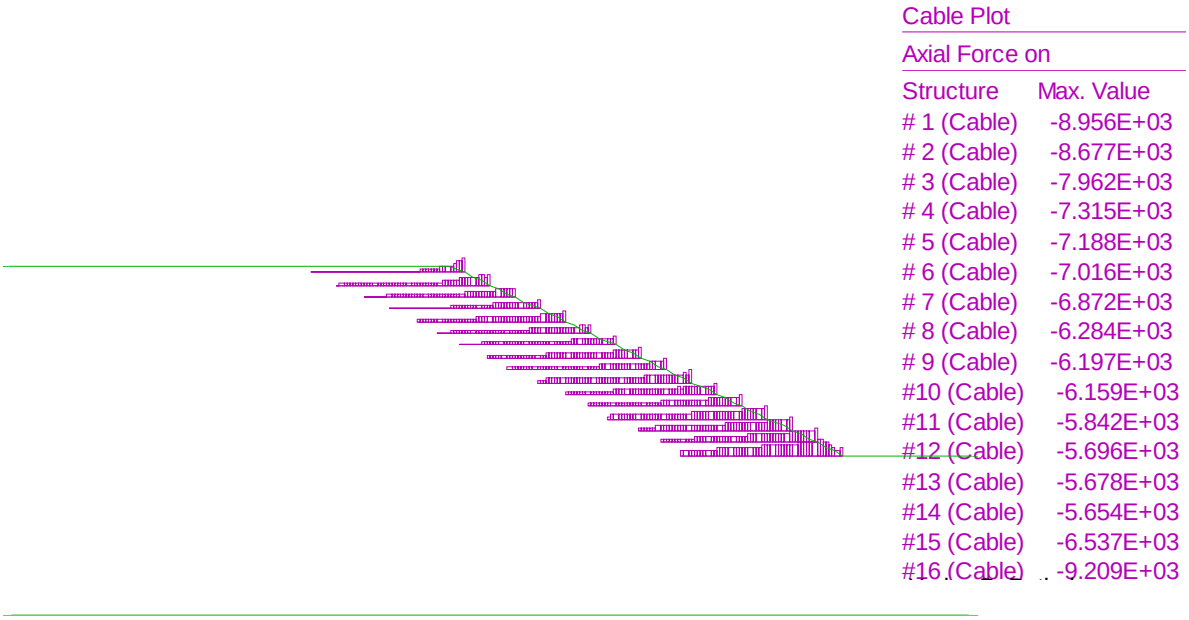

Figure 6.9 Axial force in reinforcement after full wetting of geosynthetic-reinforced clay fill

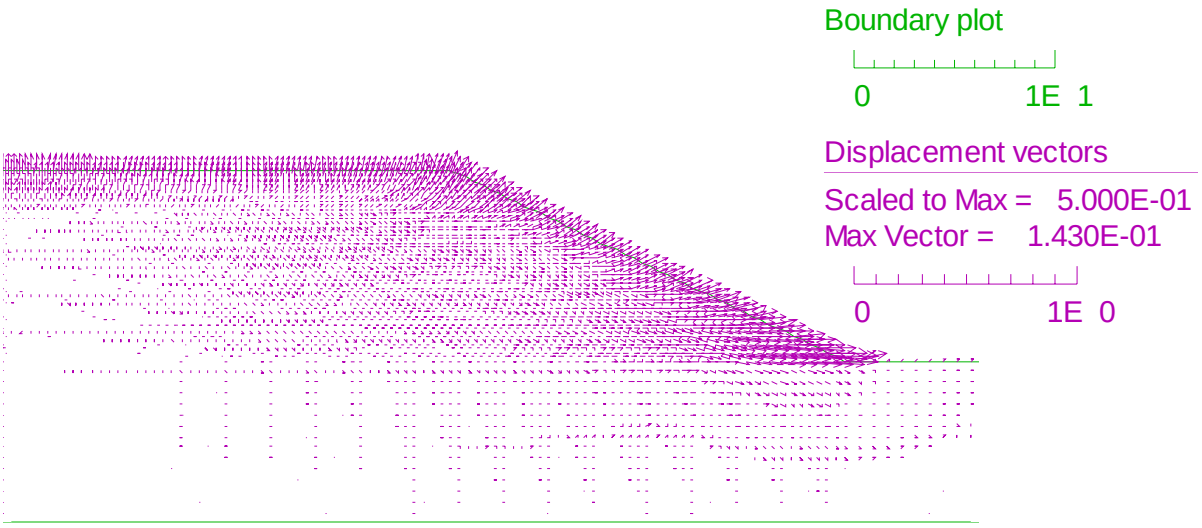

Figure 6.10 Wetting-induced displacement vectors of unreinforced clay slope in partial wetting of fill

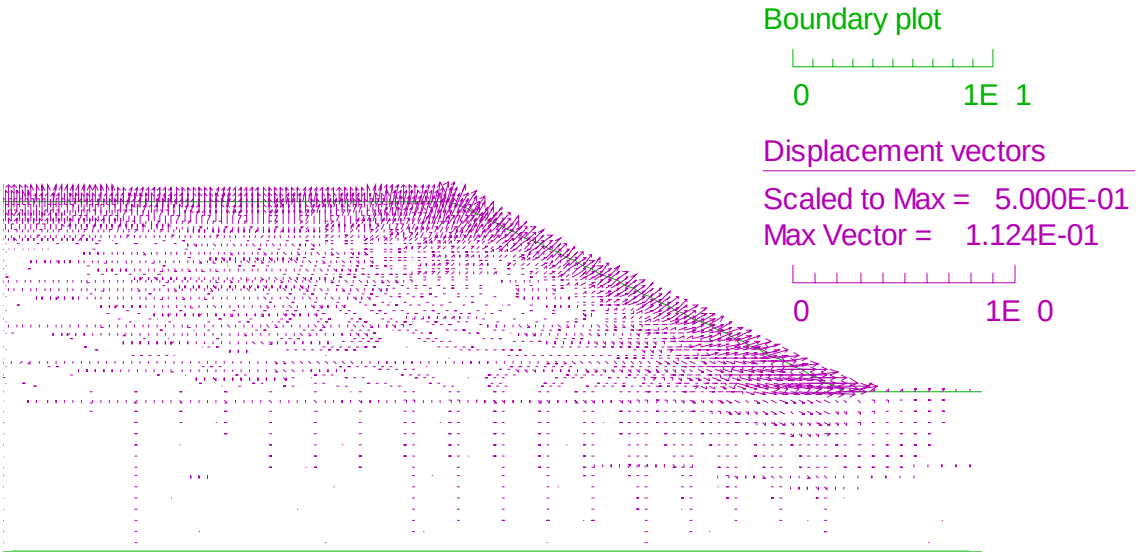

Figure 6.11 Wetting-induced displacement vectors of geosynthetic-reinforced clay slope in partial wetting of fill

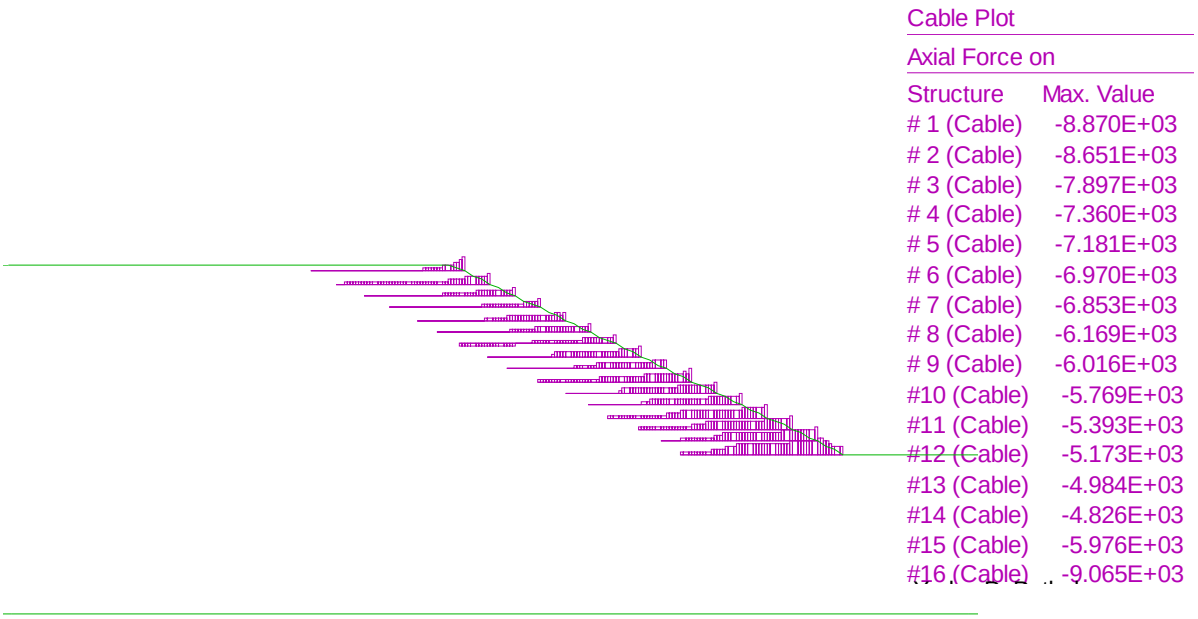

Figure 6.12 Axial force in reinforcement after partial wetting of geosynthetic-reinforced clay fill

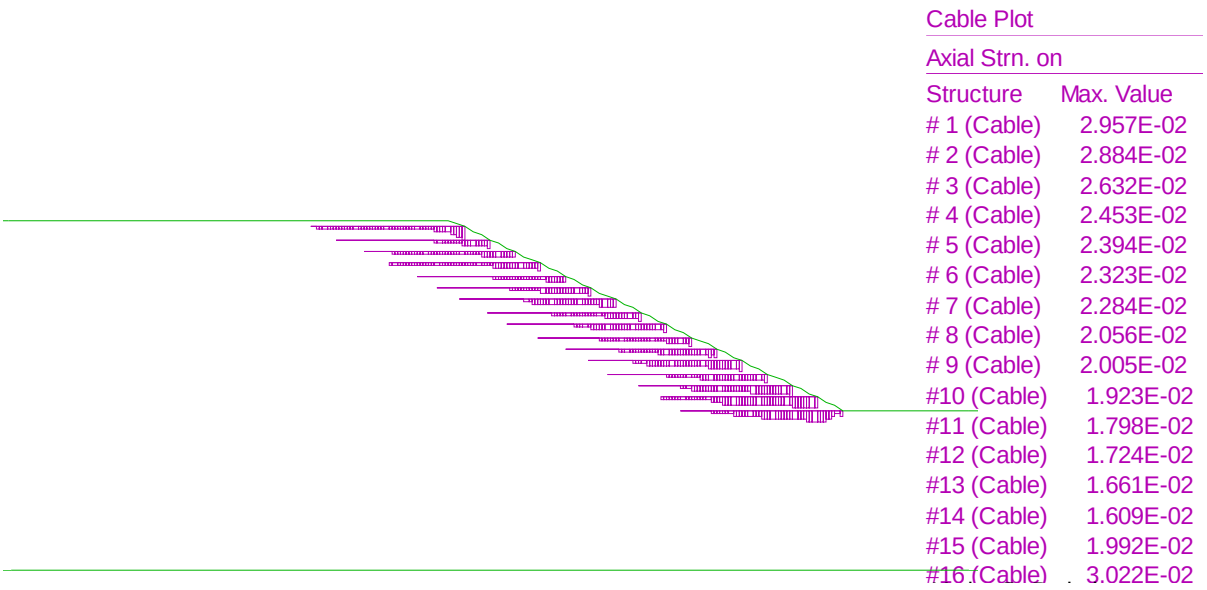

Figure 6.13 Axial strain in reinforcement after partial wetting of geosynthetic-reinforced clay fill

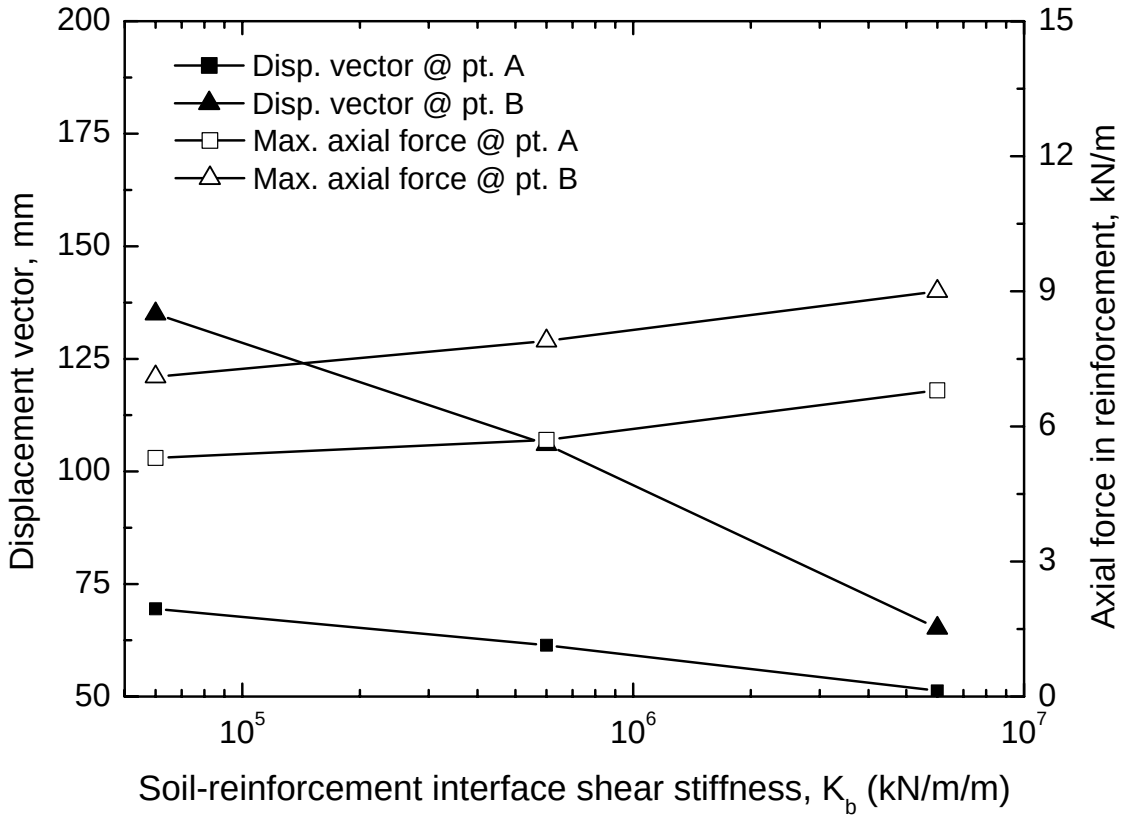

Figure 6.14 Influence of clay-reinforcement interface shear stiffness in geosynthetic-reinforced clay slope

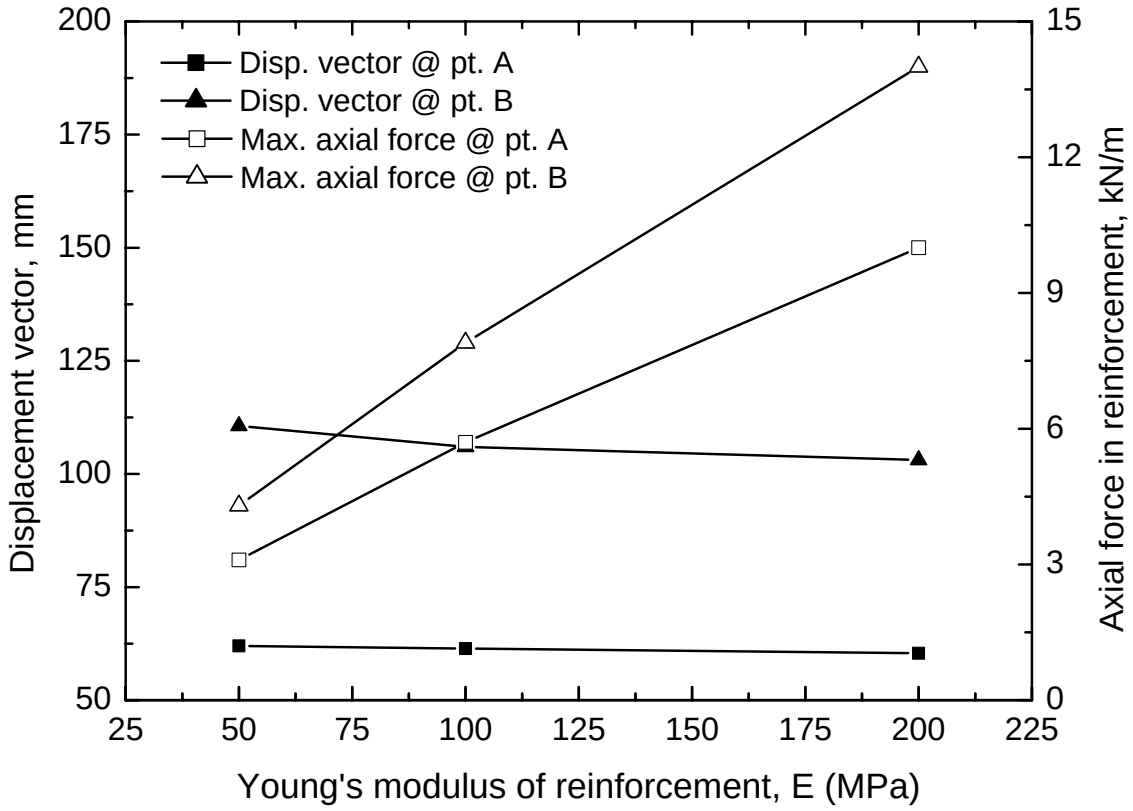

Figure 6.15 Influence of Young's modulus of reinforcement in geosynthetic-reinforced clay slope

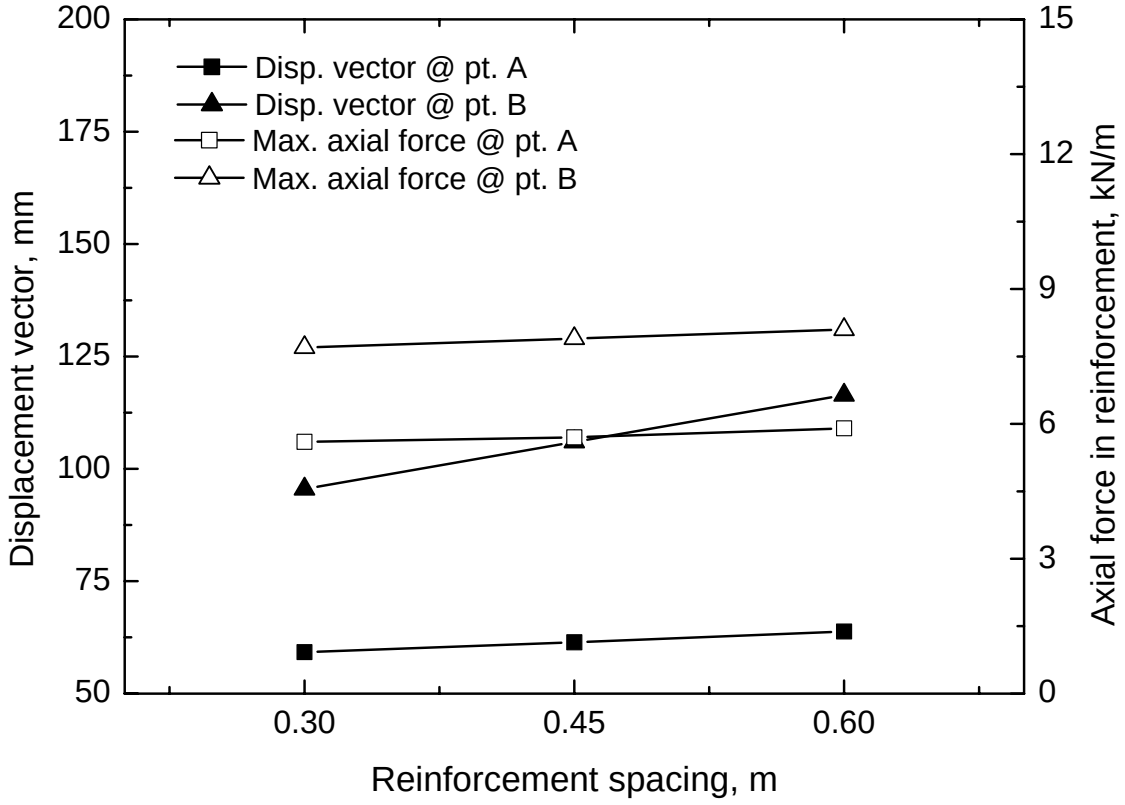

Figure 6.16 Influence of reinforcement spacing in geosynthetic-reinforced clay slope

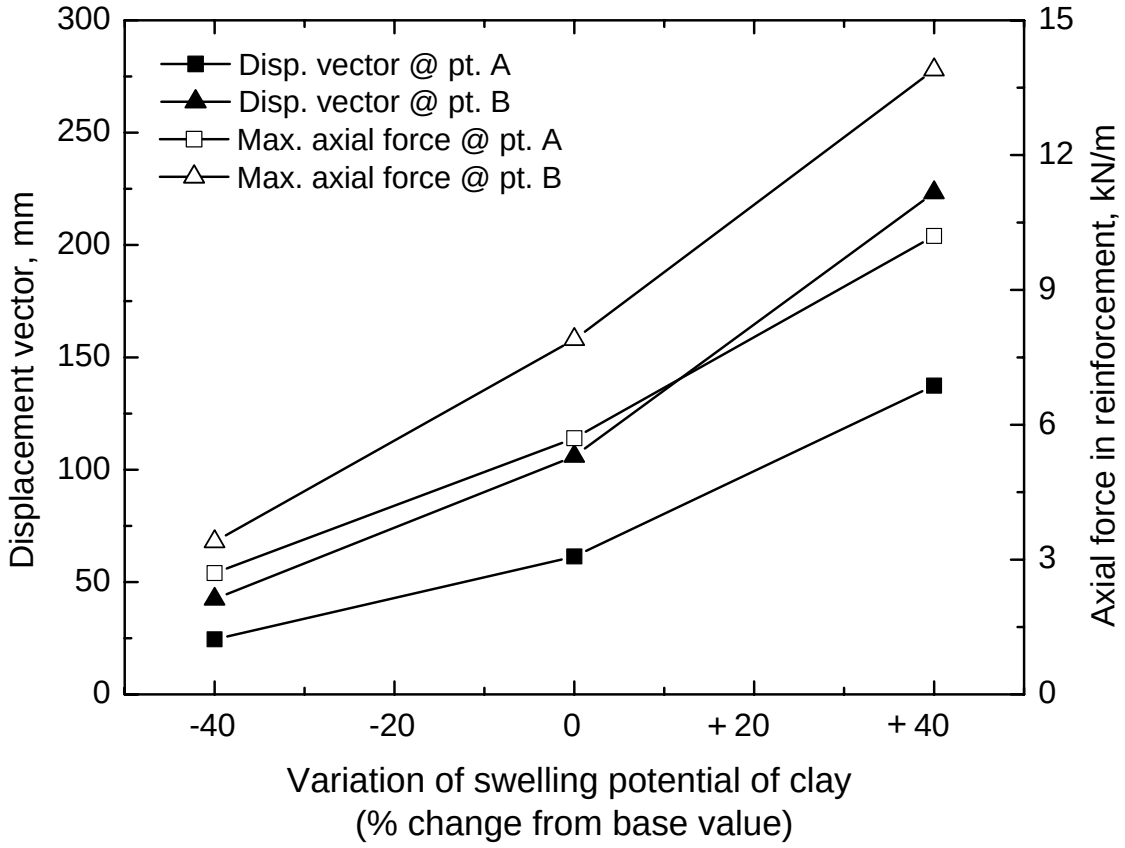

Figure 6.17 Influence of swelling potential of clay in geosynthetic-reinforced clay slope

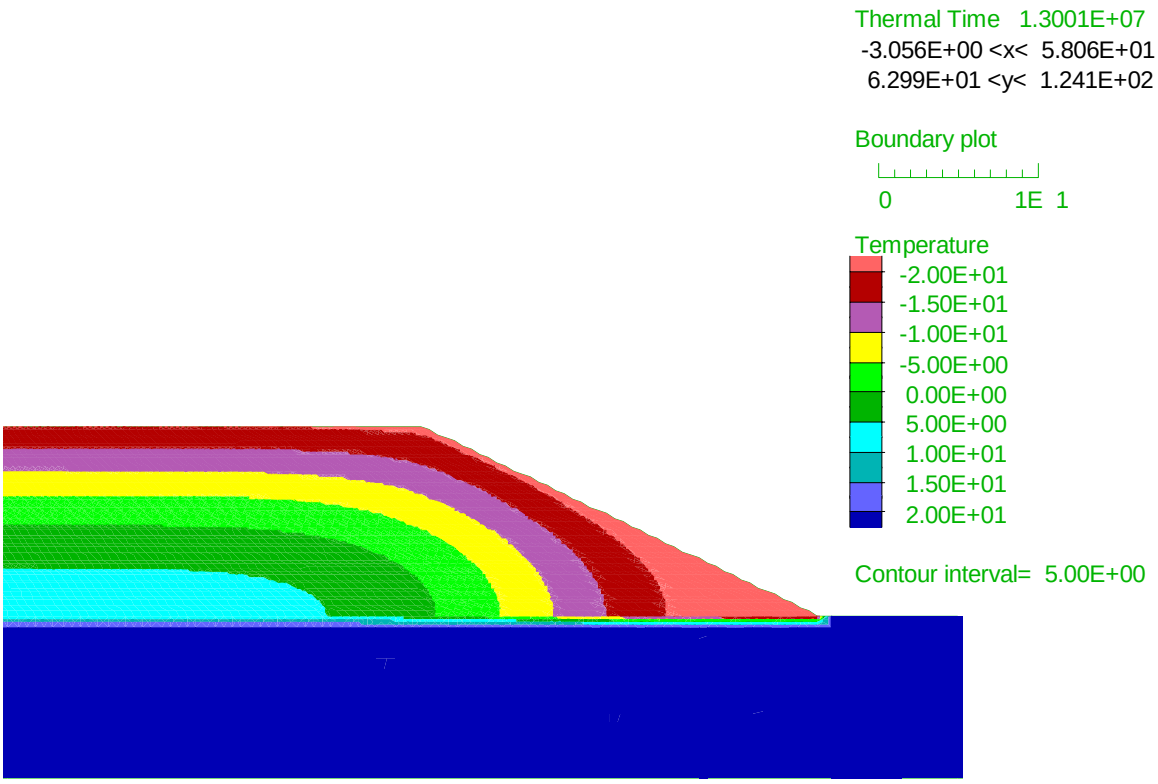

Figure 6.18 Freezing-induced temperature contours of unreinforced silt slope

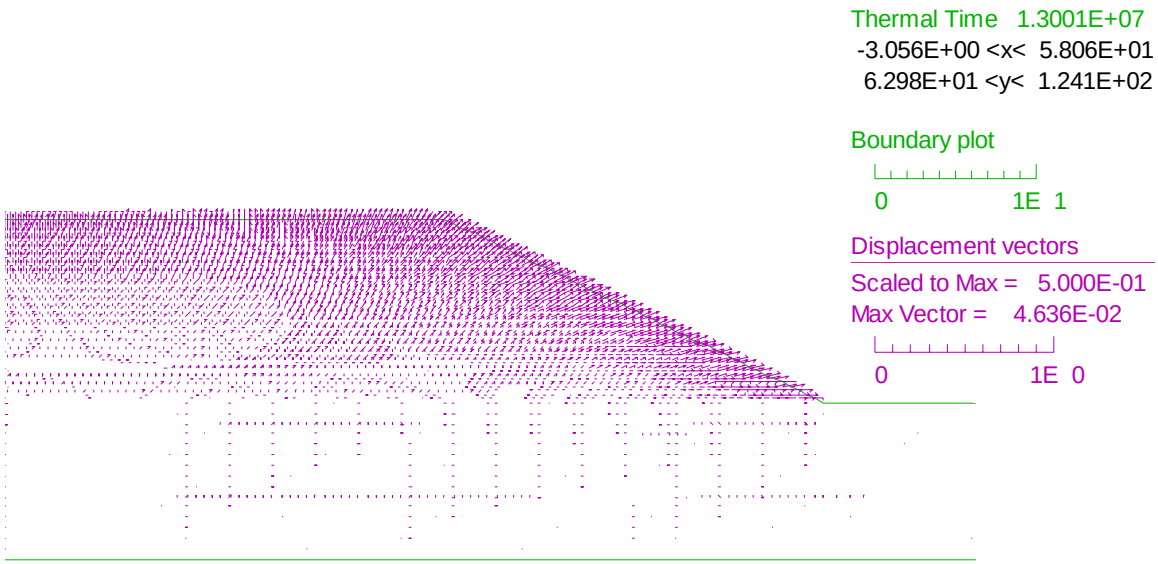

Figure 6.19 Freezing-induced displacement vectors of unreinforced silt slope

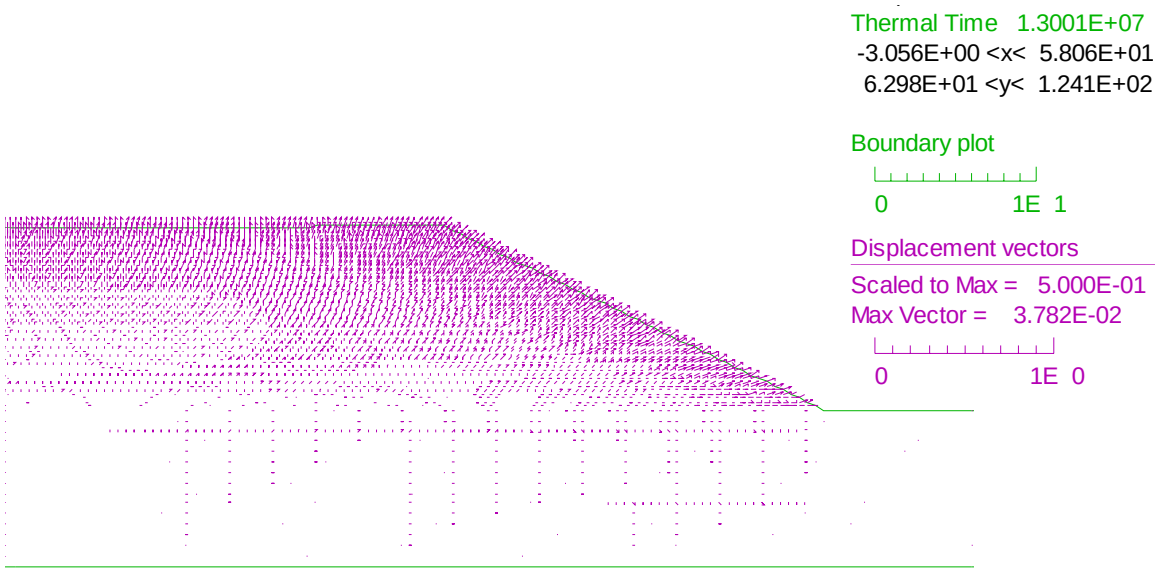

Figure 6.20 Freezing-induced displacement vectors of geosynthetic-reinforced silt slope

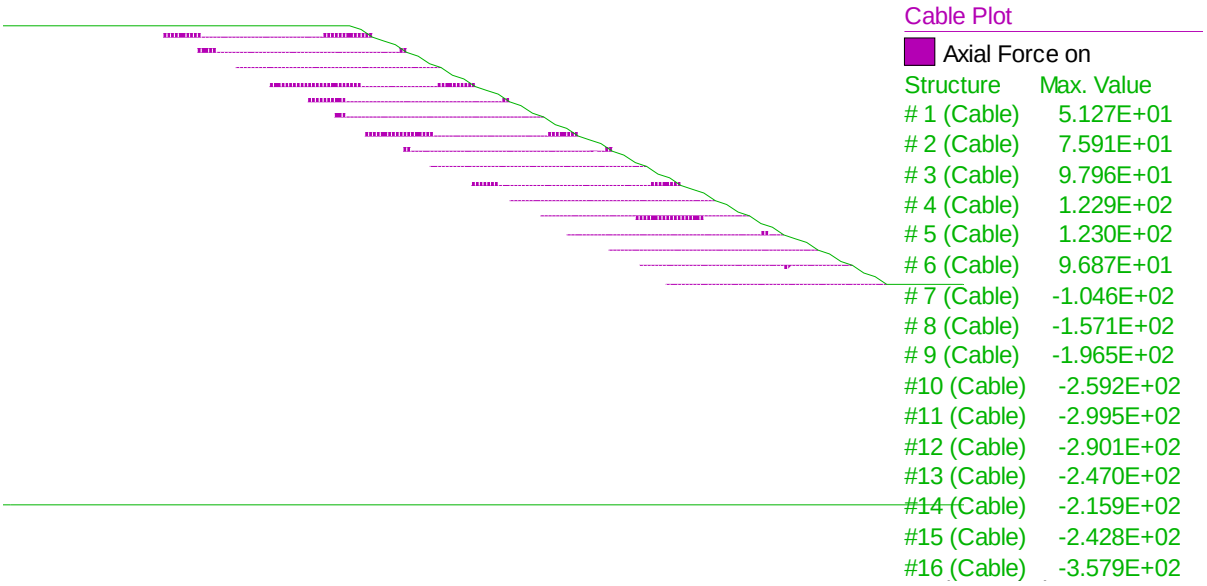

Figure 6.21 Axial force in reinforcement of geosynthetic-reinforced silt slope during mechanical loading condition

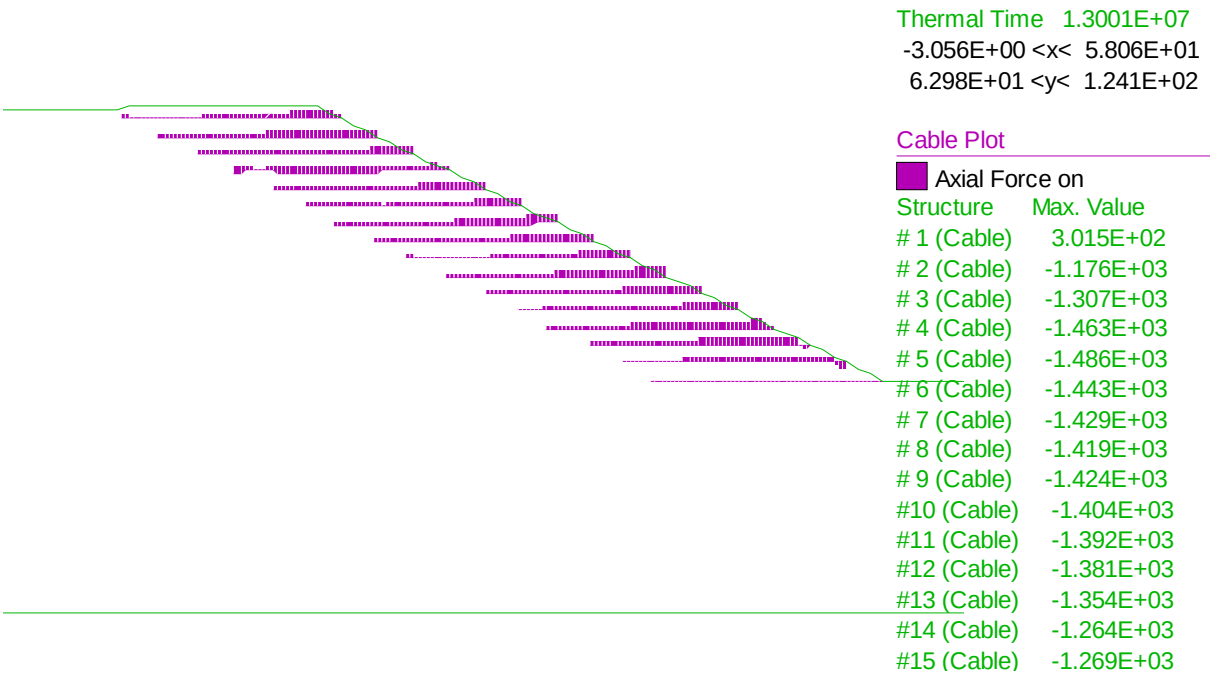

Figure 6.22 Axial force in reinforcement of geosynthetic-reinforced silt slope during freezing

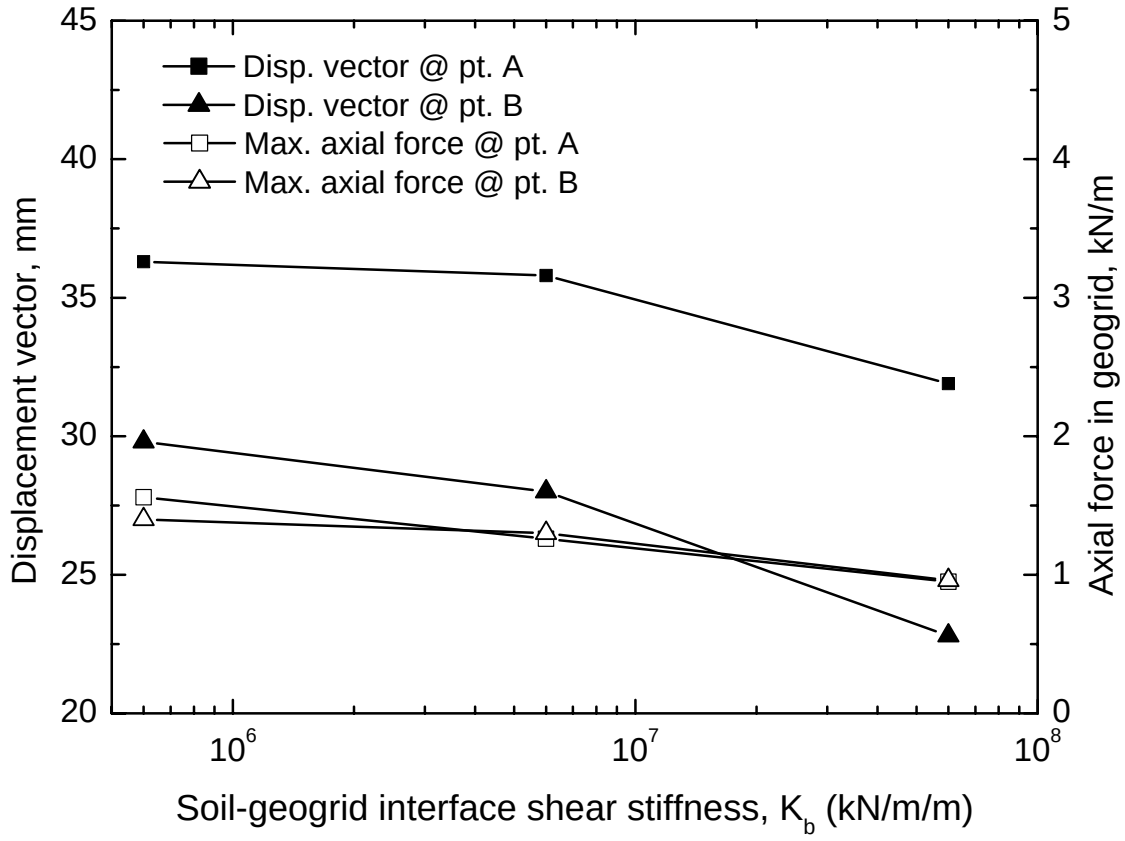

Figure 6.23 Influence of silt-reinforcement interface shear stiffness in geosynthetic-reinforced silt slope

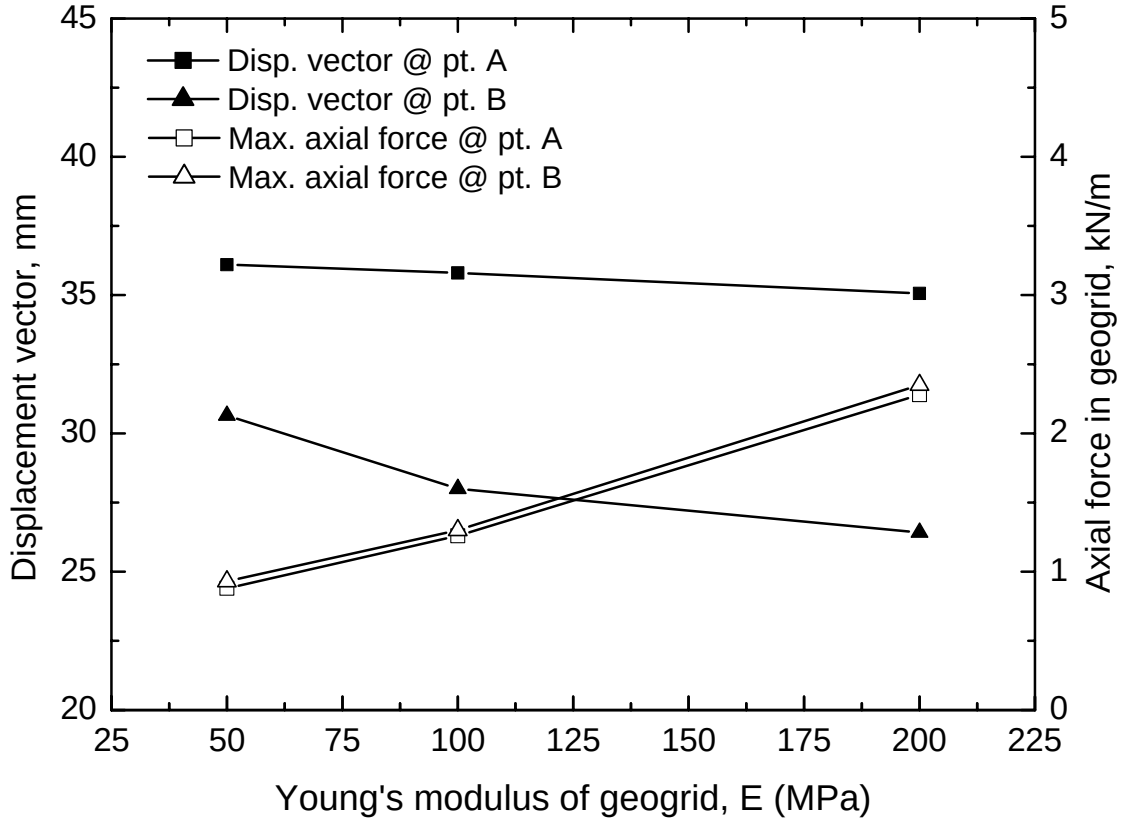

Figure 6.24 Influence of Young's modulus of reinforcement in geosynthetic-reinforced silt slope

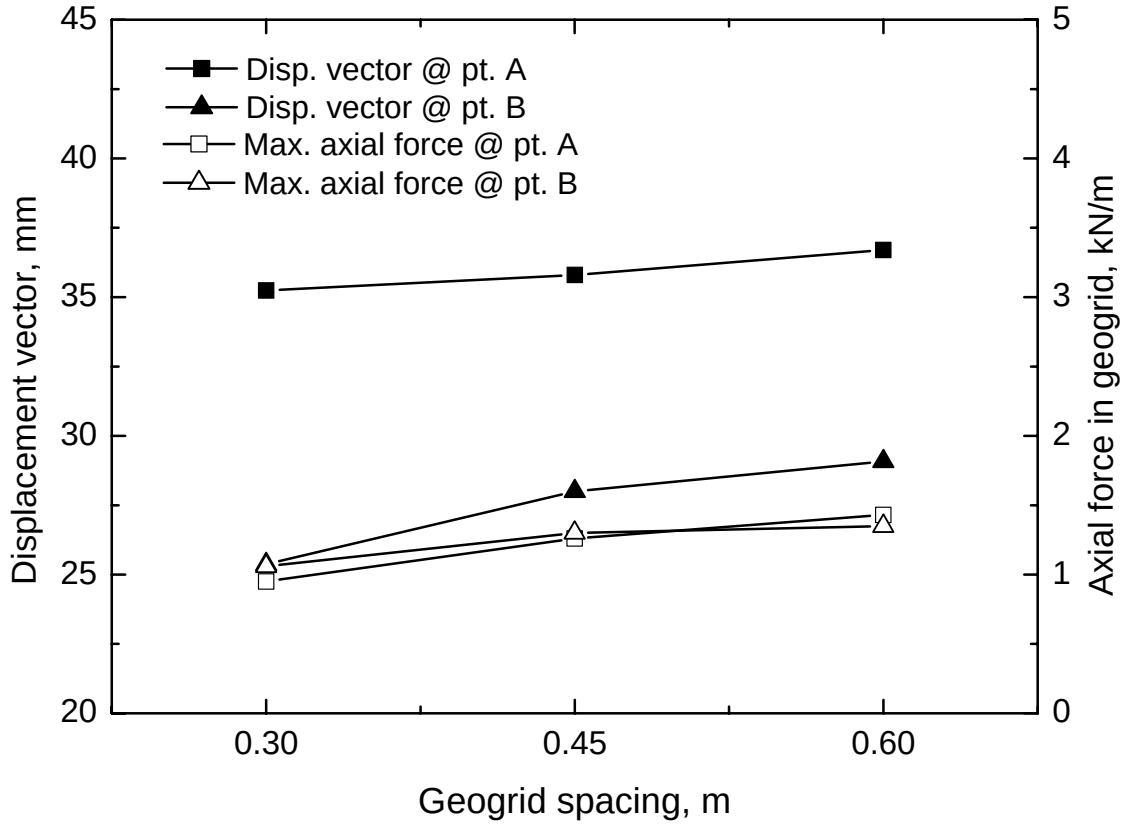

Figure 6.25 Influence of reinforcement spacing in geosynthetic-reinforced silt slope

CHAPTER 7

CONCLUSIONS AND RECOMMENDATIONS FOR FUTURE RESEARCH

7.1 GENERAL

The current design guidelines of AASHTO and FHWA for reinforced soil walls and slopes recommend granular soil with low fines for reinforced fills. Consequently, the economic benefits of reinforced soil walls and slopes are largely limited by the availability and cost of imported granular soils. Cost savings could potentially be realized by using on-site native soils or lower cost quarried materials, mostly fine-grained soils (marginal soils) found in most parts of Manitoba. Clays and silts are often readily available but granular soils need to be imported at construction sites. However, clays in Manitoba are generally swelling clay, while silts are frost susceptible. Concerns about using marginal soils as backfills in the reinforced zones of the GRS structures include the low permeability and their high susceptibility to the environmental changes, particularly wetting-drying and freezing-thawing.

When considering the use of swelling clays and frost susceptible silts for reinforced fills, swelling-shrinkage and freeze-thaw become important considerations relative to the performance of the GRS structures and reinforcing elements. There are only limited studies regarding the effects of environmental changes in GRS structures that use marginal soils as backfills. Thus, this research focused mainly on assessing the effects of environmental loading in the GRS structures. The main objectives were: 1) to evaluate the additional stresses/strains induced in the reinforcement due to frost heave and wetting-induced swelling of marginal soils, and 2) to investigate the deformations that operate in geosynthetic-reinforced soil during environmentally induced swelling and frost heave.

Laboratory testing and numerical modelling were performed to accomplish the research objectives. Laboratory tests were conducted under plane-strain conditions to simulate wetting-drying and freezing-thawing effects in geogrid-reinforced clay and silt specimens respectively. These tests include using an innovative unit cell that was developed and commissioned by the author at the University of Manitoba. They were conducted under anisotropic loading conditions.

Numerical analyses were carried out to develop an understanding of the deformations of GRS structures and reinforcement loads under wetting only induced swelling of clays and freezing only induced expansion of silts. The

numerical models were validated with the laboratory test results and then, these were used to analyse the performance of geosynthetic-reinforced slopes with swelling clay and frost susceptible silt fills. A parametric study was performed to evaluate important parameters affecting the performance of reinforced slopes.

The following sections present the conclusions based on this study and the recommendations for future studies.

7.2 CONCLUSIONS

7.2.1 Wetting-Drying Tests in Geogrid-Reinforced Clay Specimen

1) Wetting-drying of swelling clay induces additional strains (thus, additional tensile loads) in geogrid reinforcements. Measured geogrid strain during the test reached up to 0.75%. In practice, the design working strains of geogrids are generally about 1-2%. There is a possibility that irrecoverable strains during wetting-drying cycles can reach values higher than these working design strains of the geogrid.
2) Geogrid reinforcements reduced the horizontal displacements of reinforced clay specimens during wetting of clays. The reduction of horizontal swelling in the reinforced clay specimen was observed to be about 20% compared to that in the unreinforced clay specimen.

3) Relative movement (slippage) was observed between soil and geogrid during wetting. Incorporation of soil-geogrid interface elements, particularly on simulations of reinforced swelling clays, is recommended for more accurate numerical analysis of the performance of reinforced soil structures with swelling clay backfills.

7.2.2 Freezing-Thawing Tests in Geogrid-Reinforced Silt Specimen

1) Freezing-thawing of silt induces additional strains. Measured geogrid strains at the end of twelve freezing-thawing cycles in the reinforced silt specimen were in the order of 0.57%.
2) Most of the observed deformations were in the horizontal direction. Geogrids reduce the horizontal displacements during freezing-thawing cycles. The reduction of horizontal displacement in the reinforced silt specimen was observed to be about 45% compared to that in the unreinforced silt specimen.
3) Similar to that in the reinforced clay specimens, relative movement was observed between silt and geogrid. Soil-geogrid interface elements that simulate the observed slippage need to be included in the analysis of performance of GRS structures subjected to freeze and thaw.

7.2.3 Numerical Analyses of Geosynthetic-Reinforced Clay Slopes

1) The numerical models developed in this study are found to be reasonably capable of simulating the behaviour of geosynthetic-reinforced swelling clay both in mechanical loading and wetting only conditions.
2) Axial loads induced in the reinforcements due to wetting only were predicted to be a maximum 9 kN/m. It was shown that higher reinforcement loads occurred near the slope surface. This is consistent with higher deformations at this location.
3) Geosynthetic-reinforcements reduce the swelling of reinforced clay slope during wetting only. The reduction of the horizontal displacements of reinforced clay slope was predicted to be about 27% compared to that in the unreinforced clay slope.
4) Because of their superior interaction with clay backfills, the grid-type of geosynthetic reinforcement will perform better in reducing swelling-induced deformations. The grid apertures produce higher bearing and frictional resistance with clays than planar geosynthetic reinforcement.

7.2.4 Numerical Analyses of Geosynthetic-Reinforced Silt Slopes

1) The simple thermal-mechanical coupling performed in this study provided meaningful results in understanding the deformation behaviour of the geosynthetic-reinforced silt slopes during freezing only.

2) Freezing only induced deformations in the reinforced silt slopes were relatively small. This also results in smaller additional loads/strains induced in the reinforcements. The reinforcement loads are predicted to be a maximum 1.35 kN/m. It should be noted that the predicted strains are only due to initial freezing rather than the accumulated strains expected for freeze-thaw cycles.
3) Geosynthetic reinforcements reduced the horizontal expansion by 20% in a reinforced silt slope compared to that in the unreinforced slope.
4) For reinforced fills using frost susceptible silts, reinforcements that can provide higher bearing and frictional resistances are preferable because of possible slippage between the reinforcement and the fill during freezing.

7.3 RECOMMENDATIONS FOR FUTURE RESEARCH

7.3.1 Full-Scale Geosynthetic-Reinforced Clay/Silt Slopes

It is always desirable to fine-tune numerical models and laboratory test results with actual structures. This requires construction and monitoring of one or more full-scale instrumented geosynthetic-reinforced soil slopes in the field using marginal soil backfills. The instrumentation and monitoring program should be designed to record overall deformations of the fill slopes and the foundation soils, soil suctions and temperatures within the fill, the interaction between the soil and geosynthetic-reinforcements, and pore-water pressures in the slopes.

Extensometer, inclinometer, settlement plates, thermocouples or thermistors, psychrometers, strain gauges and piezometers should be installed to measure the overall performance. Both reinforced and unreinforced sections should be instrumented for comparison purposes.

7.3.2 Soil-Geogrid Interaction

Loads in geosynthetic-reinforcements are mobilized by soil movements through load transfer along the interface between the soil and the reinforcement. Interaction between the two materials becomes a key factor in understanding how this transfer of loads may be reduced, particularly during wetting or thawing conditions, or increased in drying or freezing conditions. Pullout tests where clays are wetted and dried and where the silts are frozen and thawed would provide information about the load transfer behaviour of soil-geogrid interactions under several environmental loading conditions. These require developing techniques to facilitate quick drying and wetting of thick samples of clay materials (about 40 cm thick in our pullout test apparatus at the University of Manitoba). A walk-in temperature-controlled chamber is available at the University of Manitoba for the thawing and freezing of silts. This chamber was used in the freezing-thawing tests in this study. The stiffness of reinforcement under warm and cold temperatures should also be determined so that they can be appropriately used in numerical simulations for freezing and thawing conditions.

7.3.3 Advanced Laboratory Testing and Numerical Modelling

This study can be extended further by performing advanced laboratory testing to determine the sophisticated parameters that are required in the BBM. BBM needs to be extended to incorporate wetting-drying effects in lieu of a very simplified swelling model. Thermal model parameters also need to be measured in the laboratory. In addition, water migration to negative water potentials at the freezing front needs to be modeled in the laboratory so that the numerical models used in this study can be modified to incorporate water migration mechanisms. This mechanism is most likely applicable in field conditions during freezing.

The numerical simulation in this study did not include the behaviour of the reinforced slopes under wetting-drying cycles and freezing-thawing cycles. This needs to be done to understand the long-term performance of geosynthetic-reinforced clay or silt slopes.

REFERENCES

AASHTO 2000. Standard specifications for highway bridges. American Association of State Highway and Transportation Officials, Seventeenth Edition, Washington, D.C., USA.

Allam, M.M. and Shridharan, S. 1981. Effect of wetting and drying on shear strength. Journal of Geotechnical Engineering, ASCE, 107(4): pp. 421-438.

Al-Omari, R.R. and Hamodi, F.J. 1991. Swelling resistant geogrid – a new approach for the treatment of expansive soils. Geotextiles and Geomembranes, 10: pp. 259-317.

Al-Omari, R.R. and Oraibi, W.R. 2000. Cyclic behaviour of reinforced expansive clay. Soils and Foundations, 40(2): pp. 1-8.

Alonso, E.E., Gens, A. and Josa, A. 1990. A constitutive model for partially saturated soils. Geotechnique, 40(3): pp. 405-430.

Andersland, O.B. and Ladanyi, B. 2004. Frozen Ground Engineering. Second edition, John Wiley & Sons, Inc., pp. 363.

ASTM D4546 - 1996. Standard test methods for one-dimensional swell or settlement potential of cohesive soils. Annual book of ASTM Standards, pp. 693-699.

Bergado, T.D., Menil, N.J.L., Rimoldi, P. and Douglas, R.S. 1994. Performance of full scale embankment on soft Bangkok clay with Tenax geogrid reinforcement. Proc. Fifth International Conference on Geotextiles, Geomembranes and Related Products, Singapore, 1: pp. 1-4.

Boyle, S.R. 1995. Unit cell tests on reinforced cohesionless soils. Proc. Geosynthetics'95, North American Conference, Nashville, Tennessee, USA, pp. 1221-1234.

Briscoe, R.D. 1984. Thermocouple psychrometers for water potential measurements. Proc. NATO Advanced Study Institute on 'Advanced Agricultural Instrumentation', II Ciocco (Pisa), Italy, May 27-June 9, 1984.

Broms, B.B. 1977. Triaxial tests with fabric-reinforced soil. Proc. International Conference on the use of Fabrics in Geotechnics, Paris, France, 3: pp. 129-133.

Carder, D.R., Pocock, R.G., and Murray, R.T. 1977. Experimental retaining wall facility – Lateral stress measurements with sand backfill. Transport and Road Research Laboratory, Report No. LR 766, Crowthorne, England.

Christopher, B.R. and Stulgis, R.P. 2000. The future of geosynthetics: mechanically stabilized earth walls. Geosynthetics in the Future: Year 2000 and Beyond, Geosynthetic Research Institute, pp. 172-182.

Day, R.W. 1994. Swell-shrink behaviour of compacted clay. Journal of Geotechnical Engineering, ASCE, 120: pp. 618-623.

Dif, A.E. and Bluemel, W.F. 1991. Expansive soils under cyclic drying and wetting. ASTM Geotechnical Testing Journal, 14: pp. 96-102.

Duncan, J.M., Williams, G.W., Sehn, A.L. and Seed, R.B. 1991. Estimation earth pressures due to compaction. Journal of Geotechnical Engineering, ASCE, 117(12): pp. 1833-1847.

Edil, T.B. and Motan, S.E. 1984. Laboratory evaluation of soil suction components. ASTM Geotechnical Testing Journal, 7 (4): pp. 173-181.

Eignbrod, K.D. 1996. Effects of cyclic freezing and thawing on volume changes and permeabilities of soft fine-grained soils. Canadian Geotechnical Journal, 33: pp. 529-537.

FHWA 2001. Mechanically stabilized earth walls and reinforced soil slopes, design and construction guidelines. Publication No. FHWA-NHI-00-043. Federal Highway Administration, Washington, D.C., USA.

Fredlund, D.G. 2005. Personal communication during the short course "Numerical modelling in unsaturated soils" at 57th Canadian Geotechnical Conference and 5th Joint CGS/IAH-CNC Conference, Saskatoon, Saskatchewan, Canada.

Fredlund, D.G. and Rahardjo, H. 1993. Soil Mechanics for Unsaturated Soils. John Wiley and Sons Inc., New York, pp. 517.

Gatto, L.W. and Ferrick, M.G. 2003. Overland erosion due to freeze-thaw cycling: laboratory experiments. Report No. ERDC/CRREL TN-03-3, US Army Crops of Engineers, Engineer Research and Development Center, Cold Regions Research and Engineering Laboratory, pp. 1-16.

GeoStudio 2007. Geo-Slope International Ltd., Calgary, Alberta, Canada.

Graham, J. and Au, V.C.S. 1985. Effects of freeze-thaw and softening on natural clay at low stresses. Canadian Geotechnical Journal, 22: pp. 69-78.

Henry, K.S. 1998. The use of geosynthetics to mitigate frost heave in soils. PhD Thesis, Civil Engineering Department, University of Washington, Seattle, USA, pp.333.

Hansson, K. and Lundin, L.C. 2006. Equifinality and sensitivity in freezing and thawing simulations of laboratory and in situ data. Cold Regions Science and Technology, 44: pp. 20-37.

Hayden, R.F., Schmertmann, G.R., Qedan, B.Q. and McGuire, M.S. 1991. High clay embankment over Canon Creek constructed with geogrid reinforcement. Proc. Geosynthetics ’91, North American Conference, Atlanta, Georgia, USA, pp. 799-822.

Holtz, R.D., Tobin, W.R. and Burke, W.W. 1982. Creep characteristics and stress-strain behaviour of a geotextile-reinforced sand. Proc. Second International Conference on Geotextiles, IFAI, Las Vegas, Nevada, USA, pp. 805-809.

Ingold, T.S. 1983. Reinforced clay subject to undrained triaxial loading. Journal of Geotechnical Engineering, ASCE, 109(5): pp. 738-744.

Ingold, T.S., and Miller, K.S. 1983. Drained axisymmetric loading of reinforced clay. Journal of Geotechnical Engineering, ASCE, 109(7): pp. 883-898.

Itasca Consulting Group 2001. FLAC - Fast Lagrangian Analysis of Continua. Version 4.00. Itasca Consulting Group Inc., Minneapolis, Minnesota,USA.

Janson, L. 1963. Frost penetration in sandy soil. Goteborg, Sweden: Elanders Boktrychkeri, pp. 165.

Johnston, G.H., Ladanyi, B., Morgenstern, N.R., and Penner, E. 1981. Engineering characteristics of frozen and thawing soils. Permafrost Engineering Design and Construction, edited by Johnston, G.H., John Wiely & Sons. (Source: TEMP/W manual 2004)

Kersten, M.S. 1949. Thermal properties of soils. University of Minnesota Engineering Experiment Station Bulletin No. 28. (Source: http://training.ce.washington.edu/WSDOT/Modules/04_design_programs/frost_terminology.htm)

Ketchart, K. and Wu, J.T.H. 2002. A modified soil-geosynthetic interactive performance test for evaluating deformation behaviour of GRS structures. Journal of Geotechnical Testing, 25(4): pp. 405-413.

Konrad, J.M. 1993. Sixteenth Canadian geotechnical colloquium: frost heave in soils: concepts and engineering. Canadian Geotechnical Journal, 31: pp. 223-245.

Lawton, E.C., Fragaszy, R.J. and Hetherington, M.D. 1992. Reviewing of wetting-induced collapse in compacted soil. Journal of Geotechnical Engineering, ASCE, 118(9): pp. 1376-1394.

Ling, H.I. and Tatsuoka, F. 1994. Performance of anisotropic geosynthetic-reinforced cohesive soil mass. Journal of Geotechnical Engineering, ASCE, 120 (7): pp. 1166-1184.

Liu, Y., Scott, J.D. and Sego, D.C. 1994. Geogrid reinforced clay slopes in a test embankment. Geosynthetics International, 1(1): pp. 67-91.

Massarsch, K.R. 1979. Lateral earth pressure in normally consolidated clay. Proc. Seventh European Conference on Soil Mechanics and Foundation Engineering, Brighton, England, 2: pp. 245-250.

McGown, A., Andrawes, K.Z., and Al-Hasani, M.M. 1978. Effect of inclusion properties on the behaviour of sand. Geotechnique, 28(3): pp. 327-346.

McGown, A., Yogarajah, I., Andrawes, K.Z. and Saad, M. 1995. Strain behaviour of polymeric geogrids subjected to repeated loading in air and soil. Geosynthetics International, 2(1): pp. 341-355.

Ng, C.W.W., Zhan, L.T. Bao, C.G., Fredlund, D.G. and Gong, B.W. 2003. Performance of an unsaturated expansive soil slope subjected to artificial rainfall infiltration. Geotechnique, 53 (2): pp. 143-157.

Noorany, I., Frydman, S. and Detournay, C. 1999. Prediction of soil slope deformation due to swelling. FLAC and Numerical Modeling in Geomechanics. A.A. Balkema Publishers, pp. 101-107.

Noorany, I., Sweet, J.A. and Smith, I.M. 1992. Deformation of fill slopes caused by wetting. Proc. ASCE Conf. on stability and performance of slopes and embankments II, ASCE Geotechnical special publication No. 31, New York, New York, USA, pp. 1244-1257.

Pathak, Y.P. and Alfaro, M.C. 2005b. Behaviour of geogrid-reinforced clay under wetting-drying cycle. Proc. GeoSask2005, 58th Canadian Geotechnical Conference, Saskatoon, Saskatchewan, Canada. (Proceedings in CD-ROM)

Pathak, Y.P. and Alfaro, M.C. 2005a. Laboratory simulation of seasonal wetting-drying cycles on geosynthetic-reinforced clay slopes and embankments. Proc. Geo-Frontiers 2005, ASCE Geotechnical Special Publications 130-142 and GRI-18 Geosynthetics Research and Development in Progress, Austin, Texas, USA. (Proceedings in CD-ROM).

Priyanto, D.G., Blatz, J.A., Siemens, G.A. and Graham, J. 2004. The parameter evaluation method (PEM) of elastic-plastic model properties for unsaturated high-plastic clay. Proc. 57th Canadian Geotechnical Conference, Quebec City, Quebec, Canada. (Proceedings in CD-ROM).

Rao, S.M., Reddy, B.V.V. and Mutthara, M. 2001. The impact of cyclic wetting and drying on the swelling behaviour of stabilized expansive soils. Engineering Geology, 60: pp. 223-233.

Sabatini, P.J., Bachus, R.C., Mayne, P.W., Schneider, J.A. and Zettler, T.E. 2002. Evaluation of soil and rock properties. Report on: Geotechnical Engineering Circular No. 5, FHWA-IF-02-034, pp. 266.

Skempton, A.W. 1954. The pore water coefficients A and B. Geotechnique, 4: pp. 143-147.

Stulgis, R.P. 2005a. Selecting reinforced fill materials for MSE retaining walls. Proc. Geo-Frontiers 2005, ASCE Geotechnical Special Publications 130-

142 and GRI-18 Geosynthetics Research and Development in Progress, Austin, Texas, USA. (Proceedings in CD-ROM).

Stulgis, R.P. 2005b. Full-scale MSE test walls. Proc. NAGS 2005/GRI-19 Conference, Las Vegas, Nevada, USA. (Proceedings in CD-ROM).

Tatsuoka, F., Molenkamp, F., Torii, T. and Hino, T. 1984. Behaviour of lubrication layers of platens in element tests. Soils and Foundations, 24 (1): pp. 113-128.

Tatsuoka, F. and Yamauchi, H. 1986. A reinforcing method for steep clay slopes with a nonwoven geotextile. Geotextile Geomembrane, 4: pp. 241-268.

TEMP/W Manual 2004. Geo-Slope International Ltd., Calgary, Alberta, Canada, pp. 282.

Vessely, M.J. and Wu, J.T.H. 2002. Feasibility of geosynthetic inclusion for reducing swelling of expansive soils. Transportation Research Record, 1787, paper # 02-3423: pp. 42-52.

Vidal, H. 1969. The principle of reinforced earth. Highway Research Record, No. 282, Washington, D.C., USA, pp. 1-16.

Viklander, P. 1998. Permeability and volume changes in till due to cyclic freeze/thaw. Canadian Geotechnical Journal, 35: pp. 471-477.

Viklander P. and Eigenbrod, D. 2000. Stone movements and permeability changes in till caused by freezing and thawing. Cold Regions Science and Technology, 31: pp. 151-162.

Walters, D.L. 2004. Behaviour of reinforced soil retaining walls under uniform surcharge loading. Ph.D. Thesis, Queen's University, Kingston, Ontario, Canada, pp. 404.

Whittle, A.J., Germaine, J.T., Larson, D.G., and Abramento, M. 1992. Measurement and interpretation of reinforcement stresses in the APSR cell. Proc. International Symposium on Earth Reinforcement Practice, Fukuoka, Japan, pp. 179-184.

Wood, D.M. 1990. Soil Behaviour and Critical State Soil Mechanics. Cambridge University Press, Cambridge, pp. 462.

Wu, J.T.H. 1992. Predicting performance of the Denver walls: General report, Proc. International Symposium on Geosynthetic-Reinforced Soil Retaining Walls, Denver, Colorado, USA, pp. 3-20.

Wu, J.T.H. and Helwany, S.M.B. 1996. A performance test for assessment of long-term creep behaviour of soil-geosynthetic composites. Geosynthetics International, 3 (1): pp. 107-124.

Zarnani, S., Scott, J.D. and Sego, D.C. 2005. Long term performance of geogrid strain gauges. Proc. 57th Canadian Geotechnical Conference and 5th Joint CGS/IAH-CNC Conference, Saskatoon, Saskatchewan, Canada. (Proceedings in CD-ROM).

Zornberg, J.G. and Kang, Y. 2005. Pullout of geosynthetic reinforcement with in-plane drainage capability. Proc. Geo-Frontiers 2005, ASCE Geotechnical Special Publications 130-142 and GRI-18 Geosynthetics Research and Development in Progress, Austin, Texas, USA. (Proceedings in CD-ROM).

APPENDIX

APPENDIX A

CHAPTER 4 ADDITIONAL FIGURES

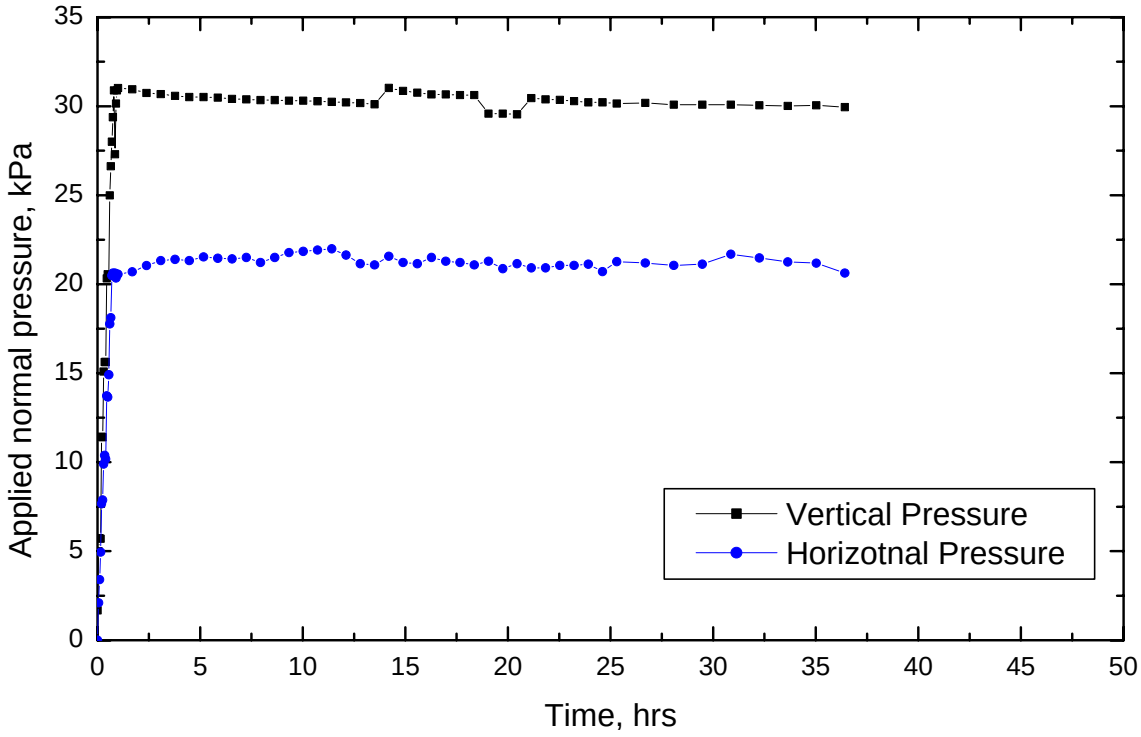

Figure A.1 Applied pressure-time history of unreinforced clay specimen during mechanical loading (Specimen UP30/21)

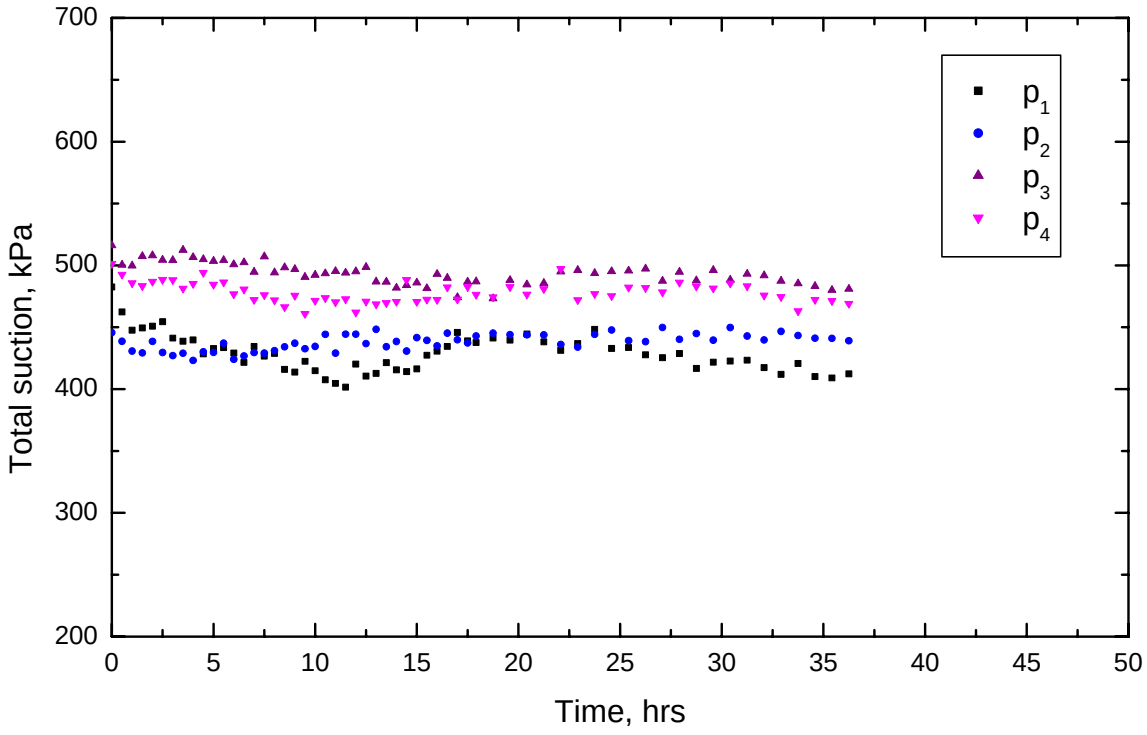

Figure A.2 Variation of suction pressures for Specimen UP30/21 during mechanical loading

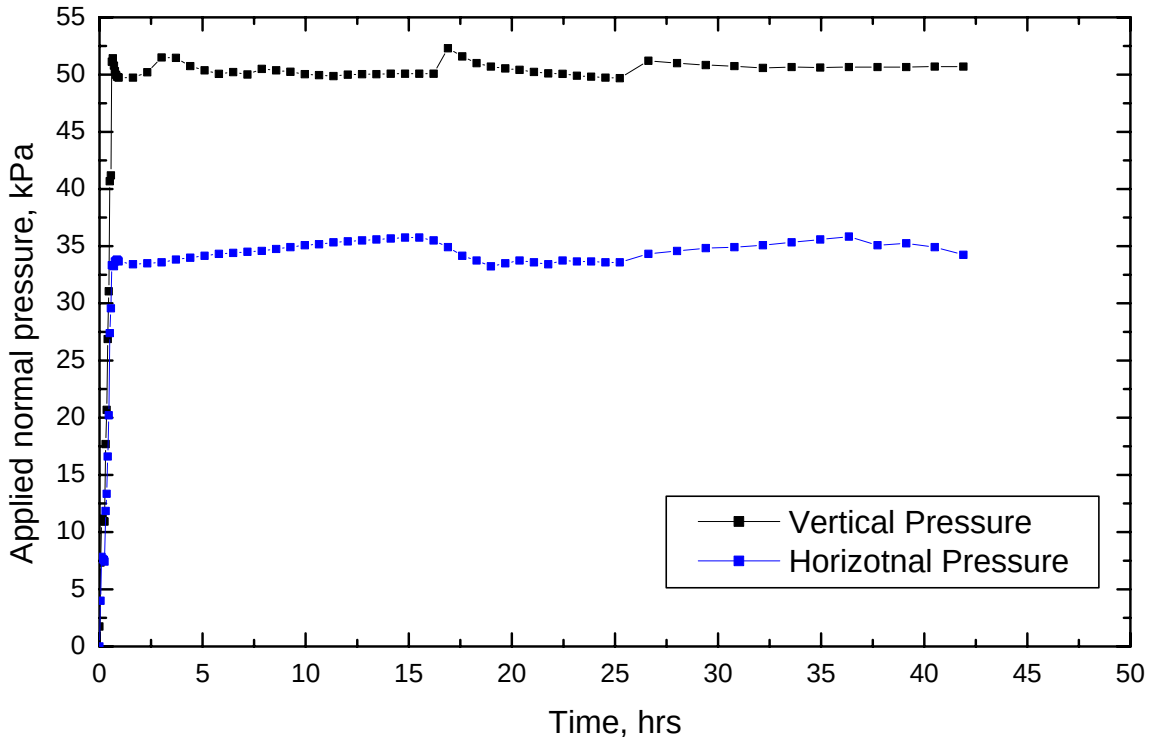

Figure A.3 Applied pressure-time history of geogrid-reinforced clay specimen during mechanical loading (Specimen RP50/35)

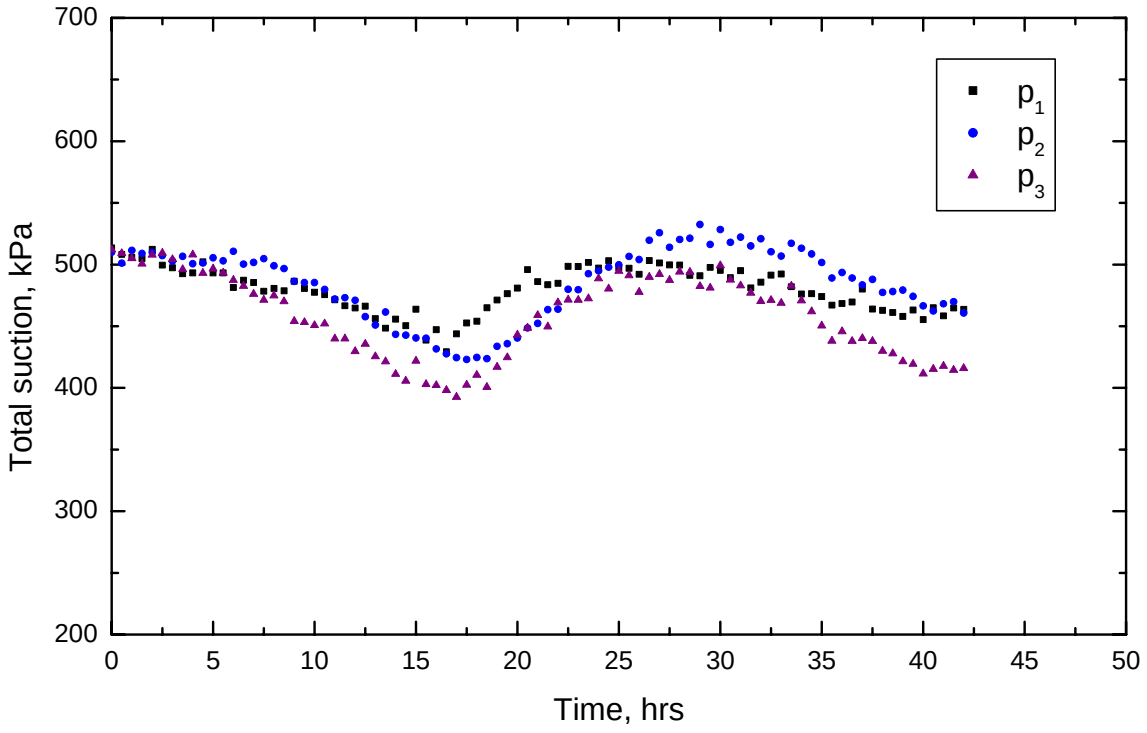

Figure A.4 Variation of suction pressures for Specimen RP50/35 during mechanical loading

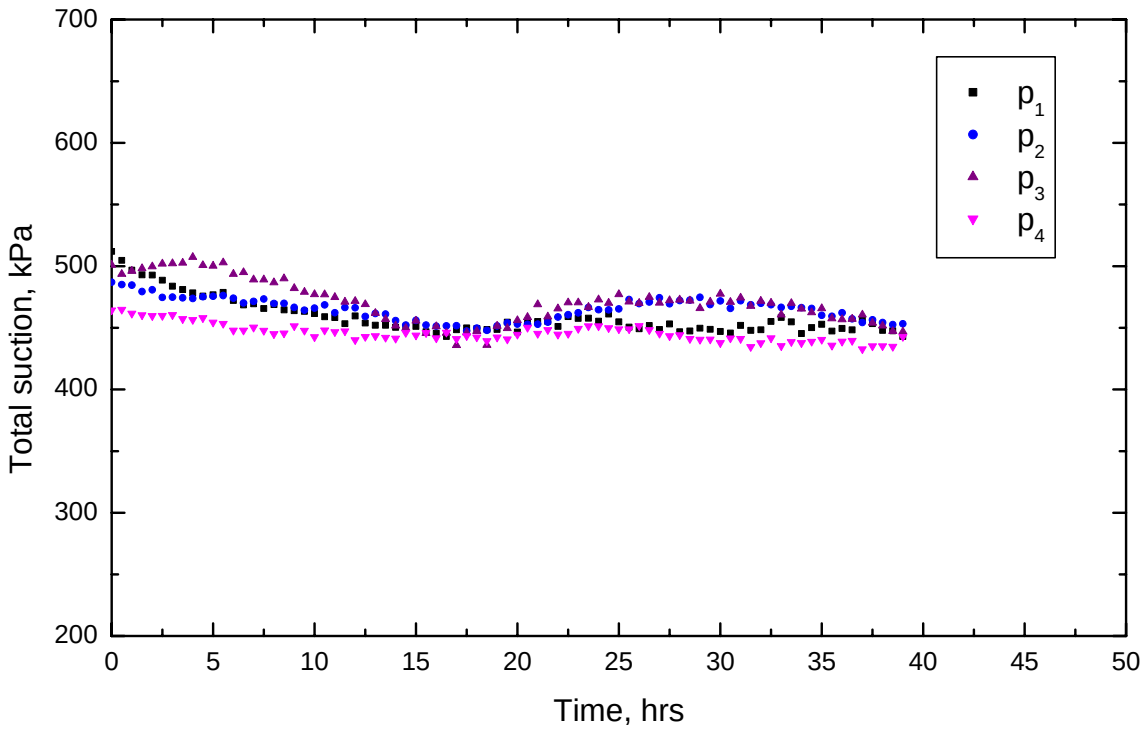

Figure A.5 Variation of suction pressures for Specimen UP50/35 during mechanical loading

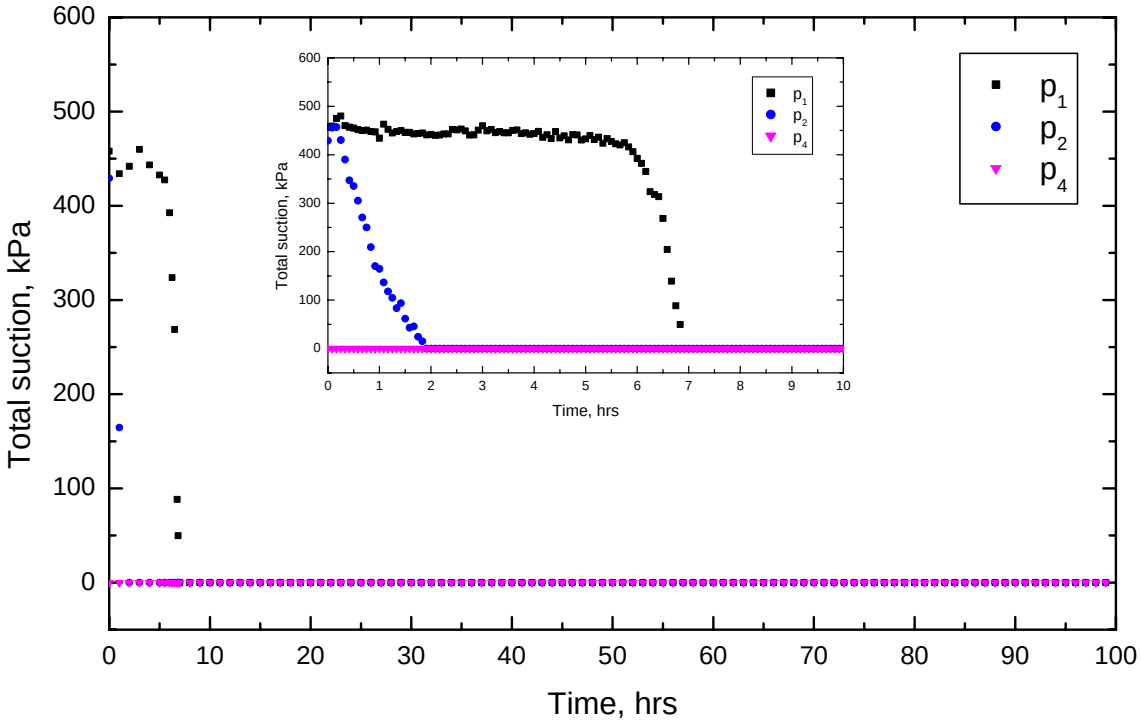

Figure A.6 Suction pressures in Specimen UP20/14 during wetting

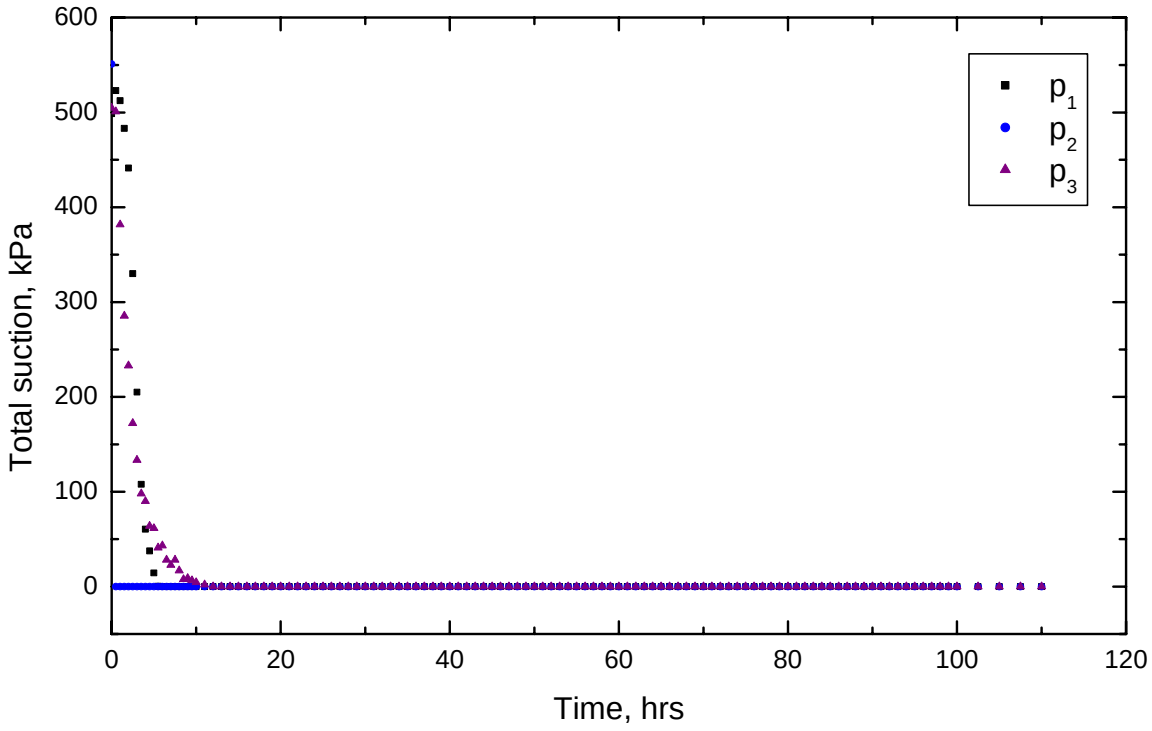

Figure A.7 Suction pressures in Specimen RP50/35 during wetting

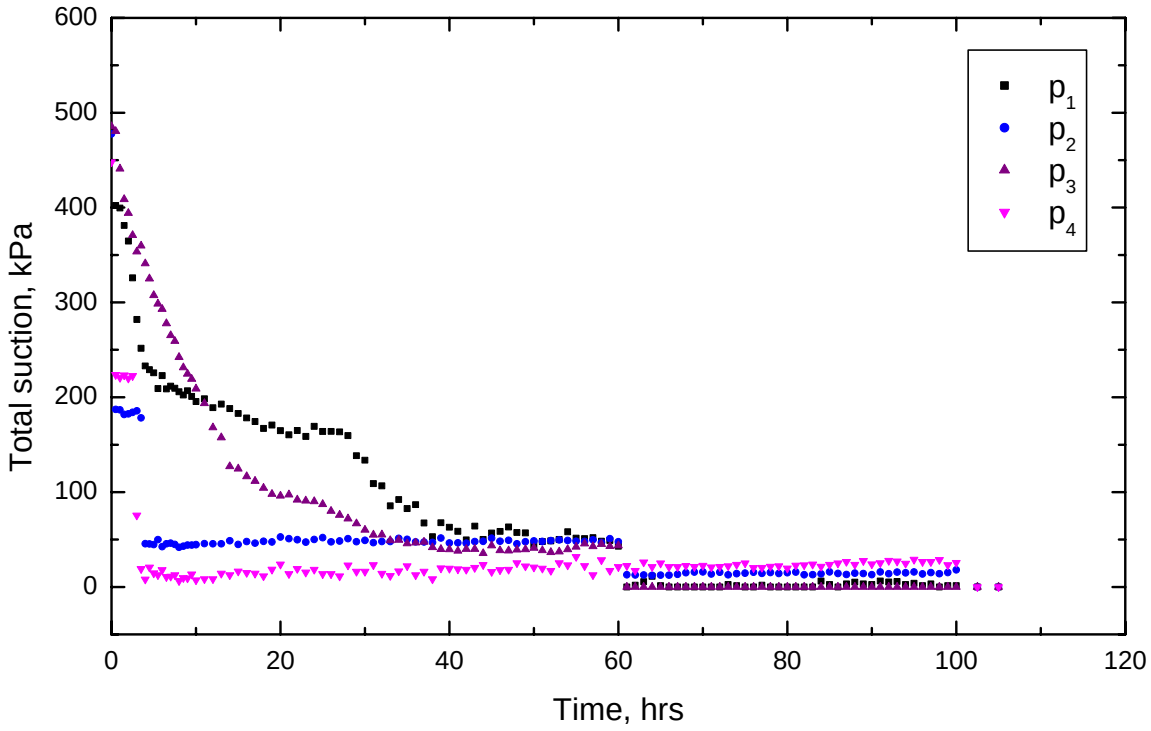

Figure A.8 Suction pressures in Specimen UP50/35 during wetting

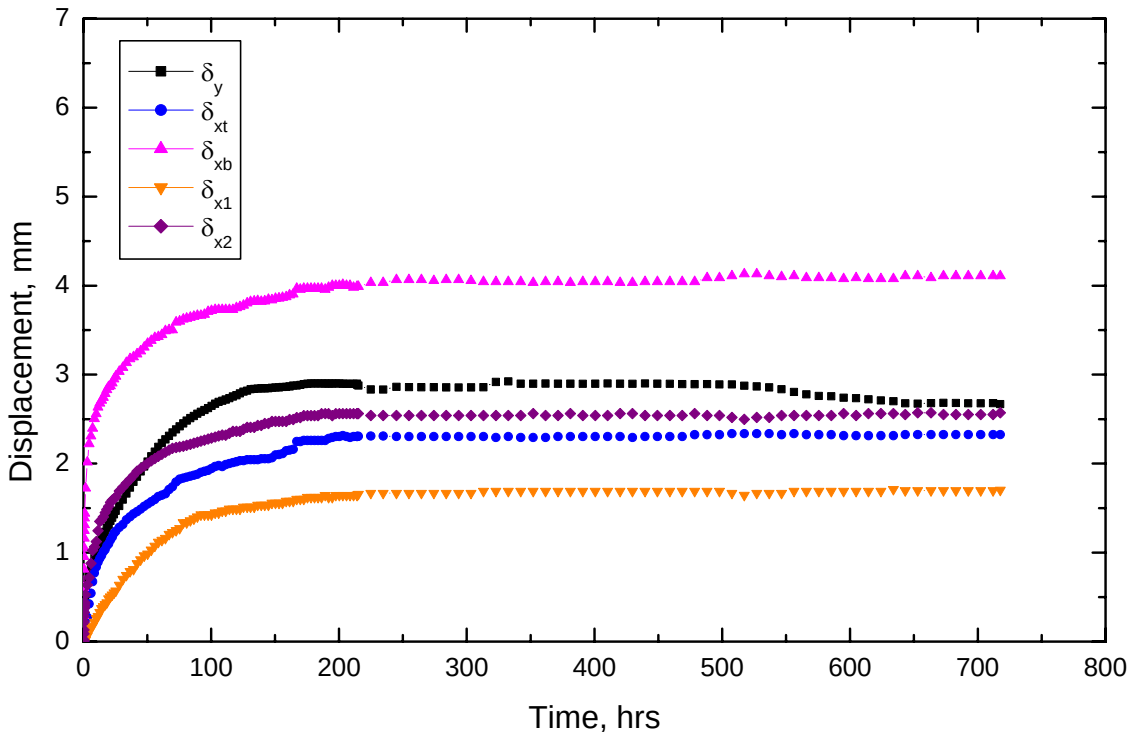

Figure A.9 Wetting-drying induced displacement in Specimen UP30/21

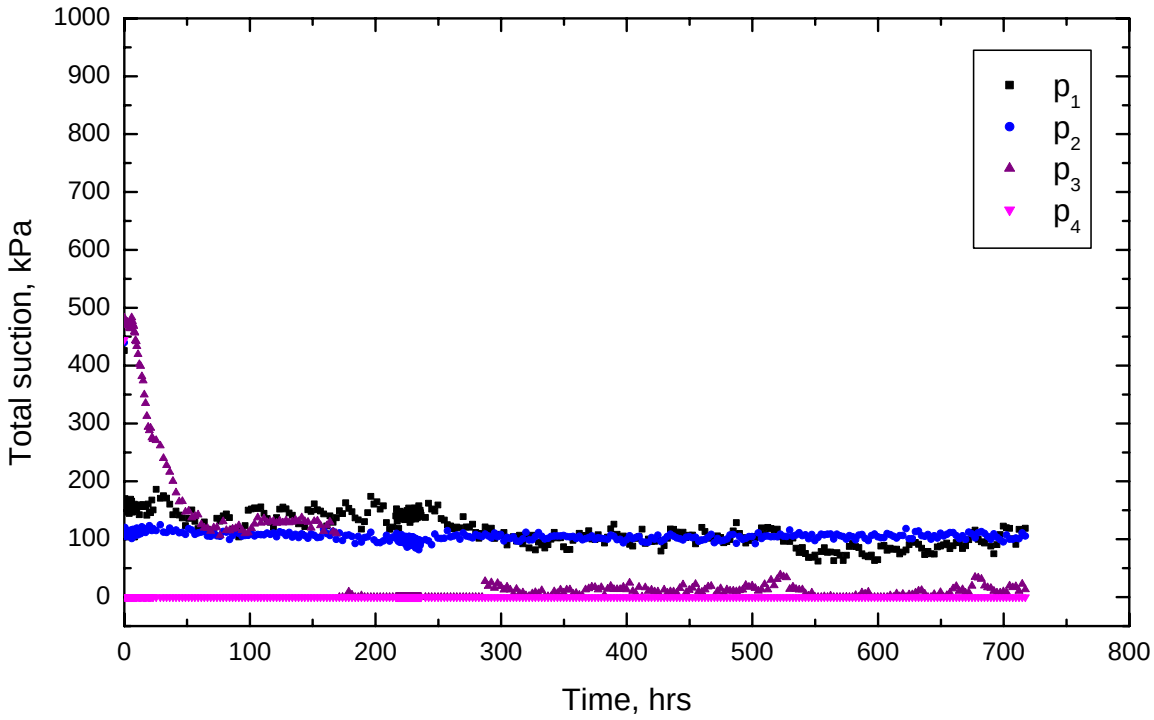

Figure A.10 Suction pressures in unreinforced clay specimen UP30/21 during wetting-drying cycle

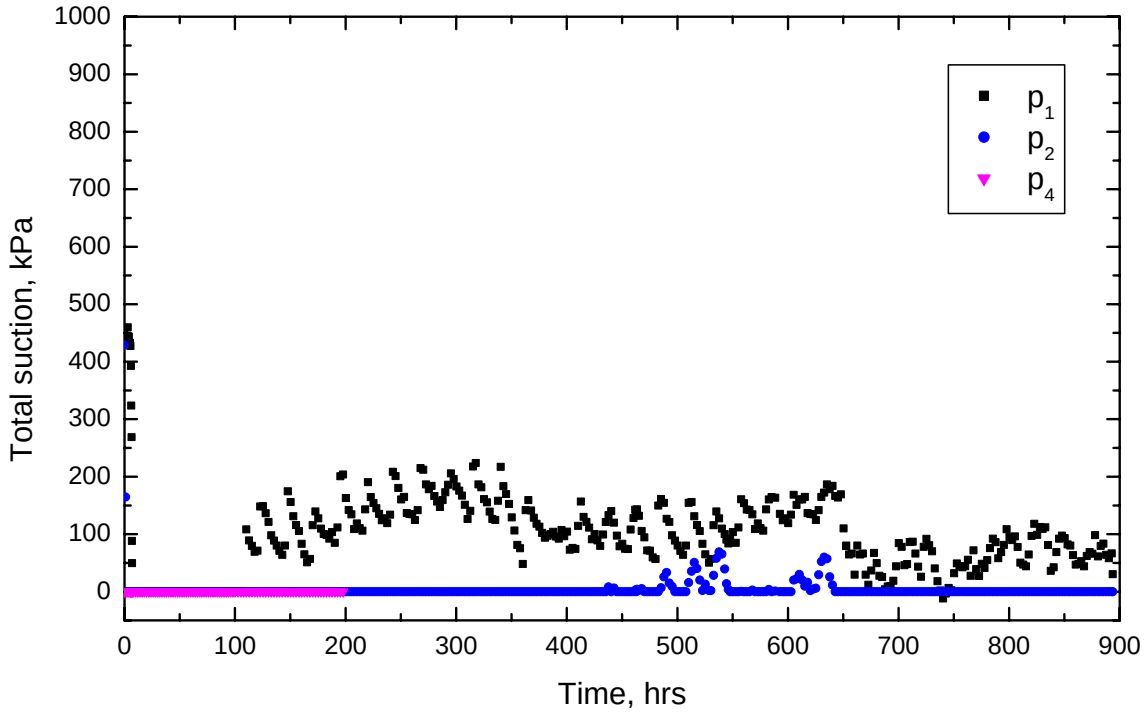

Figure A.11 Suction pressures in unreinforced clay specimen UP20/14 during wetting-drying cycle

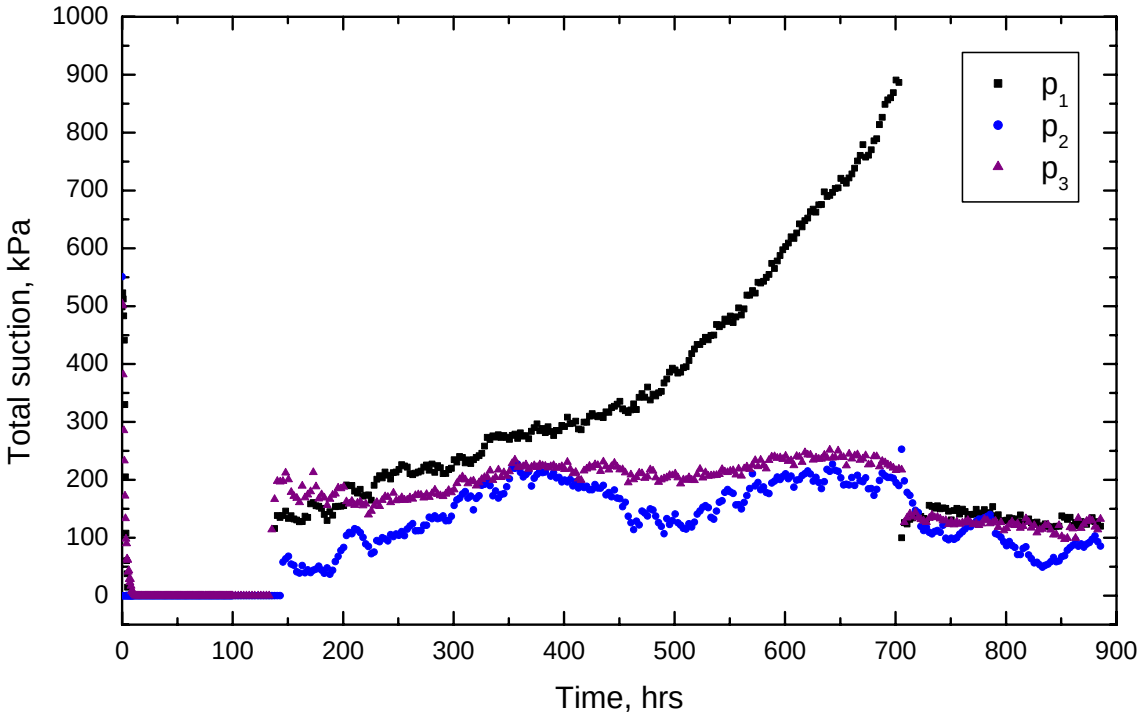

Figure A.12 Suction pressures in geogrid-reinforced clay specimen RP50/35 during wetting-drying cycle

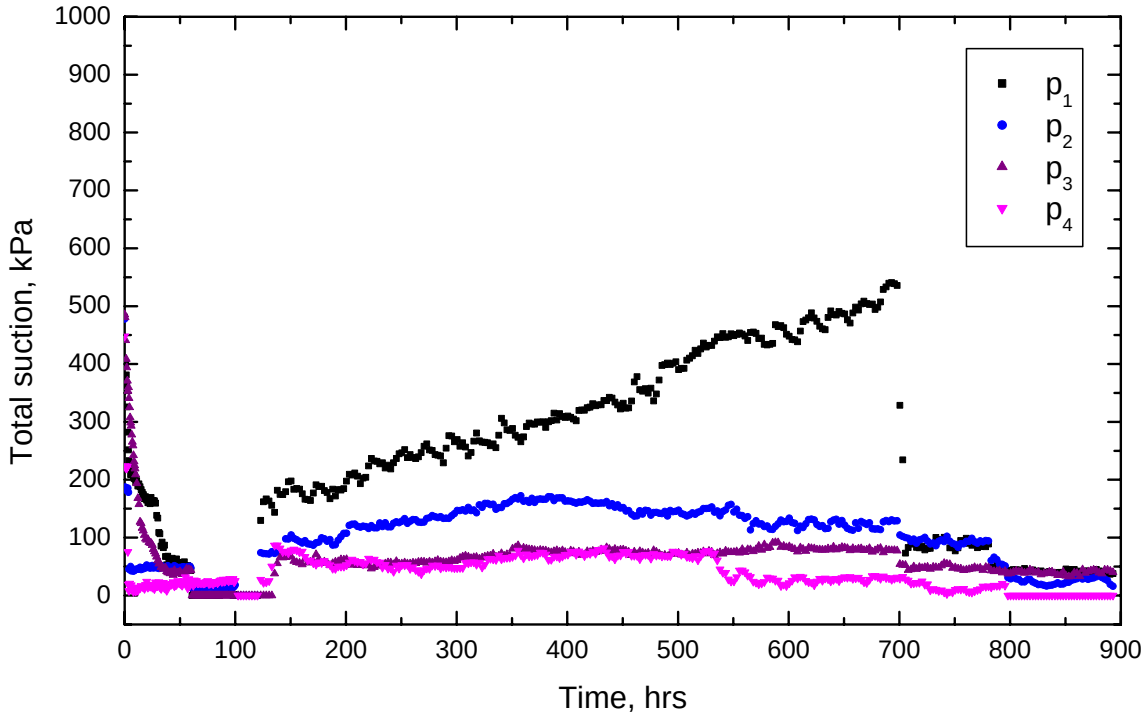

Figure A.13 Suction pressures in unreinforced clay specimen UP50/35 during wetting-drying cycle

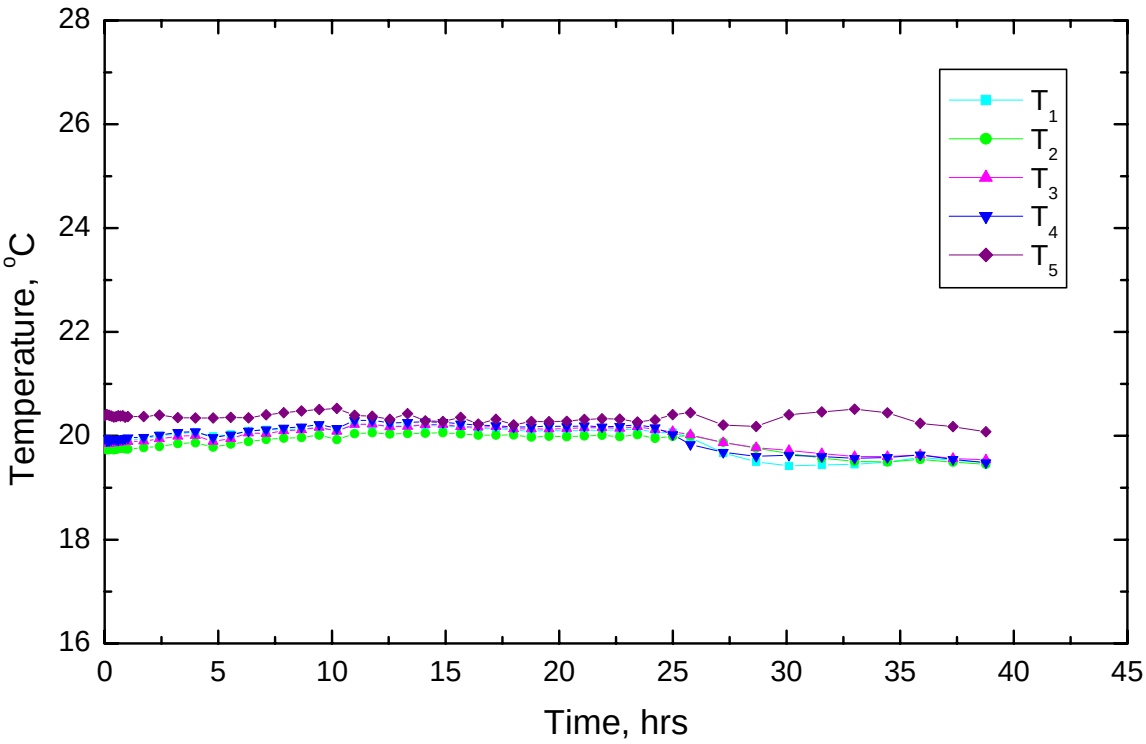

Figure A.14 Soil temperature and environmental chamber temperature-time history in Specimen UT-18°C/ +23°C during mechanical loading condition of 20 kPa vertical and 14 kPa horizontal pressure

APPENDIX B

CHAPTER 5 FISH FUNCTIONS

B.I FISH Function in FLAC for Barcelona Basic Model at Constant Suction

;**Alonso.fis**

```
;=============================================================
; FISH version of BBM (Alonso et al. 1990) model for Unsaturated Soil
; on environment of Modified Cam clay Model
; at constant suction (s = const.) and Associated flow rule
; Model must predict saturated behaviour when the value of
; suction reduces to zero (s = 0).
; Main aim of the model is the reproduction of the general
; behaviour of unsaturated soils at constant suction
; January, 2004
; m_poiss # 0.0 --- option for constant Poisson's ratio
;              = 0.0 --- default for constant shear modulus
;                 (but check the limit of Poisson's ratio)
; Yadav P. Pathak (Revised on March 27, 2005)
;-------------------------------------------------------------------
;                  Soil properties:
;
;         For saturated soil (Modified Cam clay Model)
; m_g           shear modulus, G
; m_k           maximum elastic bulk modulus, Kmax
; m_m           slope of CSL, M
; m_kappa       slope of elastic swelling, K
; m_lambda      slope of normal consolidation line (NCL), λ
; m_vl          specific volume at reference pressure on NCL at s = 0, v_λ
; m_pc          preconsolidation line at s = 0, pc (= po* in Alonso paper)
; m_p1          reference pressure, p1
; m_v0          initial value of specific volume, v0
; m_poiss       Poisson's ratio
;
```

```
;         For unsatureated soil at constant suction
; m_s           suction, s = ua - uw
; m_lambdas slope of NCL or virgin line at s = const (calculated)
; m_kappas   slope of elastic swell-shrink due to wetting -drying,Ks
; m_Ns         specific volume at reference pressure on NCL at s = const, N(s)
; m_pcs        preconsolidation line at s = const, pcs (= po in Alonso paper)
; m_ps         suction pressure (constant for s = const), ps
; m_r          (m_lambdas / m_lamda) = const
; m_beta       const
; m_ksctn      slope of suction induced cohison, k
; m_patm       atmospheric pressure, patm
; m_ua         air pressure, ua
;
;     Following need to be calculated to provide as a constant soil properties
;           (m_ps & m_lambdas are constant at s = const.)
;
;    1) m_ps = m_ksctn * m_s ; ps = k * s
;    2) m_lambdas = m_lambda * ( (1 - m_r) * exp (- m_beta * m_s) + m_r )
;       i.e. l(s) = l * ((1-r) * exp(-beta * s) + r)
;    3) $pcs = $p1*($pc/$p1)^((m_lambda - m_kappa)/($m_lambdas - m_kappa))
;       i.e. pcs = p1 * (pc/p1) ^ ((l - kappa)/(ls - kappa))
;    4) m_Ns = m_vl - kappas * ln ((m_s + m_patm)/m_patm)
;       i.e. N(s) = vl - Ks * ln ((s + patm) / patm)
;
;         Additional properties which has access to user
; m_e                   total volumetric strain, e
; m_ep                  plastic volumetric strain, ep
; m_ind                 state indicator:
;                 0     elastic
;                 1     plastic
;                 2     elastic now, but plastic in past
```

```
; m_kc          current elastic bulk modulus, K
; m_p           mean effective pressure, p
; m_q           deviator stress, q
; m_v           specific volume, v
;-------------------------------------------------------------------------------------------------------
;                   for constant suction (s = const)
;  m_r, m_beta, m_s, ps, m_lambdas, m_lambda, m_kappa, m_p1,
;  m_Ns, m_vl, m_m    are constant.
;
;                   for suction is zero i.e. saturated soil (M-Cam clay model)
;         m_s = 0, m_r = 1, m_Ns = m_v1
;          Then, m_lambdas = m_lambda; $ps = 0; $pcs = $pc
;=======================================================
;set echo off
def alonso_cc
  constitutive_model 1990
  f_prop  m_g m_k m_m m_kappa m_Ns m_pcs m_p1 m_v0
  f_prop  m_poiss m_s m_lambdas m_ps
  f_prop  m_e m_ep m_v m_p m_q m_ind m_kc
  float   $sum_p $sum_q $sum_e $sum_ep $p $q $tk $tg $mm $p1 $ps $pcs
  float   $e1 $e2 $sh2 $s11i $s22i $s33i $s12i $ds11 $ds22 $ds33 $ds12
  float   $fs $sa $sb $sc $ba $bb $bc $boa $sqr
  float   $alam $alam1 $qn $pn $add $v $vk $maxg $ming
  int     $pind
  Case_of  mode
; ----------------------------
; Initialisation section
; ----------------------------
    Case 1
; --- data check -----
      if m_poiss < 0.0 then
```

```
      nerr = 126
      error = 1
    end_if
    if m_p1 = 0.0 then
      m_p1 = 1.0
    end_if
    if m_p1 < 0.0 then
      nerr = 126
      error = 1
    end_if
    if m_pcs < 0.0 then
      nerr = 126
      error = 1
    end_if
    if m_Ns < 1.0 then
      nerr = 126
      error = 1
    end_if
    if m_kappa = m_lambdas then
      nerr = 126
      error = 1
    end_if
    if m_kappa = 0.0 then
      nerr = 126
      error = 1
    end_if
; --- initialize current bulk modulus ---
    if m_kc = 0.0 then
      m_kc = m_k
    end_if
; --- initialize current shear modulus ---
```

```
      if m_g = 0.0 then
        if m_poiss # 0.0 then
          m_g = 3.0*m_kc*(1.0-2.0*m_poiss)/(2.0*(1.0+m_poiss))
        end_if
      end_if


    Case 2
; ------------------------
; Running section
; ----------------------
      zvisc = 1.0
      if m_ind # 0.0 then
        m_ind = 2.0
      end_if
      $pind = 0
; --- define constants locally ---
      $tk = m_kc
      $tg = m_g
      $mm = m_m * m_m
      $pcs = m_pcs
      $p1 = m_p1
      $ps = m_ps
      $e1 = $tk + 4.0 * $tg / 3.0
      $e2 = $tk - 2.0 * $tg / 3.0
      $sh2= 2.0 * $tg
;--- get new trial stresses from old, assuming elastic increments ---
      $s11i = zs11 + (zde22 + zde33) * $e2 + zde11 * $e1
      $s22i = zs22 + (zde11 + zde33) * $e2 + zde22 * $e1
      $s33i = zs33 + (zde11 + zde22) * $e2 + zde33 * $e1
      $s12i = zs12 + zde12 * $sh2
;--- zone volumetric strain accumulation ------
```

```
      $sum_e = $sum_e + zde11 + zde22 + zde33
; --- mean pressure ---
      $p = - ($s11i + $s22i + $s33i) / 3.0
; --- deviatoric stresses ---
      $ds11 = $s11i + $p
      $ds22 = $s22i + $p
      $ds33 = $s33i + $p
      $ds12 = $s12i
; --- sqrt(3.0 * J2) ---
      $q = sqrt(1.5*($ds11*$ds11+$ds22*$ds22+$ds33*$ds33)+3.0*$ds12*$ds12)
; --- check for yielding ---
      $fs = $q * $q + $mm * ($p + $ps) * ($p - $pcs)
;     $pcs = $p1*($pc/$p1)^((m_lambda - m_kappa)/($m_lambdas - m_kappa))
;     $ps = m_ksctn * m_s
;
      if $fs > 0.0 then
; --- yielding in shear ---
        $sa = 6.0 * $tg * $q
        $sc = $mm * (2.0 * $p + $ps - $pcs)
        $sb = $tk * $sc
        $ba = $sa * $sa + $mm * $sb * $sb
        $bb = $sa * $q + 0.5 * $sb * $sc
        $bc = $fs
        $boa= $bb / $ba
        $sqr= sqrt($boa * $boa - $bc / $ba)
        $alam  = $boa + $sqr
        $alam1 = $boa - $sqr
        $pind  = 1
; ---    choose the smallest root ---
        if abs($alam1) < abs($alam) then
          $alam = $alam1
```

```
        end_if
        if $alam < 0.0 then
          $alam = 0.0
        end_if
        $qn = $q - $sa * $alam
        $pn = $p - $sb * $alam
; ---   new stresses ---
        if $q = 0.0 then
          $add = $pn - $p
          zs11 = $s11i - $add
          zs22 = $s22i - $add
          zs33 = $s33i - $add
          zs12 = $s12i
        else
          zs11 = ($ds11 / $q) * $qn - $pn
          zs22 = ($ds22 / $q) * $qn - $pn
          zs33 = ($ds33 / $q) * $qn - $pn
          zs12 = ($ds12 / $q) * $qn
        end_if
        $sum_p  = $sum_p  + $pn
        $sum_q  = $sum_q  + $qn
        $sum_ep = $sum_ep + $alam * $sc
        zvisc = 0.0
        m_ind = 1.0
      else
; ---   no failure at all ---
        zs11 = $s11i
        zs22 = $s22i
        zs33 = $s33i
        zs12 = $s12i
        $sum_p = $sum_p + $p
```

```
        $sum_q = $sum_q + $q
      end_if
; --- update zone parameters ---
      if zsub > 0.0 then
        m_p   = $sum_p  / zsub
        m_q   = $sum_q  / zsub
        m_e   = m_e + $sum_e / zsub
        m_ep  = m_ep + $sum_ep / zsub
        $v    = m_v0  * (1.0+m_e)       ; specific volume
        m_v   = $v
        m_kc  = $v*m_p/m_kappa
; ---    data check ---
        if $v < 1. then
          nerr = 167
          error = 1
        end_if
        if m_p > 0.0 then
          error = 0
        else
          nerr = 168
          error = 1
        end_if
        if m_kc > m_k then
          nerr = 169
          error = 1
        end_if
; ---    update cap pressure (hardening or softening)
;       only if plasticity has taken place ---
        if $pind = 1 then
          $vk   = $v + m_kappa*ln(m_p/$p1)
          m_pcs = $p1*exp( (m_Ns-$vk)/(m_lambdas-m_kappa) )
```

```
        end_if
; ---    update shear modulus ---
        if m_poiss # 0.0 then
; ---       constant Poisson's ratio ---
          m_g = 3.0*m_kc*(1.0-2.0*m_poiss)/(2.0*(1.0+m_poiss))
        else
; ---       constant G, check upper and lower bounds (nu=0 or 0.5) ---
          $maxg = 1.5*m_kc
          $ming = 0.0
          if m_g > $maxg then
            m_g = $maxg
          else
            if m_g < $ming then
              m_g = $ming
            end_if
          end_if
        end_if
; ---    reset for next zone ------
        $sum_p   = 0.0
        $sum_q   = 0.0
        $sum_ep  = 0.0
        $sum_e  = 0.0
      end_if


    Case 3
; -------------------------------------
; Return maximum modulus
; -------------------------------------
      cm_max = m_k + 4.0 * m_g / 3.0
      sm_max = m_g
```

```
    Case 4
; ----------------------------
; Add thermal stresses
; ----------------------------
;      ztsa = ztea * m_kc
;      ztsb = zteb * m_kc
;      ztsc = ztec * m_kc
;      ztsd = zted * m_kc
  End_case
end
;opt alonso_cc
; ------------------------------------------------------------------------------------------------------
; FISH function to initialize initial specific volume (v0)
;      and tangent bulk modulus (K)
;
;  Since, Initial stresses are calculated from the other models e.g. M-C
;  there is no suction effect involved. So, convert stresses into suction
;  effects. Use following values: pc,l,K,vl,s,l(s),Ks,N(s),pcs,p1
;
;  1) m_Ns = m_vl - kappas * ln ((m_s + m_patm)/m_patm)
;     i.e. N(s) = vl - Ks * ln ((s + patm) / patm)
;  2) m_lambdas = m_lambda * ( (1 - m_r) * exp (- m_beta * m_s) + m_r )
;     i.e. l(s) = l * ((1-r) * exp(-beta * s) + r)
;  3) $pcs = $p1*($pc/$p1)^((m_lambda - m_kappa)/($m_lambdas - m_kappa))
;     i.e. pcs = p1 * (pc/p1) ^ ((l - kappa)/(ls - kappa))
; ------------------------------------------------------------------------------------------------------
def set_v0
  loop i (1,izones)
    loop j (1,jzones)
      if model(i,j) = 1990 then
        p0 = -(sxx(i,j)+syy(i,j)+szz(i,j))/3.-pp(i,j)
```

```
            if p0 > 0.0 then
              p1 = m_p1(i,j)
              pcs = m_pcs(i,j)
              vcs = m_Ns(i,j) - m_lambdas(i,j)*ln(pcs/p1)
              m_v0(i,j) = vcs - m_kappa(i,j)*ln(p0/pcs)
              m_kc(i,j) = v0(i,j) * p0 / m_kappa(i,j)
            else
              nerr  = 170
              error = 1
            end_if
          end_if
        end_loop
      end_loop
end
;opt alonso_cc
;set echo on
```

B.II FISH Function in FLAC for Wetting-Induced Swell Model

```
; Swell.fis
config extra 9
set echo off
; ------------------------------------------------------------------------
; swell.fis; swelling functions
; grid must have 9 extra variables to store:
; swelling law number     [initialized by user]
;   ex_1: integer(1 for log, 2 for linear)
; property set number          [initialized by user]
;  ex_2: integer(<=p_size, the number refer to the set
```

```
;       defined in the Fish function 'setup')
; swelling stress increments
; (total stress increments/v_step): [calculated by v_str_inc]
;    ex_3: delta sxx
;    ex_4: delta syy
;    ex_5: delta szz
; swelling strains       [calculated by v_str_inc]
;    ex_6: vdey
;    ex_7: vdex
; zone centroid coordinates    [calculated by v_str_inc]
;    ex_8: xc
;    ex_9: yc
; ------------------------------------------------------------------------
; setup
; value of atmospheric pressure in relevant units
;    p_a
; function prototype to initialize arrays of properties
;    v_c3(i)     parameter  c3  corresponding to property set i
;    v_a3(i)     parameter  a3  corresponding to property set i
;    e_m3(i)   max value of horizontal swell for sigv=0
;    v_c1(i)     parameter  c1  corresponding to property set i
;    v_a1(i)     parameter  a1  corresponding to property set i
;    e_m1(i)   max value of vertical swell for sigv=0
; Notes:
;  1. this function must be present in the data file
;  2. the user must type in adequate property values and add
;      new sets as required
;  3. p_size is the maximum number of property sets and must
;      be updated as needed
; ------------------------------------------------------------------------
;def makesize
```

```
;  p_size = 10  ; max of 10 property sets
;end
;makesize
;def setup
;  p_a = (value of atmospheric pressure in units being used)
;  array v_a1(p_size), v_a3(p_size), v_c1(p_size),
;   v_c3(p_size), e_m1(p_size), e_m3(p_size)
; properties: set 1
;      v_a1(1) =
;      v_c1(1) =
;      v_a3(1) =
;      v_c3(1) =
;      e_m1(1) =
;      e_m3(1) =
; properties: set 2
;      v_a1(2) =
;      v_c1(2) =
;      v_a3(2) =
;      v_c3(2) =
;      e_m1(2) =
;      e_m3(2) =
;end
;setup
; ---------------------------------------------------------------------
;  v_str_inc
;  store swelling stress increments and zone centroids
;  input: ex_1(i,j) model number
;           ex_2(i,j) property number
;           v_step   number of substeps used to apply swelling
;                      stresses
;           table 1   wetting front elevation (zones ABOVE front
```

```
;                       are wet)
;  output: ex_3(i,j) swelling xx-stress increment (total/v_step)
;          ex_4(i,j) swelling yy-stress increment (total/v_step)
;          ex_5(i,j) swelling zz-stress increment (total/v_step)
;          ex_6(i,j) swelling yy-strain (total)
;          ex_7(i,j) swelling xx-strain = zz-strain (total)
;          ex_8(i,j) x zone centroid
;          ex_9(i,j) y zone centroid
; ---------------------------------------------------------------------
def v_str_inc
; --- basic checking -------
 if v_step <= 0 then
    v_step = 1
 endif
; ---store stress increments due to swelling ---------
   loop i (1,izones)
       loop j (1,jzones)
;          --- skip zones with null model
          if model (i,j) # 1 then
;             ---- tension cut-off ----
              sigv = - syy(i,j)
              if sigv <= 0.0 then
                   sigv = 0.0
              endif
;          ---- retrieve model number (default is 1) ---
                modnum = int(ex_1(i,j))
                if modnum = 0 then
                   modnum = 1
                endif
; --- retrieve property set number -------
               prodnum = int(ex_2(i,j))
```

```
;               -----swelling law -----
                Case of modnum
                default: no swelling stresses
                    vdex = 0.0
                    vdez = 0.0
                    vdey = 0.0
      case 1                ; LOG LAW
                if sigv = 0.0 then  ; get max swell, as defined
                   vdex = e_m3(prodnum)
                   vdey = e_m1(prodnum)
                else
                    va13 = v_a3(prodnum)
                    va11 = v_a1(prodnum)
;               ---- if a3 or a1 is negative, it is taken as 1 ----
                     if va11 <= 0.0 then
                       va11 = 1.0
                     endif
                     if va13 <= 0.0 then
                       va13 = 1.0
                     endif
                     vdex = v_c3(prodnum) * log((sigv/p_a) * va13)
                     vdey = v_c1(prodnum) * log((sigv/p_a) * va11)
                endif
;  ensure that swell is not greater than max possible value
                if vdex > e_m3(prodnum) then
                  vdex = e_m3(prodnum)
                endif
                if vdey > e_m1(prodnum) then
                  vdey = e_m1(prodnum)
                endif
    case 2          ; LINEAR LAW
```

```
                vdex = v_c3(prodnum) + (sigv/p_a)*v_a3(prodnum)
                vdey = v_c1(prodnum) + (sigv/p_a)*v_a1(prodnum)
            endcase
; --- save swelling stress increments ----
        a11 = bulk_mod(i,j) + shear_mod(i,j) * 4.0/ 3.0
        a12 = bulk_mod(i,j) - shear_mod(i,j) * 2.0/ 3.0
        ds = float(v_step)
        ex_3(i,j) = - (a11 * vdex + a12 * vdey)/ds ; dsxx
        ex_4(i,j) = - (a11 * vdey + a12 * vdex)/ds ; dsyy
        ex_5(i,j) = - (a12 * (vdex + vdey))/ds ; dszz
;       ---- save swelling strains -----
            ex_6(i,j) = vdey
            ex_7(i,j) = vdex
;       ------ save zone centroid ----------
            ex_8(i,j) = 0.25 * (x(i,j) + x(i+1,j) + x(i, j+1) + x(i+1, j+1))
            ex_9(i,j) = 0.25 * (y(i,j) + y(i+1,j) + y(i, j+1) + y(i+1, j+1))
        endif
    endloop
  endloop
end
;-------------------------------------------------------------------------------
;   app_str_inc
;   apply one swelling stress increment above wetting front
;   input: table 1  wetting front elevation (zones ABOVE
;                       front are wet)
;-------------------------------------------------------------------------------
def app_str_inc
    loop i (1, izones)
        loop j (1, jzones)
        if model(i,j) # 1 then
            xval = ex_8(i,j)
```

```
;apply swelling increments to zones above wetting front
                if ex_9(i,j) >= table (1, xval) then
                   sxx(i,j) = sxx(i,j) + ex_3(i,j)
                   syy(i,j) = syy(i,j) + ex_4(i,j)
                   szz(i,j) = szz(i,j) + ex_5(i,j)
                endif
            end_if
         endloop
    endloop
end
def swell
    loop ii (1,v_step)
        app_str_inc
        command
                cyc 500
;         solve sratio 1e-5
        end_command
    endloop
end
set echo on
```

APPENDIX C

CHAPTER 5 ADDITIONAL FIGURES

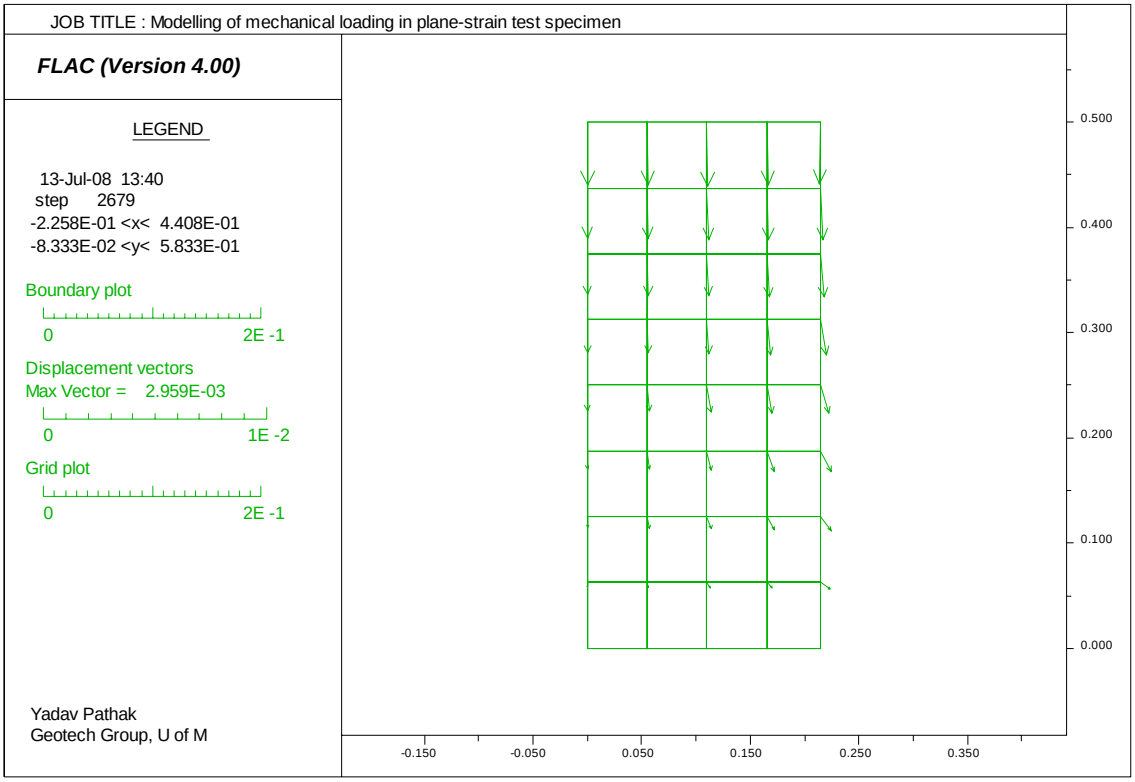

Figure C.1 Displacement vectors in unreinforced clay specimen UP30/21due to mechanical load

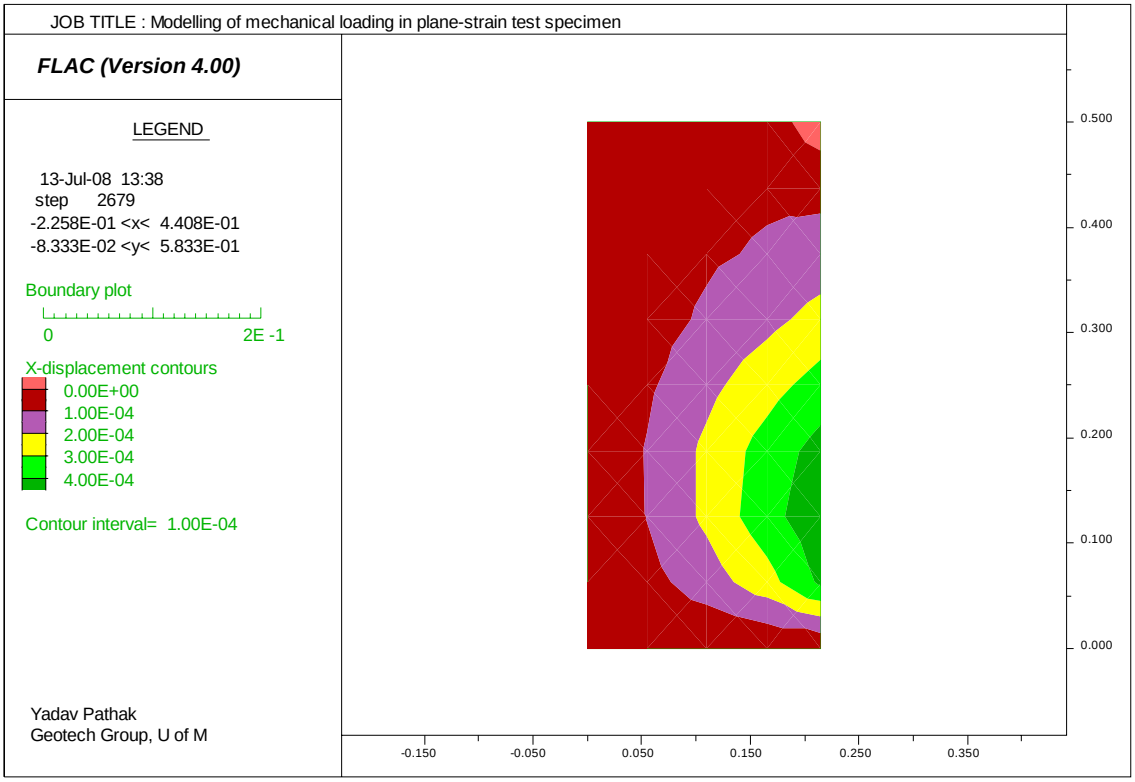

Figure C.2 Horizontal displacement contours in unreinforced clay specimen UP30/21 due to mechanical load

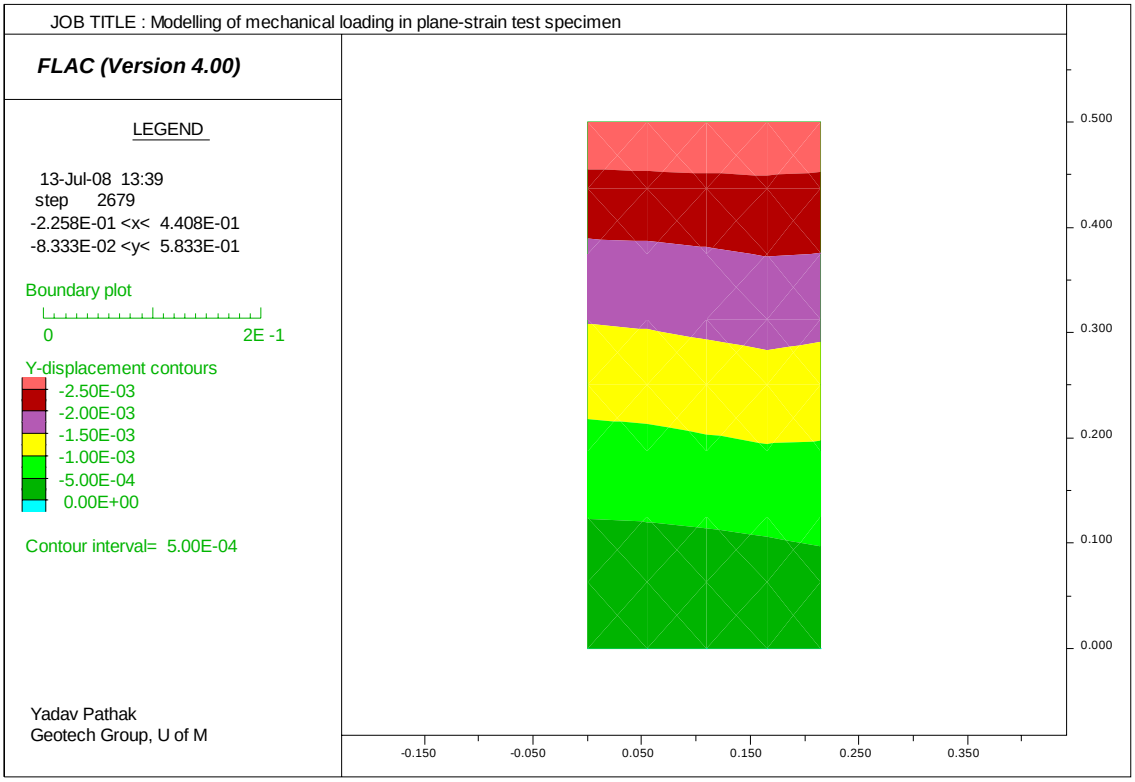

Figure C.3 Vertical displacement contours in unreinforced clay specimen UP30/21 due to mechanical load

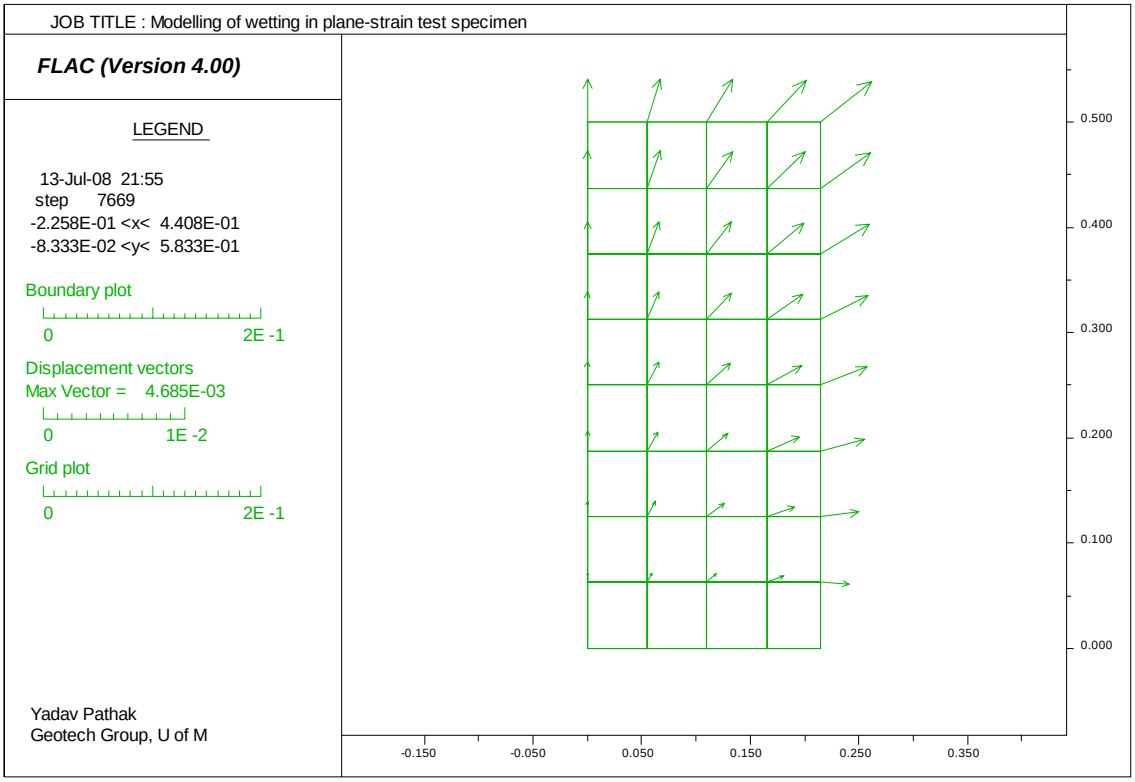

Figure C.4 Wetting-induced displacement vectors in unreinforced clay specimen UP30/21

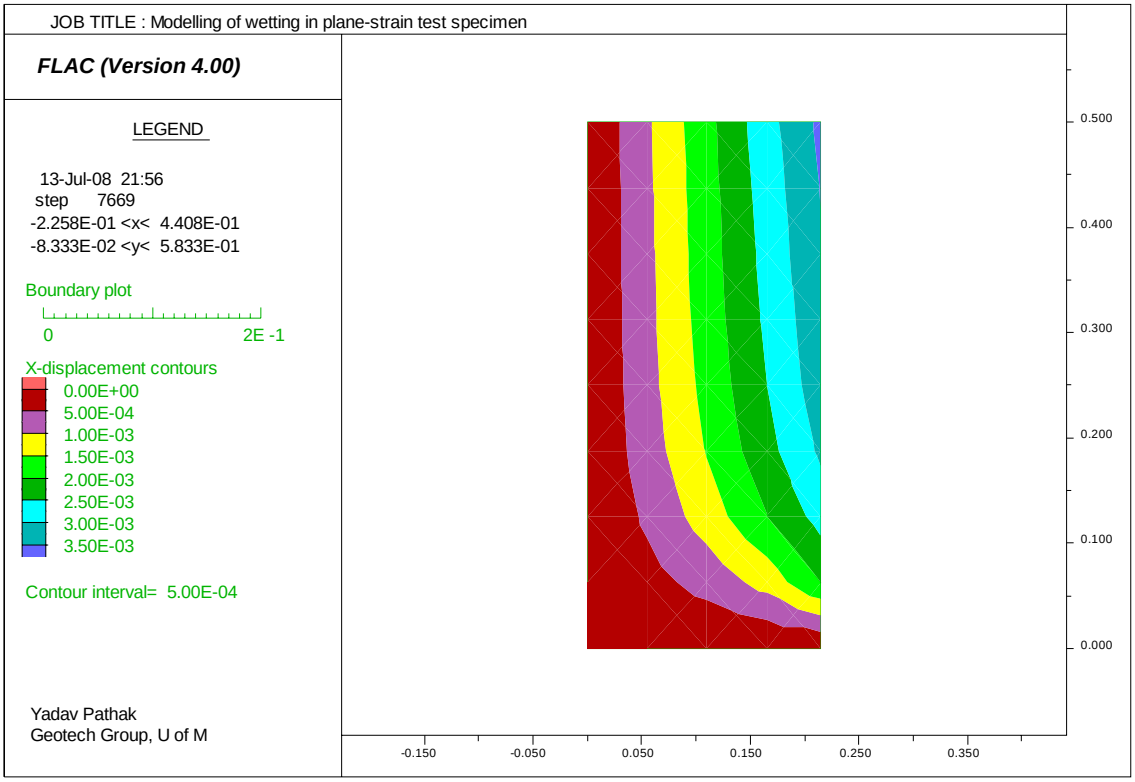

Figure C.5 Wetting-induced horizontal displacement contours in unreinforced clay specimen UP30/21

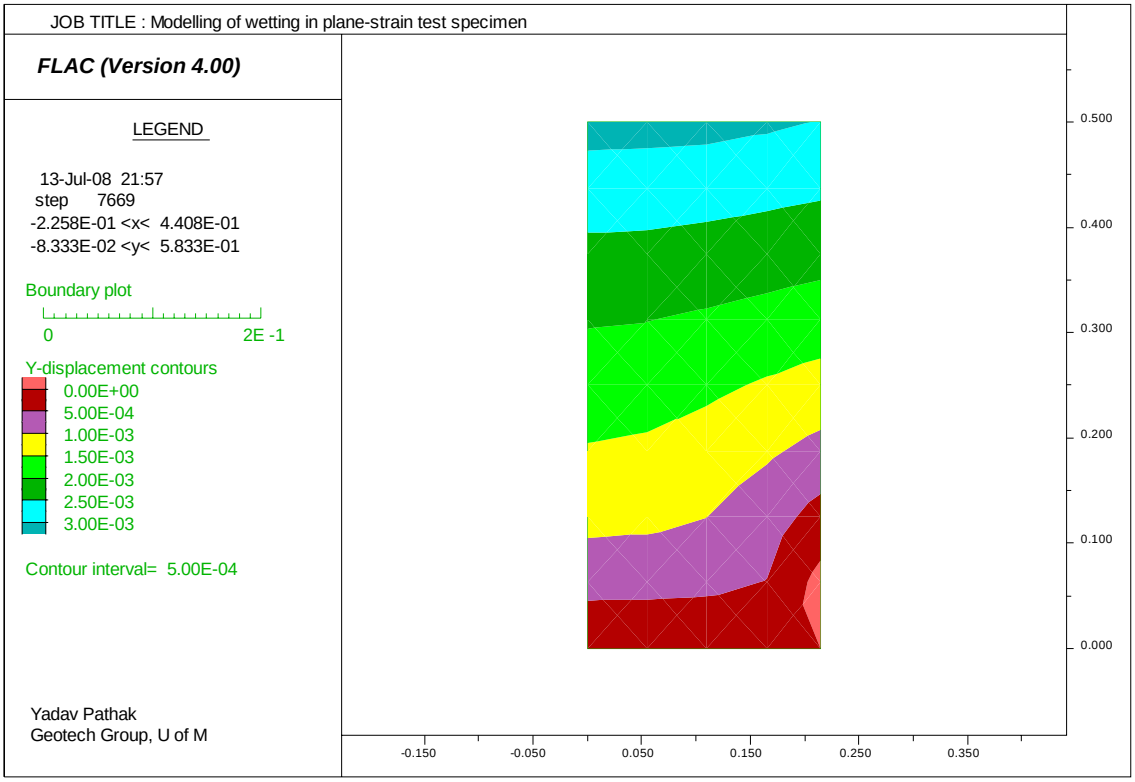

Figure C.6 Wetting-induced vertical displacement contours in unreinforced clay specimen UP30/21

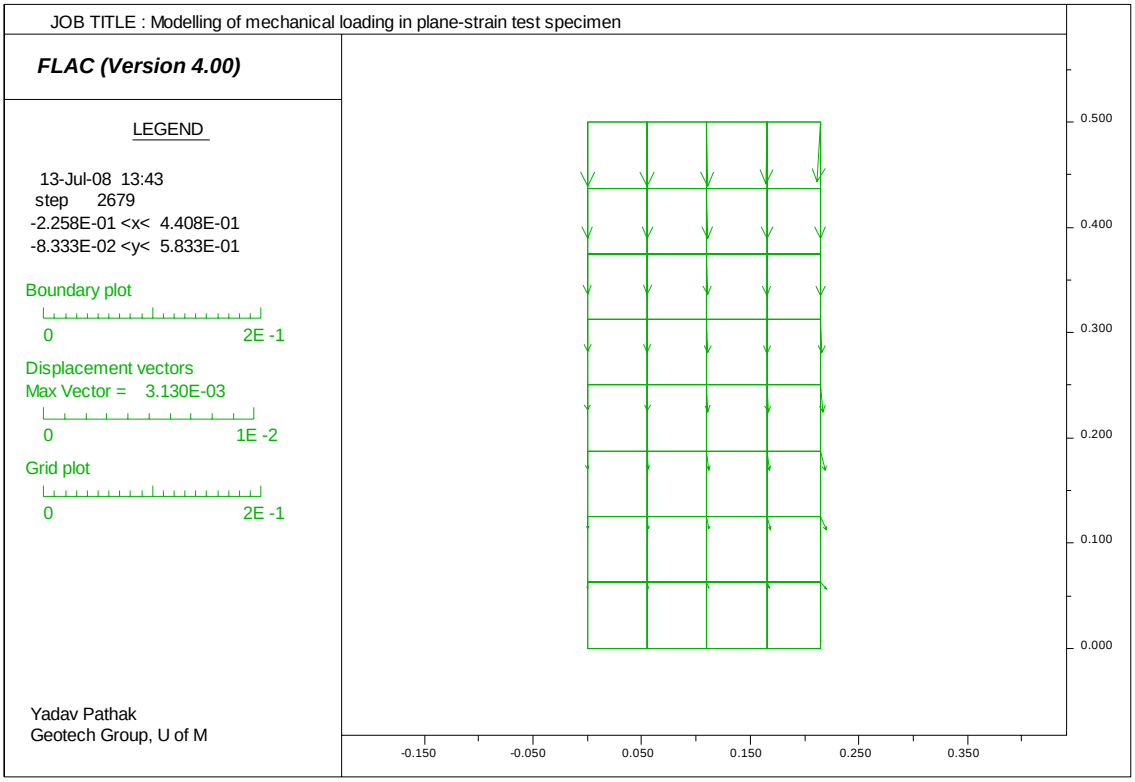

Figure C.7 Displacement vectors in unreinforced clay specimen UP50/35 due to mechanical load

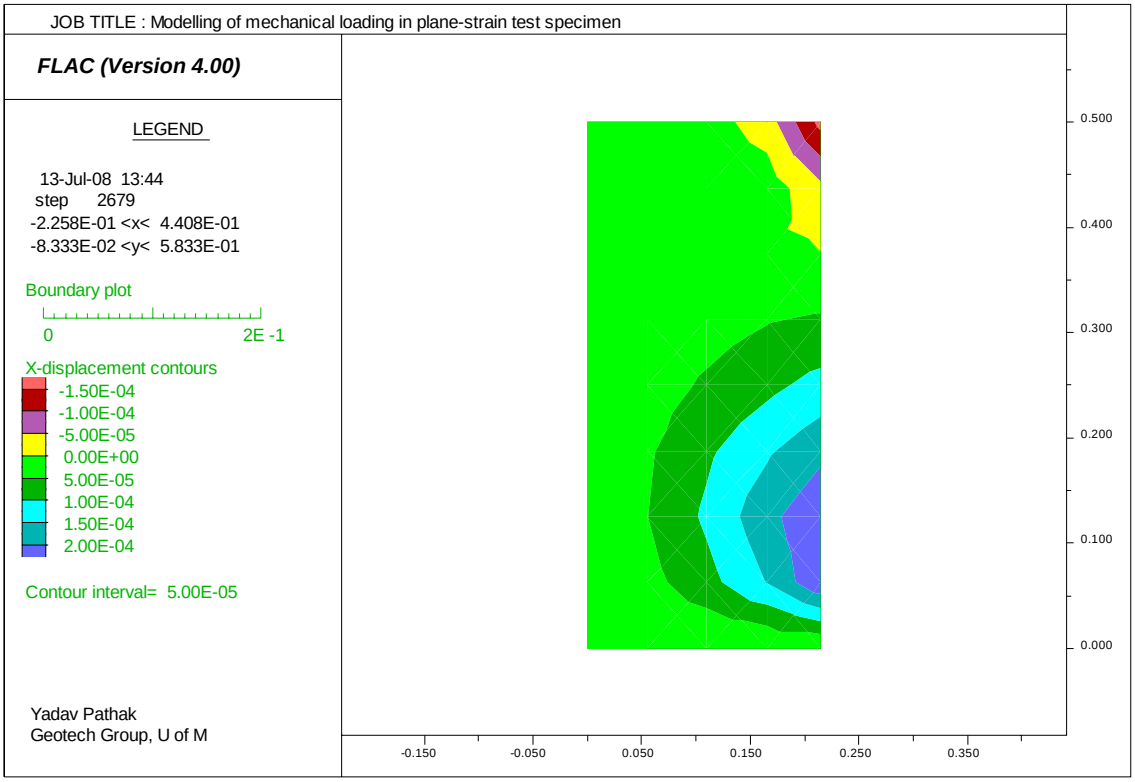

Figure C.8 Horizontal displacement contours in unreinforced clay specimen UP50/35 due to mechanical load

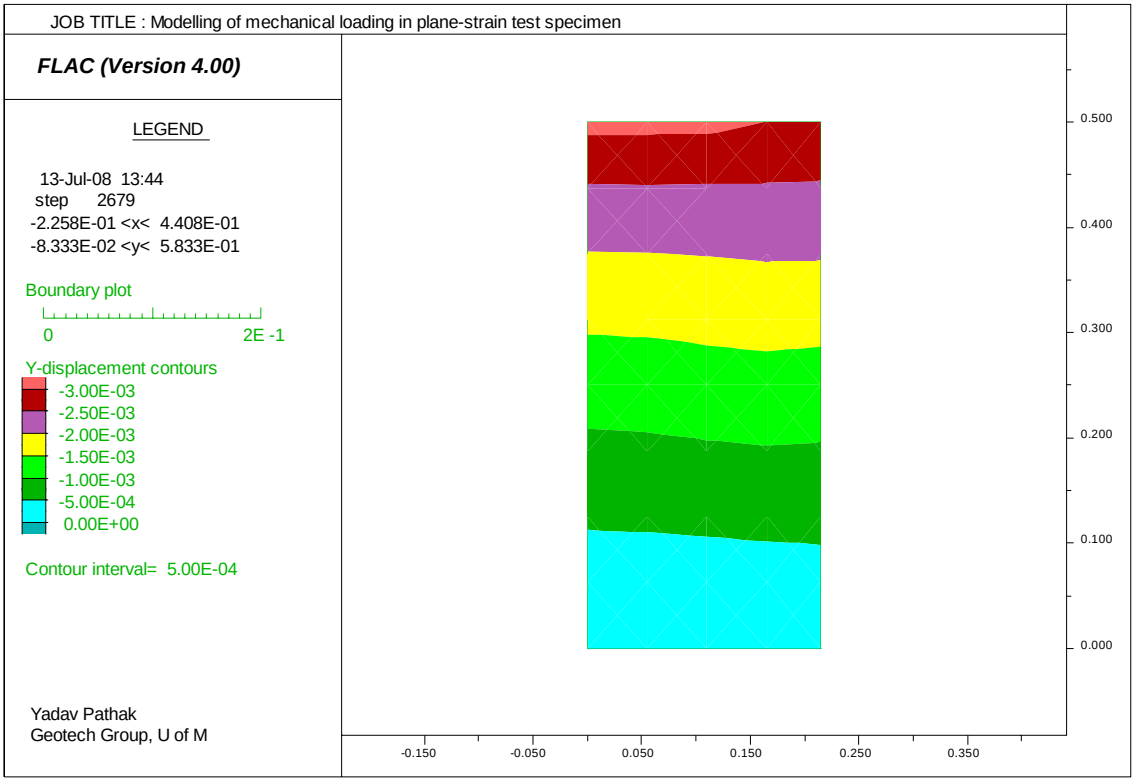

Figure C.9 Vertical displacement contours in unreinforced clay specimen UP50/35 due to mechanical load

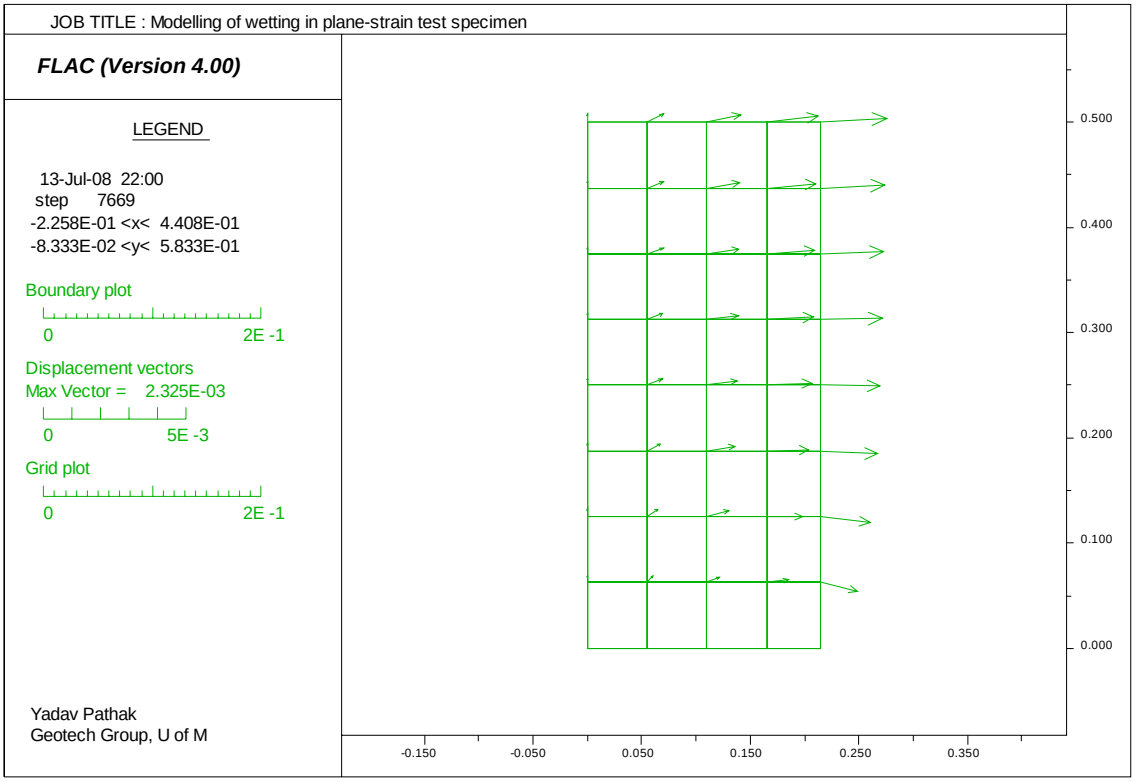

Figure C.10 Wetting-induced displacement vectors in unreinforced clay specimen UP50/35

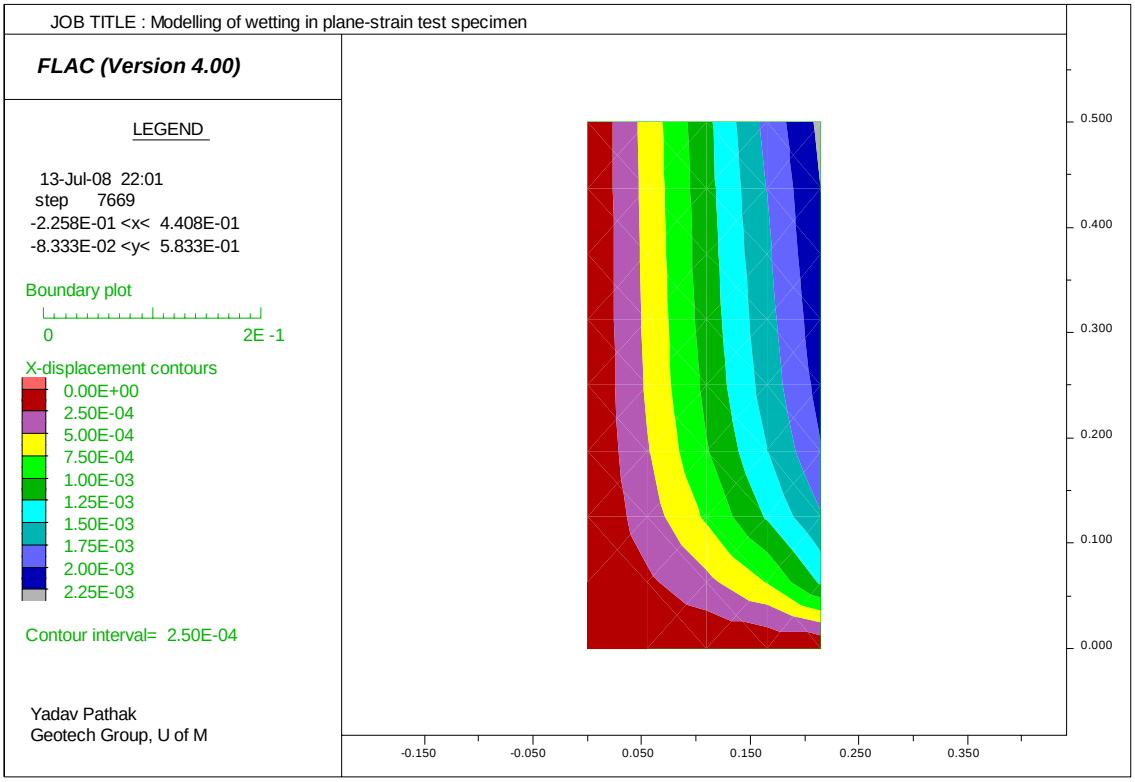

Figure C.11 Wetting-induced horizontal displacement contours in unreinforced clay specimen UP50/35

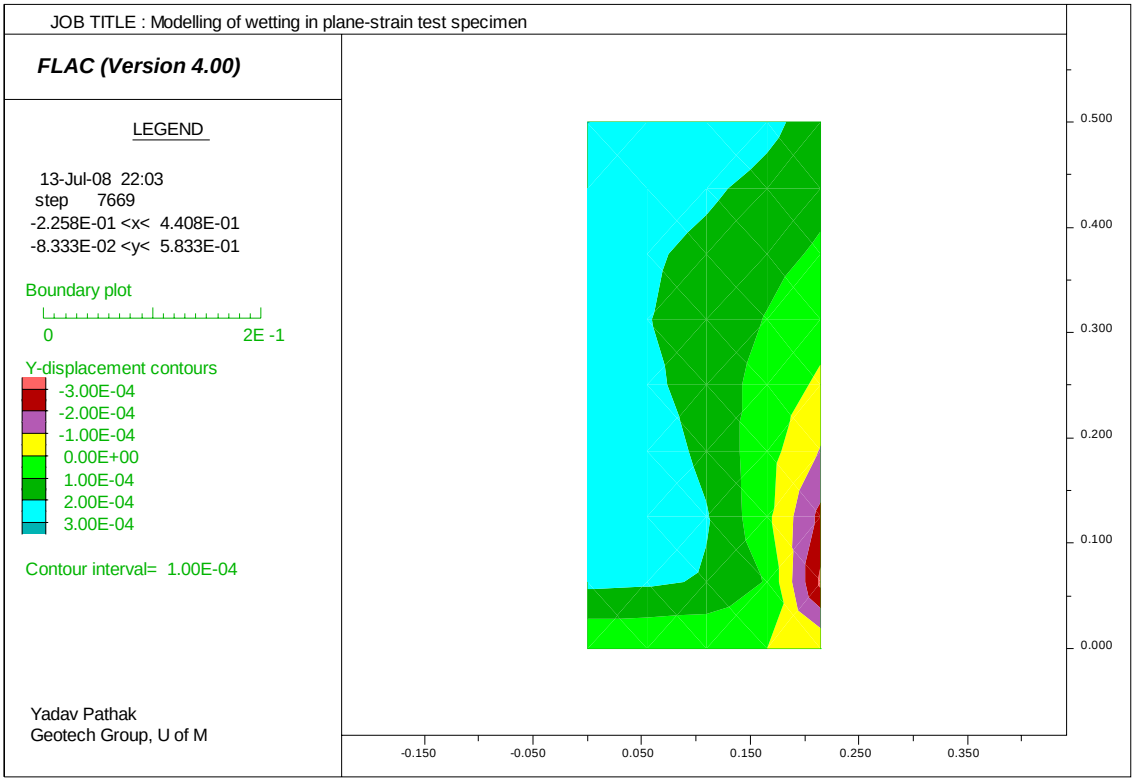

Figure C.12 Wetting-induced vertical displacement contours in unreinforced clay specimen UP50/35

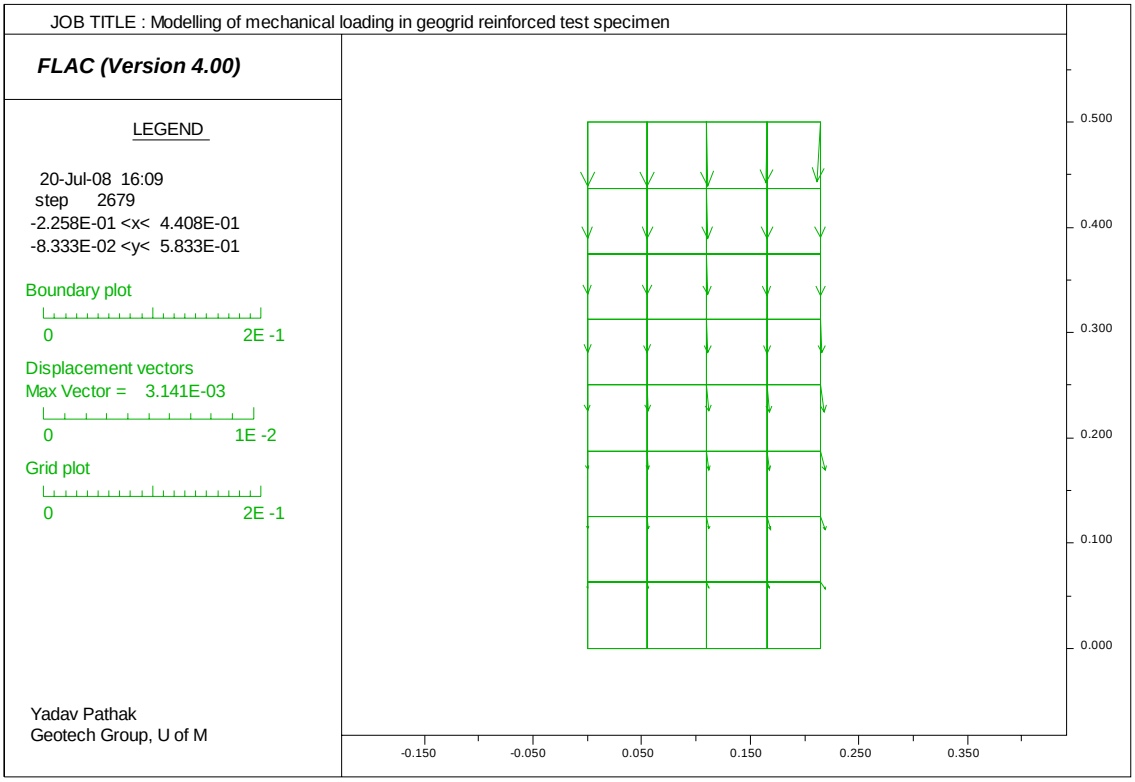

Figure C.13 Displacement vectors in geogird-reinforced clay specimen RP50/35 due to mechanical load

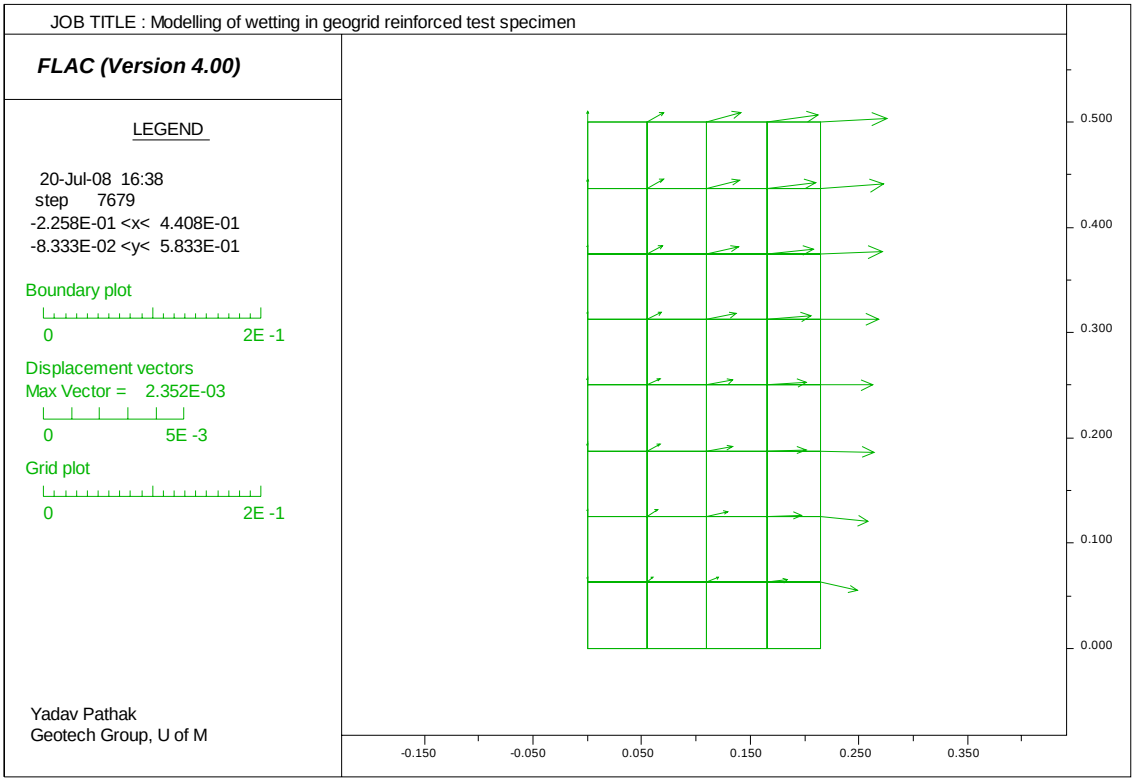

Figure C.14 Wetting-induced displacement vectors in geogrid-reinforced clay specimen RP50/35

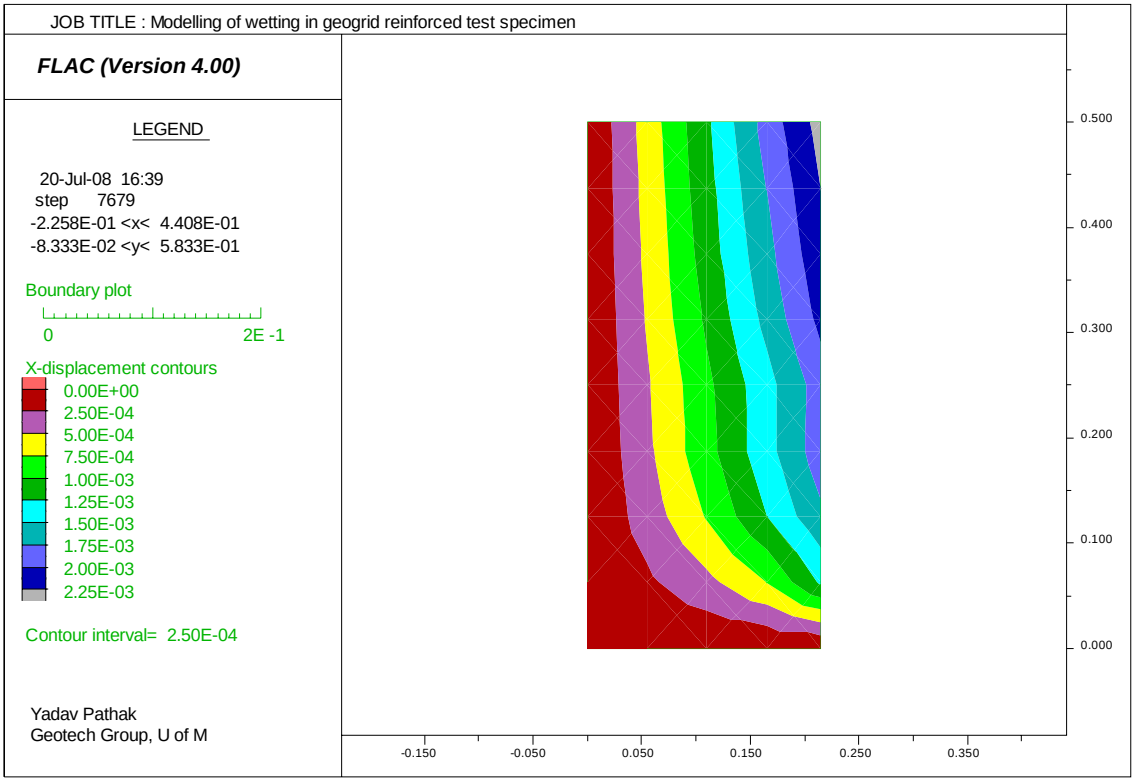

Figure C.15 Wetting-induced horizontal displacement contours in geogrid-reinforced clay specimen RP50/35

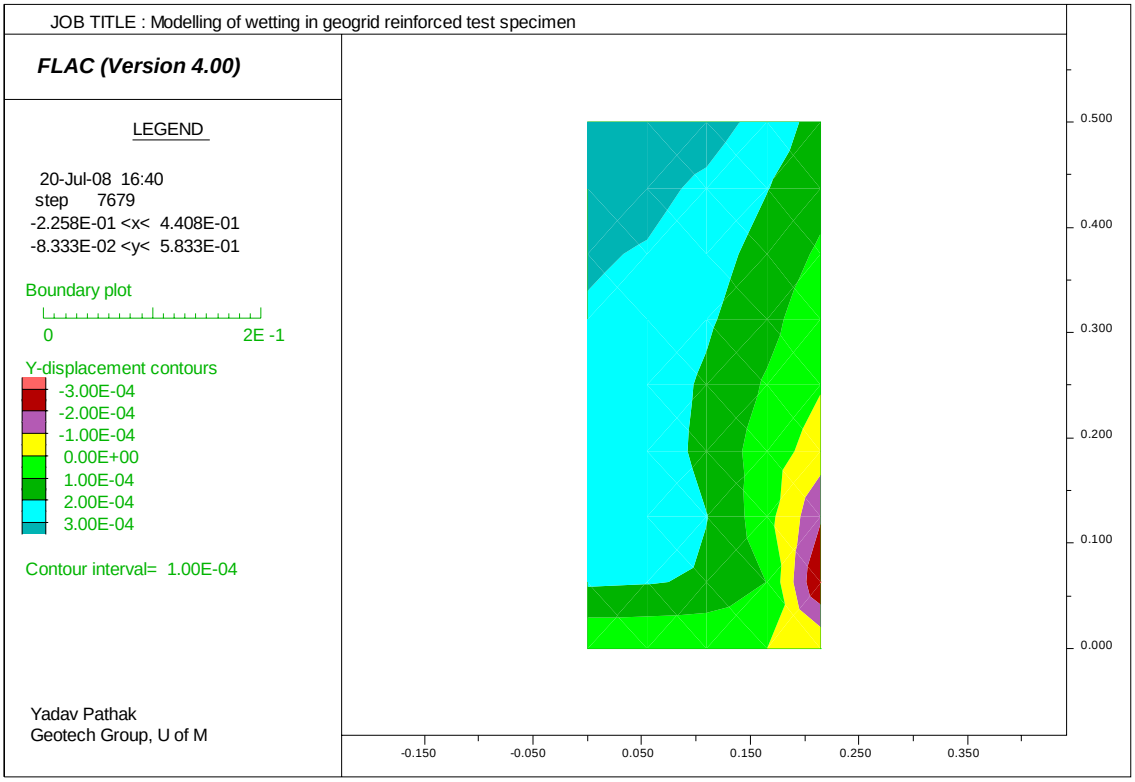

Figure C.16 Wetting-induced vertical displacement contours in geogrid-reinforced clay specimen RP50/35

APPENDIX D

CHAPTER 6 ADDITIONAL FIGURES

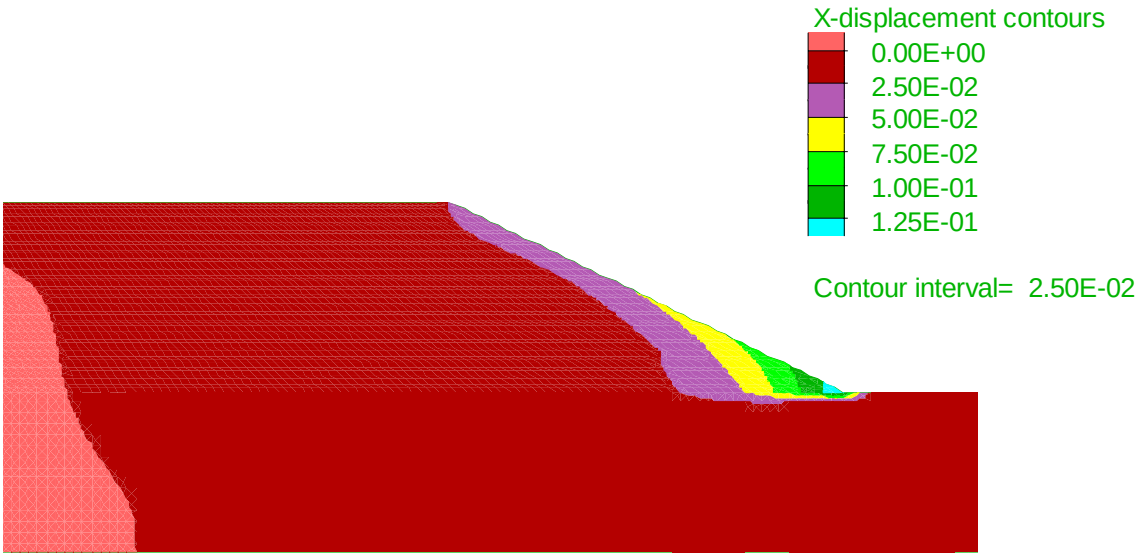

Figure D.1 Wetting-induced horizontal displacement contours of unreinforced clay slope in partial wetting of fill

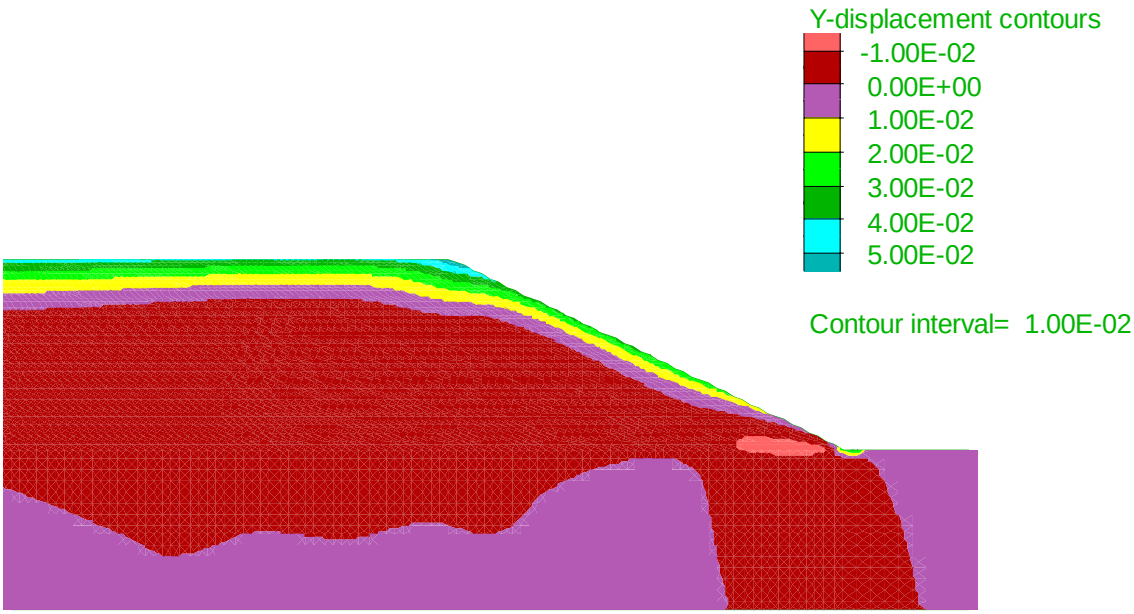

Figure D.2 Wetting-induced vertical displacement contours of unreinforced clay slope in partial wetting of fill

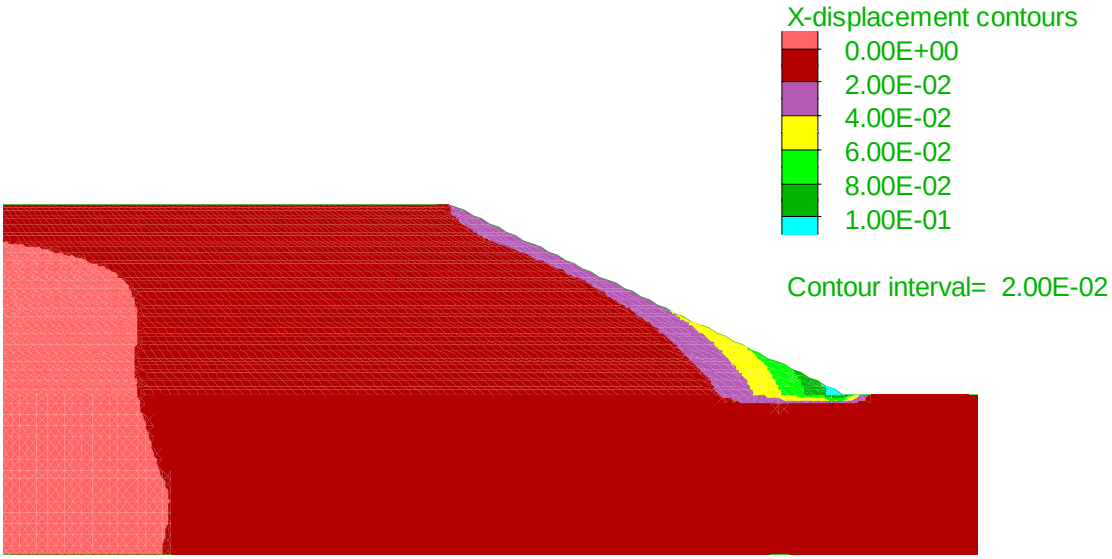

Figure D.3 Wetting-induced horizontal displacement contours of geosynthetic-reinforced clay slope in partial wetting of fill

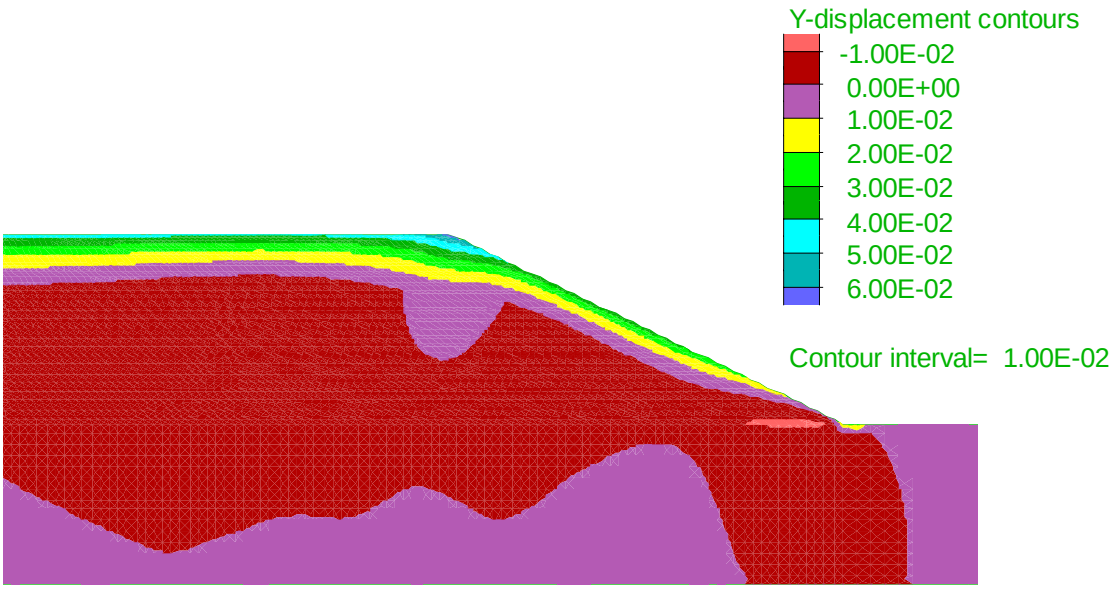

Figure D.4 Wetting-induced vertical displacement contours of geosynthetic-reinforced clay slope in partial wetting of fill

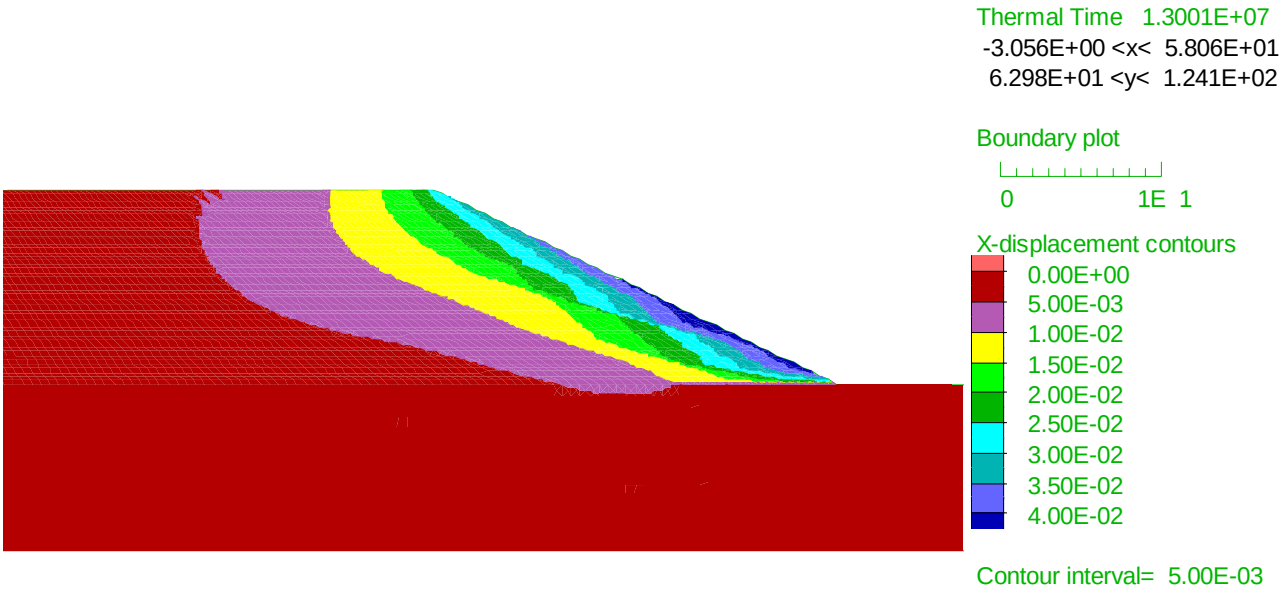

Figure D.5 Freezing-induced horizontal displacement contours of unreinforced silt slope

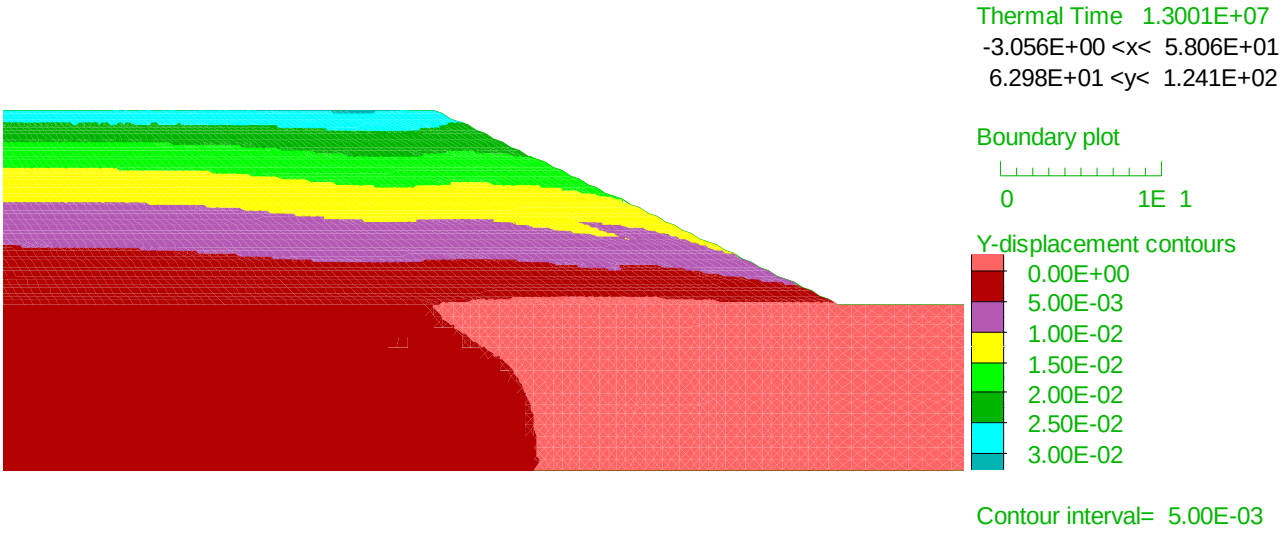

Figure D.6 Freezing-induced vertical displacement contours of unreinforced silt slope

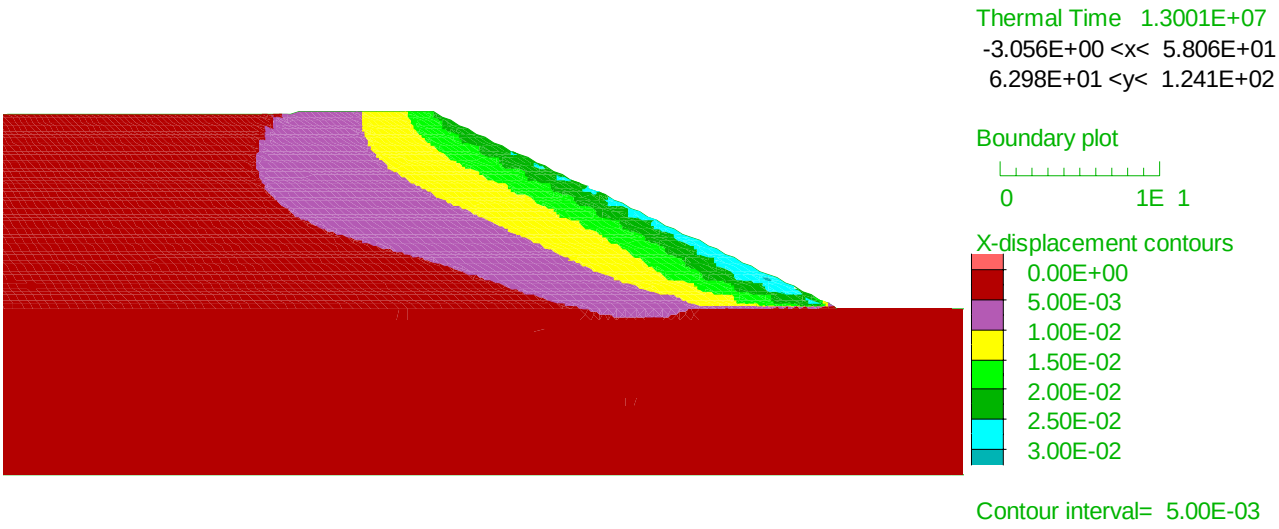

Figure D.7 Freezing-induced horizontal displacement contours of geosynthetic-reinforced silt slope

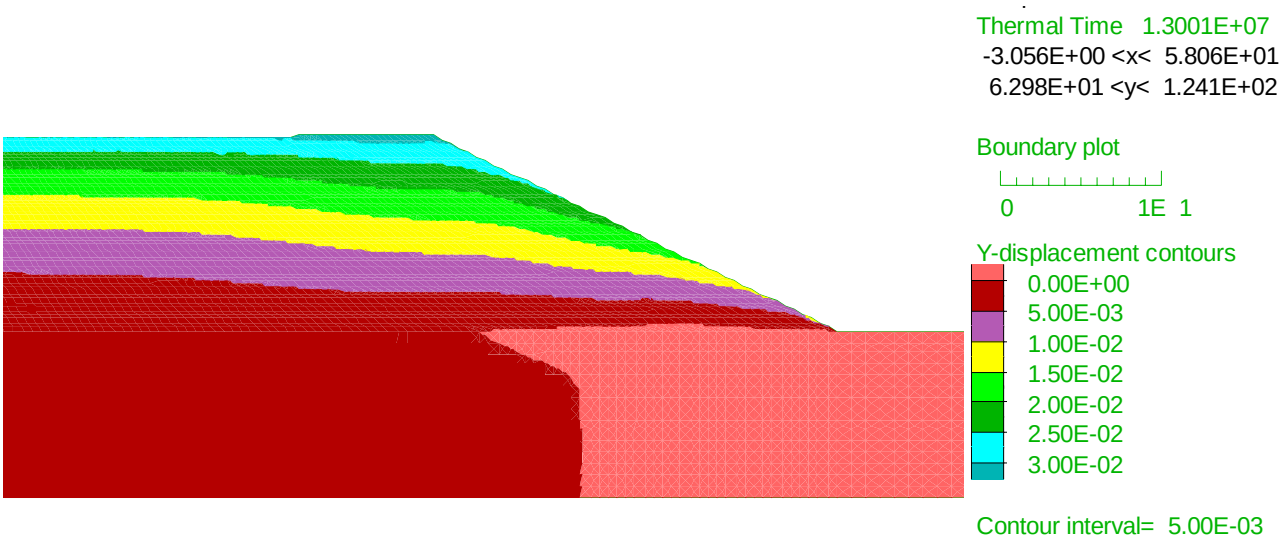

Figure D.8 Freezing-induced vertical displacement contours of geosynthetic-reinforced silt slope